



## A Bottom-Up Model for Energy Trading Markets and Prosumers Coordination in Microgrids

Wessam Ezzat Bedair Elbaz

Vollständiger Abdruck der von der Fakultät für Elektrotechnik und Informationstechnik  
der Technischen Universität München zur Erlangung des akademischen Grades eines

**Doktor-Ingenieurs (Dr.-Ing.)**

genehmigten Dissertation.

**Vorsitzender:**

Prof. Dr.-Ing. Hans-Georg Herzog

**Prüfende der Dissertation:**

1. Prof. Dr.-Ing. Ulrich Wagner
2. Prof. Dr. Gunther Friedl

Die Dissertation wurde am 17.12.2018 bei der Technischen Universität München  
eingereicht und durch die Fakultät für Elektrotechnik und Informationstechnik am  
14.03.2019 angenommen.



# Abstract

Technological advances and the need for a low-carbon economy enabled renewable energy systems to lead the energy transition. Globally, countries are altering their energy policies and adapting goals on the national and regional levels to support the integration of renewables and transform conventional consumers to prosumers. However, the developments in infrastructure cannot keep pace with energy system transformations or expected goals. Hence, advanced energy management and coordination techniques are adopted to align the infrastructure capabilities with the rapid growth in renewables and increase the overall system efficiency. At the level of microgrids, local energy trading markets can be a key solution to actively involving the prosumers in the local energy system through financial incentives. They can offer the grid operators a versatile solution for energy coordination without violating prosumer privacy.

In this dissertation, a comprehensive solution is offered for a local energy trading market that bridges the gap between simulation and real-life requirements. Hence, a bottom-up approach is adopted in designing the market model to identify the technical system constraints and dynamics at the device, building, and microgrid level. At the device level, non-linear models are presented and experimentally validated based on testbeds. Furthermore, a probabilistic forecasting system is integrated that is designed for small-scale photovoltaic systems of prosumers and microgrids. At the building level, a home energy management algorithm is presented and evaluated based on multiple generic loads that represent the current and possible upcoming flexible devices. Based on these systems, a market model is developed with device-oriented bidding strategies that are tailored to the technical constraints and limitations of the most common flexible devices in residential buildings.

Based on intensive scenario analyses, the results show considerable benefits for both the prosumers and utility. For example, the base scenario indicates that the prosumer can attain an average yearly cost savings of 23% through energy trading. Additionally, an experimental demonstration is performed to compare the results and dynamics of the simulation models to the testbed. The energetic and dynamic analyses of the demonstration prove that the model is not only capable of enabling energy trading and management in microgrids but also simulating and representing real-life dynamics accurately.

## Keywords

Microgrid, market platforms, peer-to-peer trading, probabilistic PV forecast, Modelica, testbed, co-simulation, EMS, HiL, heat pump, micro-CHP, co-simulation, experimental demonstration.



# Zusammenfassung

Verschiedene technologische Fortschritte und die Notwendigkeit einer Wirtschaft mit reduzierten CO<sub>2</sub>-ausstoß ermöglichten es erneuerbaren Energiesystemen, die Energiewende voranzutreiben. Weltweit ändern Länder ihre Energiepolitik und passen Ziele auf nationaler und regionaler Ebene an, um die Integration erneuerbarer Energien zu unterstützen und herkömmliche Verbraucher zu Prosumenten zu machen. Insbesondere Entwicklungen in der Infrastruktur können jedoch nicht mit den Veränderungen des Energiesystems und den erhofften Zielen Schritt halten. Um die Leistungsfähigkeit der Infrastruktur an das schnelle Wachstum der erneuerbaren Energien anzupassen und die Gesamtsystemeffizienz zu steigern, werden daher innovative Ansätze im Bereich Energiemanagement sowie verschiedene Koordinierungstechniken angewandt. Auf der Ebene von Microgrids können lokale Energiehandelsmärkte dabei eine wichtige Lösung sein, um Prosumenten durch finanzielle Anreize aktiv in das lokale Energiesystem einzubinden. Diese Märkte können dabei Netzbetreibern eine vielseitige Lösung für die Energiekoordination bieten, ohne gleichzeitig die Privatsphäre des Prosumenten zu verletzen.

In dieser Dissertation wird eine umfassende Lösung für einen lokalen Energiehandelsmarkt vorgestellt, wodurch die Lücke zwischen Simulation und realen Anforderungen geschlossen wird. Zu diesem Zweck wird beim Entwurf des Marktmodells ein Bottom-Up-Ansatz gewählt, wodurch die technischen Systemeinschränkungen und -dynamiken auf Geräte-, Gebäude- und Microgrid-Ebene ermittelt werden können. Auf Geräteebene werden dazu nichtlineare Modelle verwendet, die in Versuchen an Prüfständen validiert wurden. Darüber hinaus ist ein probabilistisches Prognosesystem Bestandteil, das für kleine Photovoltaikanalgen von Prosumenten konzipiert ist. Auf Gebäudeebene wird ein Algorithmus für ein Haus-Energiemanagement vorgestellt, das mit Hilfe verschiedener generischen Lasten bewertet wird, die aktuelle Geräte abbilden und eine mögliche zukünftige Flexibilisierung adressieren. Basierend auf diesen Systemen wird ein Marktmodell mit geräteorientierten Gebotsstrategien entwickelt, die auf technische Bedingungen und Einschränkungen der gebräuchlichsten flexiblen Geräte in Wohngebäuden zugeschnitten sind.

Die Ergebnisse ausführlicher Analysen in verschiedenen Szenarien zeigen, dass der vorgestellte Ansatz erhebliche Vorteile für Prosumenten und Marktanbieter eröffnet. Zum Beispiel zeigt das Basisszenario, dass Prosumenten durch den Energiehandel eine durchschnittliche jährliche Kosteneinsparung von 23% erzielen können. Zusätzlich wurden Ergebnisse und Dynamik der Simulation mit Messungen am Prüfstand verglichen. Die Ergebnisse daraus zeigen, dass das Modell nicht nur Energiehandel und -management in Microgrids abbilden kann, sondern auch die reale Dynamik mit hoher Genauigkeit simuliert und darstellt.

## **Schlagwörter**

Microgrid, Handelsplattform, Peer-to-Peer Handel, probabilistische PV-Prognose, Mod-  
elica, Prüfstand, Co-Simulation, EMS, HiL, Wärmepumpe, Mikro-KWK, Co-Simulation,  
Prüfstandsversuche.

*Progress is made by trial and failure; the failures are generally a hundred times more numerous than the successes; yet they are usually left unchronicled*

*by Sir William Ramsay*

To Nawal, Karim, Emy, and Ezzat

# Acknowledgments

This dissertation was made possible by the continuous support of several people who have been a part of my life and journey.

I would like to express my sincere gratitude to Prof. Ulrich Wagner for supervising this work. I'm grateful for your continuous support, constructive criticism, suggestion and above all the freedom to investigate and demonstrate the different aspects of this dissertation. Prof. Gunther Friedl, I'm thankful for your support and readiness to evaluate the thesis. Prof. Dr.-Ing. Hans-Georg Herzog, thank you for hosting the examination.

Dr.-Ing. Peter Tzscheuschler; I'm indebted for all you have done for me in these past years. Thank you for being my advisor. Thank you for finding time for our long meetings in your busy schedule. Thank you for the feedback and the hours spent in reviewing my papers. As a matter of fact, no words can express my gratitude!

I would like to also thank all my colleagues at the institute of energy economy and application technology. Thank you for the numerous intellectual discussion that contributed to the success of this work and deepened my knowledge not only in the scope of this dissertation but in all other energy related research. A special thanks to Mr. Guido Hilgers and Mr. Andreas Werthmüller. Without their contribution, the demonstration part of this dissertation would not have been possible. Johannes Honold, Michel Zade and Lukas Hardi, thank you for proof-reading this dissertation and your feedback.

I would like to thank my student assistants Lysander Kiesel and Lukas Mayerhofer for their support in building and testing the demonstration.

My family and friends, thank you for being by my side and supporting me through this journey. My parents, Ezzat and Oaima, I'm grateful for all the love and support you have given at every stage of my life. My brother, Karim, you have been always my window to the other world, the politics world. I'm sure you are going to be a great politician one day. Shereen, Nadia, Abdelkhalek El Wakeel, Mahmoud and Hossam, thank you for all your support.

Nawal, my wife, no words can express how grateful am I for all your love and support. You were with me in my stressful and hardest times. I cannot forget the first thing you said when I submitted this dissertation. "We did it Sam!" you said. It is "we" who did it. Without you, it would have never been made.

Munich, December 2018  
Wessam El-Baz

*Wessam El-Baz*



# Contents

<b>List of Figures</b>	<b>xiii</b>
<b>List of Tables</b>	<b>xv</b>
<b>List of Publications</b>	<b>xvii</b>
<b>Acronyms</b>	<b>xix</b>
<b>1 Introduction</b>	<b>1</b>
1.1 Background . . . . .	2
1.1.1 Microgrid Definition and Evolution . . . . .	3
1.1.2 Coordination Requirements . . . . .	4
1.1.3 Auction Design and Peer-to-Peer Trading . . . . .	6
1.2 Research Gaps . . . . .	8
1.3 Research Objectives, Design, and Questions . . . . .	9
1.4 Dissertation Structure . . . . .	10
1.5 Publication Structure . . . . .	12
<b>2 Methods</b>	<b>13</b>
2.1 Flexible Prosumer Devices in Buildings . . . . .	13
2.1.1 Heat Pump . . . . .	13
2.1.2 Micro-CHP . . . . .	17
2.1.3 Electric Vehicle . . . . .	17
2.2 Probabilistic Forecast for PV Generation . . . . .	17
2.3 Energy Management System in Buildings . . . . .	21
2.4 Market Model Architecture . . . . .	23
2.4.1 Market Platform . . . . .	25
2.4.2 Decentralized HEMS . . . . .	26
2.4.3 Market Agents . . . . .	27
2.5 Market Scenarios Design . . . . .	31
2.6 Market Co-simulation and Input Data . . . . .	32
<b>3 Results</b>	<b>35</b>
3.1 Experimental Analysis of a Ground-Source Heat Pump . . . . .	35
3.1.1 Cycling Influence and Sensors Positioning . . . . .	35
3.1.2 Heat Pump Model Accuracy . . . . .	37
3.2 Day-ahead PV Forecasting . . . . .	37
3.2.1 Point Forecast . . . . .	37

*Contents*

3.2.2	Probabilistic Forecast . . . . .	38
3.3	Load Shifting Based on Probabilistic Forecast . . . . .	40
3.3.1	Conventional Household Loads . . . . .	40
3.3.2	Different Generic Loads . . . . .	41
3.4	Market Dynamics and Benefits . . . . .	42
3.4.1	Utility and Prosumer Benefits . . . . .	42
3.4.2	Prosumer Commitment . . . . .	44
3.4.3	Scenario Analysis . . . . .	44
<b>4</b>	<b>Validation and Demonstration</b>	<b>47</b>
4.1	Testbed Components and Structure . . . . .	47
4.2	Hardware in the Loop (HiL) Type Day Simulation . . . . .	49
<b>5</b>	<b>Conclusion, Discussion and Outlook</b>	<b>51</b>
5.1	Answers to Research Questions . . . . .	51
5.2	Concluding Remarks . . . . .	53
5.3	Outlook . . . . .	54
	<b>Bibliography</b>	<b>55</b>
<b>A</b>	<b>Appendix</b>	<b>63</b>
A.1	Publication 1 . . . . .	63
A.2	Publication 2 . . . . .	94
A.3	Publication 3 . . . . .	129
A.4	Publication 4 . . . . .	159
A.5	Publication 5 . . . . .	197
A.6	Publication 6 . . . . .	224
A.7	Publication 7 . . . . .	244

# List of Figures

1.1	Development trends of energy management methods in the literature [1]. . . . .	5
1.2	Microgrid abstract structure for the energy market model. . . . .	9
1.3	Research questions at each level of the model and demonstration. . . . .	11
1.4	Appended publications in the dissertation. . . . .	12
2.1	The flow of the experimental procedures presented in Publication 1. . . . .	14
2.2	The heat pump model structure presented in Publication 1. . . . .	16
2.3	Clear sky model output and PV power measurements after the partial shading detection process as presented in Publication 2. . . . .	18
2.4	Simplified flow chart describing the process of probabilistic forecast generation as presented in Publication 2. . . . .	21
2.5	Flow chart of the load shifting algorithm as presented in Publication 3. . . . .	22
2.6	An overview of the market components and communication structure as presented in Publication 4. . . . .	24
2.7	Selected day of probabilistic forecast output and PV measurements, (a) transient (b) transient-1 min resolution as in Publication 4. . . . .	30
2.8	An overview of scenario groups as in Publication 5. . . . .	31
2.9	Model division on the co-simulation platform between Matlab and Mod- elica as presented in Publication 4. . . . .	32
2.10	74 representative household profile analyses, (a) annual energy consump- tion (b) electrical loads on a typical day as in Publication 5. . . . .	33
3.1	Cycling effect on the heat pump system performance, (a) constant con- tinuous load (b) constant return temperature as presented in Publication 1. . . . .	36
3.2	Probabilistic forecast output and PV measurements in multiple days in different seasons, (a) winter (b) winter-1 min resolution (c) summer (d) summer-1 min resolution as presented in Publication 2. . . . .	38
3.3	Comparison between the reference and the probabilistic forecast on a typ- ical day. White goods optimally shifted based on (a) reference forecast, and (b) probabilistic forecast as presented in Publication 3. . . . .	40
3.4	Different generic loads sizes shifted based on the probabilistic forecast - number of loads (colored). (a) 0.25 kW. (b) 0.5 kW. (c) 1 kW. (d) 1.5 kW as presented in Publication 3. . . . .	41
3.5	Type day profile of the whole microgrid, (a) summer day - reference (b) summer day - market (c) winter day - reference (d) winter day - market. . . . .	43

*List of Figures*

3.6	Percentage of unsatisfied bids against the $\zeta$ of the PV prediction and the available battery capacity as presented in Publication 4. . . . .	44
4.1	Simplified hydraulic scheme of the testbed. . . . .	48
4.2	The three modules and the heat pump installation in the lab. . . . .	48
4.3	Heat pump dynamics of the testbed operation with HiL and simulation model, (a) space heating thermal power (b) space heating supply and return temperatures as presented in Publication 7. . . . .	49

# List of Tables

3.1	CRPS of different training horizons as in Publication 2. . . . .	39
3.2	BS of different training horizons as in Publication 2. . . . .	39



# List of Publications

## Appended Publications

This dissertation is based on the following appended publication:

1. **W. El-Baz**, P. Tzscheuschler and U. Wagner. Experimental study and modeling of ground-source heat pumps with combi-storage in buildings, *Energies* (11), 2018. doi:10.3390/en11051174
2. **W. El-Baz**, P. Tzscheuschler and U. Wagner. Day-ahead probabilistic PV generation forecast for buildings energy management systems, *Solar Energy*, 171, 2018. doi:10.1016/j.solener.2018.06.100
3. **W. El-Baz**, M. Seufzger, S. Lutzenberger, P. Tzscheuschler, and U. Wagner. Impact of probabilistic small-scale photovoltaic generation forecast on energy management system, *Solar Energy*, 165, 2018. doi:10.1016/j.solener.2018.02.069
4. **W. El-Baz**, P. Tzscheuschler, and U. Wagner. Integration of energy markets in microgrids: A double-sided auction with device-oriented bidding strategies, *Applied Energy*, 241C, 2019. doi:10.1016/j.apenergy.2019.02.049
5. **W. El-Baz**, P. Tzscheuschler, and U. Wagner. Evaluation of energy market platforms potential in microgrids: Scenario analysis based on a double-sided auction, *Frontiers in Energy Research* 7:41. doi: 10.3389/fenrg.2019.00041
6. **W. El-Baz**, F. Sänger, P. Tzscheuschler, Hardware in the Loop (HIL) for micro CHP Systems. In *Proceedings of the Fourth International Conference on Micro-generation and Related Technologies*, Tokyo, Japan, 28–30 October 2015
7. **W. El-Baz**, L. Mayerhofer, P. Tzscheuschler and U. Wagner. Hardware in the loop real-time simulation for heating systems: Model validation and dynamics analysis, *Energies* (11), 2018. doi:10.3390/en11113159

## Supplementary Publications

Supplementary datasets and Open Source software publications:

8. **W. El-Baz**, J. Honold, L. Hardi, and P. Tzscheuschler. High-resolution dataset for building energy management systems applications. *Data in Brief*, 2018. doi: 10.1016/j.dib.2017.12.058

9. **W. El-Baz**, M. Eldakadosi, and C. Eren. P3- Prediction System. 2018. doi: 10.5281/zenodo.1412785. <https://welbaz.github.io/p3/>

## **Other Relevant Publications**

Other relevant publications that are not presented in this dissemination:

10. M. Zade, Y. Incedag, **W. El-Baz**, P. Tzscheutschler and U. Wagner. Prosumer integration in flexibility Markets: A bid development and pricing model. Proceedings of the 2nd IEEE conference on Energy Internet and Energy System Integration, Beijing, China, 20-22 October 2018.
11. D. Zinsmeister, and **W. El-Baz**. Hardware in the loop applications for intelligent energy management and coupled energy system analysis. Proceedings of ESI SimulationX User Forum 2018, Dresden, Germany, 8-9 November 2018.
12. **W. El-Baz**, and P. Tzscheutschler. Autonomous coordination of smart buildings in microgrids based on a double-sided auction. In Proceedings of IEEE Power & Energy Society General Meeting, Chicago, IL, USA, 16–20 July 2017.
13. **W. El-Baz**, C. Kandler, P. Wimmer, and P. Tzscheutschler. Practical experiences with smart homes modeling and simulation. Proceedings of ESI SimulationX User Forum 2016, Dresden, Germany, 24-25 November 2016.
14. P. Tzscheutschler, **W. El-Baz**, C. Heilek, J. Lipp, and M. Windeknecht. Optimierung von Mikro-KWK-Systemen. Lehrstuhl für Energiewirtschaft und Anwendungstechnik, Munich, Germany, 2016.
15. **W. El-Baz**, and P. Tzscheutschler. Short-term smart learning electrical load prediction algorithm for home energy management systems, Applied Energy, 147, 2015.
16. **W. El-Baz**, and P. Tzscheutschler. Co-simulation of a smart home model based on a micro electricity market. Proceedings of the Fifth German-Austrian IBPSA Conference RWTH Aachen University, 22-24 September 2014.
17. P. Tzscheutschler, and **W. El-Baz**. Smart home model based on an interactive DSM devices within a micro electricity market. Proceedings of the Fifth German-Austrian IBPSA Conference RWTH Aachen University, 22-24 September 2014.

# Acronyms

BS	Brier Score.
BSS	Brier Skill Score.
CB	Conventional Billing.
CDF	Cumulative Distribution Function.
CEMS	Centralized Energy Management System.
COP	Coefficient of Performance.
CRPS	Cumulative Ranked Probability Score.
CRPSS	Cumulative Ranked Probability Skill Score.
CSM	Clear Sky Model.
DES	Distributed Energy Systems.
DHW	Domestic Hot Water.
DSM	Demand Side Management.
DTW	Dynamic Time Warping.
EEG	Renewable Energy Sources Act.
EMS	Energy Management System.
EnEG	Energy Conversion Act.
EnWG	Energy Industry Act.
EV	Electric Vehicle.
FIT	Feed-in Tariff.
FS	Forecast Skill.
GHG	Greenhouse Gas.
GSHP	Ground-Source Heat Pump.
HEMS	Home Energy Management System.
HiL	Hardware in the Loop.
HP	Heat Pump.
ICT	Information and Communication Technology.
IIS	Information Infrastructure.
KWKG	Combined Heat and Power Act.

## *Acronyms*

MA	Market Agent.
MAE	Mean Absolute Error.
MAPE	Mean Absolute Percentage Error.
MB	Market Billing.
MBE	Mean Biased Error.
Micro-CHP	Micro Combined Heat and Power System.
P2P	Peer-to-Peer.
PV	Photovoltaic.
RES	Renewable Energy Sources.
RMSE	Root Mean Square Error.
RTP	Real Time Pricing.
SH	Space Heating.
SOC	State of Charge.
SPF	Seasonal Performance Factor.
TDI	Temporal Distortion Index.
TOU	Time-of-Use.
UP	User Preferences.
WLTC	Worldwide Harmonized Light Duty Driving Test Cycle.

# 1 Introduction

The threats of climate change to the global ecosystem are reshaping the energy policy globally. Several limitations have been imposed on Greenhouse Gas (GHG) and the use of fossil fuels. At the EU level, the 2020 climate and energy package set of legislations was imposed to cut the GHG emissions from 1990 levels and increase renewable energy generation and efficiency by 20% in 2020 [2]. In Germany, long-term goals were embraced within the climate action plan program that aim towards reaching at least 55% reduction of GHG in 2030 [3, 4]. Several regulations were introduced such as Renewable Energy Sources Act (EEG), Combined Heat and Power Act (KWKG), Energy Conversion Act (EnEG), and Energy Industry Act (EnWG) to reach these goals [5–8]. These regulations led to restructuring of the energy sector and changed the pace at which Renewable Energy Sources (RES) are being exploited.

On the supply side, the electricity grid is facing the outcomes of such energy policy transformations. Among the several regulations, the EEG has one of the most significant impacts on the grid. The act prioritizes the RES in the energy market through guaranteeing a Feed-in Tariff (FIT) and providing a risk-free environment for the investors. Enforcing this act along with the continuous decrease in investment costs of renewable energy systems led to an expansion in the installations of Photovoltaic (PV) systems and wind turbines. At the end of 2017, the number of PV installations reached 1.6 million and produced 43 GW. In addition, by the end of the same year, the share of electricity generation by wind turbines has also grown to constitute 16% of the generated energy, and a capacity of 5.4 GW. This capacity is expected to increase to 15 GW by the end of 2030 [8]. The investors in renewable energy are not exclusively the conventional energy sectors stakeholders. The current policies also attracted residential and industrial consumers. For example, 39.4% of the installed PV capacities are owned by the residential sector, and 19.2% are owned by the industrial and commercial sectors [8]. Hence, the conventional consumers are gradually being transformed into prosumers.

On the demand side, Heat Pump (HP) and Electric Vehicle (EV) loads are being continuously integrated into the electricity grid. In 2016, the HP installations in new buildings reached 31.8% representing a market share of 34% for single-family houses, 16% for multi-family houses and 13.6% for non-residential buildings. Moreover, the number of EVs as well as their power demand share is growing [9]. In Germany, a target was set to reach 1 million EVs by 2020, given that EVs are defined as vehicle producing not more than 50g CO<sub>2</sub>/km or having an electric drive range of at least 40 km [10–12]. Although HP and EV are major role players in the electrification of the energy system via coupling the heat and transportation sector to the electricity sector, they introduced new challenges to the grid operators.

## 1 Introduction

The fluctuating RES based supply and the growing loads rendered the conventional approach of managing the grid obsolete. The conventional approach is suitable for uni-directional power supply and inelastic demands, yet it is not fit to the modern digitized grid. The developments in the communication infrastructure, Information and Communication Technology (ICT), and computational powers are enabling a broad range of possibilities to manage the electricity grid. The digitalization of the grid provides the basis to connect the different Distributed Energy Systems (DES) and loads to facilitate an active participation from the prosumer side. Hence, an opportunity is available to overcome the barriers established by the energy transition if the prosumers' flexibility potential is adequately and comprehensively utilized.

Using the flexibility of the prosumers is about "putting people in the loop"[13]. The idea of using the prosumer's flexibility to shift a load between two points in time may sound simple. However, any control method does not only have to address the technical challenges of the grid but also the people's need for autonomy and maintaining their data privacy. Moreover, it has to guarantee proper incentives for the active participation in the "loop".

This dissertation presents a market model for microgrid coordination and quantifies its potential under multiple scenarios from the perspective of the prosumer and the utility. The study tries to bridge the gap between the numerical simulation and real-life environment. Hence, a detailed bottom-up approach is followed in modeling and analyzing the market model. It starts by discussing the smallest unit in the energy system, a household device, and ends at the microgrid. At the device level, devices are modeled and optimized based on testbeds to visualize the real-life system dynamics and assure the quality of the results. Furthermore, a tailored forecasting system is developed for the Home Energy Management System (HEMS) and energy markets, which addresses the generation uncertainties of the common small-scale prosumers. At the building level, the load shifting potential of a HEMS is evaluated using the developed forecasting system and multiple generic household loads. At the microgrid level, the device models, forecasting system, and HEMS are integrated into a discrete-timely double-sided auction with device-oriented bidding strategies to evaluate the market dynamics, utility and prosumers' benefits. The model dynamics and results are then demonstrated using Hardware in the Loop (HiL) real-time simulations to emphasize the practicality and accuracy of the model.

### 1.1 Background

This section highlights the most important concepts for the implementation of energy trading markets in microgrids. The microgrids are defined along with their future role in the energy systems. The challenges facing the future vision of the microgrids are discussed. Requirements and criteria for microgrids' coordination to use the prosumers' full flexibility potential are defined. Furthermore, the basics of auction markets and the potential use of their resource allocation power for microgrid coordination are presented.

### 1.1.1 Microgrid Definition and Evolution

A microgrid is defined as a group of loads and generators that are operating together in a low or medium voltage grid [14]. This concept of a microgrid is as old as the electricity network. The earliest electricity grids were microgrids before their expansion to regional or super grids. However, along with the massive penetration of RES such as PV, battery systems, in addition to Micro Combined Heat and Power System (Micro-CHP) and their heat storages, new definitions and roles emerged for the microgrids.

A more recent descriptive definition of a microgrid presented by the workgroup C6.22 of the Conseil International des Grades Réseaux Électriques (CIGRE) is “*Microgrids are electricity distribution systems containing loads and distributed energy resources, (such as distributed generators, storage devices, or controllable loads) that can be operated in a controlled, coordinated way either while connected to the main power network or while islanded,*” [15]. A similar definition was also introduced by the U.S. Department of Energy [16] and other researchers as in [17, 18]. In all these definitions, the microgrid is no longer an independent entity but rather an active component of the national grid. Hence, the grid can be seen as a network of mini and microgrids that can be islanded or connected at any time of the day.

These definitions also fit with the German vision for the role of microgrids in the national grid. Within the framework of the SINTEG C/sells project [19], the national grid is seen as multiple cells. The cell size can vary to include an individual site such as a building, a microgrid, or a whole distribution grid. Each of these cells can balance their loads and generation, and exchange energy with the other cells in the systems.

Although different roles and functions were discussed in the literature for the microgrids that fit the aforementioned definitions [20–24], the goals and expected benefits were similar. They were all oriented towards the need of minimizing the cost of operation of the grid, increasing the overall generation efficiency, minimizing energy supply cost, reducing the environmental impact and assuring the security of supply. These roles can be summarized in the following points:

- Use and control the local generation resources such as PV, batteries, and Micro-CHP to maximize the autonomy and self-consumption.
- Act as a virtual resource to deliver ancillary services (i.e., flexibility) to different locations in the grid, e.g., act as load or virtual power plant to make up for the fluctuating RES.
- Provide reliability services, such as emergency services, to serve particular sensitive loads.

Within the framework of this dissertation, a microgrid is defined as a connected entity to the national grid. In the microgrid, different DES and flexible loads are coordinated in a way that reduces costs and CO<sub>2</sub> emissions, increases efficiency, autonomy, and self-consumption. Hence, at any point of time, the microgrid is assumed to be able to exchange energy with the grid, if there is an excess or deficit in generation.

### 1.1.2 Coordination Requirements

In the literature, several models discussed the optimization techniques required for the flexible devices coordination at the prosumer and microgrid level. Examples of these techniques and algorithms are stochastic optimization [25], mixed integer quadratic programming [26], mixed integer linear programming (MILP) [27, 28], fuzzy logic [29–31], and other machine learning techniques [32]. Over the last decade, the optimization techniques did not vary, as much as the use-cases on which the model was based. Each use case and optimization technique was tailored to address either the prosumers, or utility requirements. These requirements can be summarized in the following points:

- Scalability: the coordination or control mechanism has to be scalable such that it guarantees an immediate real-time reaction independent of the number of participants or devices in the microgrid.
- Decentralization: the prosumer has to be autonomous (i.e., independent). Each prosumer has to decide about their means of participation for microgrid coordination.
- Guaranteeing the prosumers' reaction: the feedback of the prosumer has to be known to estimate the overall prosumers' reaction within the microgrid.
- Data privacy: no information should be exchanged about the prosumer or devices status (e.g., the operation starting time, ending time, manufacture of the device, or frequency of usage).
- Fair division of economic benefit: prosumers should be monetarily compensated depending on their active participation (i.e., flexibility) in the microgrid.

A prosumer controlled HEMS reacting to a Real Time Pricing (RTP) seemed to be satisfying the presented coordination requirements. Figure 1.1 (left) shows the communication structure between the utility and prosumer using this approach. The utility sends a RTP that drives the prosumers to shift their load from peak hours to off-peak hours. Several researchers studied the HEMS load shifting and economic potential of RTP from different perspectives and household configurations as in [28, 33, 34]. These studies and models did satisfy scalability, decision decentralization, and data privacy, but they did not guarantee the prosumers' reaction to the signal. If each household has a HEMS that operates autonomously, all the prosumers might switch on their loads or feed energy to the grid at almost the same time. Consequently, the overall results would be the formation of another peak, up to 50% higher [35], at another point in time. Moreover, on the prosumer-side, another requirement was imposed by device manufacturers, which is the need for decentralization at the household level as discussed in [36, 37] and the e-MOBILie Project [38]. Device manufacturers do not allow direct access to the household device if the device's warranty is to be maintained, especially for EVs. Consequently, another architecture was developed based on the RTP that enables decentralized HEMS, where the device itself handles the decision-making process. In this

case, the HEMS is used only for communicating the user preferences and initiating the optimization process. Figure 1.1 (left) shows the difference between the centralized and decentralized HEMS, where I/O is the switching signal forwarded to the device.

At the level of an island or grid-connected microgrids, the Centralized Energy Management System (CEMS) was introduced to satisfy the requirement of guaranteeing the prosumers' reaction. The CEMS receives all the User Preferences (UP) of all prosumers within the microgrid, then tries to achieve an optimal plan based on the algorithms mentioned earlier. Such a system can maximize the economic benefits, satisfy the prosumers' constraints, and exploit the maximum flexibility potential. Nevertheless, since the CEMS receives all the user information to start the optimization iterations, it violates the data privacy requirements and exhibits a limited scalability [39, 40]. The HEMS, in this case, acts as a gateway. It provides the UP and receives the switching plan of the given devices. Figure 1.1 (middle) shows the communication architecture between the HEMS and CEMS.

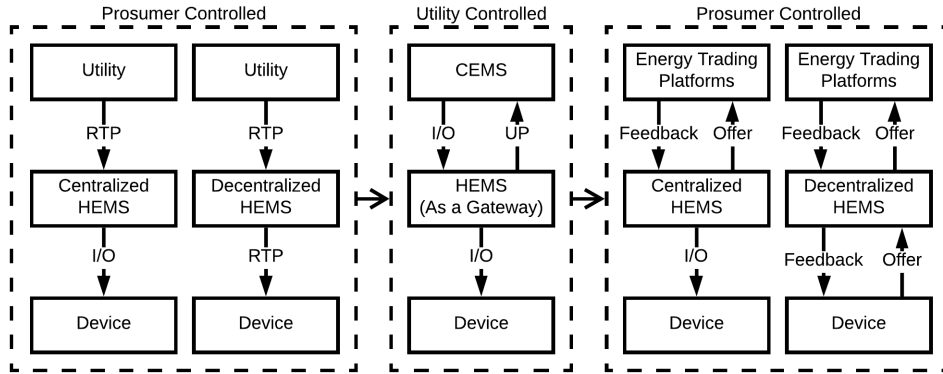


**Figure 1.1:** Development trends of energy management methods in the literature [1].

Energy trading platforms and market models are the decentralized energy management systems at the microgrid level. They are not only meant for energy trading but also coordination of the microgrid as discussed in [35]. These platforms are scalable due to the absence of a running optimization loop at the microgrid level. They are decentralized as each prosumer decides on their means of participation and optimization strategy. Moreover, they guarantee the prosumers' reaction as the platforms receive a feedback from the prosumer about their intentions and commitment to the communicated offers as in Figure 1.1 (right). They maintain the data privacy as the prosumer has to only decide on the time, volume and price of energy offered or asked. Hence, all the detailed information (e.g., EV start time, end time, load) are encrypted in the economic signal being communicated. They guarantee a fair division of economic benefit as the incentives received by the prosumers depend on their active participation in the microgrid coordination and the competitive market equilibrium.

At the prosumer level, these markets can communicate with a centralized or decentralized HEMS as in Figure 1.1 (right). In this dissertation, the market model is designed to

operate with decentralized HEMS to maintain a realistic communication structure that fits with the device manufacturer's requirements as well.

### 1.1.3 Auction Design and Peer-to-Peer Trading

A market is defined as “*a regular gathering of people for the purchase and sale of provisions, livestock, and other commodities,*” [41]. Whenever there are supply and demand for any commodity or service, a market can exist. The primary function of this market is to define two variables; the unit price  $p$  and the quantity  $q$  to be traded, such that all buyers are willing to buy at  $p$  or higher and all sellers are willing to sell for  $p$ , or lower can exchange  $q$ .

An auction market is managed by an auctioneer who is responsible for clearing the market [42, 43]. The outcomes of any auction are determined based on three factors: bidding rules, market-clearing rules, and information dissemination rules [44]. The bidding rules represent the form of the bid. For example, it can be price only, price and quantity, or quantity only. The market-clearing rules define the timing rules, closing conditions, rules for bid improvement, and final  $p$  and  $q$  (winning rules). The information dissemination rules limit the available information to the bidders. The information can be the bid prices or quantities of other bidders.

There are several types of auctions used in trading common commodities. Single-sided and double-sided auctions represent the two major categories of auction designs. In a single-sided auction, all buyers or sellers compete at the same time to acquire or sell a commodity, respectively. A simple example of the single-sided auction is eBay. A seller offers a product at a specific reserve price, and all buyers compete to get the product. In a double-sided auction, both buyers and sellers are involved and simultaneously competing to allocate their share of the available commodities [45]. In the electricity sector, single- and double-sided auctions are both implemented in wholesale markets in different forms (e.g., sealed-bid, hybrid or descending) as discussed by [43].

However, double-sided auctions are attracting more researchers for their resource allocation power and applications in online electronic markets. Compared to other auction types, there are several design parameters or attributes for double-sided auctions. These parameters directly influence the market-clearing and bidding rules [46]. Among all the possible parameters, two categorize double-sided auctions: the clearing time and the pricing mechanism.

The clearing of a double-sided auction can be continuous or discrete-timely. In continuous double-sided auction, every bid is matched immediately as soon as it is received. Remaining bids can be kept in an order book until cleared. A discrete-timely double-sided auction clears the market at fixed time intervals. As indicated by [47], this clearing can occur multiple times within the same trading period or at the end of the trading period. Several researchers discussed the advantages and disadvantages of the two mechanisms in terms of market efficiency and influence on trading behavior as in [48]. However, Haas et al. stated that continuous-time trading in online markets could be inherently flawed [49]. In a continuous double-sided auction, faster market participants might have an edge over other competitors, and the trading speed is not only a function

of the decision-making process but also the communication infrastructure. Hence, a market participant who has a fiber optic infrastructure might claim more benefits than other competitors due to a few milliseconds delay or lower latency in communication.

In double-sided auctions, there are two options for setting the market price, either by the market participants or auctioneers. The seller can indicate the acceptance of a bid if it has a higher value than the asked value, or the auctioneer can set a market clearing price for all the market participants depending on the supply and demand. These two cases are defined as the pay-as-bid or uniform pricing, which are also referred to in the literature as non-institutional and institutional pricing, respectively. The continuous double-sided auction inherently has a pay-as-bid clearing mechanism because the market has to be cleared immediately once two bids can be matched. On the other hand, the discrete-timely double-sided auction uses a uniform clearing mechanism. In the literature, several researchers discussed and compared the two mechanisms depending on the market regulations and the traded commodity as in [46,47,50]. In general, it was found that the uniform pricing is a fairer clearing mechanism since the set price is the competitive market clearing price. Hence, it encourages the sellers to bid their lowest price to increase their possibility of selling.

In auction design, several rules can be changed or imposed to change the market dynamics and market participants' trading behavior. These rules can vary depending on the nature of the commodity, traders, or state regulations. There is no "one-size-fits-all" design as discussed in [43]. Each design has its own advantages and disadvantages. Hence, in many cases, the auction design and rules have to be tailored to fit the purpose of the market.

However, Peer-to-Peer (P2P) can be any of the aforementioned auction designs. A P2P market is any market that allows two parties, a buyer and a seller, to trade their commodities [51–53]. The two parties are referred to as peers if the two parties are not wholesale retailers [53]. Hence, the platforms of Uber, Airbnb, or eBay are referred to as P2P platforms. The term platform refers to a market that is online and has no physical marketplace.

In the literature, these platforms are divided into centralized and decentralized. The centralized platforms have a centralized process to clear the market and match buyers and sellers, while the decentralized platforms enable individual selection of the peer (e.g., Airbnb) [53]. The centralized and decentralized platforms are also referred to as hybrid and pure peer-to-peer platforms, respectively [54].

The centralized and decentralized P2P platforms coexist and are often used on daily basis by average consumers, and both of them can be implemented for energy trading in microgrids. However, their efficiency can be constrained by the ICT infrastructure. In centralized markets, an auctioneer is present that collects the bids and announces the market clearing price. Hence, a single communication iteration can be required per trading period to develop a competitive market clearing price for all market participants. In contrast, peers in a decentralized market can reach the same price, if each peer can access and review all the offers of the other peers at each trading period to optimize the profit or cost. Comparing the two platform types, the decentralized P2P might lead to a proportional increase in the optimization and communication time depending on

## 1 Introduction

the number of peers and the communication technology applied. Such a communication process might still be overburdened if peers are trading in both near real-time and forwards.

### 1.2 Research Gaps

The research trends and gaps in the literature can be summarized in the following points:

- Most of the presented market models are real-time, near real-time or hour-ahead as discussed in [51,55–57], although forward trading is crucial to exploiting the full flexibility potential of the prosumers. Otherwise, the load shifting capability of the prosumer will be confined, which can lessen the economic feasibility of the energy market platforms and their infrastructure. A limited number of studies discussed forward and real-time trading such as the model of [58], where a bilateral contract network was developed to enable energy trading between prosumers and fuel-based generators.
- Complicated bidding strategies were applied to develop an optimal bid. These strategies can be hardly deployed in a real-life environment on the devices as it either requires high computational power or long wait times to communicate with all other market players. Hence, its synchronization with the energy market can be challenging.
- Most of the research focused on modeling either the electrical side or the thermal side of the prosumer, but not both. Several models are also oriented towards the integration of a specific device such as EVs [59, 60], generic consumers and generators, or aggregators as in [61]. A model that studies the bidding mechanism and integration of every possible prosumer’s consuming device (e.g., EV, and HP), generation (e.g., PV and micro-CHPs) or storage to the date of this review is not present.
- The technical constraints and physical characteristics of market participants (i.e., prosumers) are not usually modeled [61]. Consequently, the practicality and the possibility of implementation of the presented algorithms are hard to evaluate. Simple models were used for prosumers’ devices in households to minimize the computational speed of the market, yet these models can directly influence the bid volume and consequently the market dynamics.
- Forecasting systems were not often integrated into the presented models [51,55,56, 62]. Hence, forecasting uncertainties and their influence on the prosumers’ commitment to the communicated bids were not adequately discussed in the literature. As a solution to the prosumers commitment, [62] proposed that prosumers who failed to generate or supply energy have to be either charged a penalty or trade at lower prices. However, the risk the prosumer is taking and the possible penalties because of the forecasts were not quantified.

### 1.3 Research Objectives, Design, and Questions

In this dissertation, the main objective is to present a model that addresses all the aforementioned gaps and provide a comprehensive solution for the integration of energy markets in microgrids that bridge the gap between simulation and real-life environment. Hence, all the following features should be integrated into a combined model:

- A near real-time and forward trading should be possible with a fast clearing mechanism that enables the prosumers to optimize their bids and shift their load depending on their preferences.
- Simple bidding strategies should be implemented that do not require high computational power and are deployable on the current flexible devices. The bidding strategies should also be tailored to the devices' technical and physical characteristics.
- A probabilistic forecast that accounts for the prediction uncertainties should be integrated in a way that maximizes the prosumer commitment.
- Non-linear experimentally validated models or field measurements data should be used to represent all devices available in the prosumers' building such as EV, HP, Micro-CHP, and PV.
- A decentralized approach (i.e., decentralized HEMS) should be followed at the prosumer level.

A bottom-up research design approach is used in order to deliver the required features of the model. Figure 1.2 shows the abstract structure of a microgrid.

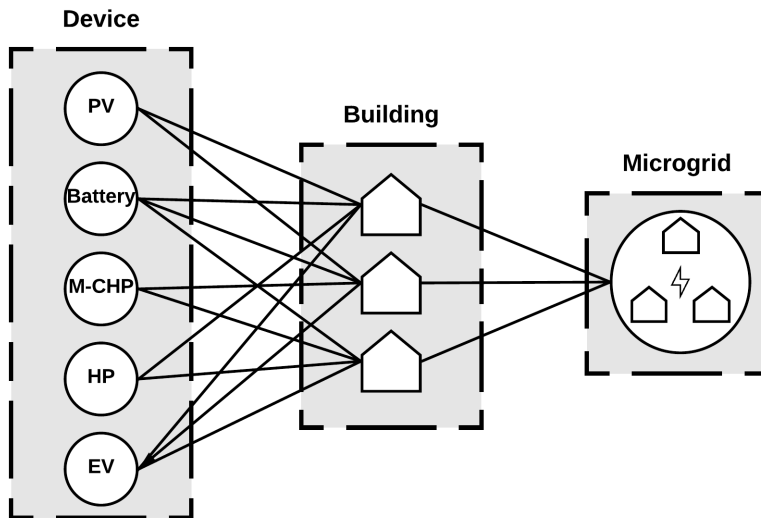


**Figure 1.2:** Microgrid abstract structure for the energy market model.

## 1 Introduction

The research is designed to start with the device level, which is the bottom level of the energy system. At this level, the device models and forecasting systems are studied. Moreover, the operation, control and forecasting requirements are defined. At the building level, these devices and forecasting systems are integrated with building models to be controlled by the HEMS. The model is then evaluated given different system constraints and configurations. At the microgrid level, integration of HEMS and devices in the market model is studied under different scenarios.

The dissertation is divided into a model and a demonstration as shown in Figure 1.3. In the model, since a bottom-up approach is followed in developing the market, multiple research questions can be investigated at the level of the device, building or microgrid. However, the most representative six questions with significant contributions are selected and documented in this dissertation. These questions are as follows:

1. What are the optimal control criteria for heat pump operation in buildings based on experimental analysis?
2. Which forecasting method is optimal and applicable for small-scale PV systems?
3. How can probabilistic forecasts be integrated in home energy management systems?
4. How will home energy management systems react to different generic loads?
5. Which market design can facilitate the integration of prosumers in energy trading platforms while satisfying the microgrid coordination requirements?
6. What is the potential of energy trading platforms in microgrids under different
  - a) market design parameters,
  - b) microgrid configurations,
  - c) prosumer behavior and energy consumption patterns?

The goal of the demonstration is to validate the results of the market model in order to guarantee its realization in real-life. Hence, another question is asked, how realistic are the model outputs and dynamics? Figure 1.3 shows the flow of research questions, and the relationship between all the aforementioned research questions within the framework of this dissertation.

### 1.4 Dissertation Structure

This dissertation is structured as follows: Chapter 2 discusses the different methods applied at the device, building and microgrid level of this dissertation. In Section 2.1, the models of the flexible devices are presented. Moreover, the experimental procedure for analyzing these models are discussed. Section 2.2 method of probabilistic forecasting for small-scale PV generation systems that is tailored for prosumers' integrations in energy markets. Section 2.3 presents a HEMS that enables load shifting based on the probabilistic forecast. Section 2.4 details the market model design and its operations

concept. Additionally, the function and bidding strategies of every market component are described.

Chapter 3 summarizes the results of the models and systems presented in this dissertation. Section 3.1 demonstrates a validated heat pump model and discusses the results of the experimental analyses. Section 3.2 presents the results of the probabilistic PV forecast and validates it based on a defined set of metrics. Section 3.3 presents two case studies and compares the behavior of the HEMS with and without the probabilistic forecast. Section 3.4 presents the results of the market model using a microgrid of single-family houses. Moreover, it shortly summarizes the results of the scenario analyses.

Chapter 4 presents the demonstration method applied to validate the models in this dissertation. Section 4.1 presents the developed heat pump testbed and its components. Moreover, it shortly discusses the HiL method. In Section 4.2, a type day is simulated and compared to the testbed results. Energetic and dynamic analyses are performed to demonstrate the accuracy of the presented model.

Chapter 5 answers the research questions, presents a conclusive summary and an outlook for future research.

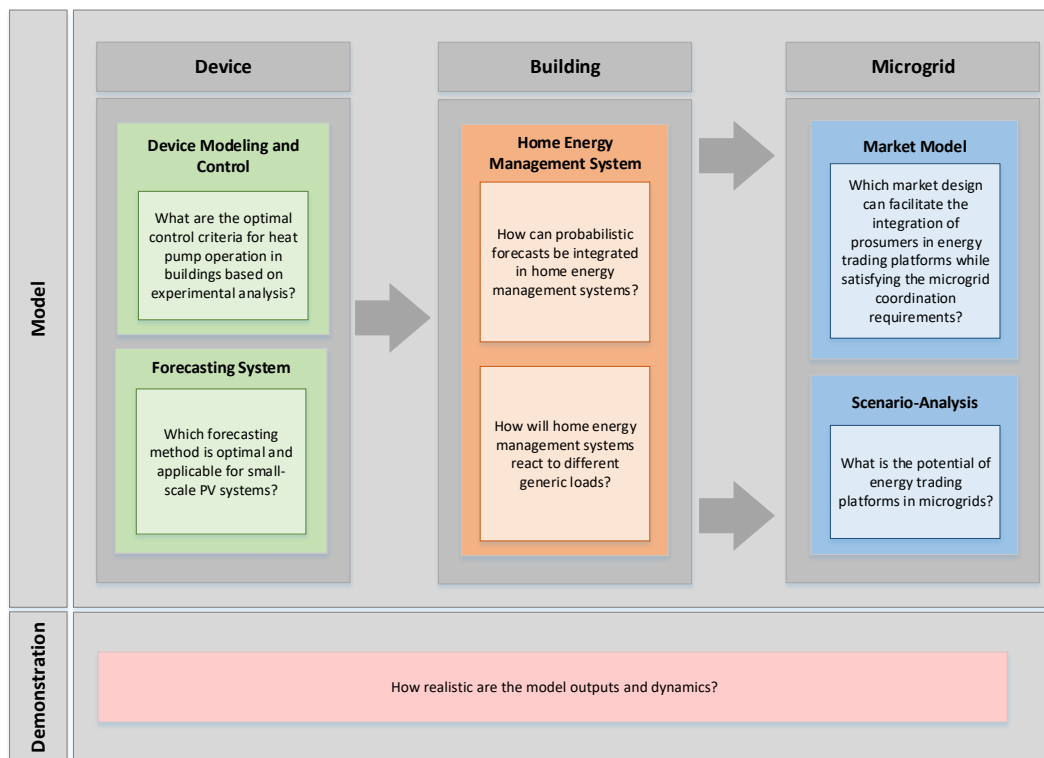


**Figure 1.3:** Research questions at each level of the model and demonstration.

## 1.5 Publication Structure

The content of this dissertation is presented in seven publications. Each publication is dedicated to answering one or more of the research questions presented earlier in Section 1.3. Figure 1.4 uses the same structure of Figure 1.3 to demonstrate the research questions covered by each publication. The seven publications are in the appendix A.1 to A.7.

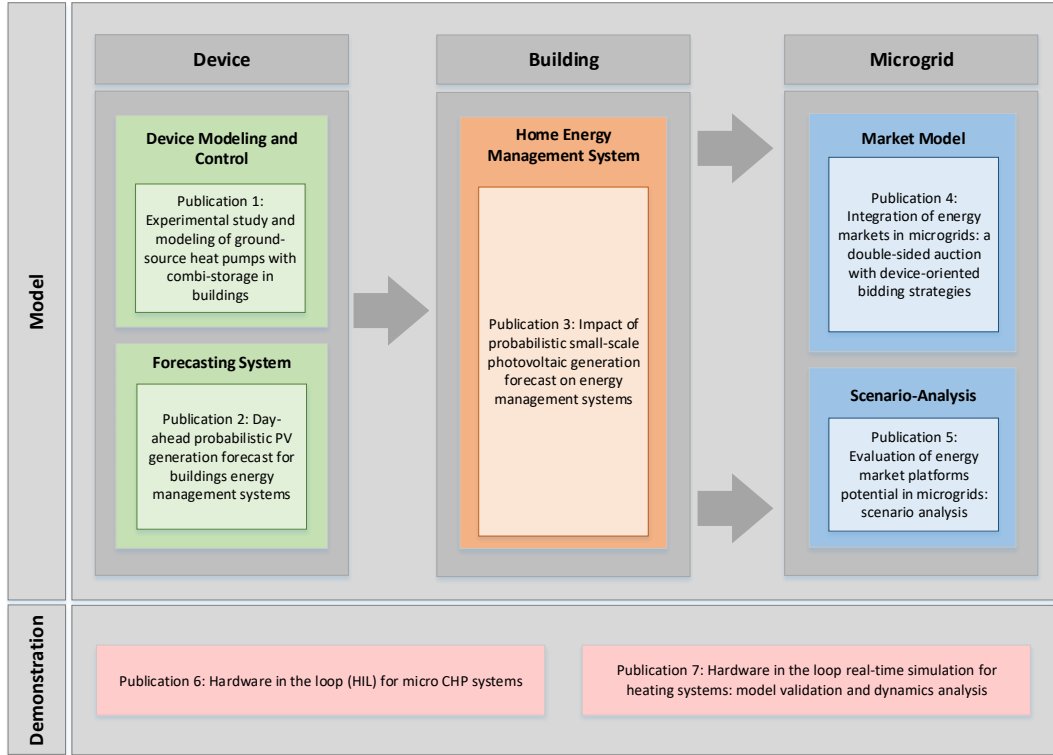


Figure 1.4: Appended publications in the dissertation.

## 2 Methods

This chapter introduces the models, data, and methods used at the level of device, building, and microgrid. Section 2.1 presents the experimentally validated heat pump model discussed in Publication 1. Other flexible devices models are also shortly discussed. Section 2.2 presents the PV forecasting system presented in Publication 2. Section 2.3 presents the HEMS operating at the building level that is used in Publication 3. Section 2.4 presents the market model where all the outputs of Publications 1-3 are used as in Publication 4. Additionally, Section 2.4 presents the scenario analysis methodology used in Publication 5.

### 2.1 Flexible Prosumer Devices in Buildings

Devices in the prosumers' buildings can be categorized as flexible and non-flexible devices. Flexible devices can shift their operation within a user-defined time frame, while non-flexible devices have a fixed time of operation. Hence, they are commonly denoted in the literature as shiftable and fixed loads, respectively. Among the flexible devices are white goods (e.g., washing machine, dishwasher or tumble dryer), HP, EV, and Micro-CHP. The flexibility potential of white goods was studied within the research project eMOBILie [63], and it was found to be minimal, compared to other devices in the household (e.g., HP). Hence, in this dissertation, the flexibility of white goods are neglected.

#### 2.1.1 Heat Pump

HP is one of the flexible devices that plays a major role in sector coupling. One driver behind this role is the progressive improvement of the Coefficient of Performance (COP) [64]. Another is the attractive costs of heat storages that maximize the overall HP system flexibility potential.

Among the HP types, Ground-Source Heat Pump (GSHP) has the highest performance. According to [65,66], GSHP has a low operating cost, no outdoor units, longer life, and a higher CO<sub>2</sub> emissions reduction. Hence, this section addresses specifically the GSHP. A method of experimental testing to identify the real-life optimal control criteria and requirements for GSHP is presented. Furthermore, an experimentally validated Modelica-based model is demonstrated that is tailored to operate with minimal computational requirements in a larger system such as microgrid simulations without compromising the accuracy of the results.

### Control Requirements

Four major experiments were performed on a GSHP in order to identify the control requirements, as in Figure 2.1. The candidate GSHP has a thermal power of 10.31 kW and a COP of 5.02 by B0/W35 according to the standard EN 14511. The first group of experiments is to define the performance map of the heat pump. This group of experiments analyzes the given heat pump performance under different heat supply temperatures and brine temperatures.

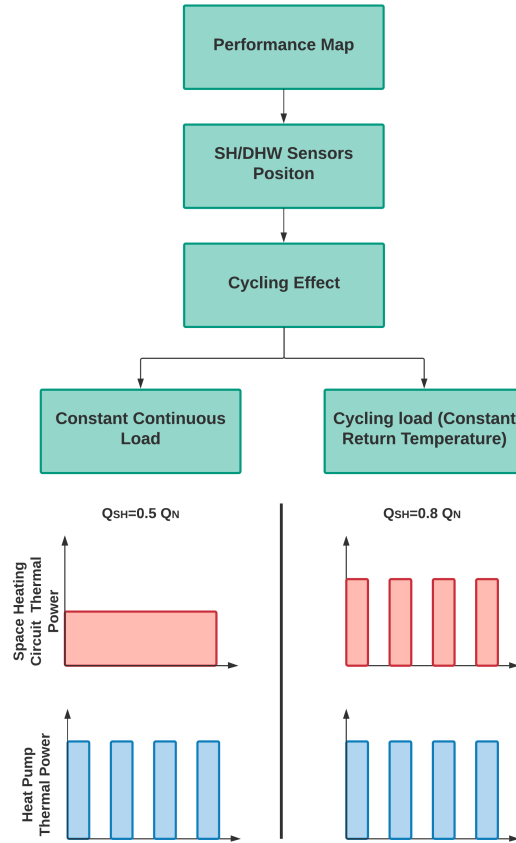


**Figure 2.1:** The flow of the experimental procedures presented in Publication 1.

The second group of experiments investigates the optimal Space Heating (SH) and Domestic Hot Water (DHW) temperature sensor positions and reveals their effect on the overall system performance in buildings. In the third and fourth group of experiments, the optimal control rules for HEMS are defined through testing the cycling effect. In cycling effect experiments with constant continuous load, the thermal load is given to the building emulator (e.g., 5 kW), constant through the whole 24 h, while the heat pump has to cycle between on and off. Within this group of experiments, four experiments are performed with a duty cycle of 50%. The switching time is varied between 1,

2, 3, and 4-h. The 6-h duration is not performed in this experiment due to the limited thermal capacity of the combi-storage. The thermal load of the space heating  $Q_{SH}$  is set to 50% of the nominal thermal power of the heat pump  $Q_N$  to maintain the energy balance. Cycling effect is also tested while trying to maintain a constant return temperature. The  $Q_{SH}$  is set to 80% of  $Q_N$ . Due to the increase of  $Q_{SH}$ , the 6-h cycle was made possible. Thus, six experiments are performed, the 1, 2, 3, 4, 6-h cycles.

Through this set of experiments, the operation characteristics of a heat pump can be clarified, and a picture can be drawn about the optimal control criteria of the GSHP. The output of this experimental analysis is used in developing and validating the heat pump model.

### Heat Pump Model

According to [67], the heat pump modeling approaches can be divided into physical, black box and grey box approaches. The physical approach can forecast the dynamic behavior of a system. Hence, it is often used for heat pump design and parameter optimization. Black boxes can be easily computed and are useful for large systems, yet they usually conceal several system dynamics to maintain simplicity. Grey box models try to achieve a balance between the two aforementioned approaches. For residential buildings modeling, three main criteria have to be satisfied:

- **Simplicity:** the model has to be easily computable as the building modeling software such as Modelica and TRNSYS are not yet powerful enough to simultaneously solve the equations of multiple complicated dynamic systems.
- **Accuracy:** the model has to minimize the uncertainties of the results.
- **Dynamics:** the model should not conceal the dynamic behavior of the heat pump under different operating conditions.

In this dissertation, a semi-empirical dynamic model is presented that was developed in Modelica as in Figure 2.2. It was designed such that it can be coupled with Open Modelica Libraries [68] or SimulationX “Green City” Package [69]. The simulated thermal power of the heat pump  $Q_{sim}$  and the coefficient of performance  $COP_{sim}$  are calculated empirically based on the four aforementioned experiments.  $Q_{sim}$  is calculated as a function of the brine temperature,  $T_b$ , and the heating supply temperature,  $T_s$ , as in Equation (2.1).  $COP_{sim}$  is also evaluated based on those two inputs either directly from the tabulated experimental data or empirically using Equation 2.2. This polynomial equation is formulated based on data fitting algorithm of the experimental data.  $R^2$  is 0.99, while the sum squared error and the root mean squared error is 0.1727 and 0.0759, respectively. The electrical power of the heat pump,  $P_{sim}$ , is then simply calculated based on Equation 2.3.

Although the power and COP of the heat pump can be accurately calculated using the presented equation, these data will not be sufficient to present the system dynamics such as system thermal losses, system inertia, operation time of the brine pump before the compressor starts, resting time between two consecutive starts, and time to full

## 2 Methods

power. Consequently, the calculated full power from Equation 2.1 is given as a prescribed thermal power to a thermal pipe directly. This pipe represents the outlet pipe of the heat exchanger of the condenser. Between the pipe and prescribed heat model, there is a thermal resistor that is empirically calibrated to present conduction losses. The inertia of the system is represented by a thermal capacitor that can be initialized based on the system water volume as in Equation 2.4, where  $C_p$  is the specific heat capacity of water,  $Vol$  is the internal water volume of the heat pump, and  $\rho$  is the density of water. The convection losses are modeled as shown in Figure 2.2, assuming that the room temperature is always fixed at a value of 18 °C. The convection heat loss factor was also empirically estimated and set as a fixed value throughout the whole simulation.

$$Q_{sim} = f(T_b, T_s) \quad (2.1)$$

$$COP_{sim} = f(T_b, T_s) \quad (2.2)$$

$$COP_{sim} = 11.16 + 0.2488 \times T_b - 0.2282 \times T_s - 0.003031 \times T_b T_s + 0.001405 \times T_s^2$$

$$P_{sim} = \frac{Q_{sim}}{COP_{sim}} \quad (2.3)$$

$$C = C_p \times Vol \times \rho \quad (2.4)$$

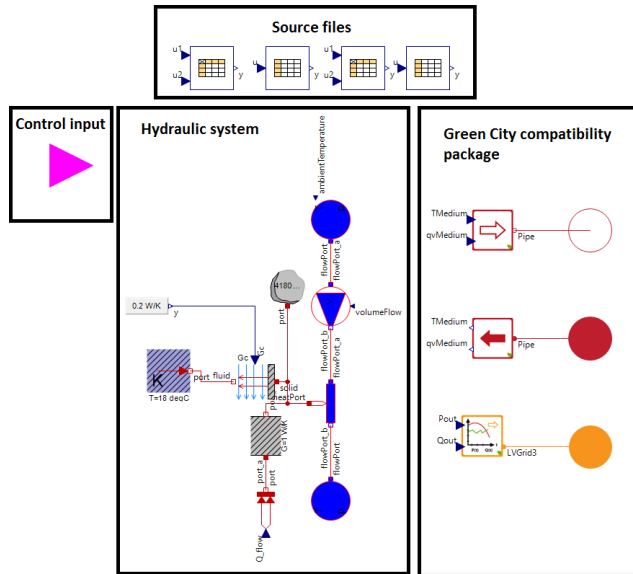


**Figure 2.2:** The heat pump model structure presented in Publication 1.

Through this model, the aforementioned criteria for heat pump modeling in building simulations can be satisfied without adding any additional modeling complexity. Integrating any further details such as a thermodynamics cycle model would not increase the quality of results.

### 2.1.2 Micro-CHP

As with the GSHP, Micro-CHPs are designed to cover the heat load of a building. However, they are also capable of supplying electricity. The dynamics and control constraints of the Micro-CHP are dependent on the engine type (e.g., an internal combustion engine (ICE), Stirling engine, or fuel cells). In the work of [70], a detailed experimental study was performed on Stirling engine based Micro-CHP and heat storages. The output of this study was used to develop the integrated Micro-CHP model.

The same model structure presented in Figure 2.2 was adapted to the Micro-CHP. Based on the empirically collected data that is a function of the Micro-CHP coefficient and  $T_s$ , the prescribed heat to the hydraulic system was calculated. More details are presented within the HiL experimental testing in Publication 6.

### 2.1.3 Electric Vehicle

EV is one of the systems that has a growing influence on the stability of modern grids. It creates an increase in energy and power demand and consequently has high connectivity and control requirements. Nonetheless, EV batteries can offer flexibility as long as they are connected to the microgrid.

In this dissertation, the EV model of [69] is adopted. The EV model is assumed to be active only when it is connected to the charging station. The implemented charging station is assumed to have a single-phase power of 3.6 kW [9]. Once the EV is connected, it acts as a battery system that needs to be charged to a specific State of Charge (SOC). All battery cells are assumed to be symmetric and have the same characteristics. A lithium-ion battery profile was chosen as it is the most common implemented system in the current EVs. Aging characteristics were deactivated to minimize the simulation time. For more details, please refer to [69].

Vehicle data, driving cycle and usage frequency define the electricity consumption of the EV and daily SOC before connecting the vehicle to the charging station. The Worldwide Harmonized Light Duty Driving Test Cycle (WLTC) of class 3 of type 2 EV was selected. A permanent vehicle usage scenario was selected such that the EV was used on working days as a private vehicle. More details about the driving cycles and vehicle usage are documented in the report of [71].

## 2.2 Probabilistic Forecast for PV Generation

The probabilistic forecast is an intuitive solution to handle the uncertainties and variabilities of PV generation. The deterministic forecast generates a single-value forecast for every time step in the forecasting horizon, which can easily expose the HEMS and the market platform to several uncertainties. The probabilistic forecast is capable of generating a range of values for the HEMS to take the most probable optimal decision. Within this section, the important features of the probabilistic forecast are comprehensively discussed. However, more details about the formulation are documented in Publication 2.

## 2 Methods

The process of generating a probabilistic forecast goes through multiple steps as shown in Figure 2.4. Before the process starts, three main inputs should be available: the historical data, weather forecast, and PV plant parameters. The initial process is the generation of clear-sky power based on the Clear Sky Model (CSM) of Bird and Hulstrom [72] and nominal PV module efficiency. The system efficiency is calculated empirically based on historical data to include different losses such as inverter losses, ohmic losses, and temperature losses, in order to calibrate the CSM.

The second process is partial shading detection. This process also involves an empirical process which analyzes three consecutive sunny days to determine the Zenith angle,  $Z$ , at which the power drop occurs. Once the right angle is found, the power drop is calculated and applied to the next days. The partial shading process is activated only once three consecutive sunny days are detected, yet the frequency of the calibration can be determined based on the user's input. Figure 2.3 shows the PV clear sky generation after calibration using the previously mentioned processes.

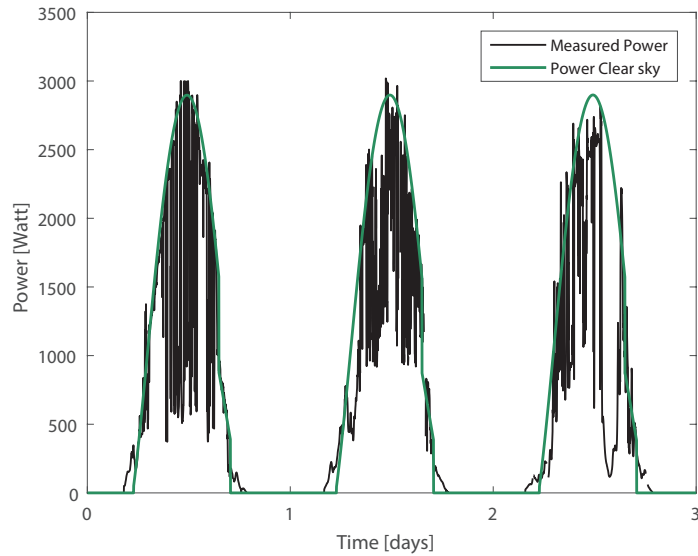


**Figure 2.3:** Clear sky model output and PV power measurements after the partial shading detection process as presented in Publication 2.

The following process constitutes of training the regression trees to generate a point forecast. These regression trees function based on dividing the data available into multiple sets and fitting them to a simple model based on a given number of branches and leaves. Such method showed its ability to provide efficient predictions using the minimal computational time. The training variable assigned to the regression trees is  $\Lambda(t_t)$ , where  $P_{pccs}$  is the clear sky power after calibration,  $P_m$  is the measured power,  $t_t$  is the training time and  $T_n$  is the end of the training period.

$$\Lambda(t_t) = \left| \frac{P_m(t_t) - P_{pccs}(t_t)}{P_{pccs}(t_t)} \right| \quad \forall t_t \in [1, 2, \dots, T_n]. \quad (2.5)$$

The prediction of the trained regression  $\Lambda_p(t_f)$  is then used to generate the point forecast  $P_{pf}$  as per Equation 2.6, where  $t_f$  is the forecasting time. Resolution of the point forecast is limited by the resolution of the given weather forecast.

$$P_{pf}(t_f) = P_{pccs}(t_f) - |\Lambda_p(t_f) \times P_{pccs}(t_f)| \quad \forall t_f \in [1, 2, \dots, 24]. \quad (2.6)$$

The  $P_{pf}$  is the base on which the probabilistic forecast is built. In this model,  $P_{pf}$  has 1-h resolution and hence, it cannot present the PV generation variabilities. Moreover, it is still exposed to uncertainties. Thus, the relative difference  $\lambda_i$  between the PV measurements and the point forecast generated by the regression tree is used to train the probabilistic forecast. Both of the PV measurements and the point forecasts provided to the probabilistic forecast model are of 1 min resolution. The point forecast is linearly interpolated to convert the forecast from 1-h to 1-min resolution.

The relative difference  $\lambda_i$  is classified into 8 categories  $i \in [1, \dots, 8]$ , representing the 8 levels of cloudiness  $[\frac{1}{8}, \dots, \frac{8}{8}]$ . Consequently, 8 Cumulative Distribution Function (CDF)s,  $F_i(\lambda_i)$ , are trained. Once the training is accomplished, the forecasted relative difference for a specific probability can be calculated as per Equation 2.7.

$$F^{-1}_i(q) = \lambda_i, \quad q \in Q = \{10\%, 20\%, \dots, 90\%\}. \quad (2.7)$$

The required probabilistic set of PV power forecast  $P_{pp}(t_f)$  can then be calculated based on Equation 2.8.

$$p_{pp_q}(t_f) = P_{pf}(t_f) \times (1 - \lambda_i) \quad (2.8)$$

$$P_{pp}(t_f) \in \{p_{pp_{10\%}}(t_f), p_{pp_{20\%}}(t_f), \dots, p_{pp_{90\%}}(t_f)\}.$$

The reason behind using CDFs to calculate the multiple curves of the probabilistic forecast is to have an intuitive, simple integration of the forecast with a HEMS. In buildings, a HEMS does not require an exact PV forecast, but rather a probability guaranteeing specific power availability at a certain time of the day to prioritize the device's scheduling.

The forecast model is validated not only based on the standard metrics but also probabilistic metrics. Among the standard metrics are the normalized Root Mean Square Error (RMSE), Mean Absolute Error (MAE) and Mean Biased Error (MBE) as in Equations 2.9, 2.10, and 2.11, respectively. The Forecast Skill (FS) is also used in order to compare the forecast model RMSE to a persistence forecast  $RMSE_{sp}$ , as in Equation 2.12. Cumulative Ranked Probability Score (CRPS) and Brier Score (BS) are used to evaluate the probabilistic forecast and guarantee its performance as in Equations 2.13 and 2.14, respectively. As with the FS, the CRPS and BS skill score are used to compare the probabilistic forecast to a persistence ensemble. The CRPS skill score is presented in Equation 2.15 and the BS skill score is in Equation 2.16.

$$RMSE = \sqrt{\frac{1}{N} \sum_1^N (P_{pf} - P_m)^2} \quad (2.9)$$

## 2 Methods

$$MBE = \frac{1}{N} \sum_1^N P_{pf} - P_m \quad (2.10)$$

$$MAE = \frac{1}{N} \sum_1^N |P_{pf} - P_m| \quad (2.11)$$

$$FS = 1 - \frac{RMSE}{RMSE_{sp}} \times 100 \quad (2.12)$$

$$CRPS = \frac{1}{8} \sum_{i=1}^8 \int_{-\infty}^{\infty} (F_i(\lambda) - F_i^0(\lambda))^2 d\lambda. \quad (2.13)$$

$$BS = \frac{1}{N} \sum_{i=1}^8 \sum_{j=1}^{N_p} (q - o_{ij})^2 \quad (2.14)$$

$$CRPSS = 1 - \frac{CRPS}{CRPS_{PeEn}} \times 100 \quad (2.15)$$

$$BSS = 1 - \frac{BS}{BS_{PeEn}} \times 100 \quad (2.16)$$

Furthermore, the Temporal Distortion Index (TDI) is used to evaluate the temporal distortion of the forecasting model [73, 74]. The metric is based on the Dynamic Time Warping (DTW) developed in the 1970s, which is used to evaluate the temporal distortion between two different time series. The DTW finds the optimal warping path (i.e., a common set of instants) by minimizing the distance between the two given time series. Then, the TDI can be calculated as in Equation 2.17, where  $i$  and  $j$  are the PV measurements time series index and forecasting model time series index, respectively.

$$TDI = \frac{1}{N^2} \sum_{l=1}^{k-1} |(i_{l+1} - i_l)(i_{l+1} + i_l - j_{l+1} - j_l)| \quad (2.17)$$

The model is available to the open-source community for HEMS applications on [75] in two different formats. The first format is the initial development format, Matlab script, for research applications. A GUI is also implemented to ease model use for the households' residents. The second format is Python, for the integration with micro-computers such as Raspberry Pis in smart homes.

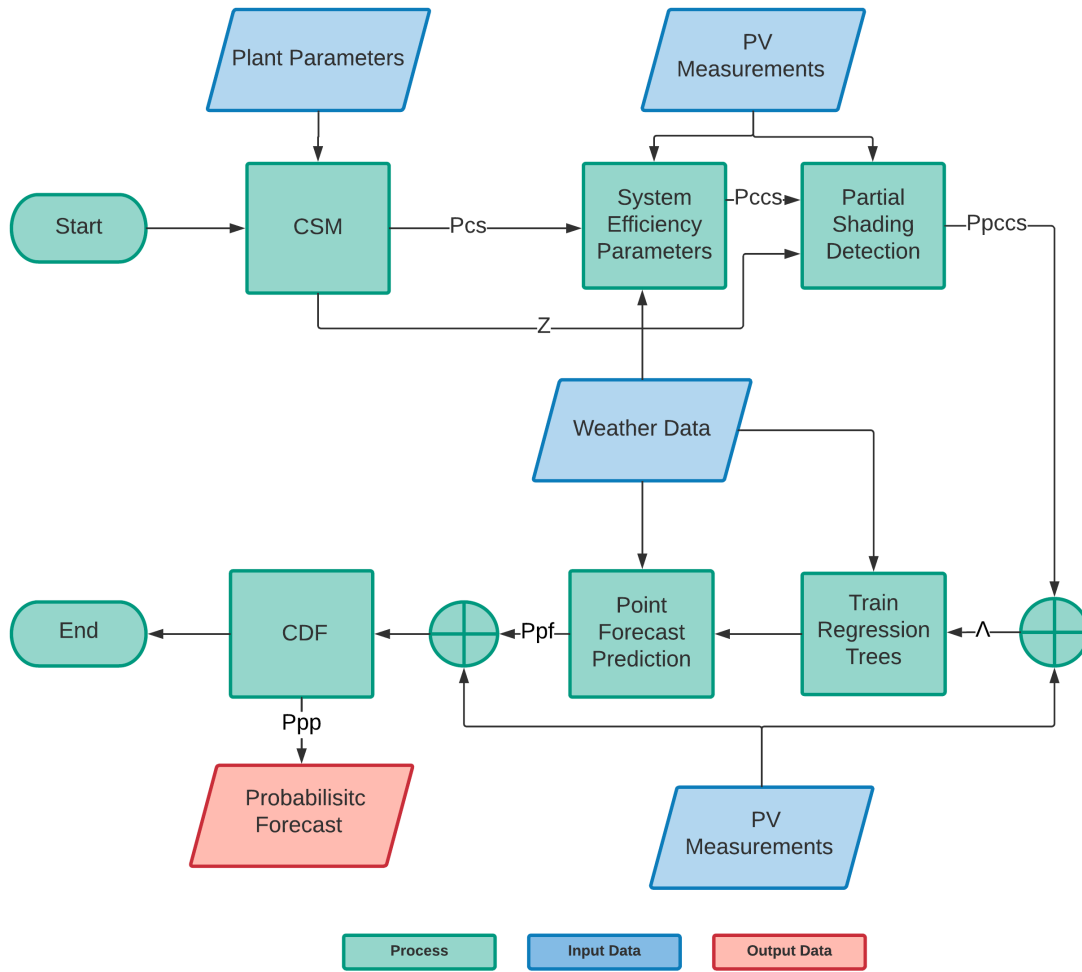


Figure 2.4: Simplified flow chart describing the process of probabilistic forecast generation as presented Publication 2.

### 2.3 Energy Management System in Buildings

The main goal of the HEMS is to integrate the probabilistic forecast output and optimize the operation plan based on the different probability curves. An algorithm is implemented based on the exhaustive enumeration method to evaluate every possible combination of loads under the given PV generation conditions. Although the exhaustive enumeration method is computationally intensive, it can guarantee the highest potential results and can lead to a fair comparison between the reference and probabilistic forecast. Figure 2.5 shows a simplified flowchart of the load shifting algorithm that is compatible with deterministic and probabilistic PV forecasts. It starts with PV forecast profiles and the flexible devices dataset. The flexible devices dataset consists of the load profile of

## 2 Methods

the device  $P_d(t)$ , earliest starting time, and latest ending time. If the earliest starting time and the latest ending time are not given, the algorithm optimizes by default over a 24-hour period, from 00:00 to 23:59.

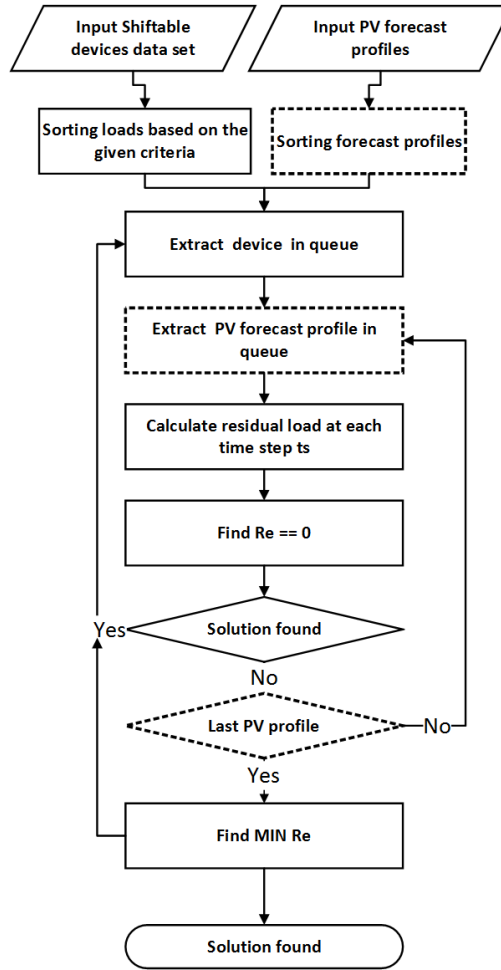


**Figure 2.5:** Flow chart of the load shifting algorithm as presented in Publication 3.

Both PV forecast profiles and flexible devices' loads are sorted. The PV forecast profiles are sorted based on their probability of occurrence,  $q$ , (i.e., 99% comes first in the queue then followed by the lower probabilities). The flexible devices are sorted based on given criteria which vary depending on the required scenario.

- Power consumption  $\Rightarrow P_{d_1} > P_{d_2} > P_{d_3}$ .
- Duration of operation  $\Rightarrow Du_{d_1} > Du_{d_2} > Du_{d_3}$ .
- Interruptibility  $\Rightarrow In_{d_1} = 1 > In_{d_2} = 0$ .
- Probability of multiple usage  $\Rightarrow Pr_{d_1} > Pr_{d_2} > Pr_{d_3}$ .

$P_{d_1}$ ,  $Du_{d_1}$ ,  $In_{d_1}$ , and  $Pr_{d_1}$  represent the device with the highest power, longest duration, interruptibility option (Boolean), and highest probability of usage, respectively.

In this dissertation, the dominant criterion being applied is power consumption, i.e., the highest power consuming device always has the highest priority. As soon as the devices are sorted, the residual load is calculated for every device under every probabilistic PV profile curve as per Equation 2.18 till a minimum is reached.

$$R_e(t) = P_L(t) - p_{pp,q}(t) \forall q \in Q. \quad (2.18)$$

Once a minimum is reached, the algorithm attempts to find a starting point for the next device in the queue until all devices are sorted under all the given probabilistic PV profile curves.

In the case of the deterministic forecast, the flowchart blocks with dashed lines shown in Figure 2.5 can be eliminated to operate in the conventional mode without the probabilistic forecast. A detailed comparison between the HEMS operation method using the deterministic and probabilistic forecast is documented in Publication 3.

## 2.4 Market Model Architecture

The proposed model is classified as a discrete-timely sealed double-sided auction with uniform pricing. The market is chosen to be discrete-timely to synchronize all traders communication with the market trading platform and to provide a fair environment to all traders where communication speed does not play a role. The market is chosen to be sealed to maintain the anonymity of the bidder. Consequently, market players cannot learn about other traders' bids to preserve their privacy. A uniform pricing mechanism is applied as it provides a fair competitive price to all the market participants independent of the given bid price. Moreover, it encourages the suppliers to bid their lowest price to increase their possibility of selling.

The double-sided auction market is designed to enable prosumers to trade their energy in the forward, day-ahead, intraday independent of the wholesale market. In a smart community with an island or a grid-connected microgrid, the number of participants is denoted by  $N$ , where  $\{N \in Z^+ : N \geq 2\}$ . A market participant can be either a prosumer or the utility. A prosumer can demand deficit energy and act as a buyer  $i$ , or supply excess energy and act as a seller  $j$ .  $i \in \mathcal{B}(t)$  and  $j \in \mathcal{S}(t)$ , where  $\mathcal{B}(t)$  and  $\mathcal{S}(t)$  are the time-dependent sets of buyers and sellers, respectively.  $t \in \mathcal{T} = \{1, 2, \dots, t_{fh}\}$  is the discrete time-step at which trading can occur, where  $t_{fh}$  is the length of finite trading horizon. Since it is a discrete-timely market, trading can occur at any defined time interval  $\Delta t$ . A market participant can communicate multiple bids  $n$  to the market platform equal to  $b_{i,n} = (p_{i,n}, q_{i,n}, t_{d_{i,n}})$ , where  $p_{i,n}$  is the price of bid  $n$  of buyer  $i$ ,  $q_{i,n}$  is the bid volume, and  $t_{d_{i,n}}$  is the delivery time.  $q_{i,n}$  must always be greater than or equal to  $q_{min}$ , where  $q_{min}$  is the constant minimum quantity of energy that can be traded. In this model, the number of participants is always assumed to be constant at any time  $t$ . A market participant can submit a buying or selling bid for a value of zero if he is not willing to trade in the market. The bid prices  $p_{i,n}$  are formed at the device level

## 2 Methods

depending on the technical constraints and dynamic behavior of the device. The bidding strategy and bid formulation are demonstrated for every device  $D$  that can communicate with the market later in this section. However, a price ceiling and floor is set for all  $D$  participating in the market such that  $p_{min} \leq p_i, p_j \leq p_{max}$ . For a grid-connected microgrid,  $p_{max}$  and  $p_{min}$  can represent the conventional utility energy consumption tariff and feed-in tariff, respectively.  $p_{max}$  can be time-dependent, if RTP is applied. The intention behind applying a pricing ceiling and floor is to keep the prices higher than feed-in tariffs for generators and less than the utility prices for consumers at all times  $t$  so that voluntary participation of the prosumers in the microgrid market can be ensured. The readiness of a prosumer to bid higher prices to use the community energy may vary depending on the background and culture of the society where the market is located. Nevertheless, quantifiable economic gain supported by environmental benefits for the whole society can attract more prosumers to participate in the market.

Figure 2.6 presents a simplified overview of the system design including the market side and prosumer side. The following steps demonstrate the simplified communication steps from forming bids to the operation of the device once the bid is accepted.

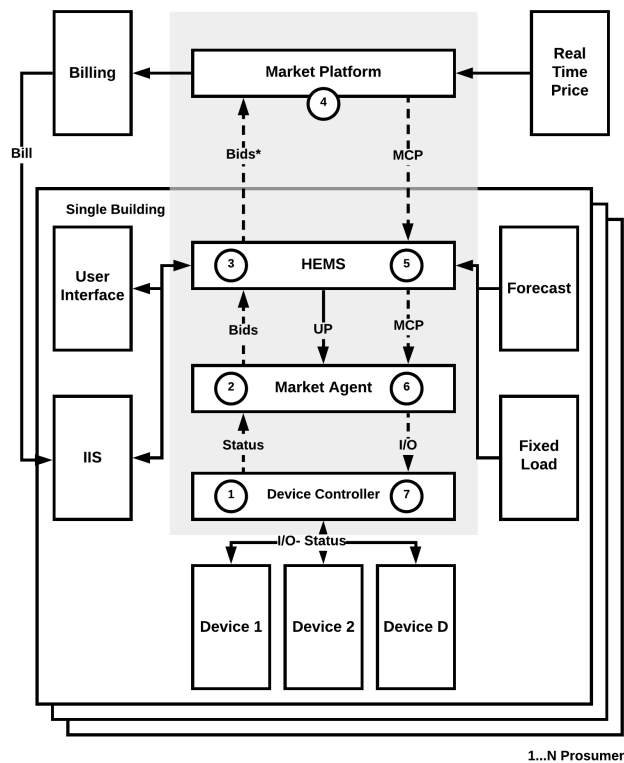


**Figure 2.6:** An overview of the market components and communication structure as presented in Publication 4.

**Step 1:** The device controller sends the status of device  $D$  to the market agent.

**Step 2:** Depending on the device status, user preference and designed bidding strategy, the market agent develops the buy and sell bids,  $b_i$  and  $b_j$ , respectively. Consequently, for each  $D$  there is a market agent to maintain a decentralized structure.

**Step 3:** The HEMS receives the bids  $b_i, b_j$  from the market agents and modifies them according to the user operation mode (standard, comfort, or cost saving)  $b_i^*, b_j^*$ , then sends them to the market platform.

**Step 4:** Applying a discrete-timely double-sided auction, the market price and volume at equilibrium are found. The market platform then forwards the market clearing price back to the HEMS.

**Step 5:** The HEMS forwards the MCP to the market agents and user through the user interface.

**Step 6:** The market agent receives the MCP to identify the accepted bids from the rejected bids.

**Step 7:** The device controller receives the operation signal from the market agent to switch the device at  $t_d$ .

### 2.4.1 Market Platform

The market platform is the place where all bids are received to clear the market. In this model, the market platform requires a market coordinator that acts as an auctioneer. The market coordinator can be the utility or the platform owner. The market coordinator roles can be summarized in the following points:

- Clearing the market and announcing the market clearing price.
- Rejecting any bid changes after the gate closure time  $t_g$ .
- Balancing the market to guarantee an equilibrium between supply and demand.
- Breaking the market ties at every trading period.

The first responsibility of the market coordinator is to clear the market. It sorts the bids such that  $b_{i,n} \geq b_{i+1,n}$  for the buyers,  $b_{j,n} \leq b_{j+1,n}$  for the sellers. The bids are aggregated as step functions  $(p_{i,n}, q_{i,n})$  and  $(p_{j,n}, q_{j,n})$ , whose resolution can be defined by limiting the maximum bid volume. The intersection of supply and demand step functions represents the competitive equilibrium and defines the market clearing price value,  $p_e$ , and the cleared volume,  $q_e$ .  $p_e$  is then communicated to all prosumers so that they can either operate at  $t_d$  or shift their loads to another time. Since the market price has a ceiling and a floor,  $p_e \leq p_{i,n} \leq p_{max}$  for all buyers, and  $p_{min} \leq p_{j,n} \leq p_e$  for the

## 2 Methods

sellers. Hence the prosumers profit  $\varpi$  can be summarized in Equation 2.19, where  $q^\alpha$  is the volume of the accepted bid.

$$\varpi = \sum_1^n (p_{max} - p_e) q_{i,n}^\alpha + \sum_1^n (p_e - p_{min}) q_{j,n}^\alpha \quad (2.19)$$

The second responsibility of the market is to manage the gate closure time. Since this model enables near real-time and forward trading, a gate closure time has to be defined as a deadline for any changes in bids or withdrawals. Assuming that  $t_g$  is set to 30 minutes, a market participant can make a bid at any  $t_d$  in the future and still change the bid up to 30 minutes before delivery.

The third responsibility of the market coordinator is to balance the market during each trading period in order to clear the market. The prosumers need to guarantee that their energy demand will be covered, even if there is no sufficient supply from the other prosumers in the market. Also, they have to make sure that their non-shiftable generation can be fed-in to the grid. Consequently, the market coordinator acts as a seller or buyer at any period: it sells the deficit energy required by consumers or buys the excess energy produced. Throughout the whole trading time horizon, the market assures that Equation 2.20 is maintained.

$$\sum_{i=1}^{\mathcal{B}} \sum_1^n q_{i,n} = \sum_{j=1}^{\mathcal{S}} \sum_1^n q_{j,n} \quad (2.20)$$

The fourth responsibility of the market coordinator is to break the ties to clear the market. Practically, the probability of having market ties is low, yet it is possible. Hence, market breaking ties rules have to be defined. In this model, the market model breaks the ties either randomly, or in favor of agents bidding the highest volume  $q_i$  or  $q_j$ . A minimal value of  $\zeta = 1 \times 10^{-4}$  is added to the favored agent in order to clear the market.

### 2.4.2 Decentralized HEMS

Although the centralized HEMS of Section 2.3 could have been used directly in the model, a decentralized approach is followed to enable the devices to bid directly in the market. Hence, the role of HEMS in the market model can be summarized as follow:

- Broadcasting  $p_e$  to market agents.
- Bidding for the non-shiftable (fixed loads) based on the load forecast such that  $b_{i,n} = (p_{max}, q_f, t_{i,n}^d)$  to guarantee their bids allocation.
- Collecting bids from all market agents (i.e., devices) and forwarding them to the market platform.
- Adjusting the bid price depending on the user preferences as shown in Equation 2.21.

$$p_{i,n}^* = \begin{cases} p_{i,n} & \text{if standard} \\ \varphi(p_{max} - p_i) + p_i & \text{if comfort} \\ \max(\gamma(p_{min} - p_{max}) + p_i, p_{min}) & \text{if cost saving} \end{cases} \quad (2.21)$$

$\varphi$  and  $\gamma$  are two variables such that  $\{\varphi, \gamma \in \mathbb{R} : 0 \leq \varphi, \gamma \leq 1\}$ .  $\varphi$  and  $\gamma$  could be set by the user to increase or decrease the comfort or cost savings, respectively.

A comparison between the results using the centralized and decentralized approach is further discussed in Publication 4.

### 2.4.3 Market Agents

As per [48], double-sided auctions are too complex to output a game-theoretic solution. In this market model, the market agent has no information about the number of bidders, the volume of bids, or the identity of bidders at any trading interval because the market is sealed to maintain the anonymity and data privacy of the prosumers, and also to avoid collusion. If a game-theoretic approach would be applied, the market agent has to evaluate all possible actions for all market participants in the microgrids to find the solution maximizing the prosumer's benefit. This strategy would lead to limiting the model scalability given the increasing computational capacity required per market participant. Moreover, the larger the number of participants in this market type, the less influential their actions are.

In this model, simple non-predictive bidding strategies are evaluated. Every device group has a symmetric pure constant bidding strategy that does not need a price prediction or complex learning mechanism to develop the bid. The bidding strategy is designed to always bid the truthful price depending on its need. Hence, an agent who is requesting energy in the next hour would bid more than an agent requesting energy in the next day. The valuation is always time/need dependent. To optimize the bidding strategy, each agent can submit multiple bids at different time steps within a specific time frame, then use a simple enumeration search optimization technique to find the cheapest accept bid and withdraw/sell the remaining additional purchased volume to the market. This concept is applied to each of the typical prosumer flexible devices and tailored to its technical and operational constraints.

### Electric Vehicle

A user communicating with the HEMS will indicate the desired starting time of the charging,  $t_s$ , and the time by which the vehicle shall be charged and ready,  $t_r$ . The latest end time is defined as  $t_e = t_r - d_o$ , where  $d_o$  is the operation duration. The typical charging power is between 3.6 kW (single phase) and 22 kW (three phase) [9].

Assuming a fixed charging power  $P_{CEV}$  is required to charge the EV at any time between  $t_s$  and  $t_e$ , the EV market agent sends bids at every possible delivery time  $t_d$  between  $t_s$  and  $t_e$ . The readiness of the market agent to pay more increases linearly as the charging time approaches the  $t_e$  as in Equation 2.22. After  $t_e$ , the market agent

## 2 Methods

always bids a fixed price of  $p_{max}$  to ensure the acceptance of the bid either from other prosumers or the utility depending on the market situation.

$$p_{i,n} = \begin{cases} \left(\frac{p_{max} - p_{min}}{t_e - t_s}\right)t_d + p_{min}, & \text{if } t_d \leq t_e \\ p_{max}, & \text{if } t_d > t_e \end{cases} \quad (2.22)$$

The set of accepted bids  $\beta_i^\alpha$  is always larger than the set of required bids  $\beta_i^r \subset \beta_i^\alpha$ , which is because the market agent creates bids for every period between  $t_s$  and  $t_e$  and bids the maximum price after  $t_e$ .

The market agent selects the most economic bids and withdraws rejected and unneeded bids. As shown in Equation 2.23, the bids with the lowest costs are selected such that the number of accepted bids,  $c(\beta_i^\alpha)$ , can satisfy the energy demand,  $E_D$ , of the charging station.

$$\min C = \min_{b_{i,n}^\alpha \in \beta_i^r, \beta_i^r \subset \beta_i^\alpha} \sum b_{i,n}^\alpha = \sum p_{i,n}^\alpha q_{i,n}^\alpha \quad (2.23a)$$

$$s.t. \beta_i^\alpha = \{b_{i,1}^\alpha, b_{i,2}^\alpha, \dots, b_{i,n}^\alpha\} \quad (2.23b)$$

$$c(\beta_i^r) < c(\beta_i^\alpha) \quad (2.23c)$$

$$b_{i,n-1}^\alpha < b_{i,n}^\alpha, \forall b_{i,n}^\alpha \in \beta_i^\alpha \quad (2.23d)$$

$$E_D = c(\beta_i^r) q_{i,n}^\alpha \quad (2.23e)$$

### Heat Pump

The behavior of heat pumps in the market platform is highly dependent on the heat pump hydraulic configuration, dynamics, modulation, predefined heating curves, and building load. Assuming that the heat pump is installed along with a combi-storage tank that can cover both the SH and DHW demand as described in [76], the capacity of the storage,  $Q$ , is defined according to Equation 2.24 of [77], where  $\rho$  is the density of water,  $C_p$  is the heat capacity of water,  $A_s$  is the cross-sectional area of the storage,  $T_s(h)$  is the storage at height  $h$  and  $T_{ref}$  is the reference temperature. In practice,  $T_s(h)$  can be measured using a set of sensors across the heat storage as in [76].

$$Q = \rho \times C_p \times A_s \times \int_0^h (T_s(h) - T_{ref}) dh \quad (2.24)$$

$$\forall T_{st}(h) > T_{ref}$$

Depending on the  $Q(t)$ , predefined set energy content  $Q_{set}$  [76], minimum energy content  $Q_{min}$  and maximum energy content  $Q_{max}$ , the heat pump can develop a bid. Equation 2.25, 2.26, and 2.27 can summarize the process of defining the bid volume and price. The market agent then selects the optimal bid to minimize the costs in a manner analogous

to the EV, as in Equation 2.23.

$$p_{i,n} = \begin{cases} 0, & t < t_{rest} \\ (\frac{p_{max} - p_{min}}{\Psi^-})t_d + p_{min}, & \dot{Q} < 0, \text{ and } Q_{min} \leq Q \leq Q_{set} \\ -(\frac{p_{max} - p_{min}}{\Psi^+})t_d + p_{max}, & \dot{Q} > 0, \text{ and } Q_{min} \leq Q \leq Q_{set} \\ p_{min}, & Q_{set} < Q \leq Q_{max} \end{cases} \quad (2.25)$$

$$\Psi^- = \frac{Q - Q_{min}}{\dot{Q}_{SH} + \dot{Q}_{DHW} + \dot{Q}_{losses}} \quad (2.26a)$$

$$\Psi^+ = \frac{Q_{set} - Q}{\dot{Q}_{HP} - \dot{Q}_{SH} - \dot{Q}_{DHW} - \dot{Q}_{losses}} \quad (2.26b)$$

$$q_{i,n} = COP \times \dot{Q}_{HP} \times \Delta t, \quad (2.27a)$$

$$\text{where } COP = f(T_{su}, T_a) \approx f(Q, T_a) \quad (2.27b)$$

$$\dot{Q}_{HP} = f(T_a) \approx f(Q) \quad (2.27c)$$

$t_{rest}$  is the resting time required between Off and On switch.  $\Psi^-$  and  $\Psi^+$  is the negative and positive load shifting potential, respectively.  $\dot{Q}_{SH}$  is the space heating load,  $\dot{Q}_{DHW}$  is the domestic hot water load,  $\dot{Q}_{losses}$  is the thermal losses,  $\dot{Q}_{HP}$  is the heat pump thermal power,  $COP$  is the coefficient of performance of the heat pump,  $T_{su}$  is the supply temperature of the heat pump, and  $T_a$  is the ambient temperature. More details about the technical constraints of the heat pump system, its control, and optimization requirements, in addition to its dynamics and validated model, are available in Publication 1.

### Micro-CHP

As discussed in Section 2.1, the micro-CHP is assumed to have the same hydraulic configuration as the heat pump. The heat storage,  $Q$ , defines the flexibility of the micro-CHP unless the system configuration enables heat dumping. Consequently, the developed bid price and bid volume can be summarized by Equations 2.28 and 2.29, where  $\kappa$  is the CHP coefficient, and  $\dot{Q}_{CHP}$  is the thermal generation power.

$$p_{j,n} = \begin{cases} 0, & t_d < t_{rest} \\ -(\frac{p_{max} - p_{min}}{\Psi^-})t_d + p_{max}, & \dot{Q} < 0, \text{ and } Q_{min} \leq Q \leq Q_{set} \\ (\frac{p_{max} - p_{min}}{\Psi^+})t_d + p_{min}, & \dot{Q} > 0, \text{ and } Q_{min} \leq Q \leq Q_{set} \end{cases} \quad (2.28)$$

$$q_{j,n} = \kappa \times \dot{Q}_{CHP} \times \Delta t, \quad (2.29)$$

## 2 Methods

### Photovoltaic

Based on the output of the probabilistic forecast presented in Section 2.2, the bid price and volume are defined. Equation 2.30 summarizes the bidding strategy of the PV system. The bidding price is formed depending on the probability  $\zeta$ . The higher the probability of the generation profile, the lower the price. Figure 2.7 shows the output of the probabilistic forecast and the measured PV power on a typical transient day.

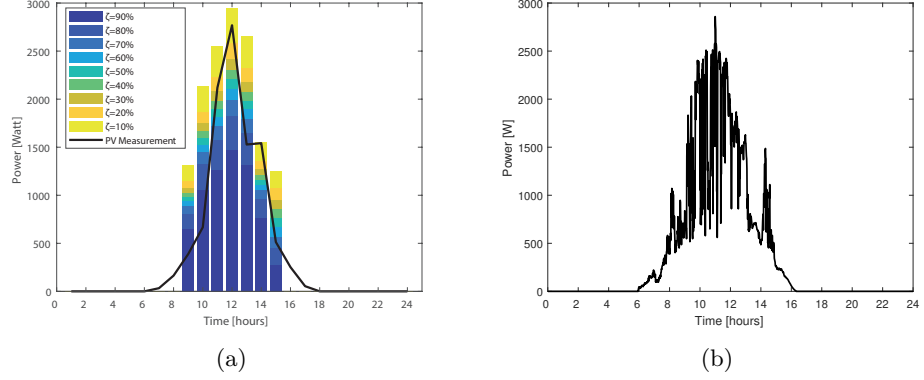


**Figure 2.7:** Selected day of probabilistic forecast output and PV measurements, (a) transient (b) transient-1 min resolution as in Publication 4.

$$p_{j,n} = p_{max} + \zeta(p_{min} - p_{max}) \quad (2.30)$$

### Batteries

The batteries are considered a backup system to maximize the prosumers' commitment in the market. Assuming that the prosumers sent a bid but could not deliver it, the battery discharges to make up for the unfulfilled bid. Equation 2.31 relates to the simplified battery charging and discharging behavior depending on the difference between the generated volume,  $q_g$ , and the accepted volume,  $\sum_1^n q_{j,n}^\alpha$ , where  $\eta_{dch}$  and  $\eta_{ch}$  are the discharging and charging efficiencies of the battery, respectively.

$$E_{Batt}(t) = \begin{cases} E_{Batt}(t-1) - \frac{1}{\eta_{dch}}(\sum_1^n q_{j,n}^\alpha - q_g), & \sum_1^n q_{j,n}^\alpha > q_g \\ E_{Batt}(t-1) - \eta_{ch}(\sum_1^n q_{j,n}^\alpha - q_g), & \sum_1^n q_{j,n}^\alpha < q_g \\ E_{Batt}(t-1), & \text{otherwise} \end{cases} \quad (2.31)$$

Operation of the battery system under these conditions can make up for the forecast errors and enable the prosumers (i.e., the market agent) to commit to the communicated bid without violating the market rules.

## 2.5 Market Scenarios Design

There is a various number of possible scenarios that can be used to analyze the behavior of an energy market in a microgrid. These scenarios can vary depending on market design parameters, microgrid configurations, flexible device loads, or user behavior. Under each of these categories, several design parameters and variables can be analyzed. However, calculating the combinations of these variables requires high computational capacity and time. Thus, specific scenarios are selected to represent the market behavior under the most probable configurations. Three scenario groups are selected as in Figure 2.8.

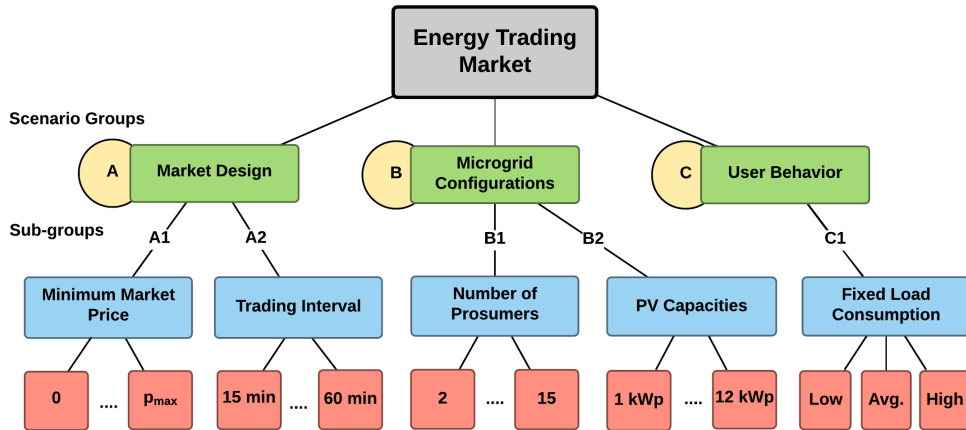


Figure 2.8: An overview of scenario groups as in Publication 5.

Group A discusses the market design variables such as the  $p_{min}$  and the trading intervals. The scenarios of A1 vary the  $p_{min}$  at a constant step size between 0 and  $p_{max}$ . The goal is to show the influence of different feed-in tariffs and foreseeable market fees on the benefits of the prosumers and utility. The influence of the trading intervals is analyzed in A2 to quantify the benefits of higher trading frequency, given the same system configuration and forecast quality. The trading interval,  $\Delta t$ , is varied between 15 and 60 minutes.

Group B discusses the microgrid configurations, where the influence of the number of prosumers and the installed PV capacities are studied. The number of prosumers is varied between 2 and 15. The PV capacities are varied from 1 kWp to 12 kWp, which are the expected PV capacities to be possibly installed at a prosumer's building. The goal behind these scenarios is to evaluate the influence of over- and under-generation capacity on the market prices, prosumer, and utility.

The last group, C, evaluates the user behavior. Fixed load consumption is used as an indicator of the user behavior and lifestyle. Three categories define the user consumption level: low, average, and high. The range of each level is explained in the next section. The goal behind this scenario group is to present the influence of the fixed load consumption magnitude on the prosumer's profitability and behavior in the market.

## 2.6 Market Co-simulation and Input Data

The model is co-simulated between Matlab, and the Modelica based software, SimulationX, as shown in Figure 2.9.

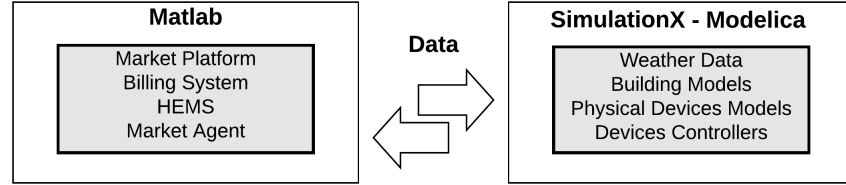


**Figure 2.9:** Model division on the co-simulation platform between Matlab and Modelica as presented in Publication 4.

The market platform model, billing systems, HEMS, and market agents are integrated into the Matlab model, while SimulationX integrates all the models of the physical devices such as the EV, HP, micro-CHP, or PVs, in addition to the building models and the device controllers. The current structure of the model emulates the real-life situation in which a market platform is integrated. All the models running on Matlab can be assumed to be running in the cloud as a service, while all the Modelica-based models are real systems.

The integrated building model is configured based on the research project data of [78]. A building of a single floor, a cellar, and an attic is integrated. The construction year is between 1984 and 1994. It has a heated living area of 150 meters and a room height of 2.5 meters. The attic and cellar are assumed to be unheated, while the living area is heated based on a supply temperature curve that varies linearly depending on the outside temperature. The hot water consumption is defined based on the standard VDI 4655. The hot water circulation consumption is based on the field measurements of [79].

The models of the flexible devices presented in Section 2.1 are integrated with their experimentally calibrated parameters. The PV system presented in [80] is used and scaled depending on the simulated scenario. The PV measurements and weather data of 2017 are used in all the presented scenarios. More details about the input data is presented in [80].

The fixed electricity profiles are based on the representative load profiles of [81]. The data includes measured high-resolution profiles of 74 residential houses managed by the same grid operator. The houses are located in the vicinity of each other. Consequently, it can be assumed the given houses lie in the same microgrid. No operation patterns of a heat pump, an EV charging, or a micro-CHP are found in the separate analysis of the household profiles. Thus, it can be deduced that there are no flexible devices in these houses and these profiles can be treated as fixed load profiles. Figure 2.10 shows yearly energy consumption and a load profile of a typical day. The households consuming between 1000-3000 kWh/a, 3001-7000 kWh/a, and 7001-9000 kWh/a are defined to be occupied by low, average, and high energy consuming prosumers, respectively.

## 2.6 Market Co-simulation and Input Data

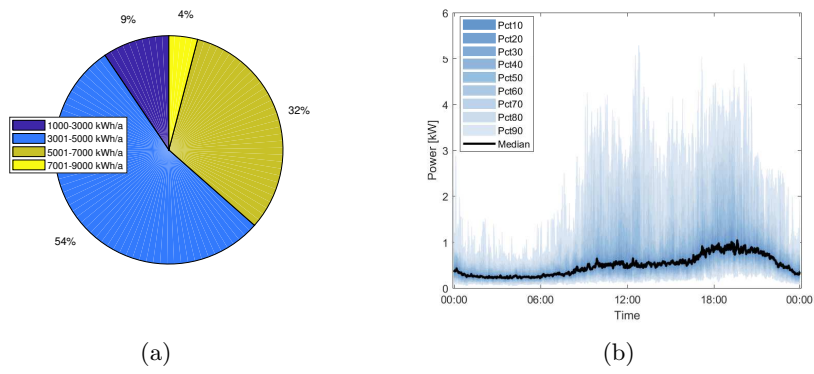


**Figure 2.10:** 74 representative household profile analyses, (a) annual energy consumption (b) electrical loads on a typical day as in Publication 5.



## 3 Results

This chapter presents a summary of the results from Publications 1-5. Section 3.1 summarizes the results of GSHP experimental analysis performed in Publication 1. Section 3.2 summarizes the results of the probabilistic forecast presented in Publication 2. Section 3.3 summarizes the evaluation of the HEMS performance using conventional and generic loads which is thoroughly discussed in Publication 3. Section 3.4 summarizes the results of the market model and the scenario analysis presented in Publication 4 and 5.

### 3.1 Experimental Analysis of a Ground-Source Heat Pump

This section discusses the cycling influence on the performance of heat pumps that can directly demonstrate the control requirements for an optimized heat pump operation. Furthermore, it demonstrates the sensitivity of the COP and heat pump operation to SH/DHW sensor position. The validation of the heat pump model is also shortly discussed. The experimental setup and the validation of the heat pump operation within the market model are discussed in Chapter 4.

#### 3.1.1 Cycling Influence and Sensors Positioning

Nine experiments were performed with the GSHP testbed to evaluate the cycling influence. Each experiment was repeated for five days, then the average was calculated. Within the first four experiments, a constant continuous load on the heat sink side (i.e., building side) was set that is equivalent to 50% of the GSHP thermal power as discussed earlier in Section 2.1.1. Figure 3.1(a) shows the thermal energy generation  $E_{th}$ , electrical energy consumption  $E_{el}$ , brine energy transferred  $E_{brine}$ , and the average COP of the GSHP for cycle duration of 1-h to 4-h on/off cycle. The 6-h cycle failed due to the insufficient capacity of the heat storage. In comparison to the Micro-CHP analysis performed in [70], the longer cycles show a lower performance compared to the short cycles. The average COP decreases by 13% from the 1-h cycle to the 4-h cycle.

In the other five experiments, the heat sink load was increased to 80%, and it was set to be cycling similar to the GSHP. The reason behind increasing the power of the heat sink and the simultaneous cycling is to consume the delivered power of the heat pump immediately and to maintain the lowest possible return temperature. Through this experiment, it can be noticed that the average COP is almost constant and is not influenced by either the long or short duration of heat pump operation as in Figure 3.1(b). The energies  $E_{th}$ ,  $E_{el}$ , and  $E_{brine}$  varied only by 2.7%, 1.5%, and 1.136%, respectively.

### 3 Results

This variation is partly due to the measurement errors and the minor difference in the initial conditions of the experiment.

To summarize the output of these experiments, it can be deduced that if a buffer or combi-storage are combined with the heat pump:

- The long operation duration to minimize the heat pump number of starts reduces the average COP and consequently can lead to a lower Seasonal Performance Factor (SPF).
- If the heat pump is delivering directly while minimally using the heat storage or without heat storage, the long duration of operation has no impact on the average COP of the system.

Hence, if a combi-storage has to be installed to minimize the number of starts per day and increase the lifetime of the heat pump, a cost of start has to be considered within the optimization. In case the heat pump has to offer flexibility to the grid, the incentives should make up for the decrease in COP that can lead in this case to a minimum of 13% increase in costs. Additionally, thermal losses of the storage have to be considered.

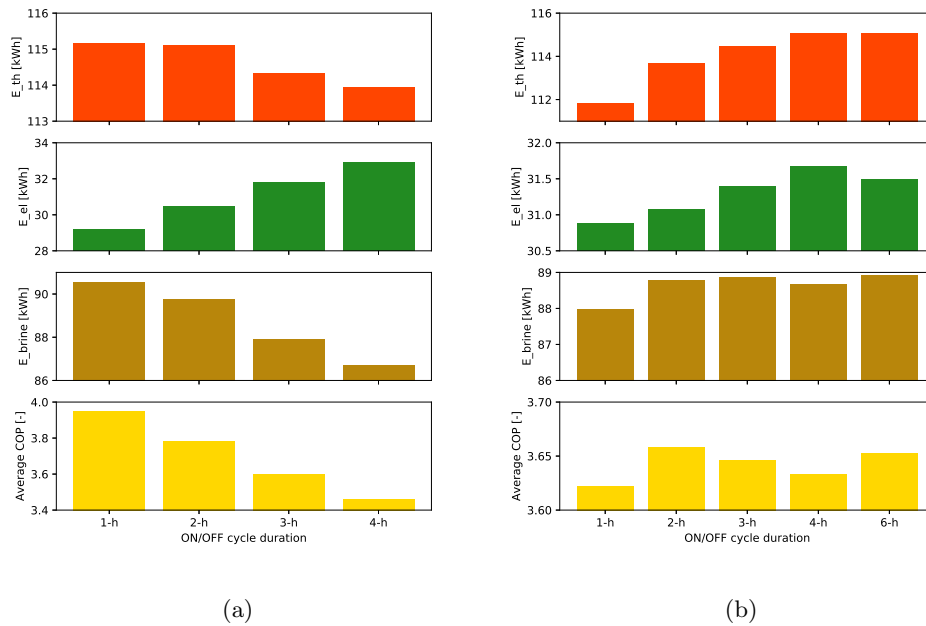


**Figure 3.1:** Cycling effect on the heat pump system performance, (a) constant continuous load (b) constant return temperature as presented in Publication 1.

GSHP system setup and configuration have a direct impact on the operation of the heat pump. SH/DHW sensor location is one of the system configurations that can significantly affect the system's operation dynamics, lifetime and efficiency. Hence, it was

discussed by several researchers such as [82–84]. The sensor position was varied between the bottom of the tank to approximately the middle of the tank. These positions are denoted in Publication 1 as T-SP-6 and T-SP-10 for the middle and bottom of the tank, respectively.

Although theoretical studies recommend installing the sensor at the lowest section of the tank to maximize comfort, the experimental study shows that this setup leads to inefficient operation. Having the sensor located at the bottom of the tank leads to a significant increase in the number of starts as the GSHP tries to maintain the whole tank capacity at the given set temperature. The higher the sensor is positioned, the lower is the number of starts per day. Having the sensor at T-SP-6 increases the COP by 21.5%, which is a significant increase considering that no intelligent control algorithms were yet deployed.

#### 3.1.2 Heat Pump Model Accuracy

The GSHP model presented in Section 2.1.1 is validated independently using the experimental testbed. Mean Absolute Percentage Error (MAPE) and RMSE are used as metrics to quantify the quality of the numerical model. The MAPE and RMSE of the thermal power are 2% and 0.7 kW, respectively. On the other hand, the MAPE and RMSE of the electrical power are 4% and 0.23 kW, respectively. The supply and return temperature are also evaluated using the same metrics in order to give an insight into the system dynamics. The MAPE and RMSE of the supply temperature are 1.5% and 0.7 K, respectively. Hence, a minor difference can be noticed on the dynamics of the supply temperature profile. Similar plausible behavior is maintained by the return temperature where the MAPE is 4% and the RMSE is 1.7 K.

Energetically, a minor difference can be noticed between the model and testbed. Using the experimental configuration discussed in Publication 1, a difference of 3% and 4% can be seen for the heat generation and electricity consumption, respectively. Hence, the model is reliable for heat pump simulation and further integration in buildings or market models.

## 3.2 Day-ahead PV Forecasting

Although the probabilistic forecast represents the main output of the model, the internally generated point forecast is also validated. The point forecast is validated based on Equations 2.9-2.12, while the probabilistic forecast is validated based on Equations 2.13-2.16. PV measurements of a 3 kW<sub>p</sub> PV system presented in [80] and a multi-purpose online weather forecast of [85] are used as a reference and input to the forecast model.

### 3.2.1 Point Forecast

Since the forecast model is designed for real-time HEMS applications, the training period is considered continuously growing over time. The initial error after one month of training had the highest value, 17.3% for the RMSE, 9.3% for the MAE and -1.5% for

### 3 Results

the MBE. After four months of training, the error reached 15.3%, 8.5% and 1.53% for the RMSE, MAE, and MBE, respectively. Considering that a multi-purpose online weather forecast is used, the minimal processing power required, and the spatial-temporal resolution of the forecast, the point forecast has an improved performance compared to other presented models in the review of [86,87].

A smart persistence model is used to benchmark the point forecast and calculate the FS. After four months of training, the FS reached 48.6%, which means that the point forecast excelled the performance of the smart persistence model. According to [88], the FS of forecasting systems with similar purposes is between 0 and 42%. For example, [89] reported FS of 31.29% for day-ahead forecast of 1.86 MW plant.

#### 3.2.2 Probabilistic Forecast

Figure 3.2 shows the forecast on a typical winter and summer day. In Figures 3.2(b) and 3.2(d), the 1-min measurements are presented to show the level of variabilities occurring on these typical days. The 1-h resolution measurements presented in Figures 3.2(a) and 3.2(c) do not show these variabilities. However, the forecast was able to predict these variabilities in the two typical days. Additional days are analyzed in Publication 2.

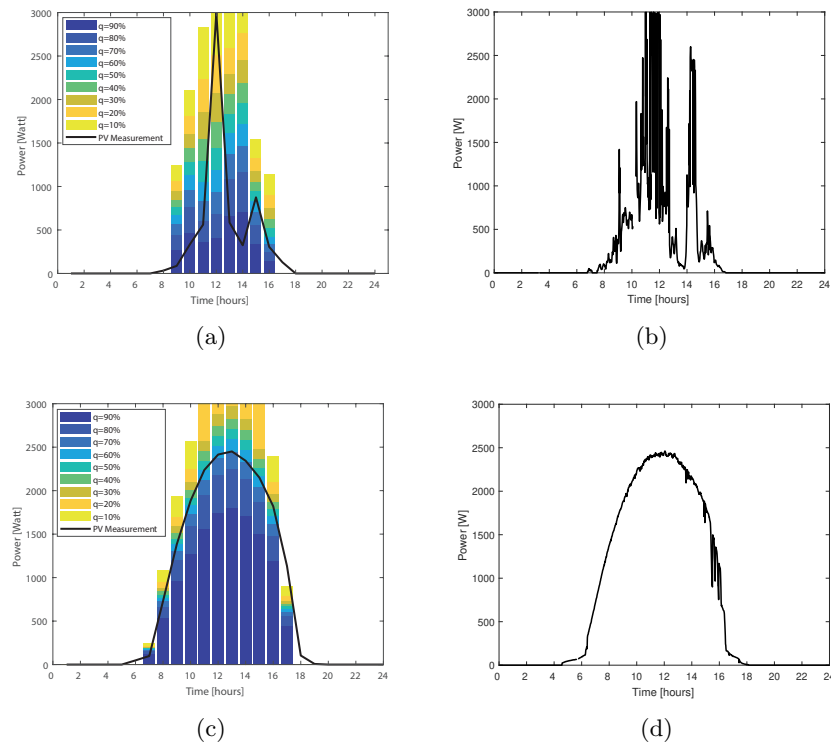


**Figure 3.2:** Probabilistic forecast output and PV measurements in multiple days in different seasons, (a) winter (b) winter-1 min resolution (c) summer (d) summer-1 min resolution as presented in Publication 2.

Table 3.1 shows the results of the CRPS for the different CDFs and training horizons. For example, having a training horizon of 1 month means that a daily forecast is made for 11 months with the same trained model. It can be noticed that CRPS's over the different training horizons did not vary significantly from the first month, which means that the model response in real-time is fast and independent of the training time. If no optimal training period is selected, the average of the CRPS over all the training periods is 5.56%. Assuming that the maximum variation of  $\lambda$  is 100% and it happens at the maximal peak power of 3 kW, the 5.56% error will lead to only 0.16 kW.

Table 3.2 shows the calculated BS at the different probabilities,  $q$ , against different training horizons. It can be noticed that the training horizon did not have a significant influence on the BS. Comparing the BS variation of  $q = 90\%$  after one month to after six months, a 6% increase in performance can be noticed. A mean for all the cases  $q$  over the different training months is only 0.12.

A reference probabilistic forecast is used to benchmark the presented forecast and calculate the Cumulative Ranked Probability Skill Score (CRPSS) and Brier Skill Score (BSS) as in [90,91]. The results in Tables 3.1 and 3.2 show the capability of the presented forecast to excel the reference forecast. After six months of training, the CRPSS and BSS are equal to 90.94% and 39.38%, respectively.

**Table 3.1:** CRPS of different training horizons as in Publication 2.

Training horizon [month(s)]	$CRPS_i$ [%]								$CRPS$ [%]	$CRPSS$ [%]
	$i = 1$	$i = 2$	$i = 3$	$i = 4$	$i = 5$	$i = 6$	$i = 7$	$i = 8$		
1	13.99	4.94	5.39	5.41	1.64	2.20	4.54	8.27	5.80	12.51
2	7.64	1.56	7.31	3.56	2.96	3.20	1.92	7.27	4.43	91.07
3	8.46	1.62	7.83	3.02	4.47	2.90	1.26	9.05	4.82	90.05
4	11.26	3.25	10.44	4.53	5.76	3.43	0.96	10.96	6.32	87.52
5	13.06	5.35	9.54	2.99	4.23	3.41	2.01	16.83	7.18	85.87
6	11.64	2.97	10.89	0.89	1.16	7.23	2.41	1.51	4.84	90.94

**Table 3.2:** BS of different training horizons as in Publication 2.

Training horizon [month(s)]	$BS$ [-]				$BSS$ [%]
	$q = 60\%$	$q = 70\%$	$q = 80\%$	$q = 90\%$	
1	0.188	0.139	0.102	0.068	43.41
2	0.195	0.143	0.106	0.072	42.72
3	0.196	0.145	0.108	0.070	40.88
4	0.195	0.144	0.107	0.071	36.29
5	0.193	0.141	0.103	0.068	36.75
6	0.189	0.140	0.09	0.064	39.38

### 3.3 Load Shifting Based on Probabilistic Forecast

This section summarizes the performance of HEMS using the probabilistic forecast under different types of loads. Two cases are presented: in the first case studies the conventional white goods loads only, while in the second case, multiple generic loads of different sizes are used along with a 3 kWp PV system. These loads emulate not only the current flexible devices but all the possible upcoming flexible devices that can be integrated into a building. In the two cases, the shifting time frame of the loads is set to 24-h in order to evaluate the potential of the HEMS without the influence of any time constraints or user behavior.

#### 3.3.1 Conventional Household Loads

This case represents the worst case scenario of a building where there is a low number of flexible devices. In this building, only a dishwasher, a dryer, and a washing machine are considered. Fixed loads are ignored within the analysis. Figure 3.3 compares the load shifting plan of the white goods using the deterministic and probabilistic forecast. In Figure 3.3(a), the white goods are allocated such that  $R_e$  is minimized and the earliest time of operation condition is satisfied as in Equation 2.18. Although this operation plan looks optimal given the input data and nature of the deterministic forecast, ignoring uncertainties and generation variabilities could not lead to an optimal operation in real-time. Using the probabilistic forecast as in Figure 3.3(b), the devices are sorted based on the certainty of the generation. The dishwasher and the dryer are placed under the  $q = 99\%$  curve, while the washing machine is placed under the  $q = 70\%$  curve. This is because it could not be set under any curve with a higher probability due to its high 2 kW peak. Hence, a higher self-consumption and self-sufficiency can be reached. Given this low number of flexible devices, a difference between the median of the self-sufficiency and self-consumption is 9.1% and 5.0%, respectively. Higher values can be reached if more flexible devices are going to be integrated.

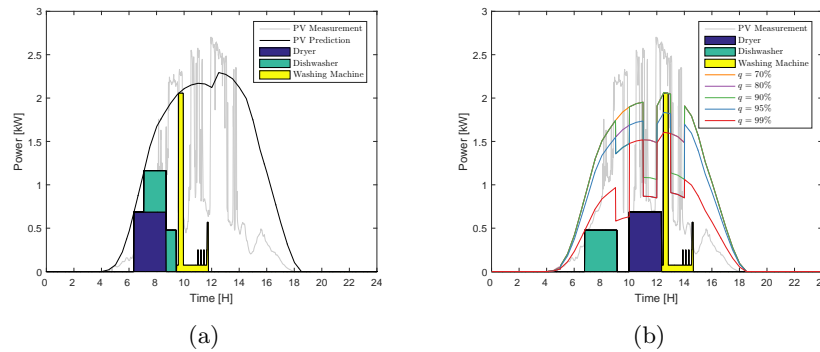


**Figure 3.3:** Comparison between the reference and the probabilistic forecast on a typical day. White goods optimally shifted based on (a) reference forecast, and (b) probabilistic forecast as presented in Publication 3.

### 3.3.2 Different Generic Loads

Generic loads are created of sizes 0.25 kW up to 1.5 kW and operated for a constant time of 1-h using the same day presented in Figure 3.3. Consequently, energy blocks were created that vary from 0.25 kWh to 1.5 kWh. These blocks can represent any of the current flexible devices such as a heat pump or an EV, and can also provide insight into the behavior of the HEMS under the influence of possible future flexible loads. The number of load blocks (devices) within the analysis is limited to 60 for the 0.25 kW loads, 30 for the 0.5 kW and 1.0 kW loads, and 15 for the 1.5 kW loads to evaluate the difference between the deterministic and probabilistic forecast.

Figure 3.4 shows the allocation of the different number of loads under the same PV forecast and generation profile. The loads are allocated such that the first load in the queue comes to operation first, followed by the rest of the devices. Hence, the first load is always sorted under the highest probability curves. It can also be graphically noticed that as the ratio of the load size to the peak load of the PV increases, the efficiency of the algorithm in managing the loads decreases.

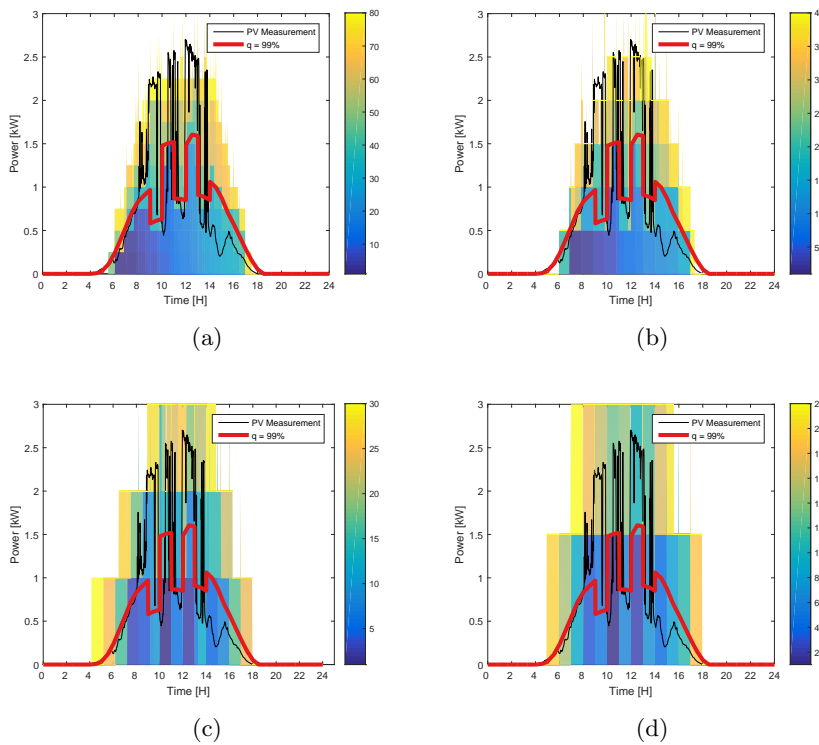


**Figure 3.4:** Different generic loads sizes shifted based on the probabilistic forecast - number of loads (colored). (a) 0.25 kW. (b) 0.5 kW. (c) 1 kW. (d) 1.5 kW as presented in Publication 3.

### 3 Results

In the analysis presented in Publication 3, the 0.25 kW loads show an increase in the mean self-sufficiency by 24.2% using the HEMS with the probabilistic forecast. On the other hand, the mean self-consumption is higher for the 0.25 kW and 0.5 load blocks by 17.7% and 16.2%, respectively. Using the multiple scenarios discussed in Publication 3, it can be deduced that as the size and number of loads increases, the added value of the probabilistic forecast and HEMS decreases.

## 3.4 Market Dynamics and Benefits

This section summarizes the results of the market model. Utility and prosumer benefits, in addition to the prosumer commitment, are discussed based on a baseline scenario of 10 single family houses located in Munich, Germany. It is assumed that these houses are occupied by low energy consuming prosumers, and are equipped with a HP, a PV system, and an EV charging station as described in Section 2.4. Further configurations are discussed through the selected 98 scenarios in Publication 5 and are summarized in this section.

### 3.4.1 Utility and Prosumer Benefits

Within this section, a comparison is made between the reference case, where no market platform or HEMS is implemented (conventional operation), and the case with the market platform. Same configuration and user preferences are used in both cases. Figure 3.5 shows the behavior of the microgrid on a summer and winter day. The case in which the market is not integrated is denoted by the reference.

In the typical summer day shown in Figures 3.5(a) and 3.5(b), it can be seen that the loads that conventionally operate before sunrise or sunset are shifted due to the low market prices to operate during the PV generation hours. Hence, a reduction in peak loads can be observed. The peak load of the microgrid export is reduced from -58 kW to -39 kW, while the import peak load is reduced from 44.5 kW to 35 kW. In winter, almost 100% PV generation power is used as shown in Figure 3.5(d), compared to Figure 3.5(c). The export peak load drops from -46 kW to -11 kW. The import power drops from 60 kW to 43 kW. Due to the high energy consumption of the heat pump in winter, the PV generation does not suffice. Thus, some loads, which are mostly heat pumps, are shifted to a later time of the day.

At the microgrid level, a one-year analysis shows that the market increases the self-sufficiency of the microgrid by 130% and the self-consumption by 120%. Also, it decreases the CO<sub>2</sub> emissions on average by 21% and the import peak load by 25%. Hence, the presented results demonstrate not only the capability of the market platform to trade and shift the loads but also the accuracy of the integrated probabilistic PV forecast in delivering profiles that maximize the efficiency of the whole model.

At the prosumer level, self-sufficiency, self-consumption, peak loads and CO<sub>2</sub> emissions are also used as metrics to quantify the benefits of the prosumer. Additionally, two cost metrics are used: cost based on the Conventional Billing (CB) and Market Billing (MB) system. In the CB system, the current conventional metering systems (no smart meters)

are used such that the prosumer pays a fixed price for the energy consumed, and earns a fixed feed-in tariff for all the generated energy. In the MB system, the energy generation and consumption prices are decided based on the market price given by Equation 2.19. In both cases, the market operations are precisely the same, and the only fundamental difference is the billing system. Using all the given metrics to perform a one-year analysis, it is found that mean self-sufficiency and self-consumption of prosumers increase by 102% and 80%, respectively. The mean peak load decreased by 16%. Additionally, the CO<sub>2</sub> emission are reduced by 26%.

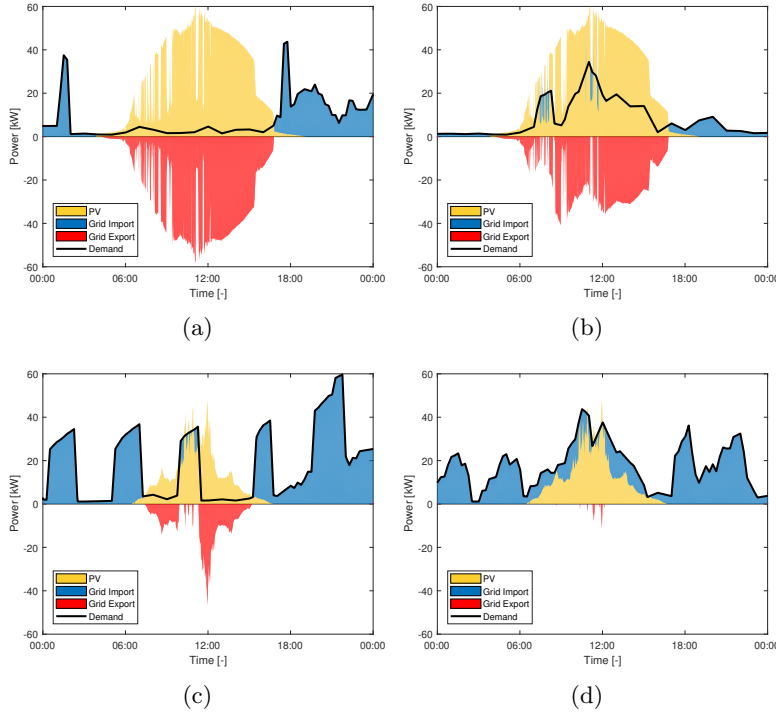


**Figure 3.5:** Type day profile of the whole microgrid, (a) summer day - reference (b) summer day - market (c) winter day - reference (d) winter day - market.

Furthermore, the market demonstrates its ability to minimize costs under both the CB and MB. The mean costs of the market under CB are 15% lower than the reference model, which is equal to 360 Euro/a. These costs are based on the current metering infrastructure. However, if the Information Infrastructure (IIS) is implemented, MB can be calculated and the market clearing price can be binding. Using the MB, the costs are 23% lower than that of the reference model, and the overall absolute savings are equal to 530 Euro/a. Thus, the expected savings from IIS could amount to an additional 170 Euro/a. These costs are calculated ignoring the transaction and service fees of the grid and market platform operator. Other fees might be considered depending on the regional regulations of the market platform. Further details and type day analyses using the same metrics are presented in Publication 4.

### 3.4.2 Prosumer Commitment

The performed analysis assumes that no penalties are paid if the prosumer does not commit to the bid. However, if the prosumer submits a selling bid of a PV system with a  $\zeta = 10$ , it is probable that the PV system would not be able to deliver the expected bid volume. As discussed in Section 2.4.3, in this situation, the battery system is responsible for fulfilling the bids. Based on a complete year analysis, Figure 3.6 demonstrates the required battery capacity per kWp PV that the prosumer needs to install to avoid any penalties. For  $\zeta \geq 58$ , no batteries are required to be installed, and 100% of the bids communicated by the PV system can be satisfied. However, the lower the  $\zeta$ , the higher the required battery capacity is. The optimal battery capacity can only be determined based on the expected platform penalty and the readiness of the prosumer to be exposed to such risks. As discussed, the PV prediction provides an indicator of the certainty of the prediction but does not decide on the amount of energy that can be traded. If the prosumer needs to avoid any penalties, it would be advised to trade up to  $\zeta = 60$ . With a lower  $\zeta$ , the profit of the prosumer can be increased as indicated by Equation 2.30, but penalties might be imposed.

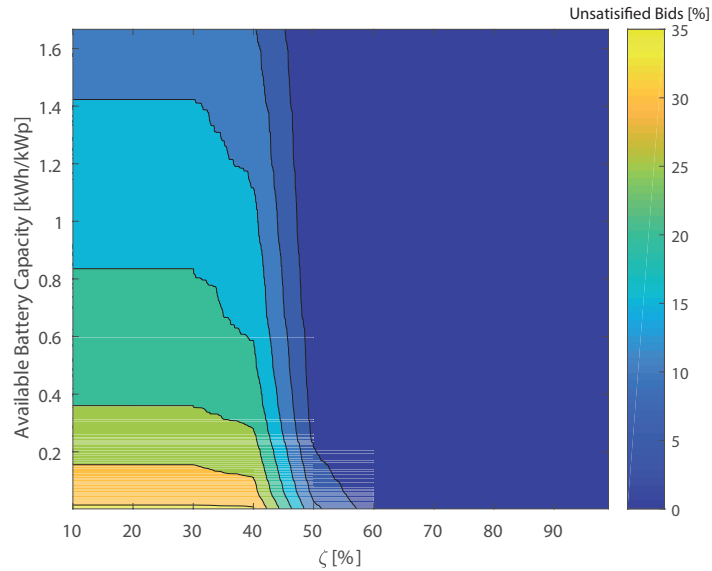


**Figure 3.6:** Percentage of unsatisfied bids against the  $\zeta$  of the PV prediction and the available battery capacity as presented in Publication 4.

### 3.4.3 Scenario Analysis

The market platform's performance is highly dependent on the nature of the market, microgrids, and prosumers. Although the models presented in the literature discuss mostly type day analysis, the co-simulation method and the tailored flexible device models enable a complete year analysis. Several scenarios could be analyzed. However, 98 scenarios are selected to quantify the potential of the market model. These scenarios

are divided into three different groups. The first group studies market design parameters, the second group studies different microgrid configuration, and the third group studies the influence of the user behavior. The results of the three scenario groups can be summarized as follows:

- Market capability to act as a decentralized energy management systems is independent of the market price ranges, transaction or service fees imposed by the service operation. The prosumer profit is the only sensitive output to the market price ranges. Hence, the utility or market coordinator should make sure that the prosumer can maintain at least a minimal profit.
- Trading intervals and resolution can improve the market operation, yet the forecast resolutions can limit their impact. Forecast resolution should match trading intervals to maximize the benefits of the utility and prosumers.
- Number of prosumers directly influences the performance of the market. The presented model is capable of operating with 2 prosumers (6 devices). As the number of devices increases, the benefits of the market increase. However, after 15 devices, the benefits of the market reaches a plateau. Hence, it is recommended to have at least 15 devices to operate the market platform.
- An increase in the installed PV capacity in the microgrid directly influences the self-sufficiency, and self-consumption, even if no market platform is integrated. However, the market model can double the self-sufficiency and self-consumption, decrease the peak loads, and annual costs of the prosumers proportionally.
- Fixed load yearly energy consumption is chosen to reflect the lifestyle and the consumption habits of the prosumers. Based on the field measurement data, it is found that the higher the share of the fixed loads, the lower is the efficiency of the market. Hence, prosumers with the lowest share of fixed loads are expected to maintain higher profits using market platforms.



## 4 Validation and Demonstration

This chapter summarizes the HiL method and heat pump testbed used to validate the heat pump model operation in the market as in Publication 6 and 7. Testbed hydraulic system and module components are discussed shortly. Furthermore, a selected type day is used to show the dynamics of the heat pump testbed using the HiL developed in Publication 6 against the heat pump model communicating with the market platform.

### 4.1 Testbed Components and Structure

The testbed consists of three modules: ground-source emulator (A), combi-storage (B), and the building load emulator (C). The testbed was designed as a modular system to enable testing multiple hydraulic configurations and integrating additional modules. Figures 4.1 and 4.2 show the current hydraulic setup and the real implementation of the testbed, respectively.

Module A includes a ground-source emulator that can provide any required brine temperature to the heat pump. It consists of 300 l heat storage, filled with a water-glycol mixture as an anti-freezing heat transfer fluid. The storage is heated by a 12.5 kW electrical heater that is controlled via a hysteresis regulator to maintain the tank temperature during the whole operation time at 40 °C. The set temperature of the tank and the hysteresis bandwidth can be defined by the user depending on the simulation goals. A mixer, similar to the conventional space heating mixers, is used to mix the supply of brine tank with the return of the heat pump to reach the required ground-source set temperature. Depending on the HiL system and the goal of the simulation, the mixer can maintain a constant brine temperature or a time-dependent temperature profile.

Module B shows the storage system of a conventional residential house. It includes a 749 l combi hygienic buffer storage to cover the space heating and domestic hot water consumption. A stainless steel heat exchanger extracts heat from the storage to cover the hot water consumption. Moreover, a coaxial pipe, pipe-in-pipe system, is used to enable the hot water circulation and maintain the pipe temperatures at a certain level. An example of the coaxial pipe circulation connection is presented in [92].

Module C is the most complex module as it represents the heat sink of the testbed. It can emulate the space heating and domestic hot water consumption depending on the building type and user behavior. The space heating circuit consists of a space heating mixer, circulation pump, and two heat exchangers. Through the mixer, the supply of the tank with the return of the space heating is mixed to reach the required space heating supply set temperature. The circulation pump is controlled according to the set flow rate, which varies depending on the heat demand. Two heat exchangers of two different sizes are used to emulate different building loads depending on their required maximum

#### 4 Validation and Demonstration

heat power. One heat exchanger is dedicated to old building heating loads that can reach up to 20 kW and have a high flow rate, while the other one is only for new buildings with a maximum power of 7 kW.

Although this testbed can operate independently and represent a real-system, one major component and source of uncertainties is missing, which is the building. Hence, the HiL system introduced in Publication 6 proposed a complete simulation solution for the integration of building models in the loop. The presented HiL is capable of minimizing these uncertainties and delivering real-system dynamics. Further details are presented in Publication 6 and 7.

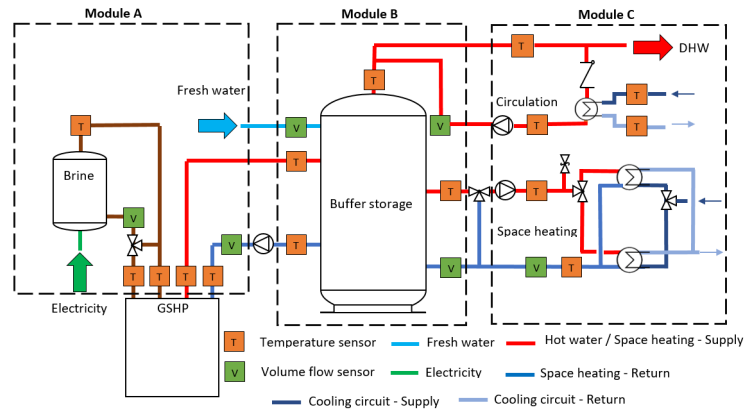


**Figure 4.1:** Simplified hydraulic scheme of the testbed.



**Figure 4.2:** The three modules and the heat pump installation in the lab.

## 4.2 Hardware in the Loop (HiL) Type Day Simulation

Using the baseline model discussed earlier in Section 3.4, a single family house is selected to be validated and demonstrated based on the HiL and the heat pump testbed. The goal of the demonstration is to compare the operation of the heat pump in the market model to that of the testbed with HiL. Figure 4.3 shows the output of the model and the testbed on a winter type day as per the VDI standard 4655. In Figures 4.3(a) and 4.3(b), it can be seen that the space heating with the simulation model and the HiL are almost identical, even though a power drop occurred around 17:00 due to low heat storage content. Hence, the model can also predict the behavior of the storage system correctly. Figure 4.3(c) shows the electrical and thermal power of the heat pump in the simulation model and using the HiL testbed. Both profiles are behaving similarly in terms of magnitude and dynamics. In this type day, the energy difference between the simulation and the HiL is 2% and 5% for the heat generation and electricity consumption, respectively.

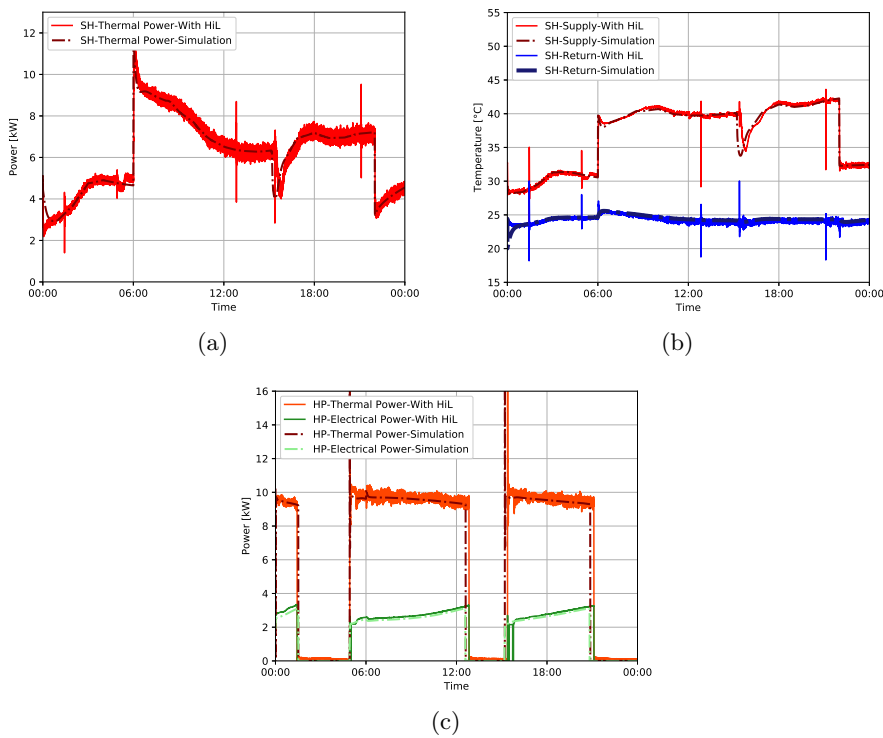


**Figure 4.3:** Heat pump dynamics of the testbed operation with HiL and simulation model, (a) space heating thermal power (b) space heating supply and return temperatures as presented in Publication 7.

An advantage of the HiL validation is its capability not only to enable energetic analysis but also dynamic analysis. For the validation of the heat pump operation in the market platform, it is important to analyze the time and volume of the heat pump bid.

#### *4 Validation and Demonstration*

Hence, TDI is used in this case as a metric as presented in Equation 2.17. The output of the TDI on this type day is 3%, which means that the temporal distortion is minimal and the heat pump dynamics and interactions with the market platform are realizable.

## 5 Conclusion, Discussion and Outlook

This chapter summarizes the answers to the major research questions raised in Publications 1-7. It shortly concludes the methods and design strategies followed to deliver this dissertation. Moreover, it presents an outlook about the potential boundless possibilities of future research in the field of flexible systems modeling, energy management systems, and local energy markets.

### 5.1 Answers to Research Questions

In this section, the research questions are answered briefly in order to provide a comprehensive picture of this dissertation.

- 1. What are the optimal control criteria for heat pump operation in buildings based on experimental analysis?**

Through the experimental analysis, it was found that the optimal control criteria are not only dependent on the heat pump, but also on several system setup parameters. Compared to other heating systems, the heat pump operation is highly sensitive to the hydraulic setup, storage system or even SH/DHW sensor's position. As in Publication 1, changing the sensor position could lead to an increase in COP by 21.5% using the same control strategy. For the implemented testbed setup, it was found that long or short control cycles have no impact on the COP. In fact, short cycles can increase the system efficiency as they maintain a lower temperature in the tank. However, these short cycles might decrease the lifespan of the compressor. Consequently, the optimal control has to include the start cost to balance the benefits of the higher COP with short cycles.

- 2. Which forecasting method is optimal and applicable for small-scale PV systems?**

Real-time monitoring over four years of a rooftop PV system of a building shows the complexity in forecasting the generation variability. These variabilities can be observed using high resolution (<1-h) measurements and is computationally hard to be deterministically forecasted given the available computational resources. Hence, the probabilistic forecast was found to be the optimal approach for PV forecasting with high variabilities. In Publication 2, the day-ahead probabilistic forecast was proposed as a solution that is currently publicly available as an open-source software for buildings [75]. This probabilistic forecast system provides multiple curves with certainties that are tailored to maximize the operation efficiency of the energy management systems and avoid misplanning.

**3. How can probabilistic forecasts be integrated in home energy management systems?**

The home energy management systems in the literature work either based on a predefined PV curve or a deterministic forecast. Hence, they are exposed to several uncertainties in real-life operation conditions. Optimization based on probabilistic forecast was presented in Publication 3. The home energy management system does not optimize based on one profile but multiple profiles that have different certainties. Hence, a potential increase in self-sufficiency and self-consumption of 24.2% and 17.7%, respectively, can be realized.

**4. How will home energy management systems react to different generic loads?**

This dissertation does not only address the current limited flexible loads but all possible future loads. Hence, different generic loads were analyzed in Publication 3. It was found that the load power can directly impact the efficiency of the home energy management system. Independent of the optimization technique or the forecasting system used, an increase in the ratio of the load to generation power can directly decrease the self-sufficiency and self-consumption.

**5. Which market design can facilitate the integration of prosumers in energy trading platforms while satisfying the microgrid coordination requirements?**

A sealed double-sided auction with uniform pricing was found to be the most suitable candidate satisfying the microgrid coordination requirements presented earlier in Section 1.1.2. A double-sided auction enables the prosumer to act as a buyer or a seller at any time of the day. Having the market sealed and communicating only a volume - price signal guarantees the prosumers' privacy while participating in the market. The discrete uniform pricing provides a fair environment to the prosumers and synchronizes all the traded bids within a specific time frame. This market model shows promising potential for the utility and the prosumers. It can increase the self-sufficiency and self-consumption of the whole microgrid while reducing the costs of an average prosumer by 23% (530 Euro/a).

**6. What is the potential of energy trading platforms in microgrids?**

The potential of energy trading platforms in microgrids cannot be evaluated based on a single scenario. Hence, three scenario groups are discussed: market design parameters, microgrid configurations, and user behavior. Through the first group, it is found that changing the price ranges of the market design cannot influence the energy management (resource allocation) functionality of the market or utility benefit, however, it can change the profit of the prosumers. The second group shows that higher generation capacities can increase the benefits of the prosumers. However, it reaches a plateau after certain capacities where there is no sufficient demand. The third group shows that users with lower fixed load consumption can achieve higher profits as a large share of their energy supply and demand can be traded at more competitive prices in the market platform.

## 5.2 Concluding Remarks

Integration of energy markets in microgrids adds additional design degrees of freedom for both of the market and energy system designers. In this case, the market design process is not bound by defining market rules, bidding rules or pricing mechanism. Several other factors have to be considered such as the market participants' technical limitations, communication latency, or even privacy constraints. In these markets, for example, the market participant is not an ordinary market seller or buyer as in conventional markets or even current online market platforms, but a high frequency automated trader of distributed energy systems that have different operation constraints and system dynamics. A market design that does not fit the nature of the prosumers and their limitations can hardly be realizable.

In this dissertation, a detailed bottom-up approach was followed to minimize the model design uncertainties and guarantee the practicality of the model in real-life. The approach started with the smallest unit of an energy system, which is the device, followed by buildings, and finally microgrids. At the three design levels, either experimental testbed or field measurements were used to maintain realistic system dynamics.

At the level of devices, multiple devices were integrated. However, heat pumps and PV systems were further discussed. A ground-source heat pump testbed was developed in order to analyze the system reaction to different operation constraints and system configurations. Based on these analyses, a non-linear heat pump model was developed that was tailored to microgrid simulations. The sensitivity of the heat pump and the model to changes in the hydraulic configurations and system dynamics emphasized the necessity of the bottom-up approach followed in this dissertation. For the PV systems, a probabilistic forecast was developed to enable energy management and trading of the prosumers' variable generation.

At the building level, the developed device models and forecasts were integrated into a home energy management system. An optimization algorithm that fits the nature of the novel probabilistic forecast was implemented. The impact of the forecast was analyzed in order to quantify its benefits. Within this analysis, not only were the modeled devices considered but also multiple generic loads of different sizes. Hence, a detailed picture can be drawn about the behavior of the forecast and home energy management systems based on the currently available devices and possible upcoming devices in the future.

At the microgrid level, a market model was developed using the data, models, and forecasting systems available at the building and device level. The presented market model was tailored to satisfy the coordination requirements of both the prosumer and utility. Device-oriented bidding strategies were designed to adapt to the operation dynamics of the common devices in a household. Using a co-simulation system, the market model was analyzed over a complete year from both the prosumer and utility perspective through 98 scenarios. These scenarios showed the market reaction to different design parameters, microgrid configuration, and even user behavior.

Although each model was independently validated, an additional system demonstration and validation using a HiL real-time simulation system was performed. A type day was selected to demonstrate the accuracy of the model and reliability of its dynamics.

### 5.3 Outlook

In every aspect discussed in this dissertation, there is still room for research. The field of energy markets for microgrids is still considered a young field. Earlier, market applications in microgrids may have been considered ambitious as they need a modern ICT infrastructure. However, using technology like blockchain, a market platform for microgrids can be realized in the next few years. Nevertheless, several design options and applications still need to be identified. These design parameters can vary based on regional regulations, infrastructure constraints, and above all, the prosumers' requirements.

These regional regulations can be proposed after evaluating the potential of market platforms at the national energy system level. In the near future, it is possible to have a local energy market in each microgrid. The impact of these multiple markets is expected to be plausible. However, no studies quantified this impact so far according to the recent literature reviews. This could be due to the high computational power requirements of the current market models.

Nevertheless, the infrastructure constraints can be easily identified through a demonstration. This demonstration can easily show the factors that can hinder the applications of energy markets in microgrids.

The prosumers' requirements might still influence a few market design parameters that can only be identified based on surveys or field studies. For example, the level of automation of the market and its interface with a human being can still be investigated. Moreover, the minimal required profit or financial incentives needed by the prosumers to participate have to be quantified. The market coordinator might impose fees on the prosumers. These fees as discussed in the presented model would not influence the benefits of the utility but the benefits of the prosumers. Thus, the system operation costs or fees should be calculated in a way that guarantees the participation of the prosumers while maintaining at least a minimal financial benefit.

Furthermore, the capability of the prosumer to bid with prices higher than the grid tariff should be studied. The grid tariff represents a ceiling to guarantee the prosumers' benefits. However, some prosumers might be interested in buying local energy supply to support the local community, even if the local supply is more expensive. This bidding range is variable from one society to another depending on the culture and level of environmental awareness.

# Bibliography

- [1] W. El-Baz, P. Tzscheutschler, and U. Wagner. Integration of energy markets in microgrids: A double-sided auction with device-oriented bidding strategies. *Applied Energy*, 241:625 – 639, 2019. doi:10.1016/j.apenergy.2019.02.049.
- [2] J. Delbeke and P. Vis. *EU Climate Policy*. European Union, 2016. doi:10.4324/9781315580623.
- [3] Umwelt Bundesamt. Climate change and energy law — Umweltbundesamt, 2018.
- [4] BMU - Federal Ministry for the Environment. Climate Action Plan 2050 – Germany’s long-term emission development strategy, 2017.
- [5] Federal Ministry for Economic Affairs and Energy. An Electricity Market for Germany ’ s Energy Transition. 2014.
- [6] Bundesministerium der Justiz und für Verbraucherschutz. Gesetz für die Erhaltung, die Modernisierung und den Ausbau der Kraft-Wärme-Kopplung (Kraft-Wärme-Kopplungsgesetz) (Renewable energy heating Act), 2016.
- [7] Federal Republic of Germany. Act on the Development of Renewable Energy Sources - RES Act 2017. (July):179, 2017.
- [8] Federal Ministry for Economic Affairs and Energy. BMWi - Federal Ministry for Economic Affairs and Energy - For a future of green energy, 2018.
- [9] S. Oberleitner. Impact of country-specific requirements on the costs of charging stations infrastructure ( Bachelor Thesis), 2017.
- [10] Federal Ministry for Economic Affairs and Energy (BMWi). The energy of the future - Forth Energy Transition Monitoring Report Summary. 63(4):60–62, 2014.
- [11] S. Bubeck, J. Tomaschek, and U. Fahl. Perspectives of electric mobility: Total cost of ownership of electric vehicles in Germany. *Transport Policy*, 50:63–77, 2016. doi:10.1016/j.tranpol.2016.05.012.
- [12] R. Loisel, G. Pasaoglu, and C. Thiel. Large-scale deployment of electric vehicles in Germany by 2030: An analysis of grid-to-vehicle and vehicle-to-grid concepts. *Energy Policy*, 65:432–443, 2014. doi:10.1016/j.enpol.2013.10.029.
- [13] S. K. Sowe, E. Simmon, K. Zettsu, F. De Vault, and I. Bojanova. Cyber-Physical-Human Systems: Putting People in the Loop. *IT Professional*, 18(1):10–13, 2016. doi:10.1109/MITP.2016.14.

## Bibliography

- [14] International Renewable Energy Agency. Solving the Energy Access Problem with Renewable Mini-Grids. Technical report, Bonn, 2016.
- [15] C. Marnay, S. Chatzivasileiadis, C. Abbey, R. Iravani, G. Joos, P. Lombardi, P. Mancarella, and J. Von Appen. Microgrid evolution roadmap. *Proceedings - 2015 International Symposium on Smart Electric Distribution Systems and Technologies, EDST 2015*, pages 139–144, 2015. doi:10.1109/SEDST.2015.7315197.
- [16] Department of Energy office of Electricity Delivery and Energy Reliability. Summary report: 2012 DOE microgrid workshop. Technical report, 2012.
- [17] T. Buehler. Microgrids. *ABB review*, pages 8–10.
- [18] A. Majzoubi and A. Khodaei. Application of Microgrids in Supporting Distribution Grid Flexibility. *IEEE Transactions on Power Systems*, 32(5):3660–3669, 2017. doi:10.1109/TPWRS.2016.2635024.
- [19] Federal Ministry for Economic Affairs and Energy. Funding programme "Smart Energy Showcases- Digital Agenda for the Energy Transition (SINTEG)".
- [20] Q. Fu, A. Hamidi, A. Nasiri, V. Bhavaraju, S. B. Krstic, and P. Theisen. The Role of Energy Storage in a Microgrid Concept: Examining the opportunities and promise of microgrids. *IEEE Electrification Magazine*, 1(2):21–29, 2013. arXiv:arXiv:1406.0223v1, doi:10.1109/MELE.2013.2294736.
- [21] M. Shahidehpour. Role of smart microgrid in a perfect power system. *IEEE PES General Meeting, PES 2010*, page 60616, 2010. doi:10.1109/PES.2010.5590068.
- [22] G. Venkataramanan and C. Marnay. A large Role for Microgrids. *IEEE Power And Energy Magazine*, (june):78–82, 2008. doi:10.1109/MPE.2008.918720.
- [23] C. Ho, R. Yan, T. K. Saha, and S. Goodwin. Design microgrid for a distribution network: A case study of the University of Queensland. *IEEE Power and Energy Society General Meeting*, pages 1–5, 2013. doi:10.1109/PESMG.2013.6672192.
- [24] N. Hatziargyriou, H. Asano, R. Iravani, and C. Marnay. Microgrids. (august), 2007. doi:10.1109/MPAE.2007.376583.
- [25] Y. Shen, X. Wen, L. Wang, and W. Guan. 2018 IEEE International Conference on Energy Internet A Visualization Compression Algorithm Considering Interactive Structure for Energy Trading of Microgrid System. *2018 IEEE International Conference on Energy Internet (ICEI)*, (3):49–54, 2018. doi:10.1109/ICEI.2018.00017.
- [26] M. Killian, M. Zauner, and M. Kozek. Comprehensive smart home energy management system using mixed-integer quadratic-programming. *Applied Energy*, 222(March):662–672, 2018. doi:10.1016/j.apenergy.2018.03.179.

- [27] A. Barbato and G. Carpentieri. Model and algorithms for the real time management of residential electricity demand. *2012 IEEE International Energy Conference and Exhibition (ENERGYCON)*, pages 701–706, sep 2012. doi:10.1109/EnergyCon.2012.6348242.
- [28] M. Wang and L. Tian. Regulating effect of the energy market-Theoretical and empirical analysis based on a novel energy prices-energy supply-economic growth dynamic system. *Applied Energy*, 155:526–546, 2015. doi:10.1016/j.apenergy.2015.06.001.
- [29] Z. Wu, H. Tazvinga, and X. Xia. Demand side management of photovoltaic-battery hybrid system. *Applied Energy*, 148:294–304, 2015. doi:10.1016/j.apenergy.2015.03.109.
- [30] Y. Han, Q. Zeng, Z. Geng, and Q. Zhu. Energy management and optimization modeling based on a novel fuzzy extreme learning machine: Case study of complex petrochemical industries. *Energy Conversion and Management*, 165(March):163–171, 2018. doi:10.1016/j.enconman.2018.03.049.
- [31] I. Ben Ali, M. Turki, J. Belhadj, and X. Roboam. Optimized fuzzy rule-based energy management for a battery-less PV/wind-BWRO desalination system. *Energy*, 159:216–228, 2018. doi:10.1016/j.energy.2018.06.110.
- [32] Y. Guo, J. Wang, H. Chen, G. Li, J. Liu, C. Xu, R. Huang, and Y. Huang. Machine learning-based thermal response time ahead energy demand prediction for building heating systems. *Applied Energy*, 221(November 2017):16–27, 2018. doi:10.1016/j.apenergy.2018.03.125.
- [33] S. Gottwalt, W. Ketter, C. Block, J. Collins, and C. Weinhardt. Demand Side Management : A simulation of household behavior under variable prices. *Energy Policy*, 39(12):8163–8174, dec 2011. doi:10.1016/j.enpol.2011.10.016.
- [34] Z. Chen, S. Member, L. Wu, and Y. Fu. Real-Time Price-Based Demand Response Management for Residential Appliances via Stochastic Optimization and Robust Optimization. 3(4):1822–1831, 2012.
- [35] W. El-Baz and P. Tzscheuschler. Autonomous coordination of smart buildings in microgrids based on a double-sided auction. In *2017 IEEE Power & Energy Society General Meeting*, number August, pages 1–5, Chicago, jul 2017. IEEE. doi:10.1109/PESGM.2017.8273944.
- [36] J. Honold, C. Kandler, P. Wimmer, B. Schropp, R. Reichle, M. Gröne, M. Bünemann, J. Klein, and M. Kufner. Distributed integrated energy management systems in residential buildings. *Applied Thermal Engineering*, 114:1468–1475, 2017. URL: <http://dx.doi.org/10.1016/j.applthermaleng.2016.10.158>, doi:10.1016/j.applthermaleng.2016.10.158.

## Bibliography

- [37] W. El-Baz and P. Tzscheutschler. Co-Simulation of a Smart Home Model Based on a Micro Electricity Market. *Fifth German-Austrian IBPSA Conference*, 2014.
- [38] Lehrstuhl für Energiewirtschaft und Anwendungstechnik. e-MOBILie - Schaufenster Elektromobilität. URL: <http://www.ewk.ei.tum.de/forschung/projekte/e-mobilie/>.
- [39] D. E. Olivares, C. A. Canizares, and M. Kazerani. A centralized energy management system for isolated microgrids. *IEEE Transactions on Smart Grid*, 5(4):1864–1875, 2014. doi:10.1109/TSG.2013.2294187.
- [40] K. Kok and S. Widergren. A Society of Devices: Integrating Intelligent Distributed Resources with Transactive Energy. *IEEE Power and Energy Magazine*, 14(3):34–45, 2016. doi:10.1109/MPE.2016.2524962.
- [41] The New Shorter Oxford English Dictionary. ”Art, N.”, 1993.
- [42] L. Tesfatsion. Auction basics for wholesale power markets: Objectives and pricing rules. *2009 IEEE Power and Energy Society General Meeting, PES '09*, (February):1–8, 2009. doi:10.1109/PES.2009.5275970.
- [43] L. T. A. Maurer and L. A. Barroso. Electricity Auctions: An Overview of Efficient Practices.
- [44] Y. Shoham and K. Leyton-Brown. *Multiagent systems*, volume 8953. Shoham and Leyton-Brown, 2008.
- [45] M. N. Faqiry, S. Member, and S. Das. Double-Sided Energy Auction in Microgrid : Equilibrium Under Price Anticipation. 2016.
- [46] S. Parsons, J. A. Rodriguez-Aguilar, and M. Klein. Auctions and bidding: A guide for computer scientists. *ACM Computing Surveys (CSUR)*, 43:10:1–10:59, 2011. doi:10.1145/1883612.1883617.
- [47] S. Parsons, M. Marcinkiewicz, J. Niu, and S. Phelps. Everything you wanted to know about double auctions, but were afraid to (bid or) ask. Technical report, Department of Computer & Information Science, City University of New York, 2006.
- [48] D. P. Friedman and J. Rust. The Double Auction Market: Institutions, Theories, and Evidence. In *Santa Fe Institute Studies in the Sciences of Complexity Proceedings*, volume 1993, pages 103–103. Routledge, 1993. doi:10.1016/j.joms.2013.02.009.
- [49] M. Haas and M.-A. Zoican. Discrete or Continuous Trading? HFT Competition and Liquidity on Batch Auction Markets. *Working Paper*, 2016.

- [50] S. F. Tierney, T. Schatzki, R. Mukerji, and S. Tierney. Uniform-Pricing versus Pay-as-Bid in Wholesale Electricity Markets: Does it Make a Difference? *Analysis Group*, (March):1–25, 2008.
- [51] W. Tushar, C. Yuen, H. Mohsenian-Rad, T. Saha, H. V. Poor, and K. L. Wood. Transforming Energy Networks via Peer to Peer Energy Trading: Potential of Game Theoretic Approaches. *IEEE Signal Processing Magazine*, 35(July):90–111, 2018. arXiv:1804.00962, doi:10.1109/MSP.2018.2818327.
- [52] J. Guerrero, A. Chapman, and G. Verbic. A study of energy trading in a low-voltage network: Centralised and distributed approaches. *2017 Australasian Universities Power Engineering Conference (AUPEC)*, pages 1–6, 2017. doi:10.1109/AUPEC.2017.8282502.
- [53] L. Einav, C. Farronato, and J. Levin. Peer-to-peer markets. *NBER Working Paper*, 8(650):1–34, 2015. arXiv:arXiv:1011.1669v3, doi:10.1017/CB09781107415324.004.
- [54] R. Schollmeier and T. Universität. A Definition of Peer-to-Peer Networking for the Classification of Peer-to-Peer Architectures and Applications. 15(1):101–102, 2002. doi:10.1007/978-1-4614-7544-6\_4.
- [55] M. Khorasany, Y. Mishra, and G. Ledwich. Auction Based Energy Trading in Transactive Energy Market with Active Participation of Prosumers and Consumers. *2017 Australasian Universities Power Engineering Conference (Aupec)*, 2017. doi:10.1109/AUPEC.2017.8282470.
- [56] M. Millisterfer. *Transaktive Kontrolle in Projekten und Aktuellen Umsetzungen (Bachelor Arbeit)*. Technical University of Munich, 2018.
- [57] E. Mengelkamp, J. Gärttner, K. Rock, S. Kessler, L. Orsini, and C. Weinhardt. Designing microgrid energy markets: A case study: The Brooklyn Microgrid. *Applied Energy*, 210:870–880, 2018. doi:10.1016/j.apenergy.2017.06.054.
- [58] T. Morstyn, A. Teytelboym, and M. D. McCulloch. Bilateral Contract Networks for Peer-to-Peer Energy Trading. *IEEE Transactions on Smart Grid*, 3053(c):1–10, 2018. doi:10.1109/TSG.2017.2786668.
- [59] A. Kriukov, B. Vicol, and M. Gavrilas. Applying a micro-market inside an electric vehicles parking facility. *Proceedings of the Universities Power Engineering Conference*, 2014. doi:10.1109/UPEC.2014.6934793.
- [60] J. Kang, R. Yu, X. Huang, S. Maharjan, Y. Zhang, and E. Hossain. Enabling Localized Peer-to-Peer Electricity Trading among Plug-in Hybrid Electric Vehicles Using Consortium Blockchains. *IEEE Transactions on Industrial Informatics*, 13(6):3154–3164, 2017. doi:10.1109/TII.2017.2709784.

## Bibliography

- [61] S. Bahrami and M. H. Amini. A decentralized trading algorithm for an electricity market with generation uncertainty. *Applied Energy*, 218(February):520–532, 2018. arXiv:1705.02577, doi:10.1016/j.apenergy.2018.02.157.
- [62] C. Zhang, J. Wu, Y. Zhou, M. Cheng, and C. Long. Peer-to-Peer energy trading in a Microgrid. *Applied Energy*, 220(February):1–12, 2018. doi:10.1016/j.apenergy.2018.03.010.
- [63] M. Beer, D. Beistler, H. Chelly, C. Hemmerle, C. Höhle, J. Honold, and B. M. Werke. *Abschlussbericht zum Förderprojekt "Energieautarke Elektromobilität im Smart-Micro-Grid vom Einfamilienhaus bis zum intelligenten Parkhaus"*. BMW AG, München, 2016. doi:10.2314/GBV:872858162.
- [64] D. Fischer and H. Madani. On heat pumps in smart grids: A review. *Renewable and Sustainable Energy Reviews*, 70(May 2016):342–357, 2017. doi:10.1016/j.rser.2016.11.182.
- [65] D. H. Li, L. Yang, and J. C. Lam. Zero energy buildings and sustainable development implications - A review. *Energy*, 54:1–10, 2013. doi:10.1016/j.energy.2013.01.070.
- [66] G. Salvalai. Implementation and validation of simplified heat pump model in IDA-ICE energy simulation environment. *Energy and Buildings*, 49:132–141, 2012. doi:10.1016/j.enbuild.2012.01.038.
- [67] M. Ljubijankic, C. Nytsch-Geusen, J. Rädler, and M. Löffler. Numerical coupling of Modelica and CFD for building energy supply systems. *Proceedings of the 8th International Modelica Conference*, pages 286–294, 2011.
- [68] Open Modelica. OpenModelica. URL: <https://www.openmodelica.org/>.
- [69] ESI ITI. SimulationX 3.8 — Green City.
- [70] J. P. Lipp. Flexible Stromerzeugung mit Mikro-KWK-Anlagen, 2015.
- [71] M. Tutuianu, A. Marotta, H. Steven, E. Ericsson, T. Haniu, N. Ichikawa, and H. Ishii. Development of a World-wide Worldwide harmonized Light duty driving Test Cycle. *Technical Report*, 03(January):7–10, 2014. doi:10.3141/2503-12.
- [72] R. Bird and R. Hulstrom. Simplified clear sky model for direct and diffuse insolation on horizontal surfaces, 1981. doi:10.2172/6510849.
- [73] L. Frías-Paredes, F. Mallor, T. León, and M. Gastón-Romeo. Introducing the Temporal Distortion Index to perform a bidimensional analysis of renewable energy forecast. *Energy*, 94:180–194, 2016. doi:10.1016/j.energy.2015.10.093.
- [74] L. Frías-Paredes, F. Mallor, M. Gastón-Romeo, and T. León. Dynamic mean absolute error as new measure for assessing forecasting errors. *Energy Conversion and*

- Management*, 162(February):176–188, 2018. doi:10.1016/j.enconman.2018.02.030.
- [75] W. El-Baz, M. Eldakadosi, and C. Eren. P3- Prediction System. sep 2018. URL: <https://welbaz.github.io/p3/>, doi:10.5281/ZENODO.1412785.
- [76] W. El-Baz, P. Tzscheutschler, and U. Wagner. Experimental study and modeling of ground-source heat pumps with combi-storage in buildings. *Energies*, 11(5), 2018. doi:10.3390/en11051174.
- [77] J. Lipp and F. Sanger. Potential of power shifting using a micro-CHP units and heat storages. Naples, Italy, 2013. Microgen3.
- [78] EPISCOPE. IEE Project TABULA, 2018.
- [79] J. Lipp and J. Jungwirth. Field Test with Stirling Engine Micro-CHP-Units in Residential Buildings. *MicroGEN II Conference*, 2011.
- [80] W. El-Baz, J. Honold, L. Hardi, and P. Tzscheutschler. High-resolution dataset for building energy management systems applications. *Data in Brief*, 54:1–5, 2018. doi:10.1016/j.dib.2017.12.058.
- [81] T. Tjaden, J. Bergner, J. Weniger, and V. Quaschnig. Representative electrical load profiles of residential buildings in Germany with a temporal resolution of one second. *Working Paper. HTW Berlin -HTW Berlin - University of Applied Sciences Research*, pages 1–7, 2015. doi:10.13140/RG.2.1.5112.0080.
- [82] M. Y. Haller, R. Haberl, I. Mojic, and E. Frank. Hydraulic integration and control of heat pump and combi-storage: Same components, big differences. *Energy Procedia*, 48:571–580, 2014. doi:10.1016/j.egypro.2014.02.067.
- [83] J. Glembin, C. Buttner, J. Steinweg, and G. Rockendorf. Thermal storage tanks in high efficiency heat pump systems - Optimized installation and operation parameters. In *Energy Procedia*, volume 73, pages 331–340. Elsevier B.V., 2015. doi:10.1016/j.egypro.2015.07.700.
- [84] J. Glembin, C. Buttner, J. Steinweg, and G. Rockendorf. Optimal Connection of Heat Pump and Solar Buffer Storage under Different Boundary Conditions. *Energy Procedia*, 91:145–154, 2016. doi:10.1016/j.egypro.2016.06.190.
- [85] Weather Underground. Weather Forecast — Weather Underground, 2017. URL: <https://www.wunderground.com/>.
- [86] J. Antonanzas, N. Osorio, R. Escobar, R. Urraca, F. J. Martinez-de Pison, and F. Antonanzas-Torres. Review of photovoltaic power forecasting. *Solar Energy*, 136:78–111, 2016. doi:10.1016/j.solener.2016.06.069.

## Bibliography

- [87] S. Pelland, J. Remund, J. Kleissl, T. Oozeki, and K. D. Brabandere. Photovoltaic and Solar Forecasting: State of the Art. Technical report, International Energy Agency, 2013. doi:978-3-906042-13-8.
- [88] R. H. Inman, H. T. C. Pedro, and C. F. M. Coimbra. Solar forecasting methods for renewable energy integration. *Progress in Energy and Combustion Science*, 39(6):535–576, 2013. doi:10.1016/j.pecs.2013.06.002.
- [89] J. Antonanzas, D. Pozo-Vázquez, L. A. Fernandez-Jimenez, and F. J. Martinez-de Pison. The value of day-ahead forecasting for photovoltaics in the Spanish electricity market. *Solar Energy*, 158(December 2016):140–146, 2017. URL: <https://doi.org/10.1016/j.solener.2017.09.043>, doi:10.1016/j.solener.2017.09.043.
- [90] M. David, F. Ramahatana, P. J. Trombe, and P. Lauret. Probabilistic forecasting of the solar irradiance with recursive ARMA and GARCH models. *Solar Energy*, 133:55–72, 2016. doi:10.1016/j.solener.2016.03.064.
- [91] S. Alessandrini, L. Delle Monache, S. Sperati, and G. Cervone. An analog ensemble for short-term probabilistic solar power forecast. *Applied Energy*, 157:95–110, 2015. doi:10.1016/j.apenergy.2015.08.011.
- [92] Domotec AG. Zirkulationssystem Pipe in Pipe (Rohr in Rohr), 2018. URL: <http://domotec.ch/wp-content/uploads/2014/07/pipe-in-pipe-d.pdf>.

# A Appendix

## A.1 Publication 1 — Experimental Study and Modeling of Ground-Source Heat Pumps with Combi-Storage in Buildings

### Abstract

There is a continuous growth of heat pump installations in residential buildings in Germany. The heat pumps are not only used for space heating and domestic hot water consumption but also to offer flexibility to the grid. The high coefficient of performance and the low cost of heat storages made the heat pumps one of the optimal candidates for the power to heat applications. Thus, several questions are raised about the optimal integration and control of heat pump system with buffer storages to maximize its operation efficiency and minimize the operation costs. In this paper, an experimental investigation is performed to study the performance of a ground source heat pump (GSHP) with a combi-storage under several configurations and control factors. The experiments were performed on an innovative modular testbed that is capable of emulating a ground source to provide the heat pump with different temperature levels at different times of the day. Moreover, it can emulate the different building loads such as the space heating load and the domestic hot water consumption in real-time. The data gathered from the testbed and different experimental studies were used to develop a simulation model based on Modelica that can accurately simulate the dynamics of a GSHP in a building. The model was validated based on different metrics. Energetically, the difference between the developed model and the measured values was only 3% and 4% for the heat generation and electricity consumption, respectively

### Author Contribution

I designed the model, performed the experimental analysis and wrote the paper; Peter Tzscheutschler reviewed the testbed design and provided technical feedback; Ulrich Wagner provided a detailed critical review on the applied methods.

# 1 Introduction

In German power sector, an ongoing increase of renewable energy integration can be witnessed. In 2016, 29% of gross generated electricity was produced from renewable energy sources (RES), which represents 192 TWh [1]. Such increase in the RESs integration is empowered by several policies such as the renewable energy act (EEG) [2]. The act guarantees the generator a fixed price over a specific term, which gives a priority to the RES in the electricity market. Having such weather dependent fluctuating RES in the market, raised the demand for flexibility to balance the generation. Sector coupling presented one way to mitigate the fluctuating RES and offer flexibility to the grid. Hence, it is receiving continuous attention not only within the research communities but also on the political and industrial level. Coupling the power to the heat sector is seen as one of the most influential and attractive approaches to decarbonize the heat sector and gain additional flexibility in power grid [3]. Considering that the consumed heat energy in Germany within different sectors was 1,373 TWh in 2016 [4], there is a substantial room for power to heat application integration. An advantage of such applications is its attractive costs due to its dependency on heat storage that has significantly lower costs compared to batteries.

The heat pump is a major role player in sector coupling due to the progressive improvement of the coefficient of performance (COP) [5]. Hence, the number of heat pumps installations are on continuous growth on yearly basis, especially in the residential sector. According to [6], the heat pump installations in new buildings in 2016 reached 31.8%. Heat pump represents 34% of the market share of the single-family houses, 16% of the multi-family houses and 13.6% of the non-residential buildings. Ground-source heat pumps (GSHP), market is expected to be largely integrated in the zero emission buildings (ZEBs). According to [7, 8], GSHP has a low operating cost, no outdoor units, longer life, and a higher CO<sub>2</sub> emissions reduction. Moreover, the high efficiency of the GSHP is expected to minimize the required photovoltaic installation area and consequently minimizes the costs of the ZEBs.

The topics discussed within the literature covered large scope such as the thermodynamic cycle and compressor optimizations [9, 10, 11, 12] hydraulic system configurations [13], performance evaluation [14, 15], and integration in district heating and smart grids [16, 5]. The research presented can be divided into experimental studies and numerical studies. The experimental studies were mostly oriented towards cycle and components optimization of the heat pumps. In [17], a carbon dioxide direct-expansion heat pump was investigated in different operating conditions. [18] studied the performance of solar ground source heat pump in dual heat source coupling modes to optimize the average system COP. Furthermore, [19] experimentally tested a gas engine driven heat pump for different operation modes. The author developed a prototype to test the

heating and cooling performance for different evaporator's inlet temperatures, ambient temperatures, and gas engine speeds. The numerical studies and simulations were utilized, where experimental studies would be costly. In [20], a heat pump was simulated to cover the load of a multi-zone office building. While in [21], a simulation model was developed to analyze the flow pumping of ground source heat pumps. [22] developed a numerical model for a reversible multi-function heat pump to evaluate its performance in summer for domestic hot water (DHW) and space cooling. The numerical model was then evaluated against a model in TRNSYS.

In the residential sector, several studies were performed on GSHPs. The presented studies were mostly numerical. Also, it is oriented towards optimizing the heat pump control, system dimension and hydraulics to minimize the operation costs and maximize the use of renewable energies within the residential building as in [23, 24, 25, 26, 27]. Although numerical studies can provide relatively proper indicator of the behavior of a system, it is exposed to several uncertainties and its accuracy is always questioned, especially if the studied object is a thermodynamic system. Studies analyzing large models on the district level or micro grid levels have mostly 1-h resolution as in the review of [3], consequently, all dynamics of the heat pump systems are concealed. Moreover, in several cases, the COP is assumed to be constant and all the nonlinearities are ignored so that the optimization problem can converge faster. Yet, this exposes the model to inevitable uncertainties. On the building level, dynamic systems simulation programs are used such as TRNSYS or Modelica-based software as Simulation X [28]. These programs can detail the dynamics of the systems, yet as discussed in [29], their calibration is complicated. Moreover, these models are mostly validated by a plausibility check. Few research presented models, which were validated based on experimental results such as [8, 30, 31]. In [8], a simplified model was validated based on the maximum absolute mean deviation of the COP, thermal power and condenser water temperature. In [31], a black-box model was validated based on the root mean square deviation of the monthly efficiency. To evaluate properly a heat pump model, a detailed analysis of the energy generation and consumption, and system dynamics has to be performed. The energetic analysis can suffice for models looking forward to heat pump performance estimation, but dynamics analysis is a necessity for heat pump models integration in building models. Field tests were also performed to investigate installed heat pump systems [14]. These studies can provide a realistic investigation of the performance of heat pumps in general and a good indicator of the factors influencing the operation of heat pumps, yet it does not offer the flexibility of an experimental system. In a field test, the system parameters are usually fixed. Thus, there is no room for experimenting, but rather monitoring and analyzing the current status of a system. An experimental setup enables varying different parameter to understand the system behavior in any custom configuration. Moreover, the investment in field tests usually minimize the measurement points, which can lead to concealing several details that can contribute to a better understanding of the system dynamics.

## **Objectives**

To provide realistic, reliable results, numerical studies have to be always supported by experimental results. Otherwise, any presented control system, mathematical model, or simulation model might be exposed to imminent uncertainties. In this paper, an experimental study is performed to validate a numerical model and present the optimal control requirements for a GSHP in a residential building. The experimental study does not only include a residential, commercial heat pump and combi-buffer storage but also a building load emulator to integrate the real space heating (SH) and DHW load of a building. The objectives of this paper can be summarized in the following:

- Presenting a novel modular heat pump testbed design that emulates a complete residential house. It includes a ground-source emulator, combi-buffer heat storage, and a building load emulator. The testbed is designed to be integrated with different heat pump types and hydraulic connections so that it can be used for standardization applications, control and optimization methods performance testing, and models validation
- Based on multiple experimental testing, the real-life optimal control criteria for a commercial, residential GSHP under the given constraints of the heat pumps manufactures have been identified.
- Demonstrating a Modelica-based heat pump model that can be easily integrated into building and district simulations due to its minimal computational requirements. The model was also validated and calibrated based on the experimental data of the presented testbed.

The structure of this paper is as follows: Section 2 describes the design and components of the testbed. Moreover, it introduces the measurements system used and discusses the testbed control dynamics. Section 3 presents the experimental testing procedure and its purpose. Section 4 presents the validated Modelica heat pump model and its structure. Section 5 discusses the results of the experimental testing and the validation of the Modelica model. Section 6 presents a conclusive summary of the experimental study and the model performance.



## 2 Experimental System Description

### 2.0.1 Overview

The testbed consists of 3 different modules: ground-source emulator (A), combi-storage (B), and the building loads emulator (C). Figures 2.1 and 2.2 show a simplified hydraulic scheme and the real testbed, respectively. The presented hydraulic configuration is not a permanent configuration, but rather the one used for the experiments documented in this paper. Other possible configuration can be also implemented such as a direct connection between the heat pump and module C, replacing module B with a DHW tank module, or having two separate modules for a DHW tank and a buffer tank. Each module has its independent control and measurement system to facilitate the integration of different modules. The GSHP used is a STIEBEL ELTRON WPF10 heat pump with a thermal power of 10.31 kW and a COP of 5.02 by B0/W35 according to the standard EN 14511. A brine pump and heating system circulation pump is already integrated within the GSHP. Moreover, the GSHP is also equipped with an emergency/backup electrical heater of 8.8 kW.

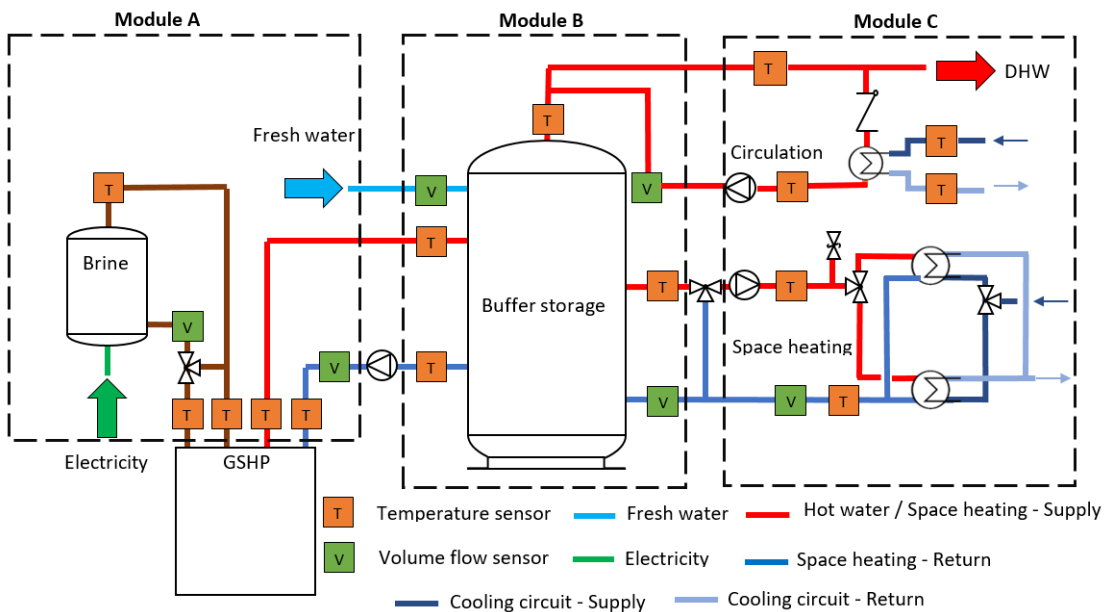


Figure 2.1: Simplified hydraulic scheme of the testbed.



**Figure 2.2:** The three modules and the heat pump installation in the lab.

## 2.1 Module A: Ground-Source Emulator

Module A emulates a ground-source, which is equivalent to a controlled environment room for the ASHP. The module consists of 300-liter storage that is heated by a 12.5 kW electrical heater. This storage is filled with a water-glycol mixture as an anti-freezing heat transfer fluid. The electrical heater is controlled via a hysteresis regulator to maintain a maximum set-temperature for the whole tank of 40 °C. The hysteresis limits can be adjusted based on the user settings. To deliver a specific temperature profile to the heat pump, a conventional SH mixer is used to mix the supply of the storage with the return of the heat pump till it reaches the required temperature. This types of mixers can lead to a slow reaction towards changes in the set points but provides a rather stable output as discussed later in Section 2.5.

## 2.2 Module B: Combi-Storage Module

This module represents one of the storage system configurations in a residential household. The storage system consists of a 749 l combi-hygienic buffer storage for SH and DHW consumption. The cold water is heated via a stainless steel heat exchanger that goes through the height of the tank to supply DHW. Furthermore, a coaxial pipe is inserted in this heat exchanger to enable DHW circulation and maintain proper hot water temperature in the pipes. An example of the coaxial pipe circulation connection can be presented in [32].

## A Appendix

To assess the energetic content of the buffer storage over time, ten temperature sensors are placed over the length of the tank as shown in Figure 2.3. T-SP-1 refers to the sensor on the top of the tank, while T-SP-10 refers to the sensor at the bottom of the tank. The sensors are placed at equidistant distances of 15 cm. Through this sensors' set, the energy at each layer of the tank as well as the overall tank content can be evaluated. This data represents a necessary input to the energy management systems (EMS) and control algorithms to decide on the load shifting potential and the available flexibility that can be offered to the grid. Further information about the storage management system can be found in [33]. On the left side of the tank, the heat pump buffer sensor, HP sensor, is installed. According to the installation manual of the heat pump, this sensor has to be placed at the bottom of the tank. Within this paper, the sensor position will vary to show its influence on the system performance as shown in Section 3.

Figure 2.3 shows as well the inlet and outlet pipes of the storage, where 1, 2, 3, 4, 5, and 6 are space heating supply, space heating return, heat pump supply, heat pump return, fresh water, and domestic hot water, respectively. Those inlets and outlets were chosen to maximize the stratification efficiency and avoid mixing within the tank.

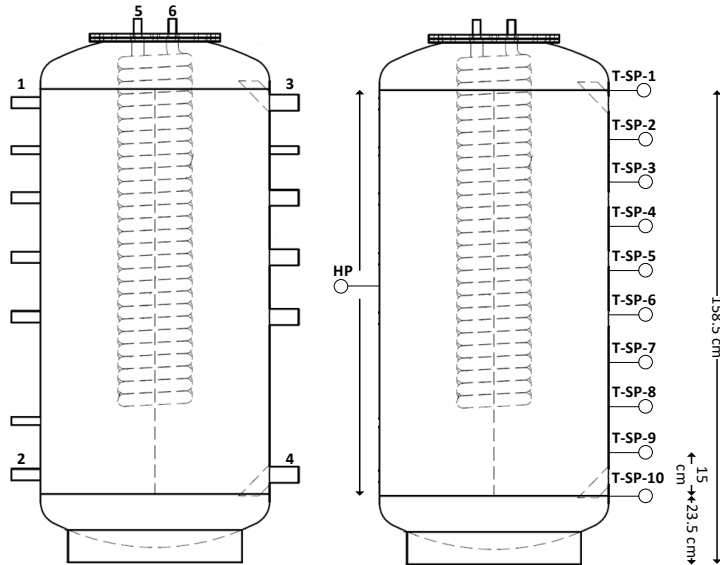


**Figure 2.3:** Inlet and outlet pipes positions of the storage (left) sensors position across the combi-storage (right). Technical design of the storage [34].

## 2.3 Module C: Building Loads Emulator

This module is the most complicated as it has to represent the SH and DHW consumption of a household. The SH circuit consists of a mixer, as in Figure 2.1, that mixes the hot water supply of the tank with the return of the SH circuit to reach the required set temperature. The building heating load is then made present via using heat exchangers that are cooled via a cooling system. The flow rate of the cooling system is the one

influencing the building load magnitude and defining the return temperature of the SH circuit. Such flow rate is controlled via a motor control valve that positions the valve according to the required set point. Within the SH circuit, two heat exchangers are available of different powers and capacities. One heat exchanger is dedicated to old building heating loads that can reach up to 20 kW and have a high flow rate, while the other one is only for new buildings with a maximum power of 7 kW. Two motor valves are used to switch between the two heat exchanger as per the testbed setup.

The hot water consumption is realized via three magnetic valves representing three different types of taps within the household. These valves can present various activities such as showering, washing, and cooking. The flow rate of the valves can be adjusted manually to match the standard flow rate of the activity. To show the effect of the hot water consumption on the heat storage, a household profile of hot water consumption can be delivered to the testbed. The opening and closing time and duration of the water tapping is defined for the different valves based on the given profile. Consequently, a similar energetic profile can be executed.

The DHW circulation pump is managing the circulation exactly as in a conventional household circulation pump. The pump can be switched on or off based on a circulation schedule or hot water temperature in the pipe. The circulated load is presented via a heat exchanger that is cooled via the cooling system, similar to the SH circuit heat exchanger. Such design was adopted for different testbeds in the labs of the Institute for energy economy and application technology (IfE) as shown in [35].

## 2.4 Measurement System

For the temperature measurements, four wire PT100 sensors are used. The sensors accuracy class is F0.15 (Class A) according to the DIN EN 60751, which means that the tolerance is  $\pm(0.15 + 0.002|T|)$ . Hence, for a temperature  $T$  of 65 °C, the tolerance is  $\pm 0.28$  °C. To maximize the accuracy further, a temperature sensor calibration device of a higher accuracy was used.

Magnetic inductive flow measurements devices are used to measure the volume flow rate. The flow measurements devices were already calibrated by the manufacturer. Consequently, no additional calibration was performed. For the nominal flow rate, the error of the devices varied between 0.2% and 0.5% depending on the sensor type and the size of the pipe.

The electrical power of the heat pump is measured via a 3-phase electricity meter (KDK PRO 380) of class B accuracy, which is 1% according to the EN 50470-1/3. The meter is connected to the measurement system via MODBUS RTU connection, which communicates the power, currents, and voltages of the 3 phases each second.

The sensors and actuators of the whole testbed are connected to National Instruments (NI) compact reconfigurable IO (cRIO) chassis and modules that receive and send different digital or analog inputs and outputs. The control program and data logger are based on LabVIEW that runs on a conventional PC.

## 2.5 System and Control Dynamics

The main purpose of the testbed is to show the detailed dynamics of a heat pump system to be able to develop and validate a realistic numerical model. In Figure 2.4a, the start dynamics of the heat pump are shown. As soon as the heat pump starts, the brine pump operates for 24 s; then the compressor is switched on. It takes the testbed 393 s to reach the steady state due to the mixer control dynamics, yet it does not influence the thermal power of the heat pump significantly. The brine power fluctuations between 2.5 till 15.1 kW led only to variations of  $10 \pm 2.5 \text{ kW}_{th}$ , within those 393 s. The brine power represents the power supplied by the heat source. The mixer controller effect can be more clearly described in Figure 2.4b. For a set temperature of  $0 \text{ }^\circ\text{C}$ , the mixer started to mix the tank temperature with the return of the heat pump. Due to both of the start dynamics of the mixer supply and heat pump return, the fluctuations occurred within the time to steady state. Once a steady state is reached, the mixer controller can maintain the set temperature, while minimizing the fluctuations.

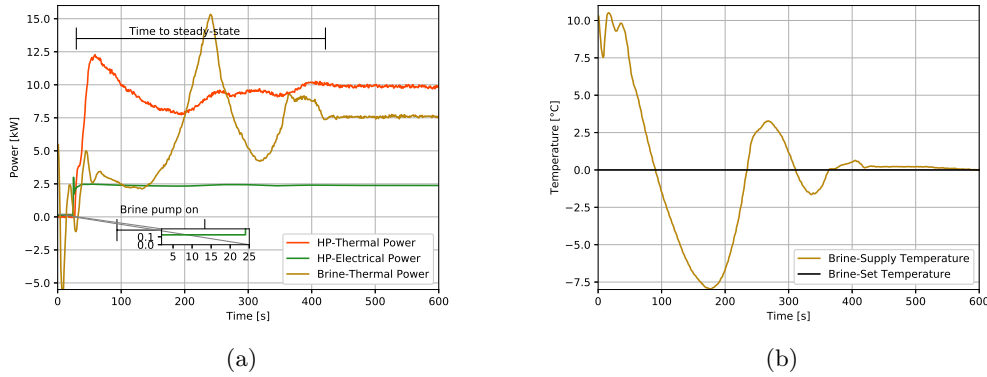


**Figure 2.4:** Starting dynamics of the heat pump testbed, (a) heat pump (HP) thermal and electrical power, in addition to the brine thermal power (b) brine supply temperature dynamics because of the mixer circuit.

For the control system in module C, Figure 2.5 shows the control dynamics of the temperature of the flow rate. In Figure 2.5a, the measured and set heating circuit supply and return temperatures are plotted against two hours of time to show the system dynamics. The control tolerance of the supply temperature mixer is  $\pm 0.5 \text{ K}$ , which is significantly better than the control in realistic buildings, where the tolerance reaches  $\pm 3 \text{ K}$ . A smaller tolerance was required to accurately emulate a building load profile on the testbed. The return temperature was more accurately controlled as the motor valve has a continuous PID controller. Consequently, a tolerance of  $\pm 0.1$  to  $\pm 0.15 \text{ K}$  was achieved, which is challenging considering the low inertia of the system (i.e., the water volume of the system is small compared to a real building).

The volume of the flow rate of the heating system circulation pump was also controlled

via a PID controller. In Figure 2.5b, the measured set and measured flow rate are presented. It can be deduced that the pump and the controller were able to flow accurately the set point with a tolerance less than 0.01 l/s. The graph was plotted against the same time of measurements of the supply and return temperature, to be able to show the dynamics of the two graphs simultaneously.

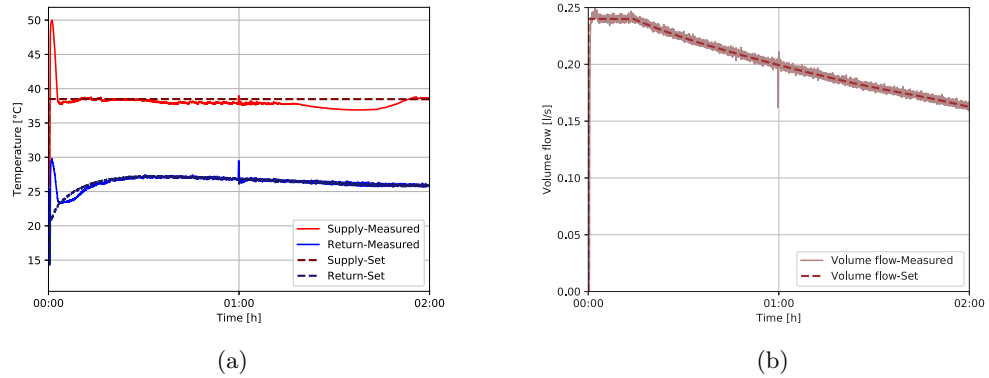


**Figure 2.5:** Control dynamics of module C, (a) supply and return temperature of the space heating circuit (b) the flow rate of the space heating circuit.

### 3 Experimental Testing Procedure

Four major experiments are covered within the scope of this paper, as in Figure 3.1. The first group of experiments is to define the performance map of the heat pump. This group of experiments analyzes the given heat pump performance under different heating supply temperature and brine temperatures.

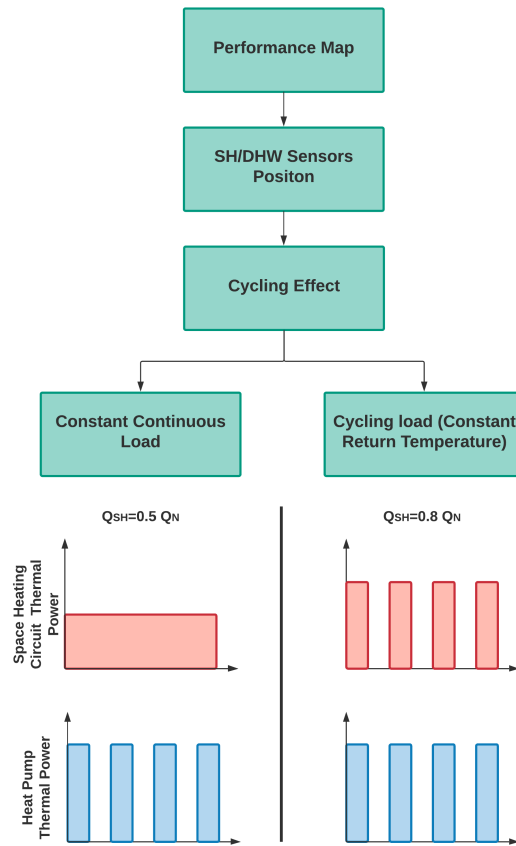


**Figure 3.1:** The flow of the experimental procedures.

The second group of experiments investigates the optimal SH and DHW sensor position and reveals its effect on the overall system performance in buildings. In the third and fourth group of experiments, the optimal control rules for EMS are defined through testing the cycling effect. In a residential heat pump, the control parameters are limited to a boolean signal to switch the heat pump on or off. Consequently, an EMS in a resi-

dential building does not have any influence on other technical parameters such as the flow rate of brine pump or the controller of the heating circuit between the heat pump and the combi-storage. Based on these constraints, the heat pump optimal control rules can be defined. In cycling effect experiment with constant continuous load, the thermal load is given to the building emulator (e.g., 5 kW), constant through the whole 24 h, while heat pump had to cycle between on and off. Within this group of experiments, four experiments were performed with a duty cycle of 50%. The switching time was varied between 1, 2, 3, and 4 h. The 6 h duration was not performed in this experiment due to the limited thermal capacity of the combi-storage. To maintain the energy balance, the thermal load  $Q_{SH}$  was limited to 50% of the nominal thermal power of the heat pump  $Q_N$ . Cycling effect was also tested while trying to maintain a constant return temperature. The  $Q_{SH}$  was limited to 80% of  $Q_N$ . Due to the increase of  $Q_{SH}$ , the 6-h cycle was made possible. Thus, six experiments were performed, the 1, 2, 3, 4, 6 h cycles.

Through this set of experiments, the characteristic of the operation of the heat pump can be clarified, in addition to the impact of sensor installation position. Moreover, the results of the cycling effect experiments can provide a clear picture of the optimal control criteria of GSHP.

## 4 Modelica Based Model

According to [36], the heat pump modeling approaches into physical, black box and grey box approach. The physical approach can forecast the dynamic behavior of a system. Hence, it is often used for heat pump design and parameters optimization. Black boxes can be easily computed and are useful for large systems, yet it is usually concealing several system dynamics to maintain its simplicity. Grey box models try to achieve a balance between the two aforementioned approaches. For residential buildings modeling, three main criteria have to be satisfied:

- **Simplicity:** the model has to be easily computable as the building modeling software such as the Modelica and TRNSYS are not yet powerful enough to solve the equations of multiple complicated dynamic systems simultaneously
- **Accuracy:** the model has to minimize the uncertainties of the results
- **Dynamics:** the model should not be concealing the dynamic behavior of the heat pump under different operating conditions.

In this paper, a semi-empirical dynamic model is presented that was developed on Modelica. Figure 4.1 shows a view of the structure of the model in Modelica. It was designed such that it can be coupled with Open Modelica Libraries [37] or Simulation X “Green City” Package [38]. Consequently, the basic model components were designed based on an Open Modelica Library, yet a separable interface was included to connect to the “Green City” package. The simulated thermal power of the heat pump  $Q_{sim}$  and the coefficient of performance  $COP_{sim}$  are calculated empirically based on the collected experiments performed in Section 3. The  $Q_{sim}$  is calculated as a function of the brine  $T_b$  and the heating supply temperature  $T_s$  as in Equation (4.1).  $COP_{sim}$  is also evaluated based on those two inputs either directly from the experimental tabulated data or from the empirical equation given in Equation (4.2). This polynomial equation was formulated based on data fitting algorithm of the experimental data. The  $R^2$  is 0.99, while the sum squared error and the root mean squared error is 0.1727 and 0.0759, respectively. The electrical power of the heat pump  $P_{sim}$  is then simply calculated based on Equation (4.3).

$$Q_{sim} = f(T_b, T_s) \quad (4.1)$$

$$COP_{sim} = f(T_b, T_s) \quad (4.2)$$

$$COP_{sim} = 11.16 + 0.2488 \times T_b - 0.2282 \times T_s - 0.003031 \times T_b T_s + 0.001405 \times T_s^2$$

$$P_{sim} = \frac{Q_{sim}}{COP_{sim}} \quad (4.3)$$

Although the powers and COP of the heat pump can be accurately calculated using the presented equation, these data will not be sufficient to present the system dynamics such system thermal losses, system inertia, operation time of the brine pump before the compressor starts, resting time between two consecutive starts, and time to full power. Consequently, the calculated full power from Equation (4.1) is given as a prescribed thermal power to a thermal pipe directly. This pipe represents the outlet pipe of the pipe and the prescribed heat model, there is a thermal resistor that was empirically calibrated to present conduction losses. The inertia of the system is represented by a thermal capacitor that can be initialized based on the system water volume as in Equation (4.4), where  $C_p$  is the specific heat capacity of water,  $Vol$  is the internal water volume of the heat pump,  $\rho$  is the density of water. The convection losses were modeled as shown in Figure 4.1, assuming that the room temperature is always fixed at a value of 18 °C. The convection heat loss factor was also empirically estimated and set as fixed value throughout the whole simulation.

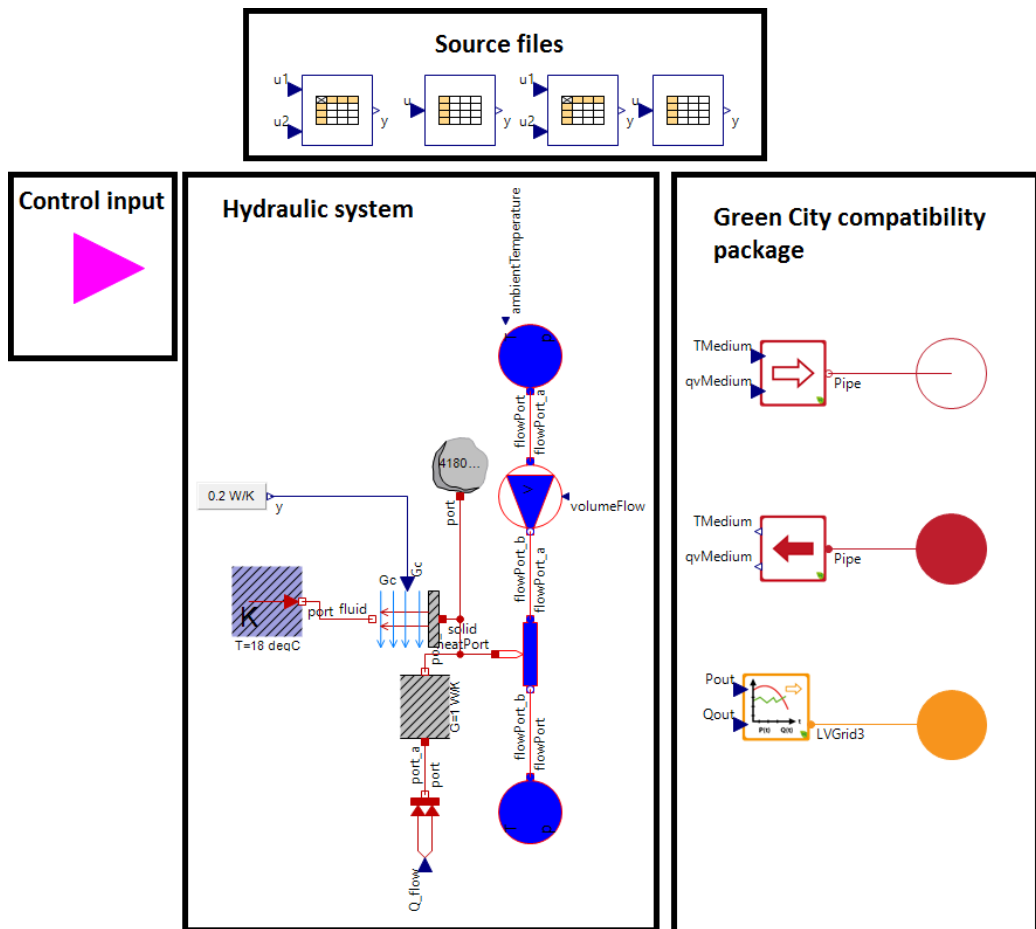


Figure 4.1: The heat pump model structure.

## A Appendix

Through the presented model, the aforementioned criteria for heat pump modeling for building simulations can be satisfied without adding any additional complexity to the heat pump model. Adding any additional details such as modeling the thermodynamic cycle would not contribute to the quality of the results in this situation as these variables are not monitored within the study of the dynamic behavior of a building.

$$C = C_p \times Vol \times \rho \quad (4.4)$$



## 5 Results

### 5.1 Experimental Analysis

#### 5.1.1 System Performance

As explained in Section 3, the initial phase of the experimental study is to analyze the performance map of the given heat pump. Figure 5.1a shows the behavior of the COP as a function of the supply temperature and the brine temperature. At each of the measured points of  $T_b$  and  $T_s$ , the set points were held constant, and measurement was taken as an average of 40 minutes of operation to maintain a proper steady and accurate measurements. The set points are defined as a discrete set of integers such that  $T_s \in \{35, 40, 45, 50, 55, 60, 65\}$  and  $T_b \in \{-5, 0, 10, 15, 20\}$ .

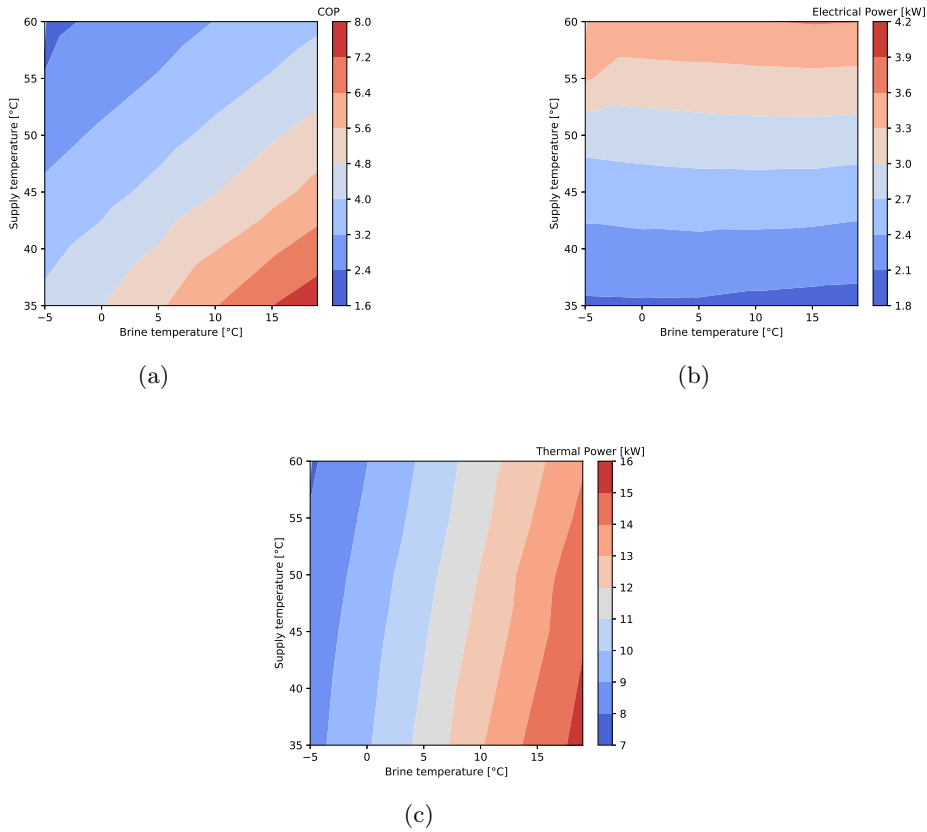


**Figure 5.1:** Performance map of the integrated GSHP (a) COP (b) electrical power (c) thermal power.

In Figure 5.1a, the measurements at 65 °C was eliminated, as the heat pump cannot operate at  $T_b = -5$  °C and  $T_s = 65$  °C, simultaneously. As shown, the COP increases as the supply temperature decreases and the brine temperature increases. The range of the COP is quite wide between 1.6 and 8.0. This means that the costs of operation of the heat pump to generate 1 kWh of heat can reach up to 500% compared to the cost of the most optimal possible operation. Consequently, it is a must to supply the numerical models with an accurate measured data, otherwise building model can be exposed to high uncertainties. Figure 5.1b,c show the electrical power consumption and thermal power generation against different supply temperature and brine temperature, respectively. It can be noticed that the electrical power is not influenced by the brine temperature as much as the supply temperature. For the same brine temperature of 0 °C, the electrical power consumption can vary from 1.8 to 3.6 kW, depending on the supply temperature. On the other hands, the thermal power generation is more influenced by the brine temperature. Depending on the brine temperature, the thermal power can vary between 7 to 16 kW.

### 5.1.2 Sensors Position

System setup and configuration in the building also has a significant influence on the behavior of the COP of the heat pump. In the field study of [14], the impact of efficient planning and installation on the heat pump seasonal performance factor was investigated. The installation process does not only include hydraulic system but also the DWH and SH sensors positioning on the storage system. Although direct connection of the SH circuit to the buildings without any buffer storage can lead to the most optimal operation, buffer storages are necessary to offer flexibility as in [39]. In the literature, different research discussed the sensor position. In [13], different sensors positions along a combi-storage were tested based on a simulation model. It was found that as the distance increases between the DHW sensor and the SH zone, the number of starts per year decreases. In [40, 28], it was stated that the DHW sensor has no influence on the performance of the heat pump, yet the higher the position the better. Moreover, the author stated that sensors at a lower position could help in decreasing the set temperature while maintaining comfort.

Within this experimental study, one sensor was set in different position across the combi-storage to analyze the behavior of the heat pump and the heat storage as well. This sensor is referred to as the HP sensor. Additional sensors connections to the control of the heat pump manufacturer were not possible. The set temperature of the sensor was adjusted to a fixed value of 50 °C. On the brine side, a constant temperature of 0 °C was maintained. Figure 5.2 shows the average number of starts, average COP and average tank temperature at different sensors positions. The average COP is calculated according to Equation (5.1), where  $E_{th}$  and  $E_{el}$  is the accumulated thermal and electrical energy within a defined period, respectively.

$$COP_{Average} = \frac{E_{th}}{E_{el}} \quad (5.1)$$

The sensor positions on the x-axis can be clarified through Figure 5.2. For each sensor

## A Appendix

position, the measurement was repeated for three consecutive days, then the average of the three days was taken. At T-SP-10 and T-SP-9 which are the lowest two sensors, the value of the number of starts is similar and significantly higher than the rest of positions. This means that if a sensor has to be allocated at a lower position on the tank as per the theoretical studies, this zone (below T-SP-9) has to be ignored for sensors allocations. The lowest sections of the tank are the sections which are cooled immediately once the heat pump switches off. Having a sensor at this position means that the heat pump has to keep always the whole capacity of the storage at the set temperature. Thus, the heat pump will not be using the heat storage capacity to increase its resting time. As the sensor is positioned more towards the upper zone of the tank, the lower is the number of starts per day. This also means that the storage heat content decreases because the useful volume that is kept at the set temperature decreases as indicated in Equation (5.2) [41], where  $A_s$  is cross-sectional area of the storage,  $T_{set}$  is the required set temperature and  $T_{storage}(h)$  is the temperature across the height of the storage  $h$ .

$$E_{storage} = \rho \times C_p \times A_s \times \int_0^h (T_{storage}(h) - T_{set}) dh \quad (5.2)$$

$$\forall T_{storage}(h) > T_{set}$$

On the other hands, as the average tank temperature decreases, the average COP also linearly increases, which fits the behavior presented by the performance map in Figure 5.1a. Between T-SP-10 and T-SP-6, the average COP increased by 21.5%, which is a significant increase that influences the economics of the heat pump considering that no intelligent control algorithms were yet deployed. The direct correlation between the average COP and the average tank temperature shows that COP is solely dependent on the tank set temperature.

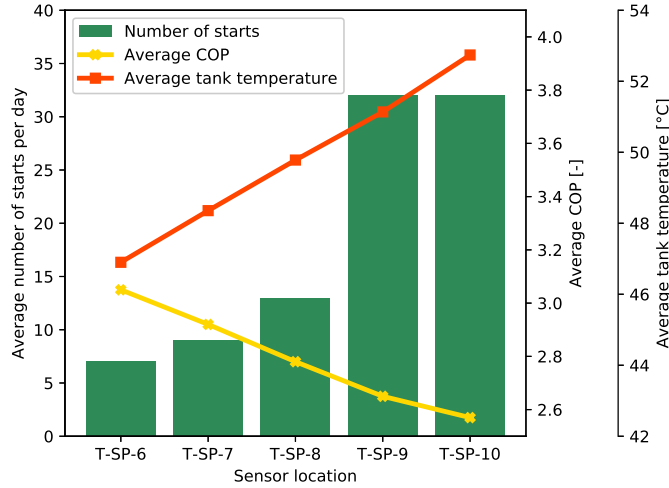


**Figure 5.2:** Sensor location influence on the number of starts, average COP, and average tank temperature.

### 5.1.3 Cycling Influence on the System Performance

In the first experiment, as explained in Section 3, a constant continuous load is set for SH circuit, which is almost equal to 50% of the nominal heating power of the heat pump. Hence, the space heating load was set to  $Q_{SH} = 5.0$  kW. On the brine side, a constant temperature of 0 °C was maintained. For the combi-storage, an initial heat content was set for all the experiments of 3 kWh. Figure 5.3a shows  $E_{th}$ ,  $E_{el}$ ,  $E_{brine}$  and the average COP for 1-h on/off cycle till 4-h on/off cycle, where  $E_{brine}$  is thermal energy extracted from the brine circuit. 1-h on/off cycle means that the number of starts per day is 12, where 4-h means three starts per day. A 6-h cycle was not performed in this case due to the limited storage capacity that does not enable the heat pump to charge the storage for six hours continuously. In this experiment, the highest average COP was achieved by the 1-h cycle. It can be noticed that the energy extracted from the brine circuit is the highest, while the electricity consumed is the lowest. The heat generated is almost constant. It has varied only between 113.85 kWh to 115.2.

Although 1-h cycle has the highest number of starts, it achieved the highest COP because it maintained the lowest possible tank temperature. Having the heat pump operating for four hours then stopping for four hours while having a constant demand from the SH circuit means that the heat pump has to heat the buffer storage to higher temperatures to satisfy the demand during the off (i.e., resting time). Although the 4-h cycle minimized the number of starts to only three times per day, it does not lead to an optimal, efficient operation. The average COP was lowered by 13%. The lower number of starts might increase the lifetime of the compressor, yet this is not a measurable factor that can be assessed easily by a testbed or even within a field study at the moment. If it would be included, a cost of start has to be evaluated to reach an optimal control schedule.

In the second experiment, the  $Q_{SH}$  was increased to 8 kW, and the  $Q_{SH}$  was not set to be continuous, but cycling similar to the heat pump. Same initial conditions and brine set temperature of the constant continuous load were maintained. The reason behind increasing the power of the load and the simultaneous cycling is to consume immediately the delivered power of the heat pump and to maintain the lowest possible return temperature  $T_r$ . In this case, 1-h to 6-h cycles were used as the heat storage was barely used. Through this experiment, it can be noticed that the average COP is almost constant and was not influenced by either the long or short duration of heat pump operation. The energies  $E_{th}$ ,  $E_{el}$ , and  $E_{brine}$  varied only by 2.7%, 1.5% ,and 1.136%, respectively. Such variation is partially due to the measurement errors and the minor difference in the initial conditions of the experiment.

To summarize the output of these experiments, it can be deduced that if a buffer or combi-storage are combined with the heat pump:

- The long operation duration to minimize the heat pump number of starts reduces the average COP and consequently can lead to a lower seasonal performance factor (SPF)
- If the heat pump is delivering directly while minimally using the heat storage or

## A Appendix

without a heat storage, the long duration of operation has no impact on the average COP of the system

Consequently, if a combi-storage has to be installed to minimize the number of starts per day, a cost of start has to be considered within the optimization. In case the heat pump has to offer flexibility to the grid, the incentives should be making up for the decrease in COP that can lead in this case to a minimum of 13% increase in costs. Additionally, thermal losses of the storage have to be considered.

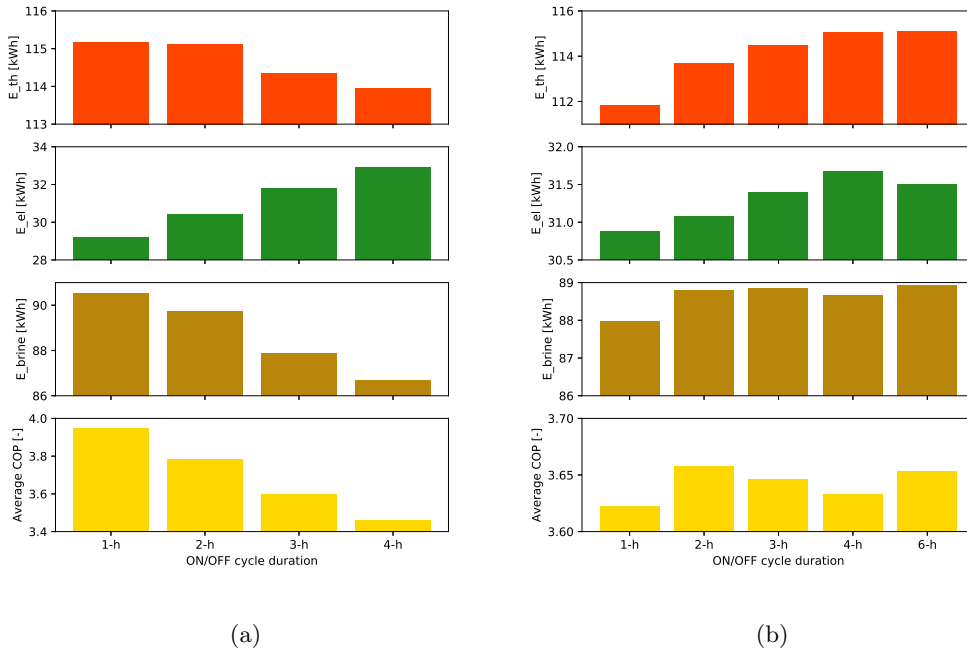


**Figure 5.3:** Cycling effect on the heat pump system performance, (a) a constant continuous load is maintained throughout the day (b) a constant return temperature is maintained throughout the day.

## 5.2 Model Validation

To validate the model, the heat pump described in Section 4 was integrated with SimulationX heat storage and building model described in [38]. Figure 5.4 shows the heat pump on the right side and the controller. The storage is presented by the storage icon, which is connected to the heat pump on one side and a mixer on the other side. On the far right side comes the building model and the weather data. The most important parameters of the storage are indicated in Table 5.1. The default parameters have been used for the rest of the components. The heat pump controller has two different hysteresis models that control both of  $T_s$  and  $T_{storage}$ . Hence, the heat pump can only

be switched on when both of the controllers generate a true signal. Different building models can be integrated from [38], yet a generic model was set to model a cycling load similar to the one presented in Section 5.1.3 so that the dynamics of both the thermal and electrical power, in addition to the supply and return temperatures can be visualized and validated. The cycle period of 1-h was chosen, along with  $Q_{SH} = 5$  kW.

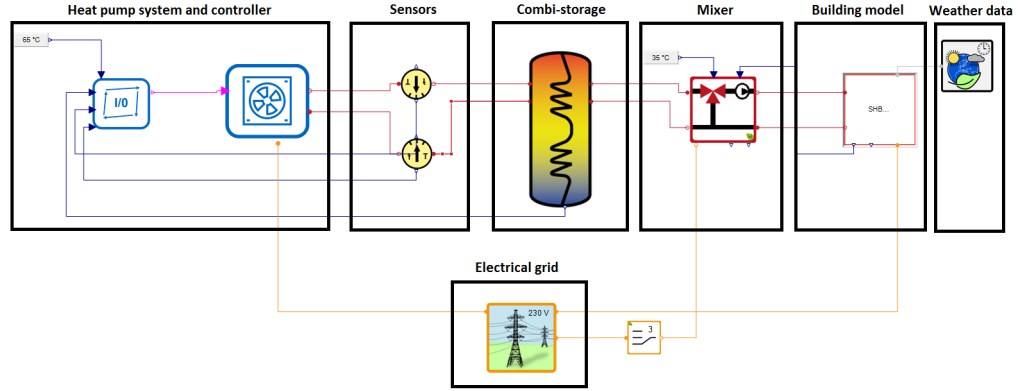


**Figure 5.4:** Modelica heat pump model integrated with the building and storage model of Simulation X.

**Table 5.1:** Heat storage parameters.

Description	Value	Units
Heat storage Volume	749	l
Diameter of heat storage	0.79	m
Heat Conductance of isolation	2	$\frac{W}{K}$
Number of heat storage layers	10	-
Ambient temperature	18	$^{\circ}C$
Maximum layer temperature	65	$^{\circ}C$
Heat transmission coefficient for neighboring layers	465	$\frac{W}{m^2 \cdot K}$

Figure 5.5a demonstrates both of the measured thermal and electrical power versus the simulation. It can be noticed graphically that the model was able to simulate the dynamics of the heat pump in terms of power amplitudes and switching times. The dynamics of the start, which is shown as the thermal power spikes at every start, was also simulated by the model. The model was also able to simulate the electrical power at every point of that presented day. The stand-by power was neglected as it has a value of 9 to 10 watts, which represents 0.5% of the nominal power. To quantify the quality of the model numerically, the mean absolute percentage error (MAPE) and the root mean square deviation (RMSD) were used as metrics. The MAPE and RMSD of the thermal power are 2% and 0.7 kW, respectively. On the other hands, the MAPE and RMSD of the electrical power are 4% and 0.23 kW respectively. To look further into the dynamics,

## A Appendix

it can be noticed in Figure 5.5b that the supply temperature of the heat pump and the simulation model are graphically simultaneous and fitting. The MAPE and RMSD of the supply temperature is 1.5% and 0.7 K, respectively. The return showed a plausible behavior when the heat pump is on, but it deviates when the heat pump is off. The reason behind this behavior is that the pipe between the heat storage and the heat pump is not modeled. Thus, the model is using directly the temperature of the tank. The MAPE and RMSD of the return are 4% and 1.7 K, respectively. The behavior of the return temperature did not reflect on the quality of the results, as this behavior occurs only when the system is off. Figure 5.6 shows the energy generated throughout the day. It can be noticed that the difference between the model and the measurement is only 3% and 4% for heat generation and electricity consumption, respectively. These minor variations indicate that the presented model can accurately simulate the heat pump and deliver proper results once it is integrated into a building model.

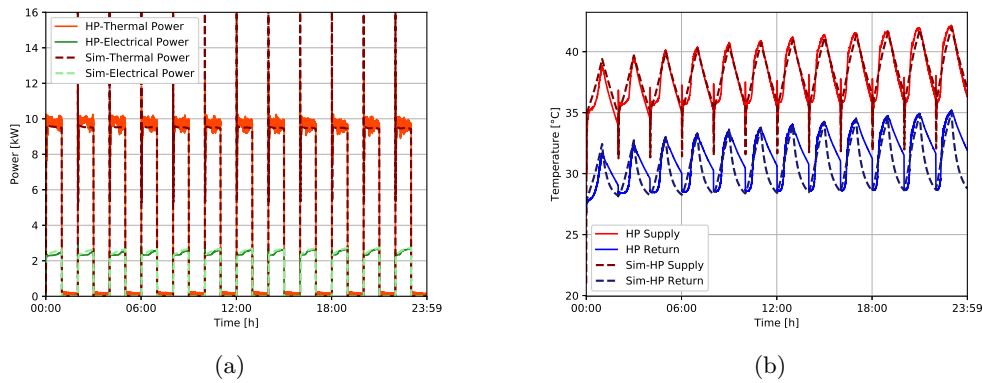


**Figure 5.5:** Temperatures and power dynamics of both the simulation model and the measurements of the testbed, (a) thermal and electrical power (b) supply and return temperatures.

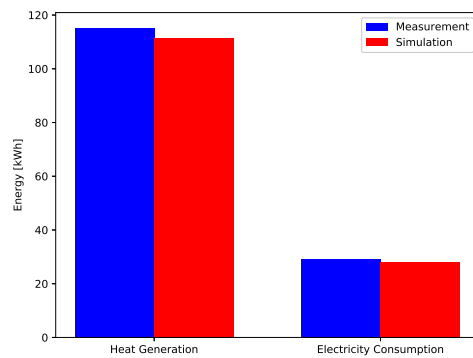


**Figure 5.6:** Comparison between the measurements and the simulation model based on the heat generation and the electricity consumption.

The computational speed of the model was also tested on Simulation X. A backward differentiation formula (BDF) solver was used to compute the model on a personal computer having the minimum calculation step size, maximum calculation step size, absolute tolerance, relative tolerance, minimum step size, and recording of the results equal to 10 ns, 900 s, 10  $\mu$ s, 10  $\mu$ s, 1 ps and equidistant 1 s, respectively. The computational time for one year of one second resolution was only 22.3 s.

## 6 Conclusions

In this paper, an experimental investigation on a commercial, residential GSHP in combination with a combi-storage was conducted. The goal of the investigation is to analyze experimentally the performance of the GSHP under different operation conditions and system configurations. Through the study, optimal sensors integration, in addition to different cycling duration impact on the performance of GSHP were investigated. In the optimal sensors integration experiments, the heat pump buffer sensor was integrated on different heights to investigate the GSHP performance and reaction to the sensor position. In the different cycle duration experiment, the heat pump was operated once against a constant space heating load, and another time against a cycling space heating load to show their impact on the average COP of the GSHP. The experiments were performed on a modular testbed that can emulate the behavior of the ground source, as it can deliver a profile of brine temperatures in real-time. Moreover, it can emulate loads of space heating and domestic hot water consumption for different building sizes and ages. Through the experimental investigation, the main findings can be summarized in the following:

- DHW/SH sensor position influence the number of starts and might lead to short cycling, yet it is not the main parameter influencing the COP
- Tank set temperature has a direct impact on COP. Thus, for the same required supply temperature, having a sensor at a higher position along with a high set temperature could be exactly equal to having a sensor at a lower position with a low set temperature
- Short cycles do not always lead to a lower COP, it can increase the average COP of the system as it maintains a lower temperature in the tank
- In case the heat pump is delivering directly to the building without storage, or once there is a consumption from storage, the long or short cycles do not have an impact on the COP
- A higher number of starts might lead to a shorter life of the compressor. Consequently, a cost of start has to be included to balance the benefit of the higher COP with short cycles. Otherwise, the EMS might tend to increase the number of starts per day of the heat pump, if no flexibility is required from the grid

The aforementioned experimental data was used to develop a Modelica model that can accurately model the dynamic behavior of the heat pump. Comparing the daily energy consumption of the measurements of the testbed to the model, it was found

that the difference in heat generation and the electricity consumption is only 3% and 4%, respectively. The electrical and thermal power, in addition to supply and return temperatures profiles, were evaluated based on MAPE and RMSD to show the capability of the model to represent the dynamics of the heat pump testbed. The MAPE and RMSD of the temperature profiles reached a value of 1.5% and 0.7 K, respectively.

Moreover, the model can be easily solved for a one-year time horizon of one-second resolution in 22.3 seconds on a personal computer. Thus, it can be easily integrated into a complete building model without slowing down the solver.

The developed testbed opens the horizon towards several other investigations and demonstration of multiple methods. As a next step, it is planned to integrate the testbed as part of hardware in the loop (HiL) system as presented in [42]. Through that HiL system, a communication can be performed with different models to emulate real-life conditions.

## Bibliography

- [1] Bundesministerium für Wirtschaft und Energie. BMWi - Erneuerbare Energien.
- [2] R. Wüstenhagen and M. Bilharz. Green energy market development in Germany: effective public policy and emerging customer demand. *Energy Policy*, 34(13):1681–1696, 2006. doi:10.1016/j.enpol.2004.07.013.
- [3] A. Bloess, W. P. Schill, and A. Zerrahn. Power-to-heat for renewable energy integration: A review of technologies, modeling approaches, and flexibility potentials. *Applied Energy*, 212(August 2017):1611–1626, 2018. URL: <https://doi.org/10.1016/j.apenergy.2017.12.073>, doi:10.1016/j.apenergy.2017.12.073.
- [4] Umwelt Bundesamt. Energieverbrauch für fossile und erneuerbare Wärme — Umweltbundesamt. URL: <https://www.umweltbundesamt.de/daten/energie/energieverbrauch-fuer-fossile-erneuerbare-waerme-#{#}textpart-1>.
- [5] D. Fischer and H. Madani. On heat pumps in smart grids: A review. *Renewable and Sustainable Energy Reviews*, 70(May 2016):342–357, 2017. doi:10.1016/j.rser.2016.11.182.
- [6] Bundesverband Wärmepumpe e.V. Neubau-Statistik 2016: Wärmepumpe fest etabliert. URL: <https://www.waermepumpe.de/presse/pressemitteilungen/details/neubau-statistik-2016-waermepumpe-fest-etabliert/>.
- [7] D. H. Li, L. Yang, and J. C. Lam. Zero energy buildings and sustainable development implications - A review. *Energy*, 54:1–10, 2013. URL: <http://dx.doi.org/10.1016/j.energy.2013.01.070>, doi:10.1016/j.energy.2013.01.070.
- [8] G. Salvalai. Implementation and validation of simplified heat pump model in IDA-ICE energy simulation environment. *Energy and Buildings*, 49:132–141, 2012. URL: <http://dx.doi.org/10.1016/j.enbuild.2012.01.038>, doi:10.1016/j.enbuild.2012.01.038.
- [9] J. Braun, P. Bansal, and E. Groll. Energy efficiency analysis of air cycle heat pump dryers. *International Journal of Refrigeration*, 25(7):954–965, nov 2002. URL: <https://www.sciencedirect.com/science/article/pii/S0140700701000974>, doi:10.1016/S0140-7007(01)00097-4.
- [10] P. Neksa. CO2 heat pump systems. *International Journal of Refrigeration*, 25(4):421–427, jun 2002. URL: <https://www.sciencedirect.com/science/article/pii/S0140700701000330>, doi:10.1016/S0140-7007(01)00033-0.

- [11] X. Wang, Y. Hwang, and R. Radermacher. Two-stage heat pump system with vapor-injected scroll compressor using R410A as a refrigerant. *International Journal of Refrigeration*, 32(6):1442–1451, sep 2009. URL: <https://www.sciencedirect.com/science/article/pii/S0140700709000814>, doi:10.1016/J.IJREFRIG.2009.03.004.
- [12] K. J. Chua, S. K. Chou, and W. M. Yang. Advances in heat pump systems: A review. *Applied Energy*, 87(12):3611–3624, 2010. URL: <http://dx.doi.org/10.1016/j.apenergy.2010.06.014>, doi:10.1016/j.apenergy.2010.06.014.
- [13] M. Y. Haller, R. Haberl, I. Mojic, and E. Frank. Hydraulic integration and control of heat pump and combi-storage: Same components, big differences. *Energy Procedia*, 48:571–580, 2014. URL: <http://dx.doi.org/10.1016/j.egypro.2014.02.067>, doi:10.1016/j.egypro.2014.02.067.
- [14] M. Miara, D. Guenther, T. Kramer, T. Oltersdorf, and J. Wapler. Heat Pump Efficiency - Analysis and Evaluation of Heat Pump Efficiency in Real-life Conditions. page 42, 2011. URL: [wp-effizienz.ise.fraunhofer.de](http://wp-effizienz.ise.fraunhofer.de).
- [15] A. Zottl, R. Nordman, M. Miara, and C. Number. Benchmarking method of seasonal performance. 2012.
- [16] M. Sayegh, P. Jadwiszczak, B. Axcell, E. Niemierka, K. Bryś, and H. Jouhara. Heat pump placement, connection and operational modes in European district heating. *Energy and Buildings*, 166:122–144, 2018. URL: <http://linkinghub.elsevier.com/retrieve/pii/S0378778817338410>, doi:10.1016/j.enbuild.2018.02.006.
- [17] H. M. C. Bastos, P. J. G. Torres, and C. E. Castilla Álvarez. Numerical simulation and experimental validation of a solar-assisted heat pump system for heating residential water. *International Journal of Refrigeration*, 86:28–39, 2018. URL: <https://doi.org/10.1016/j.ijrefrig.2017.11.034>, doi:10.1016/j.ijrefrig.2017.11.034.
- [18] W. Yang, L. Sun, and Y. Chen. Experimental investigations of the performance of a solar-ground source heat pump system operated in heating modes. *Energy and Buildings*, 89:97–111, 2015. URL: <https://doi.org/10.1016/j.energy.2018.02.043>, doi:10.1016/j.enbuild.2014.12.027.
- [19] F. G. Liu, Z. Y. Tian, F. J. Dong, G. Z. Cao, R. Zhang, and A. B. Yan. Experimental investigation of a gas engine-driven heat pump system for cooling and heating operation. *International Journal of Refrigeration*, 86:196–202, 2018. URL: <https://doi.org/10.1016/j.ijrefrig.2017.10.034>, doi:10.1016/j.ijrefrig.2017.10.034.
- [20] N. Harmathy and V. Murgul. Heat Pump System Simulation towards Energy Performance Estimation in Office Buildings. In *Procedia Engineering*, volume 165, pages 1845–1852. Elsevier, jan 2016. URL: <https://www.sciencedirect.com/science/article/pii/S187770581634293X>, doi:10.1016/j.proeng.2016.11.932.

- [21] A. Zarrella, G. Emmi, and M. De Carli. A simulation-based analysis of variable flow pumping in ground source heat pump systems with different types of borehole heat exchangers: A case study. *Energy Conversion and Management*, 131:135–150, jan 2017. URL: <https://www.sciencedirect.com/science/article/pii/S019689041630975X>, doi:10.1016/j.enconman.2016.10.061.
- [22] C. Naldi and E. Zanchini. Dynamic simulation during summer of a reversible multi-function heat pump with condensation-heat recovery. *Applied Thermal Engineering*, 116:126–133, apr 2017. URL: <https://www.sciencedirect.com/science/article/pii/S1359431116334573>, doi:10.1016/j.applthermaleng.2017.01.066.
- [23] C. Verhelst, F. Logist, J. Van Impe, and L. Helsen. Study of the optimal control problem formulation for modulating air-to-water heat pumps connected to a residential floor heating system. *Energy and Buildings*, 45:43–53, 2012. URL: <http://dx.doi.org/10.1016/j.enbuild.2011.10.015>, doi:10.1016/j.enbuild.2011.10.015.
- [24] C. Ellerbrok. Potentials of demand side management using heat pumps with building mass as a thermal storage. *Energy Procedia*, 46(0):214–219, 2014. doi:10.1016/j.egypro.2014.01.175.
- [25] R. Nordman, K. Andersson, M. Axell, and M. Lindahl. *Calculation methods for SPF for heat pump systems for comparison, system choice and dimensioning*. 2010.
- [26] S. Poppi, N. Sommerfeldt, C. Bales, H. Madani, and P. Lundqvist. Techno-economic review of solar heat pump systems for residential heating applications. *Renewable and Sustainable Energy Reviews*, 81(March 2017):22–32, 2018. URL: <http://dx.doi.org/10.1016/j.rser.2017.07.041>, doi:10.1016/j.rser.2017.07.041.
- [27] S. Ikeda, W. Choi, and R. Ooka. Optimization method for multiple heat source operation including ground source heat pump considering dynamic variation in ground temperature. *Applied Energy*, 193:466–478, 2017. URL: <http://dx.doi.org/10.1016/j.apenergy.2017.02.047>, doi:10.1016/j.apenergy.2017.02.047.
- [28] J. Glembin, C. Büttner, J. Steinweg, and G. Rockendorf. Optimal Connection of Heat Pump and Solar Buffer Storage under Different Boundary Conditions. *Energy Procedia*, 91:145–154, 2016. URL: <http://dx.doi.org/10.1016/j.egypro.2016.06.190>, doi:10.1016/j.egypro.2016.06.190.
- [29] K. X. Le, N. Shah, M. J. Huang, and N. J. Hewitt. High Temperature Air-Water Heat Pump and Energy Storage : Validation of TRNSYS Models. II, 2017.
- [30] A. Moreno-Rodríguez, A. González-Gil, M. Izquierdo, and N. Garcia-Hernando. Theoretical model and experimental validation of a direct-expansion solar assisted heat pump for domestic hot water applications. *Energy*, 45(1):704–715, 2012. URL: <http://dx.doi.org/10.1016/j.energy.2012.07.021>, doi:10.1016/j.energy.2012.07.021.

- [31] J. Ruschenburg, T. Čutić, and S. Herkel. Validation of a black-box heat pump simulation model by means of field test results from five installations. *Energy and Buildings*, 84:506–515, 2014. doi:10.1016/j.enbuild.2014.08.014.
- [32] Domotec AG. Zirkulationssystem Pipe in Pipe ( Rohr in Rohr ), 2018.
- [33] U. Wehmhörner. Multikriterielle Regelung mit temperaturbasierter Speicherzustandsbestimmung für Mini-KWK-Anlagen. 2012. URL: <http://mediatum.ub.tum.de/doc/1084367/1084367.pdf>.
- [34] TWL-Technologie. Hygiene-Kombispeicher bis 1.000 Liter - TWL-Technologie GmbH. URL: <http://www.twl-technologie.de/de/138098-Hygiene-Kombispeicher-bis-1000-Liter{#}start>.
- [35] H. Mühlbacher. Verbrauchsverhalten von Wärmeerzeugern bei dynamisch variierten Lasten und Übertragungskomponenten. page 127, 2007.
- [36] M. Ljubijankic, C. Nytsch-Geusen, J. Rädler, and M. Löffler. Numerical coupling of Modelica and CFD for building energy supply systems. *Proceedings of the 8th International Modelica Conference*, pages 286–294, 2011.
- [37] Open Modelica. OpenModelica. URL: <https://www.openmodelica.org/>.
- [38] ESI ITI. SimulationX 3.8 — Green City. URL: <https://www.simulationx.com/simulation-software/simulationx3-8.html>.
- [39] W. El-Baz and P. Tzscheutschler. Autonomous Coordination of Smart Buildings in Microgrids based on a Double-Sided Auction. In *IEEE Power and Energy Society General Meeting*, number August, Chicago, 2017.
- [40] J. Glembin, C. Büttner, J. Steinweg, and G. Rockendorf. Thermal storage tanks in high efficiency heat pump systems - Optimized installation and operation parameters. In *Energy Procedia*, volume 73, pages 331–340. Elsevier B.V., 2015. URL: <http://dx.doi.org/10.1016/j.egypro.2015.07.700>, doi:10.1016/j.egypro.2015.07.700.
- [41] J. Lipp and F. Sängler. Potential of power shifting using a micro-CHP units and heat storages. Naples, Italy, 2013. Microgen3.
- [42] W. El-Baz, F. Sängler, and P. Tzscheutschler. Hardware in the Loop ( HIL ) for micro CHP Systems. In *The Fourth International Conference on Microgeneration and related Technologies*, Tokyo, Japan, 2015. Microgen4.

## **A.2 Publication 2 — Day-Ahead Probabilistic PV Generation Forecast for Buildings Energy Management Systems**

### **Abstract**

The photovoltaic (PV) generation forecast is a key element to an efficient building energy management system (EMS) operation. The forecast's uncertainties and generation variabilities exposes the loads to misplanning, and hence decrease building autonomy, self-sufficiency and potential costs savings. In this paper, a novel approach for a day-ahead PV power generation probabilistic forecast is proposed that is especially optimized for building EMS applications. The model consists of several modules to develop the probabilistic forecast. Initially, a clear sky model is tuned to incorporate the system and temperature losses and partial shading. The deviation of the PV power from the clear sky power is used to train a bagging regression tree, which produces a deterministic point forecast. The probabilistic forecast is developed based on the probabilistic analysis of the point forecast and regenerating it based on the given weather conditions. The model is developed based on the available data in buildings such as the historic PV measurements acquired from the inverter and the weather forecasts. The probabilistic forecast was validated over a complete-year data set of a rooftop PV system in Munich, Germany, where the results showed its capability to provide an accurate and reliable forecast for EMS applications.

### **Author Contribution**

I collected the data, developed the probabilistic PV prediction algorithm, and wrote the paper; Peter Tzscheuschler helped in structuring and revising the paper; Ulrich Wagner provided a detailed critical review.

# 1 Introduction

The German energy transition has paved the way towards renewable energy sources' (RES's) integration to replace nuclear and fossil energy resources. The current goal for the electricity consumptions derived from renewables is to reach 40-45% by the end of 2025, and at least 80% by 2050 [1]. These goals are supported by several policies and regulations such as the renewable energy act, Erneuerbare Energien Gesetz (EEG), which was introduced in 2000 [2] to support RES penetration to the grid. The EEG was set to guarantee the RES plant owner an energy purchase at a fixed tariff to give priority access to the RES in the grid over other energy sources. Consequently, the installed RES capacities grew between 2002 and 2017 from 18 GW to 111 GW [3]. The share of photovoltaic (PV) generation within the same time frame grew from 0.3 GW to 42.71 GW to represent a major share of the installed RES capacities up until this moment. Hence, it is crucial to maintain a smooth integration of the PV systems in different sectors and to find balance between an economic operation for both the generator and the power grid.

In the residential sector, the installed PV capacities reached 39.4% [4], thus substantial research was oriented towards the optimal integration of PV systems in buildings. The research focused on applying different demand side management (DSM) strategies to increase self-consumption, self-sufficiency, and to minimize  $CO_2$  emissions or costs. In all the presented cases in the literature, the DSM strategies were applied through an energy management system (EMS) that is responsible for optimize both the electrical and thermal heating system plans within buildings.

An accurate PV forecast is generally crucial main input required for optimal load and resource scheduling and specifically for the operation of the EMS in buildings. As shown in [5], an improper forecast can significantly influence the battery discharging behavior. In [6], the researcher showed the necessity of better forecasting for PV generation to maintain a grid-friendly PV + Battery system. In [7], the influence of a PV forecast on the EMS was demonstrated. It was found that a less accurate forecast can lead to different operation plans for households devices and, consequently, higher operation costs, lower self-sufficiency and lower self-consumption. As a solution, several researchers developed an online, real-time controller in addition to a battery storage system to make up for the PV forecasting error [8, 9]. An online controller can increase the efficiency of the EMS in this case, but the maximal potential still cannot be reached. In addition to that, the gained economic benefit from the online controller cannot recover the additional investment costs in the additional battery system.

A better forecast is always the favored economic solution for load scheduling. Several researchers over the past years focused on improving PV generation forecasts, as in [10, 11, 12]. The developed forecasts cannot be equally compared, as each depends on the purpose of the application, the forecasting time horizon, temporal resolution,

spatial resolution, and, above all, the local climate. For building EMS applications, the forecast requirements can be deduced out of presented algorithms and methods in literature. As in [13, 14, 15, 16, 17], the desired forecasting time horizon required is in range of 6 h up to 48 h for proper resource and load scheduling and optimization. A shorter time horizon can be only considered if power to heat devices is not integrated such as, heat pumps, as they always need a relatively longer time horizon for thermal system optimization. The temporal resolution required is between 15 min to 1 h. Based on the given time horizon and temporal resolution, the most practical candidate is the numerical weather prediction (NWP), which is associated with statistical post processing [18, 19, 20, 21]. Consequently, NWP represented a major component of several models in the literature. [22] used NWP input data to develop a multi-model ensemble. In [23], a deterministic approach was implemented using an NWP model, where a transposition and a power estimation model were used to generate the day-ahead forecast. In [24], predictors of a NWP model were used to compare several forecasts for a day-ahead hourly PV prediction. [25] presented a comparison of multiple NWP models performance using different configuration and in different locations. The goal behind the comparison was to have a standardized evaluation of the presented forecasting approaches performance, so that users can choose the most suitable forecasting technique for their application. The main problem with NWP, as many other point forecasts, is that it is designed for a spatial resolution greater than 1 km, which is larger than the surface area of a single family house or even a multi-story building. Thus, the forecasting of a rooftop PV system power generation would be exposed to relatively higher uncertainties. As mentioned in [18], for an area as large as Germany, the uncertainty is 64% less than a point forecast. Based on a questionnaire performed by [18] on different PV forecasting models developed by different institutes and tested in multiple locations, it was found that the RMSE can reach 72% of persistence RMSE. Thus, using this approach for Building EMS applications would not lead to an optimal operation, as it is more oriented to support large scale applications for the sake of load flow regulation, or unit commitment of regional power as in [26].

Probabilistic forecast is an alternative solution handling the high uncertainty and variability of PV generation, especially in building EMS applications. Conventional approach, which is also denoted by deterministic approach, is generating a forecast  $P_{pv}$  at time  $t$  for time  $t+t_f$ , where  $t_f$  is the forecasting time horizon. Feeding such single  $P_{pv}$  value to an EMS, makes the optimization algorithm behind the EMS exposed to the high uncertainty of the forecasted value. Yet, a probabilistic forecast can generate a range of  $n$  values  $[P_{pv_1}, \dots, P_{pv_n}]$  to give a chance for the EMS, via providing a full information about the uncertainty, to reach the most probable optimum operation schedule. According to the review of [27] and [28], the frequency and maturity of research in the probabilistic solar power forecasting is low compared to the conventional approaches, although the probabilistic approach was often used for wind and loads forecasting. This trend fits the text mining review of [29].

In the literature, probabilistic approach was presented in different forms for diverse applications. In [30], probabilistic approach was implemented to estimate PV production on the regional scale. Instead of using a set of reference plant models with fixed parameters for upscaling the PV production in different control areas, the author estimated

the plant parameters using the most frequent modules orientation angles. The output power was then weighted according to its probability of occurrence. The approach resulted in an improvement in the root mean square error (RMSE), although one single weather model is used. In [31], the probabilistic forecast was implemented for short-term solar forecasting in the range of 10 min up to 6 hour. The solar irradiance was handled similarly to financial time series. Hence, a combination of two linear models was used: the recursive autoregressive moving average (ARMA) and the generalized autoregressive conditional heteroskedasticity (GARCH). The recursive estimation method was used to estimate the parameters of the two linear models. Using the ARMA-GARCH model, a point forecast was generated with a confidence interval. A normal distribution was assumed for the point forecast within this model, although, in reality, errors cannot be represented by the Gaussian law. In [32], a short-term probabilistic forecast was also developed with a forecasting time horizon in the range of a few minutes to one hour ahead. The author implemented a nonparametric approach to generate the forecast density function. An extreme learning machine (ELM) was used as a regression solver along with a gradient-free optimization to estimate the parameters. In [33], short-term probabilistic power forecast based on an analog ensemble (AnEn) was presented. The approach generates a set of the most likely PV predictions using a historical PV measurement in addition to meteorologically forecasted variables such as global horizontal irradiance, temperature, cloud cover, solar azimuth and elevation. The AnEn showed better performance than the referenced Persistence Ensemble (PeEn) and quantile regression model, yet it operates with relatively large spatial and temporal resolution, which can not be suitable building for EMS applications. In [34], the direct normal irradiance was forecasted using a short-term probabilistic approach, but for concentrated solar power plants. The focus of the model is to generate an intra-hourly forecast within the time horizon of 5 to 20 min. The author used the k-nearest neighbor (kNN) ensemble to produce arbitrary probability density functions to estimate the direct normal solar irradiance. In [35], the capability of probabilistic forecast to estimate the daily PV energy production was discussed. The forecast was dedicated to facility operations to optimize maintenance costs. Consequently, the model has a forecasting horizon of two days to serve that application.

To summarize the current status quo of PV power forecasts in relevance to building EMS applications, given the required forecasting horizon, spatial and temporal resolution:

- Deterministic forecasts cannot lead to an optimal solution due to the high uncertainty of the forecast and variability of PV power generation, which leads to a decrease in the efficiency of the building energy management system or an investment in additional battery capacities to make up for the forecast error
- Little research was done on probabilistic forecasts compared to the deterministic forecasts, and the probabilistic approach was not only used to estimate the PV power output, but also to estimate the most probable PV power plant parameters for upscaling applications

## A Appendix

- Most research discussing the probabilistic approach is oriented towards short-term forecast with low spatial resolution (e.g. regional) to maintain the power quality, regulation costs, or load generation imbalance

Within this paper, a novel probabilistic forecasting model is presented, which features a complete open-source solution for building EMS applications. The model focuses on a probabilistic analysis and forecast of high resolution error of a bagging regression trees point forecast, which is of a lower resolution. It classifies the error depending on the cloud cover in different cumulative distribution functions to increase the model accuracy and reliability. Moreover, the model is designed to perform with a high accuracy, even though the number of input parameters is minimal and a conventional online low spatio-temporal resolution weather forecast is supplied. The output of the model is prepared to facilitate the integration of the probabilistic forecasts with the EMS and DSM algorithms, as further explained in [7]. Furthermore, it can generate results within milliseconds on personal computers once it is trained to ease its implementation on microcomputer or cloud EMS.

The paper is structured as follows: Section 2 details the PV measurement and weather forecast data used to train and validate the forecasting model. Section 3 presents the approach used to develop the probabilistic forecast. Section 4 presents the validation of the model based on a defined set of metrics. Section 5 briefly describes the open-source implementation of the model for different applications. Section 6 presents a conclusive summary of the whole study.

## 2 Data

In a building with an integrated PV system, two types of data can be available: the weather forecast and PV measurements. The weather forecast is usually offered by an online service provider and has to be available for thermal load management and the optimization of the building. The PV measurements can be acquired either via a smart meter or directly from the PV inverter depending on the system setup and the inverter type. Thus, these two data types are already accessible by the EMS nowadays. Accordingly, only these two data types will be fed to the probabilistic forecast model.

In this study, the data is acquired from a 3 kWp rooftop PV system in Munich, Germany. The latitude of the power plant is  $48.14951^\circ$ , the longitude  $11.56999^\circ$ , and the elevation 516 m. The system consists of 12 modules, each  $1.67 \text{ m}^2$ . The tilt angle  $\beta$  is  $30^\circ$ , while the azimuth angle  $\phi$  is  $200^\circ$ . The data is directly called from the PV inverter, with no additional metering devices, to emulate the situation in a building. The detailed technical information of the PV system, along with the data, is presented in the data article [36]. Figure 2.1 shows the measured PV power peak for the year 2016. The overall electricity generated in that year is 2.85 MWh.

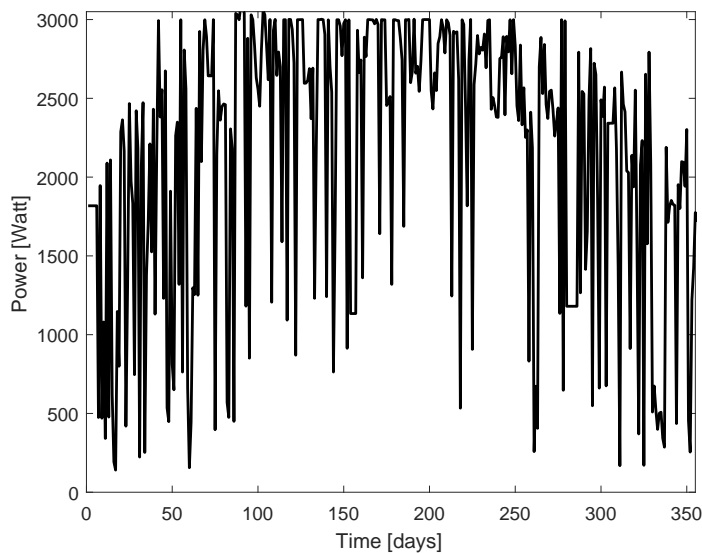


**Figure 2.1:** Daily PV power peak for the year 2016.

There are several weather forecast providers who distribute weather forecasts for developers through a public API. In this contribution, [37] was used, yet data from other

## A Appendix

service providers can be also used. The called data from the API is a 10 days-ahead weather forecast that includes temperatures, wind direction, wind speed, cloudiness, and humidity. Data was aggregated on a daily basis to develop a historical forecast database for the sake of testing the probabilistic forecasting algorithm. Table 2.1 represents the most import forecast variables delivered by the online forecast.

**Table 2.1:** Data provided by the online weather forecast.

Description	Abbreviation	Units
Dew point	$Dp_{wf}$	$^{\circ}\text{C}$
Temperature	$Te_{wf}$	$^{\circ}\text{C}$
Cloudiness	$CC_{wf}$	%
Wind speed	$Ws_{wf}$	$\frac{m}{s}$
Wind direction	$Wd_{wf}$	deg
Humidity	$H_{wf}$	%
Mean sea level pressure	$MSLP_{wf}$	Pa

Missing or corrupted data from the raw PV measurements is ignored. The reason behind using the raw data directly is to emulate a real-life situation in buildings, where EMS or PV forecasting systems are not associated with data treatment modules.

## 3 Approach

### 3.1 Overview

The procedure for generation a probabilistic forecast goes through different processes. Figure 3.1 shows the simplest form of the model structure to provide an overview of the forecasting process. The first process is the clear sky model (CSM), which provides an initial numerical base for forecast generation. The CSM model is calibrated based on the live PV measurements by specific factors to make up for different system losses. Following the calibration, the partial shading detection process starts based on the PV measurements. The next process is bagging regression trees training, where different trees are trained based on the absolute difference between the PV measurements and the calibrated CSM forecast. The regression trees enable the model to generate a forecast for the next 24 hours with 1 h resolution. Eventually, an error analysis of the generated point forecast is used to set up the cumulative distribution function based on which the probabilistic forecast is generated.

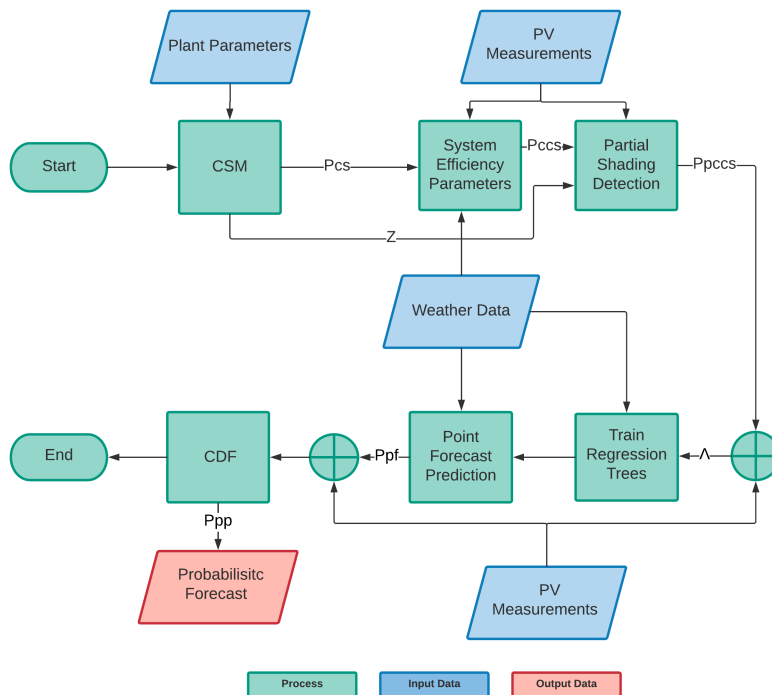


**Figure 3.1:** Simplified flow chart describing the process of probabilistic forecast generation.

### 3.2 Clear sky model

The initial process of the algorithm is to calculate the clear sky solar irradiation, where clouds are considered theoretically absent. Thus, the production of the PV system is calculated under stationary conditions, where PV generation is only affected by the solar geometry.

To calculate the direct normal irradiance (DNI), the extraterrestrial solar irradiance  $I_0$  has to be calculated using Equation 3.1, where  $I_c$  is the solar constant, equals  $1360 \frac{W}{m^2}$ , and where  $n_d$  is the day number of the year to associate the change of the distance between the sun and earth.

$$I_0 = I_c \times \left(1 + 0.033 \times \cos \frac{360 \times n_d}{365}\right) \quad (3.1)$$

Applying the simplified Birds and Hulstrom model [38] as in equations 3.2, 3.3 and 3.4, the direct  $I_d$ , scattered  $I_{as}$ , and total solar irradiance  $I_T$  can be calculated.  $Z$  is the zenith angle.  $T_R$ ,  $T_o$ ,  $T_{UM}$ ,  $T_W$ ,  $T_A$  and  $T_{AA}$  are the transmittance of Rayleigh scattering, ozone absorption, uniformly mixed gases absorption, water vapor absorption, aerosol absorption and scattering, and aerosol absorption, respectively. The  $r_g$  and  $r_s$  are the ground and sky albedo. For the detailed equations of the transmittance factors, please refer to [38].

$$I_d = 0.9962 \times I_0 \times \cos(Z) \times T_R T_o T_{UM} T_W T_A \quad (3.2)$$

$$I_{as} = 0.79 \times I_0 \times \cos(Z) \times T_o T_{UM} T_W T_{AA} \quad (3.3)$$

$$I_T = (I_d + I_{as}) / (1 - r_g r_s) \quad (3.4)$$

Using the calculated solar irradiation, in addition to the orientation angles of the PV system and an initial module efficiency, PV clear sky power generation  $P_{cs}$  is calculated.

### 3.3 System efficiency calculation

Since  $P_{cs}$  is calculated based on an initial guess of the module efficiency, it has to be calibrated to find the correct module efficiency. Moreover, different system losses have to be included such as the inverter, ohmic and temperature losses [39], yet the integration of additional models to calibrate  $P_{cs}$  for these losses can lead to a slowing down of the overall model and hinder its integration with an EMS. Consequently, a simplified semi-empirical method was used to calibrate the clear sky model and inherit the system losses in the prediction.  $\kappa_c$  and  $\kappa_t$  are the two correction factors used to generate the calibrated clear sky power of the PV system  $P_{ccs}$  as in Equation 3.5, where  $\kappa_t$  inherits the temperature losses, when the ambient temperature,  $T_{e_a}$ , is above  $25^\circ\text{C}$  and  $\kappa_c$  inherits other different types of losses for any generic systems.

$$P_{ccs} = \begin{cases} \kappa_t \kappa_c \times P_{cs}, & \text{if } T_a > 25^\circ\text{C} \\ \kappa_c \times P_{cs}, & \text{otherwise} \end{cases} \quad (3.5)$$

Once the algorithm functions in real-time, it aggregates the weather forecast and PV measurements as indicated in Section 2. Once the algorithm has recognized three consecutive clear days as per the given weather forecast and the relative daily measured energy production, it (re)calibrates the  $P_{ccs}$ . The calibration is done via linear minimization of the mean absolute percentage error (MAPE) over the 3 given days. Equation 3.6 shows the objective function of the linear optimization, where  $\Upsilon_{MAPE}(\kappa_c, \kappa_t)$  is the MAPE error,  $N_d$  is the number of time steps in the given days, and  $P_m(t)$  is the measured power at time (t).

$$\min \Upsilon_{MAPE}(\kappa_c, \kappa_t) = \min \frac{100}{N_d} \sum_{j=1}^{N_d} \left| \frac{P_{ccs}(t) - P_m(t)}{P_m(t)} \right|, \quad (3.6)$$

where  $0 < \kappa_c < 1, \kappa_c \in \mathbb{R}$   
and  $\kappa_t = 1$

As soon as  $\kappa_c$  is calculated,  $\kappa_t$  is optimized using the same equation in 3.6, while maintaining  $\kappa_c$  as constant and  $0 < \kappa_t < 1$ . It should be noticed that  $\kappa_t$  is calibrated only once every three consecutive clear sky days with an average ambient temperature above 25°C. The process of optimization occurs only a few times per year and can be limited programmatically to a finite number of times per season.

In the events when the temperature is below the 25°C and the sky is clear, a higher PV power can be produced. If these events occurred for three consecutive days,  $\kappa_c$  is recalculated to calibrate the clear sky power. Otherwise, it is ignored. Within the testing phase of this model [40], it was found out that the events where  $P_{ccs} < P_m$  occurred only in 10.2% of the hours of the year with a mean normalized power increase of 3.6%.

The goal behind this optimization is not to reach an accurate forecast for direct applications, but to feed the best possible data to the regression trees as mentioned in Section 3.5. In other words, the model tries to solve as much as possible in terms of what it knows according to the physical properties of the system and solar geometry, and leaves the rest of the unknowns to the regression trees.

### 3.4 Partial shading detection

PV installation locations throughout a building are always optimized under specific area constraints, yet PV modules might still be partially exposed to the building's shade at certain times of the day, which can lead to a power drop of more than 50% at a specific time of the day. Figure 3.2 shows an example of the effect of neighboring buildings' shading on the 7th of May. The decrease in power, especially between 15:00 to 18:00, can be noticed. To take into account the partial shading within the clear sky model for a specific PV system, an empirical estimation can be made for the power drop at specific  $Z(t)$ . Yet, the goal of the algorithm is to be generic for buildings with different partial shading conditions.

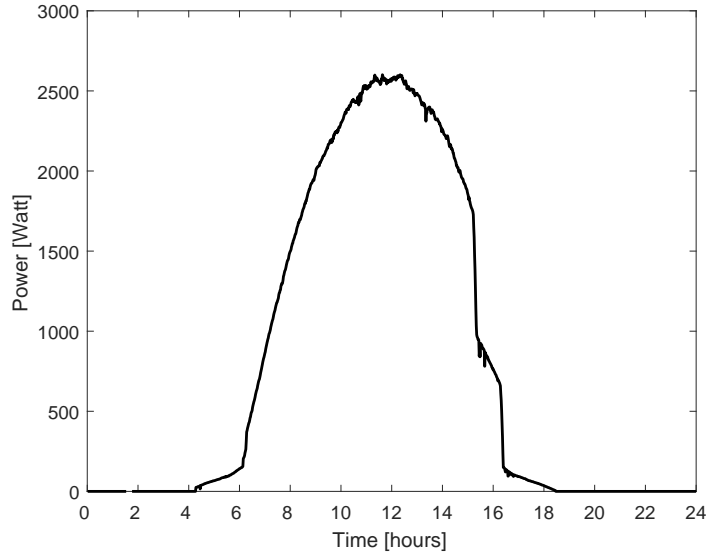


**Figure 3.2:** PV measurement on 07.05.2016.

Consequently, the first step was to detect such an abrupt change by satisfying the condition in Equation 3.7.  $\chi$  is a constant and  $\Delta t$  is 1 h to avoid the detection of the PV variability due to weather conditions. Applying Equation 3.7 to three consecutive clear sky sunny days as in Section 3.3, the algorithm searches for the  $Z$  at which partial shading starts,  $\theta$ . The algorithms search the three days of measurements  $P_{m1}$ ,  $P_{m2}$ , and  $P_{m3}$  for a point of time in which the condition in Equation 3.8 applies.  $\kappa_{ps}$  is calculated as shown in Equation 3.9 to define the decrease in PV generation due to partial shading.  $\kappa_{ps}$  is then used as a constant value to determine the new PV clear sky value while taking into account the partial shading  $P_{pccs}$ .

$$|P_m(t + \Delta t) - P_m(t)| \geq \chi|\Delta t| \quad (3.7)$$

$$\begin{aligned} \Delta|P_{m1}(t + \Delta t) - P_{m1}(t)| \wedge \Delta|P_{m2}(t + \Delta t) - P_{m2}(t)| \wedge \Delta|P_{m3}(t + \Delta t) - P_{m3}(t)| \\ \longrightarrow \theta = Z(t) \end{aligned} \quad (3.8)$$

$$\kappa_{ps} = |P_m(t + \Delta t) - P_m(t)|/P_m(t) \quad (3.9)$$

$$P_{pccs} = \begin{cases} \kappa_{ps} \times P_{ccs}, & \text{if } Z(t) > \theta \text{ and } \frac{dZ}{dt} > 0 \\ P_{ccs}, & \text{otherwise} \end{cases} \quad (3.10)$$

Figure 3.3 shows  $P_{pccs}$  of three consecutive days in May, where the last algorithm calibration has been performed earlier in April. It can be shown that the partial shadowing detection was able to model the shading and associates it to the clear sky model. On

the other hands, a difference can be noticed in the middle of each day between the  $P_{pccs}$  and the measured power. Such difference is due to the failure of the weather forecast. In these three days, the weather forecast provided a lower  $T_a$  than the measured values. Consequently, the  $P_{ccs}$  was higher than the measured power, yet the  $P_{pccs}$  was still able to adapt to the partial shading conditions. Even on days with high variability due to partial cloudiness and wind speed, as in Figure 3.4, the model was able to forecast the maximum generation to a good extent.

Lorem ipsum

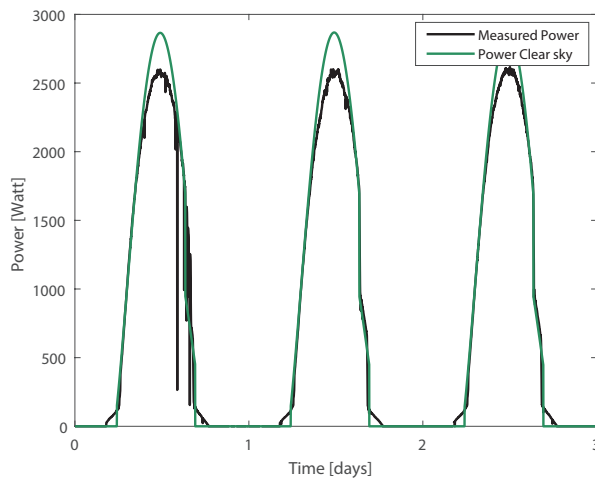


**Figure 3.3:** Clear sky model output and PV power measurements from 06.05.2016 to 08.05.2016.

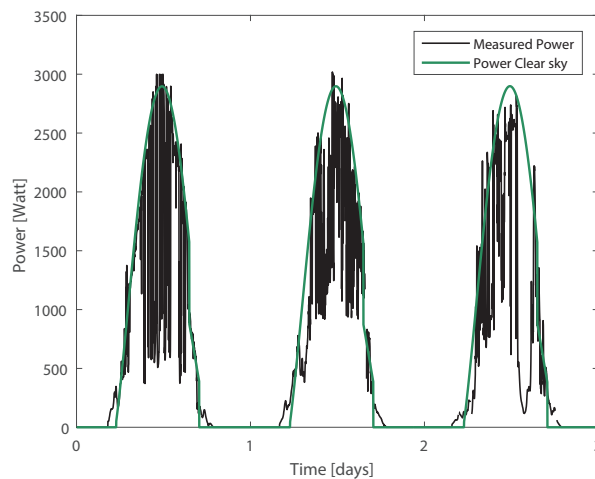


**Figure 3.4:** Clear sky model output and PV power measurements from 26.05.2016 to 28.05.2016.

## A Appendix

In [41, 42, 43], tuning routines were also presented that take into account partial shading. These methods were targeting regional solar resource assessment for the distribution system operators (DSO) and transmissions service operators(TSO). Consequently, these models have a higher complexity as they are dealing with systems of bigger scale and higher uncertainties. In [41], light detection and ranging data (LiDAR) is required to estimate PV module orientation and model the possible shading of the nearby buildings or nearby surrounding objects such as mountains. Another presented approach is the QCPV-tuning model, which initially performs a data quality control and a parametrization process to determine the module orientation and loss factors. In this paper, the PV system installer is assumed to be aware of the module orientation and position. Consequently, these plant parameters are assumed to be known as in Figure 3.1. The main advantages of the presented algorithm are the three days persistence technique to calibrate the forecast which is not computationally intensive, its high performance without a need to any earlier data processing, or satellite-derived data. On the other hands, if the calibration was not performed due to the weather conditions, the quality of the clear sky forecast might decrease.

### 3.5 Regression trees

In a desert climate zone, the CSM optimized model can be sufficient, as the major days of the year are clear. In a tropical or a continental climate, PV generation variabilities increase significantly due to clouds' motion and speed as in [44], which makes it challenging to predict or model, especially in systems of a small-scale. As an example, Figure 3.5 shows two different transient days in the fall, 07.10.2016, and in spring, 20.04.2017. Although the CSM model is able to forecast the maximum power of the PV system, it can not be used to model the variability or the power decrease due to cloudiness.

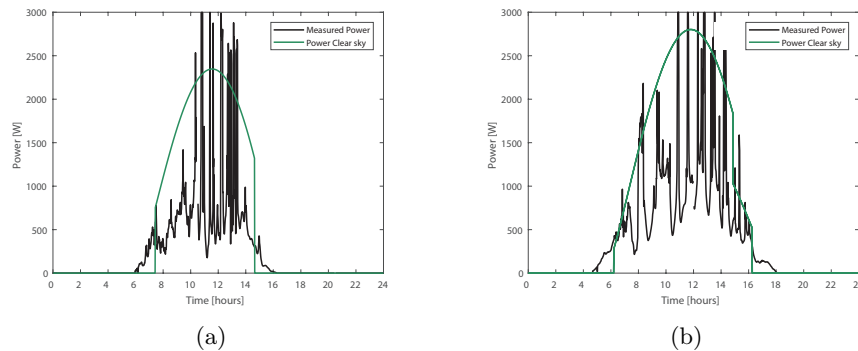


**Figure 3.5:** PV variability on two different transient days of 1-min temporal resolution, (a) 07.10.2016 (b) 20.04.2017.

Regression trees are used to predict the power drop due to different weather conditions. They are a machine-learning method used to classify and construct forecasting models

based on the given data. Regression trees method was developed in 1984 by [45, 46]. The goal behind the regression trees is to predict a variable based on multiple input variables. Consequently, the regression trees learns through recursive binary splits. It splits the learning data sample into smaller subsets to answer some basic questions that can be categorical or numerical. Hence, The output of the regression trees can vary depending on several parameter such as the tree size, or the splitting criterion [47].

The major benefits of regression trees over other nonparametric methods such as, nearest neighbors and kernel-based methods, are their ability to generate a fast prediction without computationally expensive calculation, their high performance even if the dataset is incomplete, and the transparency they provide to track the most important variables affecting the prediction. Moreover, the regression trees have the ability to split outliers into separate branch not to increase the accuracy of the predictor. Hence, regression trees is one of the powerful statistical techniques being used for data mining, analysis and prediction in different research fields [48, 49, 47]

Regression trees are trained based on the absolute difference between the PV measurement and the CSM model,  $\Lambda(t_t)$  as in Equation 3.11, where  $t_t$  is the training time and  $T_n$  is the end of the training period.

$$\Lambda(t_t) = \left| \frac{P_m(t_t) - P_{pccs}(t_t)}{P_{pccs}(t_t)} \right| \quad \forall t_t \in [1, 2, \dots, T_n] \quad (3.11)$$

The  $\Lambda(t_t)$  was classified based on 2 variables of the weather forecast,  $Te_{wf}$  and  $CC_{wf}$ . Other variable combinations were tested in [40], yet it was found that  $Te_{wf}$  and  $CC_{wf}$  are the most effective variables in training the given regression trees without increasing the complexity of the model. Bagging is a technique that is used to improve the performance of the regression trees as in [46]. The main idea behind bagging is dividing the available training data into several bootstrap samples to train various trees instead of one tree and then averaging the output to generate the main prediction. In [40], other different methods were tested for the optimization of the presented algorithm, and it was confirmed that the bagging regression trees lead to the lowest error and highest efficiency. The prediction of the regression trees  $\Lambda_p(t_f)$  is then used to generate a point generation forecast  $P_{pf}(t_f)$  as in Equation 3.12, for the next 24 h. The temporal resolution is always limited by the temporal resolution of the supplied weather forecast, which is 1 h.

$$P_{pf}(t_f) = P_{pccs}(t_f) - |\Lambda_p(t_f) \times P_{pccs}(t_f)| \quad \forall t_f \in [1, 2, \dots, 24] \quad (3.12)$$

### 3.6 Probabilistic forecast

The difference between the forecasted PV generation provided by the bagging regression trees and the real PV measurements is the main drive behind the probabilistic forecast. The relative difference between  $P_{pf}$  and  $P_m$  is classified into  $i = 8$  categories depending on the forecasting cloudiness  $CC_{wf}$   $[\frac{0}{8}, \dots, \frac{8}{8}]$  within the time of the day. It is calculated such that  $P_{pf}$  and  $P_m$  are of 1 min resolution, where  $P_{pf}$  is interpolated linearly to be

## A Appendix

converted from 1 h time step to 1 min, so that PV output variability can be included. The overall probabilistic forecast relative difference training set can be represented by  $\lambda_i$  such that  $i \in [1, \dots, 8]$ . Each of the 8 training sets are fitted automatically to different cumulative distribution functions (CDF) until an optimal distribution  $F_i(\lambda_i)$  is found. Having multiple distributions can easily show the  $\lambda_i$  behavior at each cloudiness conditions for an optimized aggregated forecast. For each  $F_i(\lambda_i)$ , the classification represents a data filtering of unnecessary information and focuses only on the forecasting behavior at a specific weather condition. Figure 3.6 shows the 8 different CDFs after a training period of 4 months between 01.05.2016 till 01.09.2016. The effect of the  $CC_{wf}$  over the relative difference  $\lambda_i$  can be clearly noticed. Using the presented distributions, it can be shown that for  $CC_{wf} = 0/8$  (i.e. clear sky),  $F_1(0) = Pr(\lambda_i \leq 0) = 0.7$  as in Figure 3.6(a). This value can be compared to  $F_8(0) = 0.05$  as in Figure 3.6(h).

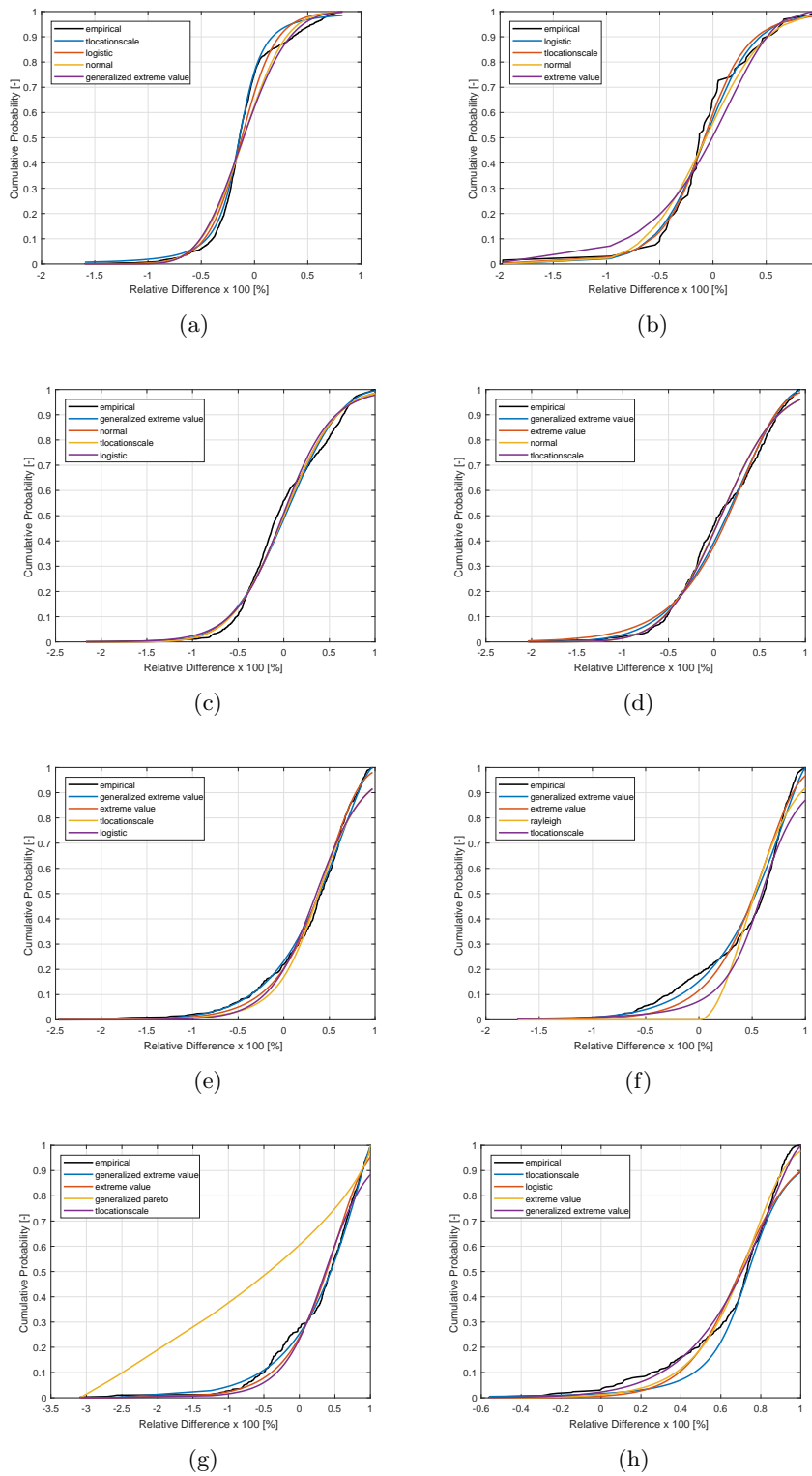


**Figure 3.6:** The 8 CDFs for different cloud covers over a training period of 4 months (a)  $CC_{wf} = 1/8$  (b)  $CC_{wf} = 2/8$  (c)  $CC_{wf} = 3/8$  (d)  $CC_{wf} = 4/8$  (e)  $CC_{wf} = 5/8$  (f)  $CC_{wf} = 6/8$  (g)  $CC_{wf} = 7/8$  (h)  $CC_{wf} = 8/8$ . The legend consists of the empirical forecast and the top 4 matching forecasts. 109

## A Appendix

The range of values of  $F_i(0)$  between  $F_1(0)$  and  $F_8(0)$  is gradually decreasing, and the distribution is shifted more towards positive relative difference values ( $(P_{pf}-P_m) / P_{pf} > 0$ ). Under-forecasting, as described in the earlier sections, does not occur with a high frequency compared to the over-forecasting as  $CC_{wf}$  increases.

The choice of the best fit to the empirical data is made based on the Bayesian information criterion (BIC)[50]. The BIC is capable of fitting and selecting the best distribution without increasing the model complexity. The lower the BIC, the better the fit of the model. The general equation of the BIC can be represented in Equation 3.13, where  $k_e$  is the number of estimated parameters,  $\hat{F}_i$  is the maximum value likelihood estimate of  $F_i$  [50].

$$BIC = -2\log(\hat{F}_i) + k_e\log(N_d) \quad (3.13)$$

The best 4 fitting distributions are presented in Figure 3.6. For each category  $i$ , the fitting distribution can differ from one category to another. Moreover, it can vary over time. Every day, the model can choose a different distribution with new parameters depending on the behavior over the point forecast within that day. As an example, Figure 3.7 shows the best fitting distribution after two different training horizons. Figure 3.7(a) represents the most fitting 4 distributions after one month, and Figure 3.7(b) after 4 months.

Having 8 distributions will help the probabilistic forecast to function under different conditions. If the weather is mostly clear, only the first distribution  $F_1$ , where  $CC_{wf} = 0/8$ , will be trained and used for prediction. The more overcast, cloudy, or partly cloudy days there are within the years, the more training data will be available and the more data can be used to find the best distribution.

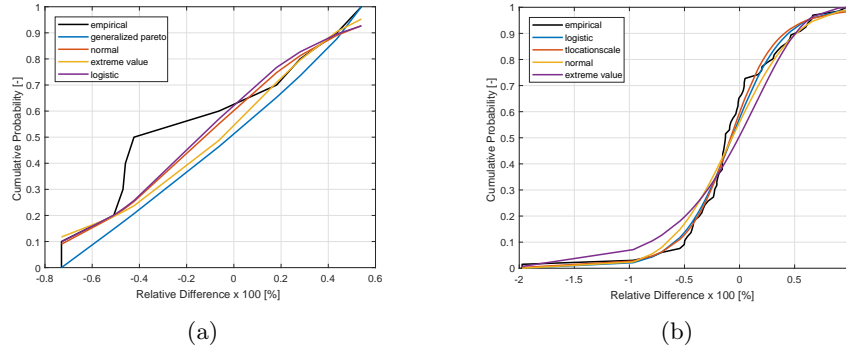


**Figure 3.7:** CDF after different training times (a) 1 month training time 01.05.2016 to 01.6.2016 (b) 4 months training time 01.5.2016 to 01.09.2016.

The goal of the probabilistic forecast is to deliver a range of values to the DSM algorithms operating within the EMS to reach the most optimal decisions. The range that can be supplied by the given CDFs is continuous, yet a discrete set is sufficient as in [7] for the EMS applications. Within this paper, the discrete range  $Q$  is defined  $Q = \{10\%, 20\%, \dots, 90\%\}$ . The  $\lambda_i$  is calculated using the inverse CDF,  $F_i^{-1}(q)$ , as shown

in Equation 3.14, where  $q$  is the selected discrete probability at which  $\lambda_i$  is calculated.  $q = 90\%$  represents the highest probability of the the discrete set  $Q$ . Thus, it leads to the highest relative difference and the most guaranteed PV power expected to be generated. On the other hands,  $q = 10\%$  would lead to the lowest relative difference and the least guaranteed PV power.

$$\begin{aligned} F_i^{-1}(q) &= \lambda_i, q \in Q = \{10\%, 20\%, \dots, 90\%\} \\ & i \in [1, \dots, 8], \\ \text{and } i &= 8 \times (CC_{wf}(tf)) + 1 \end{aligned} \quad (3.14)$$

Using the given  $\lambda_i$ , the set of probabilistic PV curves  $P_{pp}(tf)$  is calculated as in Equation 3.15. The set always consists of  $n_Q$  curves, where  $n_Q$  is the number of elements in  $Q$ . Each curve in the set varies over time depending on the  $P_{pf}$ ,  $\lambda_i$ , and the  $CC_{wf}$ .

$$\begin{aligned} p_{ppq}(tf) &= P_{pf}(tf) \times (1 - \lambda_i) \\ p_{ppq}(tf) \in P_{pp}(tf) &= \{p_{pp10\%}(tf), p_{pp20\%}(tf), \dots, p_{pp90\%}(tf)\} \end{aligned} \quad (3.15)$$

In Figure 3.8, the output of the probabilistic forecast in the different seasons of the year. The curves of the different  $q$  are visualized as stacked bars to easily identify the available power at each  $q$ . It can be noticed in Figure 3.8(e) that the power available with  $q = 90\%$  is the highest compared to all other seasons, as the PV variability in that day was relatively low. In comparison, Figure 3.8(a) and 3.8(g) show a power peak at noon correlated to  $q = 10\%$ , due to the high variability on that day. Figure 3.8(b) to 3.8(h) show the PV power at a higher resolution, 1 min instead of 1 h to show the PV power variability. These variabilities led to an error in the point forecast that was captured by the probabilistic PV forecast. In other words, the hardly predictable unrepresentable variabilities that occur in the point forecast were presented as curves with lower  $q$  by the probabilistic forecast.

The reason for presenting the probabilistic forecast with CDFs and the multiple curves  $q$  is its intuitive and simple possibilities for integration with an EMS. An EMS system would not need an exact PV forecast at certain time of the day, but rather a guaranteed power to avoid putting off or rearranging loads. As an example, assuming a heat pump (HP) or an electrical vehicle (EV), and a mini-washing machine submitted a scheduling request to an EMS simultaneously, the EMS would choose to place the HP or the EV under  $q = 90\%$  or higher, and the mini-washing machine at any lower  $q$ . The EMS prioritized the HP and EV as they work for longer duration and higher power. Consequently, they would need to be scheduled at the most guaranteed PV generation times with the lowest possible variability. If the PV generation is higher than the highest probability curve, it would not cause any problem with the plan, as the rest of energy would be either feed-in to the grid or stored in batteries. On the other hand, having the mini-washing machine or similar devices with low power and short durations, scheduled at a lower  $q$  would not affect the economics of the schedule or the EMS as a whole.

## A Appendix

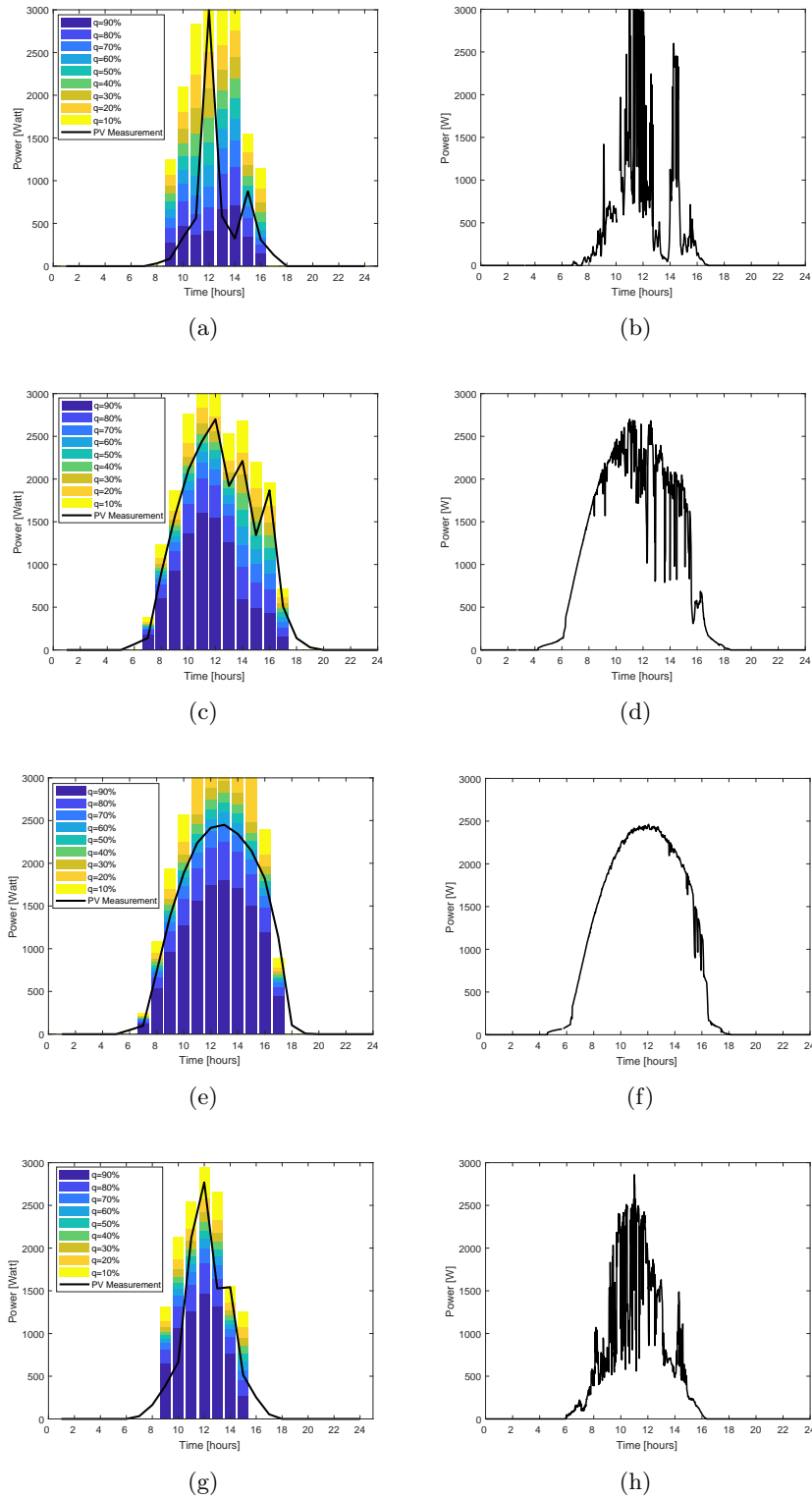


**Figure 3.8:** Probabilistic forecast output and PV measurements in multiple days in different seasons, (a) Winter (b) Winter-1 min resolution (c) Spring (d) Spring-1 min resolution (e) Summer (f) Summer-1 min resolution (g) Fall (h) Fall-1 min resolution.

## 4 Model validation

PV forecast models are usually validated by evaluating the discrepancy between the forecast and the actual measurement using various statistical metrics such as RMSE, mean absolute error (MAE), and mean biased error (MBE) [18]. Other factors such as the continuous ranked probability score (CRPS) and the brier score (BS) are used to evaluate the probabilistic forecast [51, 52]. Each of these metrics has a benefit in understanding the characteristics of the developed forecasting model. As an example, the RMSE measures the quadratic average magnitude of the error and, consequently gives higher weights to larger errors. The MAE measures the average magnitude without considering the error direction, while the MBE measured the direction to show whether the model is over- or under-forecast. Recent metrics were introduced and discussed in [53, 54, 55]. These metrics were designed to complement the statistical metrics so that a precise analysis of the forecast performance can be demonstrated. One of these metrics is the temporal distortion index (TDI) [53], which can analysis the temporal distortion due to time shift between the forecast and the actual measured values.

In this section, the forecasting model is validated against the different metrics to present a comprehensive image of the performance of the model in real-time operation. Moreover, only daylight hours were considered in the validation to avoid the influence of the non PV generation hours on the metrics.

### 4.1 Point forecast

Since the model is tested for real-time EMS applications, the training period of the regression trees and the whole model is considered, initially, to be continuously growing on a daily basis from 01.05.2016 to 01.05.2017. The model is meant to run once a day shortly before midnight to enable the EMS to start the scheduling at 00:00 every day. Using equations 4.1, 4.2 and 4.3, the RMSE, MBE and MAE are calculated.

$$RMSE = \sqrt{\frac{1}{N} \sum_1^N (P_{pf} - P_m)^2} \quad (4.1)$$

$$MBE = \frac{1}{N} \sum_1^N P_{pf} - P_m \quad (4.2)$$

$$MAE = \frac{1}{N} \sum_1^N |P_{pf} - P_m| \quad (4.3)$$

## A Appendix

Figure 4.1 demonstrates the average daily error for different cumulative training periods of an hourly temporal resolution. The error was normalized to the rated value of the PV system. The initial value starts in June after one month of training, representing the highest value, 17.3% for the RMSE, 9.3% for the MAE and -1.5% for the MBE. After four months of training, the RMSE dropped to 15.3%. On the other hands, the MAE and the MBE were 8.5% and 1.53%, respectively. Considering that a multi-purpose online weather forecast is used, the integration of PV plant losses, the minimal processing power required, and the spatial-temporal resolution of the forecast, the point forecast  $P_{pf}$  has an improved performance compared to other presented models in the review of [27, 18]. The MBE presented comparative results to short-term forecasts, (10 min to 60 min), with higher spatial resolutions.

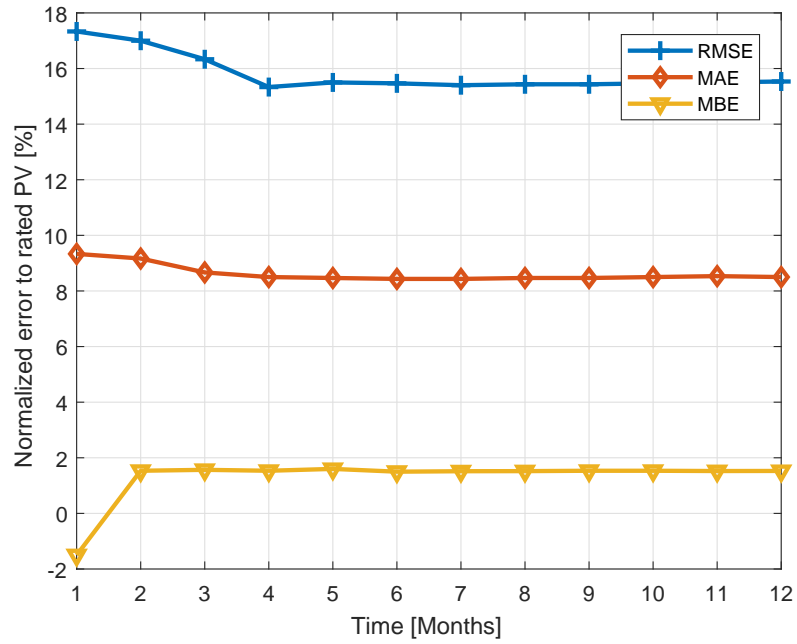


**Figure 4.1:** Error against training horizons.

To benchmark the point forecast, a smart persistence model is used as a reference to calculate the forecast skill (FS) [56]. A persistence model projects the current generation conditions at time  $t$  into the future  $t + t_f$ . The smart persistence model shares the same method of a persistence model, yet it assumes a constant clear-sky index [57, 58]. The FS is calculated based on Equation 4.4, where  $RMSE_{sp}$  is the root mean square error of the smart persistence model.

$$FS = 1 - \frac{RMSE}{RMSE_{sp}} \times 100 \quad (4.4)$$

The normalized RMSE of the smart persistence was calculated using the same temporal resolution, testing horizon and forecasting horizon. After one month of the point forecast

training, the FS was 44%. After 4 months of training, the FS raised to 48.6%, which means that point forecast model excelled the performance of the smart persistence model in all the cases. The FS presented in the literature varied between 0% and 42% according [59]. In the review of [27], FS of the day-ahead forecasts ranged between 14% to 43%. [60] reported FS of 31.29% for a day-ahead forecast of a 1.86 MW plant. Considering the scale of the household PV plant used, temporal resolution and the forecasting horizon used, the point forecast prediction showed its capability to deliver a proper forecast to the EMS. Although the point forecast is not the main output of the model, it was important to show the quality of the forecast used to generate the probabilistic forecast.

To analyze the temporal distortion of the forecast, TDI of [53] is evaluated. This metric was developed based on the Dynamic Time Warping (DTW) algorithm that was presented earlier in the 70s, which can quantify the distortion between two time series. In this case, the two time series are the point forecast and measurements time series, respectively. Using the DTW algorithm an optimal path is through minimizing the distances between the two given time series. The optimal warping path is returned as such that the forecast with index  $ti$  and the measurement with index  $ri$  have the smallest distance between them. The TDI can be calculated based on  $ti$  and  $ri$  according to Equation 4.5, where  $k$  is the length of the index set.

$$TDI = \frac{1}{N^2} \sum_{l=1}^{k-1} |(ti_{l+1} - ti_l)(ti_{l+1} + ti_l - ri_{l+1} - ri_l)| \quad (4.5)$$

The TDI can vary between a value of 0 and 1. The lower the value of the TDI, the lower is the temporal distortion. Using the fourth month training horizon as a reference for the required training period, the TDI was calculated to 2.6%. Thus, the forecast showed a minimal temporal distortion compared to the measurements.

## 4.2 Probabilistic forecast

The error and uncertainty of the point forecast is the main drive behind of the probabilistic forecast. The point forecast is often evaluated in the literature against measurement data of the same resolution (between 30 min and 1 h), which hides lots of information about the PV variability. In this case, the point forecast, which is of hourly resolution, is evaluated against the minute resolution of the measurement to build an accurate and reliable error distribution. The probabilistic forecast is usually generated either from a single distribution based on the error of the point forecast as in [31] or the ensemble forecast. In this model, 8 different distributions are used to generate the probabilistic forecast, where each is used to calculate a certain probability at a specific time according to the weather forecast. Moreover, the fitting distribution to empirical distribution varies over time depending on the new data sample collected. Consequently, every distribution has to be validated to show its capability to forecast future errors.

The *CRPS* is used to compare the CDF against observation to assess the quality and the integrated accuracy over the complete distribution function as shown in equation

## A Appendix

4.6, where  $F_i^0(\lambda)$  is the empirical distribution

$$CRPS = \frac{1}{8} \sum_{i=1}^8 \int_{-\infty}^{\infty} (F_i(\lambda) - F_i^0(\lambda))^2 d\lambda. \quad (4.6)$$

Considering a complete year of data, the model was trained on different horizons to show the variation of the CDF depending on the training time, which is a criterion for the EMS applications. The rest of the year is used for testing. Table 4.1 shows the results for different training horizons. For example, having a training horizon of 1 month means that a daily forecast was made for 11 months with the same trained model. It can be noticed that  $CRPS$ 's over the different training horizons have not varied significantly from the first month, which means that the model response in real-time is fast and independent of the training time. These variation is mainly due to the change of the training and testing data set. In the the training horizon of the one to three months, the CRPS variations were rather close as those three month represent May, June and July. After the fifth month, the CRPS peaked due to the start of the new season, then it decreased back after the sixth month. This decrease is due to the availability of a more representative training data. Such behavior can be analyzed in details for specific  $i$ . After fifth month of training,  $i = 8$ , which corresponds to  $CC_{wf} = 8/8$ , had the highest CRPS values, because the training data set was not reliable enough for this CDF to deliver a forecast. After six months of training,  $i = \{1, 2, 4, 5, 8\}$  dropped compared to the five months of training, due to the introduction a larger training data set that includes more representative days. Selective training set can lead to better results, yet it is computationally expensive for EMS applications. Moreover, the expected improvement would not pay for the additional required computational capacity. If no optimal training period is selected, the average of the  $CRPS$  over all the training periods is 5.56%. Assuming that the maximum variation of  $\lambda$  is 100% and it happens at the maximal peak power of 3 kW, the 5.56% error will lead to only 0.16 kW.

The  $BS$  is another metric to measure the accuracy of the probabilistic forecast by comparing the probability of the occurrence of an event to the forecasted probability as equation in 4.7.  $o_{ij}$  is the observation of an event. If the event occurs  $o_{ij} = 1$ , otherwise  $o_{ij} = 0$ .  $N_p$  is the number of pairs occurring under the given conditions of one of the 8 distributions. An example of event states,  $\lambda$  should be less than or equal to 0.2% at the given  $q$ . A perfect  $BS$  is equal to 0; the higher the  $BS$  is, the lower the performance.

$$BS = \frac{1}{N} \sum_{i=1}^8 \sum_{j=1}^{N_p} (q - o_{ij})^2 \quad (4.7)$$

Table 4.2 shows the calculated  $BS$  at the different probabilities  $q$  against different training horizons. It can be noticed that the training horizon did not have significant influence on the  $BS$ . Comparing the variation of the  $BS$  of the  $q = 90\%$  after one month to after 6 months, a 6% increase in performance can be noticed. Moreover, considering the mean of the whole cases  $q$  over the different training months, the mean  $BS$  is 0.12.

A reference probabilistic forecast is used to benchmark the presented probabilistic

forecasting model and evaluate its skill. Persistence ensemble is a commonly used reference model for probabilistic forecasts as in [31, 33]. In this paper, the reference is formed based on the last 20 observations of the same hour. The behavior of the persistence ensemble cannot be easily foreseen, as the persistence ensemble has to predict the  $\lambda$  of the point forecast. Based on the performance of the persistence ensemble, the continuous ranked probability skill score (CRPSS) and the Brier skill score (BSS) are calculated as in equations 4.8 and 4.9, respectively.

$$CRPSS = 1 - \frac{CRPS}{CRPS_{PeEn}} \times 100 \quad (4.8)$$

$$BSS = 1 - \frac{BS}{BS_{PeEn}} \times 100 \quad (4.9)$$

Tables 4.1 and 4.2 present the benchmarking results of the CRPSS and the BSS. For different training horizons, the CRPSS indicates that the probabilistic forecast outperforms the persistence ensemble. After one month of training, the CRPSS score was 12.51%, as point forecast was not yet completely trained and the persistence ensemble could still forecast the error behavior. In the second month of training, the performance of the persistence ensemble decreased dramatically leading to a significant increase in the CRPSS. The reason behind such a drop is  $\lambda$ 's independence of the time of the day. If persistence ensemble were used to directly forecast the PV power generation, better results could have been achieved. Persistence ensemble was required to forecast  $\lambda$ , similarly to the presented model, to be a valid reference. For the BSS, the results showed that the demonstrated probabilistic forecast model excelled the persistence ensemble even after one month of training.

**Table 4.1:** CRPS of different training horizons.

Training horizon [month(s)]	$CRPS_i$ [%]								$CRPS$ [%]	$CRPSS$ [%]
	$i = 1$	$i = 2$	$i = 3$	$i = 4$	$i = 5$	$i = 6$	$i = 7$	$i = 8$		
1	13.99	4.94	5.39	5.41	1.64	2.20	4.54	8.27	5.80	12.51
2	7.64	1.56	7.31	3.56	2.96	3.20	1.92	7.27	4.43	91.07
3	8.46	1.62	7.83	3.02	4.47	2.90	1.26	9.05	4.82	90.05
4	11.26	3.25	10.44	4.53	5.76	3.43	0.96	10.96	6.32	87.52
5	13.06	5.35	9.54	2.99	4.23	3.41	2.01	16.83	7.18	85.87
6	11.64	2.97	10.89	0.89	1.16	7.23	2.41	1.51	4.84	90.94

**Table 4.2:** BS of different training horizons.

Training horizon [month(s)]	<i>BS</i> [-]				<i>BSS</i> [%]
	<i>q</i> = 60%	<i>q</i> = 70%	<i>q</i> = 80%	<i>q</i> = 90%	
1	0.188	0.139	0.102	0.068	43.41
2	0.195	0.143	0.106	0.072	42.72
3	0.196	0.145	0.108	0.070	40.88
4	0.195	0.144	0.107	0.071	36.29
5	0.193	0.141	0.103	0.068	36.75
6	0.189	0.140	0.09	0.064	39.38

## **5 Open-source software**

The model will be available for the open-source community for EMS application on [61] in two different formats. The first format is the initial development format, Matlab script, for research applications. A GUI is implemented for ease of application to the households' residents and a direct integration with open-source energy monitoring societies such as [62]. The second format is Python, for the integration with micro-computers such as Raspberry Pis within smart homes.

## *A Appendix*

## 6 Conclusions

This paper proposes a probabilistic forecasting model that can provide an EMS with better information to avoid failures in load scheduling and reach an efficient, cost-optimal operation. The model shows different features that make it convenient for EMS application. These features can be summarized in the following:

- Forecasting using commonly available data within a building with a PV system, such as the historic PV measurements and an online weather forecast
- Detecting shading and system losses automatically without any predefined parameterization
- Delivering multiple probabilistic curves to the EMS in a form that fits with the requirements of the DSM algorithms
- Minimal training time, as the probabilistic forecast was able to perform even after one month of training
- Minimal computational power as it can generate the forecast in milliseconds once it is trained. Moreover, it can run on microcomputers such as a Raspberry pi

The model was validated via multiple metrics as discussed in Section 4 using real measurements to show its capability to serve EMS's, yet the most important evaluation metric is the one evaluating the performance of the forecast once integrated in an EMS. In [7], the probabilistic forecast and a reference forecast are integrated into the same EMS to evaluate the influence of the probabilistic forecast on the performance of the EMS. It was found that the probabilistic forecast led to a significant increase in self-consumption and self-sufficiency of a building under different load conditions and different PV capacities. Consequently, [7] confirms the capability of the probabilistic forecast to enhance the EMS decision-making process and performance.

Looking forward, to test the generality of the model, a test of the model in different climates and locations is planned. Also, the performance of a sensitivity analysis on the online weather forecast or the use of different forecasts to show how far the online forecast influences the learning curve of the probabilistic forecast are planned.

*A Appendix*

## Bibliography

- [1] R. Wüstenhagen and M. Bilharz. Green energy market development in Germany: effective public policy and emerging customer demand. *Energy Policy*, 34(13):1681–1696, 2006. doi:10.1016/j.enpol.2004.07.013.
- [2] Federal Ministry for Economic Affairs and Energy. Renewable Energy Sources in Figures. *National and Interantional Developments*, page 84, 2015.
- [3] Bundesministerium für Wirtschaft und Energie. BMWi - Erneuerbare Energien, 2017.
- [4] H. Maron, H. Klemisch, and B. Maron. Marktakteure erneuerbare Energie-Anlagen in der Stromerzeugung. (August):1–92, 2011.
- [5] R. Hanna, J. Kleissl, A. Nottrott, and M. Ferry. Energy dispatch schedule optimization for demand charge reduction using a photovoltaic-battery storage system with solar forecasting. *Solar Energy*, 103:269–287, 2014. doi:10.1016/j.solener.2014.02.020.
- [6] A. L. Klingler and L. Teichtmann. Impacts of a forecast-based operation strategy for grid-connected PV storage systems on profitability and the energy system. *Solar Energy*, 158(July):861–868, 2017. doi:10.1016/j.solener.2017.10.052.
- [7] W. El-Baz, M. Seufzger, S. Lutzenberger, P. Tzscheutschler, and U. Wagner. Impact of probabilistic small-scale photovoltaic generation forecast on energy management systems. *Solar Energy*, 165:136–146, may 2018. URL: <http://linkinghub.elsevier.com/retrieve/pii/S0038092X18302020>, doi:10.1016/j.solener.2018.02.069.
- [8] a. Barbato and G. Carpentieri. Model and algorithms for the real time management of residential electricity demand. *2012 IEEE International Energy Conference and Exhibition (ENERGYCON)*, pages 701–706, sep 2012. doi:10.1109/EnergyCon.2012.6348242.
- [9] Z. Wu, H. Tazvinga, and X. Xia. Demand side management of photovoltaic-battery hybrid system. *Applied Energy*, 148:294–304, 2015. doi:10.1016/j.apenergy.2015.03.109.
- [10] M. Q. Raza, M. Nadarajah, and C. Ekanayake. On recent advances in PV output power forecast. *Solar Energy*, 136:125–144, 2016. doi:10.1016/j.solener.2016.06.073.

- [11] M. P. Almeida, O. Perpiñán, and L. Narvarte. PV power forecast using a nonparametric PV model. *Solar Energy*, 115:354–368, 2015. doi:10.1016/j.solener.2015.03.006.
- [12] Q. Ni, S. Zhuang, H. Sheng, G. Kang, and J. Xiao. An ensemble prediction intervals approach for short-term PV power forecasting. *Solar Energy*, 155:1072–1083, 2017. doi:10.1016/j.solener.2017.07.052.
- [13] W. El-Baz and P. Tzscheutschler. Autonomous coordination of smart buildings in microgrids based on a double-sided auction. In *2017 IEEE Power & Energy Society General Meeting*, number August, pages 1–5, Chicago, jul 2017. IEEE. URL: <http://ieeexplore.ieee.org/document/8273944/>, doi:10.1109/PESGM.2017.8273944.
- [14] W. El-Baz, C. Kandler, P. Wimmer, and P. Tzscheutschler. Practical experiences with smart homes modelling and simulati. In *ESI SimulationX User Forum*, Dres, 2016. ESI ITI.
- [15] W. El-Baz and P. Tzscheutschler. Co-simulation of a smart home model based on a micro electricity market. *Proceedings of the Fifth German-Austrian IBPSA Conference RWTH Aachen University*, pages 30–37, 2014.
- [16] G. R. Aghajani, H. A. Shayanfar, and H. Shayeghi. Demand side management in a smart micro-grid in the presence of renewable generation and demand response. *Energy*, 126:622–637, 2017. doi:10.1016/j.energy.2017.03.051.
- [17] B. Jiang, A. Muzhikyan, A. M. Farid, and K. Youcef-Toumi. Demand side management in power grid enterprise control: A comparison of industrial & social welfare approaches. *Applied Energy*, 187:833–846, 2017. doi:10.1016/j.apenergy.2016.10.096.
- [18] S. Pelland, J. Remund, J. Kleissl, T. Oozeki, and K. D. Brabandere. Photovoltaic and Solar Forecasting: State of the Art. Technical report, International Energy Agency, 2013. doi:978-3-906042-13-8.
- [19] R. Haider and C.-H. Kim. *Integration of Distributed Energy Resources in Power Systems*. 2016. doi:10.1016/B978-0-12-803212-1.00007-6.
- [20] R. A. Verzijlbergh, P. W. Heijnen, S. R. de Roode, A. Los, and H. J. Jonker. Improved model output statistics of numerical weather prediction based irradiance forecasts for solar power applications. *Solar Energy*, 118:634–645, 2015. doi:10.1016/j.solener.2015.06.005.
- [21] J. Huang and M. Thatcher. Assessing the value of simulated regional weather variability in solar forecasting using numerical weather prediction. *Solar Energy*, 144:529–539, 2017. doi:10.1016/j.solener.2017.01.058.

- [22] M. Pierro, F. Bucci, M. De Felice, E. Maggioni, D. Moser, A. Perotto, F. Spada, and C. Cornaro. Multi-Model Ensemble for day ahead prediction of photovoltaic power generation. *Solar Energy*, 134:132–146, 2016. URL: <http://dx.doi.org/10.1016/j.solener.2016.04.040>, doi:10.1016/j.solener.2016.04.040.
- [23] M. Pierro, F. Bucci, M. De Felice, E. Maggioni, A. Perotto, F. Spada, D. Moser, and C. Cornaro. Deterministic and Stochastic Approaches for Day-Ahead Solar Power Forecasting. *Journal of Solar Energy Engineering*, 139(2):021010, 2016. URL: <http://solarenergyengineering.asmedigitalcollection.asme.org/article.aspx?doi=10.1115/1.4034823>, doi:10.1115/1.4034823.
- [24] M. Zamo, O. Mestre, P. Arbogast, and O. Pannekoucke. A benchmark of statistical regression methods for short-term forecasting of photovoltaic electricity production, part I: Deterministic forecast of hourly production. *Solar Energy*, 105:792–803, 2014. URL: <http://dx.doi.org/10.1016/j.solener.2013.12.006>, doi:10.1016/j.solener.2013.12.006.
- [25] R. Perez, E. Lorenz, S. Pelland, M. Beauharnois, G. Van Knowe, K. Hemker, D. Heinemann, J. Remund, S. C. Müller, W. Traunmüller, G. Steinmayer, D. Pozo, J. A. Ruiz-Arias, V. Lara-Fanego, L. Ramirez-Santigosa, M. Gaston-Romero, and L. M. Pomares. Comparison of numerical weather prediction solar irradiance forecasts in the US, Canada and Europe. *Solar Energy*, 94:305–326, 2013. doi:10.1016/j.solener.2013.05.005.
- [26] E. Lorenz, J. Kühnert, A. Hammer, and D. Heinemann. Solar Resource and Forecast Data for High PV Penetration PV production forecast of balance zones in Germany. *SHC Task*, 46(110), 2013.
- [27] J. Antonanzas, N. Osorio, R. Escobar, R. Urraca, F. J. Martinez-de Pison, and F. Antonanzas-Torres. Review of photovoltaic power forecasting. *Solar Energy*, 136:78–111, 2016. doi:10.1016/j.solener.2016.06.069.
- [28] T. Hong, P. Pinson, S. Fan, H. Zareipour, A. Troccoli, and R. J. Hyndman. Probabilistic energy forecasting: Global Energy Forecasting Competition 2014 and beyond. *International Journal of Forecasting*, 32(3):896–913, 2016. doi:10.1016/j.ijforecast.2016.02.001.
- [29] D. Yang, J. Kleissl, C. A. Gueymard, H. T. Pedro, and C. F. Coimbra. History and trends in solar irradiance and PV power forecasting: A preliminary assessment and review using text mining. *Solar Energy*, (November):0–1, 2018. URL: <http://dx.doi.org/10.1016/j.solener.2017.11.023>, doi:10.1016/j.solener.2017.11.023.
- [30] Y. M. Saint-Drenan, G. H. Good, and M. Braun. A probabilistic approach to the estimation of regional photovoltaic power production. *Solar Energy*, 147:257–276, 2017. doi:10.1016/j.solener.2017.03.007.

- [31] M. David, F. Ramahatana, P. J. Trombe, and P. Lauret. Probabilistic forecasting of the solar irradiance with recursive ARMA and GARCH models. *Solar Energy*, 133:55–72, 2016. doi:10.1016/j.solener.2016.03.064.
- [32] F. Golestaneh, P. Pinson, and H. B. Gooi. Very Short-Term Nonparametric Probabilistic Forecasting of Renewable Energy Generation; With Application to Solar Energy. *Power Systems, IEEE Transactions on*, PP(99):1–14, 2016. doi:10.1109/TPWRS.2015.2502423.
- [33] S. Alessandrini, L. Delle Monache, S. Sperati, and G. Cervone. An analog ensemble for short-term probabilistic solar power forecast. *Applied Energy*, 157:95–110, 2015. doi:10.1016/j.apenergy.2015.08.011.
- [34] Y. Chu and C. F. Coimbra. Short-term probabilistic forecasts for Direct Normal Irradiance. *Renewable Energy*, 101:526–536, 2017. URL: <http://dx.doi.org/10.1016/j.renene.2016.09.012>, doi:10.1016/j.renene.2016.09.012.
- [35] M. Zamo, O. Mestre, P. Arbogast, and O. Pannekoucke. A benchmark of statistical regression methods for short-term forecasting of photovoltaic electricity production. Part II: Probabilistic forecast of daily production. *Solar Energy*, 105:804–816, 2014. doi:10.1016/j.solener.2014.03.026.
- [36] W. El-Baz, J. Honold, L. Hardi, and P. Tzscheuschler. High-resolution dataset for building energy management systems applications. *Data in Brief*, 54:1–5, 2018. doi:10.1016/j.dib.2017.12.058.
- [37] Weather Underground. Weather Forecast — Weather Underground, 2017. URL: <https://www.wunderground.com/>.
- [38] R. Bird and R. Hulstrom. Simplified clear sky model for direct and diffuse insolation on horizontal surfaces, 1981. doi:10.2172/6510849.
- [39] C. Baltus, J. Eikelboom, and R. van Zolingen. Analytical monitoring of losses in PV systems. *14th European Photovoltaic Solar Energy Conference*, (July):1547–1550, 1997.
- [40] M. Seufzger. *Evaluation and Optimization of an Energy Management System based on PV Prediction Certainty (master’s thesis)*. Technical University of Munich, Munich, 2017.
- [41] D. Lingfors, S. Killinger, N. A. Engerer, J. Widén, and J. M. Bright. Identification of PV system shading using a LiDAR-based solar resource assessment model: An evaluation and cross-validation. *Solar Energy*, 159(September 2017):157–172, 2018. doi:10.1016/j.solener.2017.10.061.
- [42] S. Killinger, J. M. Bright, D. Lingfors, and N. A. Engerer. A tuning routine to correct systematic influences in reference PV systems’ power outputs. *Solar Energy*, 157(November):1082–1094, 2017. doi:10.1016/j.solener.2017.09.001.

- [43] S. Killinger, J. M. Bright, D. Lingfors, and N. A. Engerer. Towards a Tuning Method of PV Power Measurements to Balance Systematic Influences. *ISES Solar World Congress 2017, Abu Dhabi, United Arab Emirates, October 29 - November 2, 2017*, pages 1–11, 2017.
- [44] R. Perez, M. David, T. E. Hoff, M. Jamaly, S. Kivalov, J. Kleissl, P. Lauret, and M. Perez. Spatial and Temporal Variability of Solar Energy. *Foundations and Trends® in Renewable Energy*, 1(1):1–44, 2016. doi:10.1561/27000000006.
- [45] L. Breiman. *Classification and regression trees*. Wadsworth International Group, 1984.
- [46] L. Breiman. Arcing classifier (with discussion and a rejoinder by the author). *The Annals of Statistics*, 26(3):801–849, 1998. arXiv:0010, doi:10.1214/aos/1024691079.
- [47] X. Ma. *USING CLASSIFICATION AND REGRESSION TREES : a practical primer*. INFORMATION AGE PUB, 2018. URL: <http://www.infoagepub.com/products/Using-Classification-and-Regression-Trees>.
- [48] C. R. C. R. Rao, E. J. Wegman, and J. L. Solka. *Data mining and data visualization*. Elsevier North Holland, 2005.
- [49] L. Rokach and O. Maimon. *Data Mining with Decision Trees*, volume 81 of *Series in Machine Perception and Artificial Intelligence*. WORLD SCIENTIFIC, oct 2014. URL: <http://www.worldscientific.com/worldscibooks/10.1142/9097>, doi:10.1142/9097.
- [50] G. Schwarz. Estimating the Dimension of a Model. *The Annals of Statistics*, 6(2):461–464, 1978. arXiv:arXiv:1011.1669v3, doi:10.1214/aos/1176344136.
- [51] A. P. Weigel, M. A. Liniger, and C. Appenzeller. Generalization of the Discrete Brier and Ranked Probability Skill Scores for Weighted Multimodel Ensemble Forecasts. *Monthly Weather Review*, 135(7):2778–2785, 2007. doi:10.1175/MWR3428.1.
- [52] A. Jordan, F. Krüger, and S. Lerch. Evaluating probabilistic forecasts with the R package scoringRules. (2014):1–20, 2017. arXiv:1709.04743.
- [53] L. Frías-Paredes, F. Mallor, T. León, and M. Gastón-Romeo. Introducing the Temporal Distortion Index to perform a bidimensional analysis of renewable energy forecast. *Energy*, 94:180–194, 2016. doi:10.1016/j.energy.2015.10.093.
- [54] L. Vallance, B. Charbonnier, N. Paul, S. Dubost, and P. Blanc. Towards a standardized procedure to assess solar forecast accuracy: A new ramp and time alignment metric. *Solar Energy*, 150:408–422, 2017. doi:10.1016/j.solener.2017.04.064.
- [55] L. Frías-Paredes, F. Mallor, M. Gastón-Romeo, and T. León. Dynamic mean absolute error as new measure for assessing forecasting errors. *Energy Conversion and*

## A Appendix

- Management*, 162(February):176–188, 2018. URL: <https://doi.org/10.1016/j.enconman.2018.02.030>, doi:10.1016/j.enconman.2018.02.030.
- [56] C. F. Coimbra, J. Kleissl, and R. Marquez. Overview of Solar-Forecasting Methods and a Metric for Accuracy Evaluation. In *Solar Energy Forecasting and Resource Assessment*, pages 171–194. Elsevier, 2013. doi:10.1016/B978-0-12-397177-7.00008-5.
- [57] A. Kaur, L. Nonnenmacher, H. T. Pedro, and C. F. Coimbra. Benefits of solar forecasting for energy imbalance markets. *Renewable Energy*, 86:819–830, 2016. doi:10.1016/j.renene.2015.09.011.
- [58] H. T. C. Pedro and C. F. M. Coimbra. Assessment of forecasting techniques for solar power production with no exogenous inputs. *Solar Energy*, 86(7):2017–2028, 2012. doi:10.1016/j.solener.2012.04.004.
- [59] R. H. Inman, H. T. C. Pedro, and C. F. M. Coimbra. Solar forecasting methods for renewable energy integration. *Progress in Energy and Combustion Science*, 39(6):535–576, 2013. doi:10.1016/j.pecs.2013.06.002.
- [60] J. Antonanzas, D. Pozo-Vázquez, L. A. Fernandez-Jimenez, and F. J. Martinez-de Pison. The value of day-ahead forecasting for photovoltaics in the Spanish electricity market. *Solar Energy*, 158(December 2016):140–146, 2017. URL: <https://doi.org/10.1016/j.solener.2017.09.043>, doi:10.1016/j.solener.2017.09.043.
- [61] W. El-Baz. P3-Probabilistic PV Prediction Algorithm. URL: <https://gitlab.lrz.de/ga29pos/pvpredictiongit>.
- [62] OpenEnergyMonitor.org. Open Energy Monitor Website, 2010. URL: <https://emoncms.org/http://openenergymonitor.org/emon/>.

### **A.3 Publication 3 — Impact of Probabilistic Small-Scale Photovoltaic Generation Forecast on Energy Management Systems**

#### **Abstract**

Demand-side Management (DSM) algorithms are exposed to several uncertainties due to their dependency on renewable energy generation forecasts. On the large scale, generation and load forecasts can be relatively accurate, yet on the residential scale, forecasting errors increase due to higher uncertainties. One potential solution is to incorporate a probabilistic PV forecast into an optimal DSM algorithm instead of the existing deterministic PV forecasting algorithms. Hence, in this contribution, a numerical analysis that compares the potential of using a probabilistic PV forecast instead of the conventional deterministic algorithms in a DSM algorithm, is presented. Results show that under different household energy system configurations, the DSM algorithm with the probabilistic PV generation forecast leads to an increase in self-sufficiency and self-consumption by 24.2% and 17.7%, respectively, compared to the conventional deterministic algorithms. These results indicate that probabilistic PV forecasting algorithms may indeed have a higher potential compared to the conventional deterministic ones.

#### **Author Contribution**

I designed the model and wrote the paper; Sandra Lutzenberger developed the initial analysis; Michel Seufzger optimized the model operation; Peter Tzscheutschler and Ulrich Wagner revised the paper and provided a detailed critical review.

# 1 Introduction

Recent energy policies currently play an influential role in reshaping the electricity grid infrastructure globally. Green energy incentives were introduced over the past 25 years to enable the integration of more renewables, and embrace a low-carbon economy. In Germany, the renewable energy sources act Erneuerbare Energien Gesetz (EEG), was introduced in 2000, along with amendments till 2014 to prioritize the access of renewable energy sources (RES) to the grid [1]. This act enabled rapid integration of wind energy and photovoltaics (PV) through guaranteeing the supplier an energy purchase at a fixed tariff [2]. Enforcing similar acts, along with the consistent decrease of investment costs in PV systems, led to a boost in the installation of PV systems, especially in the residential sector. In this sector, the installed capacities represents 39.4% of the overall capacities compared to 19.2% for the commercial and industrial sectors [3]. Consequently, PV integration within the residential sector has become a continuous research topic, with crucial economic implications for single households [4].

For these households, electricity bills need to be minimized to reduce the investment costs for the residents [5, 6, 7]. In addition, autonomy and self-consumption need to be considered, yet they are byproducts of cost optimization and electricity bill minimization. Cost optimization is reached via applying demand side management (DSM), through which the loads are shifted and coordinated to maximize the use of the available PV generation within the residential household. Several research projects detailed the type of shiftable loads that could be integrated such as the white goods (e.g. washing machine, dish washer and the tumble dryer), heat pumps, or electrical vehicles [EV][8, 9, 10]. Others integrated thermal and electrical storages, or a micro combined heat and power cycle (micro-CHP) as an additional in-house energy supply source. All these components are always connected together through an energy management system (EMS), where the DSM strategy is realized. In all such possible configurations, the PV system was a dominant component. Thus, PV generation forecast is necessary for shifting the desired loads to the most suitable time-slot in the future.

Applied DSM strategy performance is highly dependent on the quality of the PV forecast. [11] showed the impact of forecast error on battery discharging behavior, where the forecast errors in specific days reached twice to ten times the battery energy capacity and led to a void dispatch schedule. [12] demonstrated the need for a better PV forecasting data for a grid friendly PV + Battery system. At the moment, there is a gap in the research tackling or providing solutions to the small-scale residential PV forecast implications on DSM. In other words, no clear answers are presented in the literature addressing and defining the required accuracy for rooftop PV forecast, the variability and uncertainty effect on the DSM in the residential sector, or the forecast type (i.e. probabilistic, or deterministic) required for DSM algorithms in real-life conditions.

## **1.1 Study objectives**

Hence, the objective of this contribution is to provide answers to these questions via analyzing the potential of incorporating a probabilistic forecast instead of a conventional deterministic one in the DSM algorithm. This potential is then analyzed based on defined metrics to demonstrate whether the probabilistic forecast would lead to a different operation plan for the household devices, and whether the new operation plan would lead to a significant increase in self-energy consumption and autonomy of the household. To show the effect of the forecast independently on the operation of the DSM algorithm, a simple algorithm was implemented that can fit to both the probabilistic forecast and the conventional deterministic forecast. In a separate publication [13], the probabilistic PV-forecast algorithm was detailed, where multiple PV generation curves were produced based on a statistical probabilistic analysis. In this contribution, the impact of such an algorithm on an EMS is presented to evaluate the potential of probabilistic forecast.

This contribution is structured as follows: Section 2 provides a background of the related literature in the field of DSM and PV generation forecasts. Section 3 presents the methodology and metrics used to evaluate the potential of DSM. Section 4 presents the results of a comparison between the potential of DSM under the probabilistic forecast and a conventional reference forecast. Section 5 provides the concluding remarks.

## 2 Background

### 2.1 DSM in households

DSM was introduced in the late 1970s [14] to encourage consumers to alter their load to produce a desired load profile for the utility. This means that the customer in this case needs to alter both the magnitude and the time pattern of the load to fit to the utility's plan. Thus, the scope of DSM incorporates several strategies such as peak clipping, valley filling, load shifting, strategic conservation, strategic load growth, and flexible load shaping [15]. The utility encourages the consumers to shift their own loads using financial incentives. Therefore, Real-Time Price (RTP) and Time-of-Use (ToU) tariffs were introduced so that the customers can shift their load from the peak hours to the off-peak hours [16].

Several theoretical studies and pilot projects investigated the potential of DSM strategies on different scales [17, 18, 19, 20]. To study the impact of DSM on different electricity tariffs, [20] developed a model to generate household load profiles and simulated them under flat-tariffs and time-based tariffs. The author found that several household loads are available for shifting, which benefit the utility to balance the supply and demand. To simulate real-world factors, [21] included in his contribution not only the electricity tariffs, but also the environmental performance and residents' behavior. The authors found that a combination of optimal DSM along with local energy supply sources could significantly reduce the electricity import from the grid and minimize the expenditure. Storage systems such as batteries and heat storages, in addition to the thermal mass of the buildings, also play a major role in enabling the DSM. [6, 22, 23] among others used storages to enable shifting and reducing the loads for extended hours depending on the consumer's demand and building type.

Different algorithms were presented in the literature, which applied different techniques such as artificial neural networks (ANN) [24], stochastic optimization [25], mixed-integer nonlinear programming (MINLP) [26], or greedy approach [23]. Along with the variations in the algorithms, the combinations with the PV systems varied. PV along with batteries, EV, or heat pumps were considered. In all these cases, PV forecast was used for the control algorithm to make DSM decisions 6 h, 12 h or 24 h ahead [24]. These algorithms are categorized as open-loop: the DSM strategy defined the optimal plan of the loads in future time-slots based on the current forecast without considering any uncertainties of supplied forecasts. Few publications tried to consider the effect of uncertainties in both the PV and demand forecast. [27] implemented an optimal open-loop control for a PV-Battery hybrid system, and enclosed it within a closed-loop that was based on model predictive control (MPC) to make up for the disturbances resulting from the PV forecast and load demand. The forecast supplied to the model was only based

on the average of winter or summer values of a PV output of hourly resolution. Such resolution on its own can generate enough disturbances in real-time operation, which is another reason highlighting the necessity of a closed-loop controller in this case. In [28], two optimization models were presented: an online and an offline model. The offline model, a Mixed Integer Linear Programming (MILP) model, acquired all the users' inputs along with the forecasts to schedule the loads for the next 24 hours over 96 time-slots (i.e., quarter hourly). The uncertainties of the forecasts were then handled by an online optimization model, which rescheduled the loads in real-time to make the output profile as close as possible to the one planned by the offline model. In both [27, 28], the battery system was the key to compensating for the disturbances generated from the forecast uncertainties and the time resolution of the control or the optimization model.

## 2.2 PV forecasting for DSM

For an enhanced DSM strategy implementation, real-life dynamics, such as weather and user behavior, have to be considered. Unforeseeable weather dynamics can lead to significant uncertainties in PV generation. Such uncertainties represent the current major challenges hindering the production of a high quality forecast. This is because their influence could vary depending on different factors such as the forecasting time horizon, the temporal resolution, the spatial resolution, and the local climate. Consequently, developing one single forecasting algorithm serving all applications is rather challenging.

The PV generation variability for a rooftop PV system can only be observed using continuous high temporal-resolution measurements and it can visually vanish as the temporal resolution decreases. These variabilities in the PV generation can be attributed to two phenomena: the first is the sun's motion across the sky and the distance between the sun and the earth, and the second is the cloud motion and speed. While the first phenomenon can be easily foreseeable and integrable in current forecast systems, the second can be rather challenging to predict [29].

Consequently, for a desert climate with a majority of sunny days, PV generation variability would be rather low compared to continental or tropical climates. Table 2.1 summarizes the PV output variability based on the weather condition. In case of an absolute sunny weather with (0/8) cloudiness, a rather stable generation could be witnessed. Thus, PV clear sky models (CSM) could be useful in this case such as [30, 31, 32, 33]. Depending on the cloudiness, the solar irradiation intensity is affected and so is the PV generation power. As the clouds move, especially on a partial-cloudy day, the power variabilities show up in the generation profile depending on the clouds' speed.

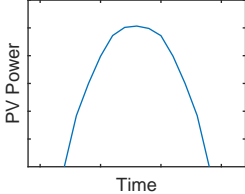
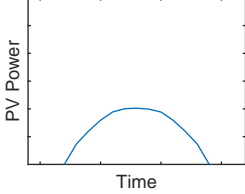
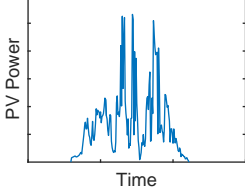
Variabilities in PV generation were intensively investigated in the literature only because of their large-scale effects on the grid [34, 35, 36, 37, 38, 39, 40]. According to [40], it was found that PV variability is highest for a single point, compared to a geographically dispersed system. Thus, for residential single family homes with a rooftop PV ranging from 1 kW<sub>p</sub> to 9 kW<sub>p</sub>, the variability in PV generation can be significantly higher compared to the micro-grid or the national grid.

## A Appendix

Currently available forecasting algorithms and models try to incorporate all possible factors affecting PV generation, yet the output is still exposed to considerable uncertainties. According to the IEA PVPS Task 14 [41], the forecasting approaches presented in the literature are divided into physical or statistical approaches. The physical approach focuses on using PV models, numerical weather prediction (NWP) or total sky imagery, while the statistical approach depends primarily on historical data and stochastic learning techniques. As the DSM algorithms are always operating with 6 h up to 48 h ahead forecast, the only feasible technique that can be used is the NWP, which is a physical approach that is commonly combined with a statistical post-processing model [42]. Yet, these models are designed for a spatial resolution  $> 1$  km, and demonstrated an uncertainty RMSE of 18% up to 64% for hourly forecasts 24 h ahead, which can even be significantly higher for a rooftop PV system [41]. According to [43], the uncertainty of an area size as large as Germany is 64% less compared to a point forecast.

The research towards PV forecasting focuses on serving large PV fleets to support baseline ramps, regulations load following, and unit commitment of regional power, but not DSM on the residential level. As explained, for a rooftop integrated PV system, the forecast is exposed to high variabilities and uncertainties due to the size of the system. Hence, considering such variability and uncertainty in the forecast supplied to the DSM algorithms can help realize a better integration of renewables in the household, an increase in cost savings, and autonomy for the consumer side.

**Table 2.1:** Effect of cloudiness over PV generation.

Weather		Effect on PV power generation	
	no clouds	reference power	
	partial or total cloudiness	reduced power	
	partial cloudy and windy	depending on cloud speed: - reduced power - variability	



## 3 Methodology

### 3.1 Overview

Conventional DSM algorithms operate based on a 15 min to 1 h resolution, depending on the available computational power and the expected smart metering infrastructure. Consequently, DSM algorithm developers look for a PV forecast in the same temporal-resolutions, where generation variability is concealed and uncertainty is rather high, as mentioned in Section 2. Throughout this section, a methodology of evaluating the DSM potential based on a statistical probabilistic forecast is described. The forecast supplies the DSM algorithms with multiple probabilistic PV generation profiles rather than one deterministic profile, so that the most certain possible decisions for load shifting are taken.

### 3.2 Input Data

#### 3.2.1 Real reference measurements

A 3 kWp rooftop PV system was used for the evaluation of this study. The PV system consists of 2 arrays, each of 6 modules. The first array has mono-crystalline modules (Solarworld SW 260 Mono), while the second array has poly-crystalline modules (Solarworld SW 250 Poly). The two arrays are connected to a PV inverter SMA sunnyboy TL 300. No smart meters were directly installed to monitor the PV system, but the data were directly acquired from the PV inverter via a UDP connection every 5 seconds. More technicals details about the PV system and the measurement method are available in [44].

### 3.3 Reference forecast

In [45], a PV hourly forecasting algorithm was developed based on a clear sky model for DSM applications in households. The model estimates the PV generation in the next 24 hours based on the cloudiness data available. The cloudiness of each layer (low, medium, and high) is given as a value between 0 and 100%. Based on a python program, the cloudiness values were extracted from an online weather service provider to supply the algorithm [46]. Equation 3.1 presents how the forecast was developed, where  $P_{cs_r}$  is the PV clear sky power generation, and  $cc_{low}$ ,  $cc_{med}$ ,  $cc_{high}$  are the low-level, mid-level and high-level cloudiness, respectively. This cloud level classification is based entirely on the height of the clouds as per table 3.1 [47].  $k$ ,  $f$ , and  $j$  are three empirical coefficients

that are estimated based on an error minimization optimization between the historical measured data and forecast data.

**Table 3.1:** Cloud classification.

Cloud level	Height
Low-level clouds	0 - 2 km
Mid-level clouds	2 - 7 km
High-level clouds	5 - 13 km

$$P_{f_r}(t) = P_{cs_r} \times [k \times \frac{100 - cc_{low}}{100} + f \times \frac{100 - cc_{mid}}{100} + j \times \frac{100 - cc_{High}}{100}]. \quad (3.1)$$

Based on weighted relative root mean squared error (wrRMSE), the author evaluated the reference algorithm over 30 days, using an hourly temporal resolution. The wrRMSE is formulated as per Equation 3.2, where  $n$  represents the number of the forecast hours,  $P_m$  is the measured PV power output, and  $P_{daily_{max}}$  is the maximum PV power on the evaluated day. The results showed a minimum wrRMSE of 10% and a mean value for all the input days to be 25%.

$$wrRMSE = \sqrt{\frac{1}{n} \sum_1^n \left( \frac{P_m - P_{f_r}}{P_{daily_{max}}} \right)^2}. \quad (3.2)$$

This algorithm was used because of its ease of application with DSM algorithms, yet any alternative favored algorithm can be applied as a reference algorithm.

### 3.4 Probabilistic forecast

The probabilistic forecast is an intuitive solution to handle the uncertainties and variabilities of the PV generation. The reference deterministic forecast generates a single-value forecast for every time step in the forecasting horizon, which can easily expose the EMS to several uncertainties. The probabilistic forecast is capable of generating a range of values for the EMS to take the most probable optimal decision. Within this section, the important features of the probabilistic forecast will be comprehensively discussed, as the detailed formulation is already presented in [13].

The process of generation a probabilistic forecast goes through multiple steps as shown in Figure 3.2. Before the process starts, 3 main inputs should be accessible: the historical data, weather forecast and PV plant parameters. The initial process is the generation of the clear-sky power based on the CSM of Bird and Hulstrom [48] and using the nominal PV module efficiency. To calibrate CSM, the system efficiency is calculated empirically based on historical data to include different losses such as the inverter losses, ohmic losses and temperature losses.

## A Appendix

The second process is the partial shading detection. This process involves also an empirical process which analyzes 3 consecutive sunny days to determine the Zenith angle  $Z$  at which the power drop occurs. Once the right angle is found, the power drop is calculated and applied to next days. The partial shading process is activated only once 3 consecutive sunny days are detected, yet the frequency of the calibration can be determined based on the user's input. Figure 3.1 shows the PV clear sky generation after calibration using the previously mentioned processes.

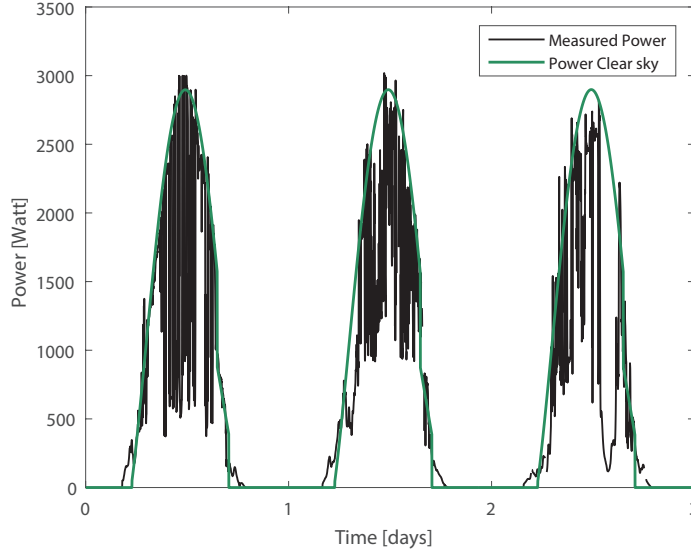


**Figure 3.1:** Clear sky model output and PV power measurements after the partial shading detection process [13].

The following process is the training of regression trees to generate a point forecast. These regression trees function based on dividing the data available into multiple sets and fitting it to a simple model based on a given number of branches and leafs. Such method showed its ability to provide an efficient predictions using the minimal computational time as in [13]. The training variable given to the regression trees is  $\Lambda(t_t)$ , where  $P_{pccs}$  is the clear sky power after calibration,  $t_t$  is the training time and  $T_n$  is the end of the training period.

$$\Lambda(t_t) = \left| \frac{P_m(t_t) - P_{pccs}(t_t)}{P_{pccs}(t_t)} \right| \quad \forall t_t \in [1, 2, \dots, T_n]. \quad (3.3)$$

The prediction of the trained regression  $\Lambda_p(t_f)$  is then used to generate the point forecast  $P_{pf}$  as per Equation 3.4, where  $t_f$  is the forecasting time. The resolution of the point forecast is limited by the resolution of the given weather forecast.

$$P_{pf}(t_f) = P_{pccs}(t_f) - |\Lambda_p(t_f) \times P_{pccs}(t_f)| \quad \forall t_f \in [1, 2, \dots, 24]. \quad (3.4)$$

The  $P_{pf}$  is the base on which the probabilistic forecast is built. In this model,  $P_{pf}$  has 1 h resolution and hence, it can not present the PV generation variabilities. Moreover, it is still exposed to uncertainties. Thus, the relative difference  $\lambda_i$  between the PV measurements and the point forecast generated by the regression tree is used to train the probabilistic forecast. Both of the PV measurements and the point forecasts provided to the probabilistic forecast model are of 1 min resolution. The point forecast is linearly interpolated to convert the forecast from 1 h to 1 min resolution.

The relative difference  $\lambda_i$  is classified to 8 categories  $i \in [1, \dots, 8]$ , representing the 8 levels of cloudiness  $[\frac{0}{8}, \dots, \frac{8}{8}]$ . Consequently, 8 cumulative distribution functions  $F_i(\lambda_i)$  are trained. Once the training is accomplished, the forecasted relative difference for a specific probability can be calculated as per Equation 3.5.

$$F^{-1}1_i(q) = \lambda_i, q \in Q = \{10\%, 20\%, \dots, 90\%\}. \quad (3.5)$$

The required probabilistic set of PV power forecast  $P_{pp}(tf)$  can then be calculated based on Equation 3.6.

$$p_{pp_q}(tf) = P_{pf}(tf) \times (1 - \lambda_i) \quad (3.6)$$

$$p_{pp_q}(tf) \in P_{pp}(tf) = \{p_{pp_{10\%}}(tf), p_{pp_{20\%}}(tf), \dots, p_{pp_{90\%}}(tf)\}.$$

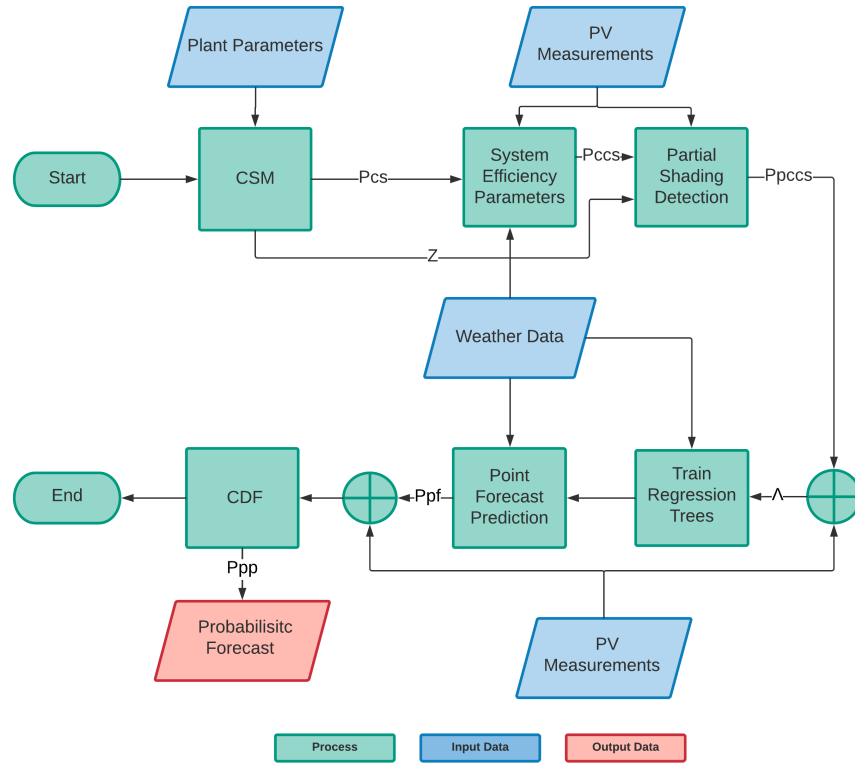


**Figure 3.2:** Simplified flow chart describing the process of probabilistic forecast generation [13].

The reason behind using CDFs to calculate the multiple curves of the probabilistic forecast is to have an intuitive simple integration of the forecast with an EMS. In buildings, an EMS does not require an exact PV forecast, but rather a probability guaranteeing specific power availability at certain time of the day to prioritize the devices scheduling, as discussed in Section 3.5.

The probabilistic forecast model was validated based on different standard metrics and probabilistic metrics as shown in [13]. Using the standard metrics, the results shows 15.3%, 8.5% and 1.56%, for the normalized root mean square error (RMSE), mean absolute error (MAE) and mean biased error (MBE), respectively. Using the probabilistic metric, the average cumulative ranked probability (CRPS) is as low as 5.56%, while the Brier score (BS) is 0.12. Yet, the real metric based on which the probabilistic forecast can be truly judged is the real life performance via integrating it in an EMS. Within the upcoming sections, such performance will be presented.

### 3.5 Loads planning

As the main goal is to evaluate the potential of the probabilistic forecast compared to the reference forecast under the same level of intelligence of the load shifting algorithm, an algorithm was implemented based on the exhaustive enumeration method to evaluate every possible combination of loads under the given PV generation conditions. Although the exhaustive enumeration method is computationally intensive, it can guarantee the highest potential results and can lead to a fair comparison between the reference and probabilistic forecast. Figure 3.3 shows a simplified flowchart of the load shifting algorithm including the probabilistic PV forecast. It starts with PV forecast profiles as discussed in the previous section, and the shiftable devices dataset. The shiftable devices dataset consists of the load profile of the device  $P_d(t)$ , earliest starting time, and latest ending time. If the earliest starting time and the latest ending time are not given, the algorithm optimizes by default over a 24-hour period, from 00:00 to 23:59.

Both PV forecast profiles and shiftable loads are sorted. The PV forecast profiles are sorted based on their probability of occurrence  $q$ , (i.e., 99% comes first in queue then followed by the lower probabilities). The shiftable devices are sorted based on a given criteria which vary depending on the required scenario.

- Power consumption  $\Rightarrow P_{d_1} > P_{d_2} > P_{d_3}$
- Duration of operation  $\Rightarrow Du_{d_1} > Du_{d_2} > Du_{d_3}$
- Interruptibility  $\Rightarrow In_{d_1} = 1 > In_{d_2} = 0$
- Probability of multiple usage  $\Rightarrow Pr_{d_1} > Pr_{d_2} > Pr_{d_3}$

$P_{d_1}$ ,  $Du_{d_1}$ ,  $In_{d_1}$ , and  $Pr_{d_1}$  represent the device with the highest power, longest duration, interruptibility option (Boolean), and highest probability of usage, respectively.

Within this contribution, the dominant criterion being applied is the power consumption, i.e. the highest power consuming device always has the first priority. As soon

as the devices are sorted, the residual load is calculated for every device under every probabilistic PV profile curve as per Equation 3.7 till a minimum is reached.

$$R_e(t) = P_L(t) - p_{pp,q}(t) \forall q \in Q. \quad (3.7)$$

Once a minimum is reached the algorithm starts to find a starting point for the next device in the queue until all devices are sorted under all the given probabilistic PV profile curves.

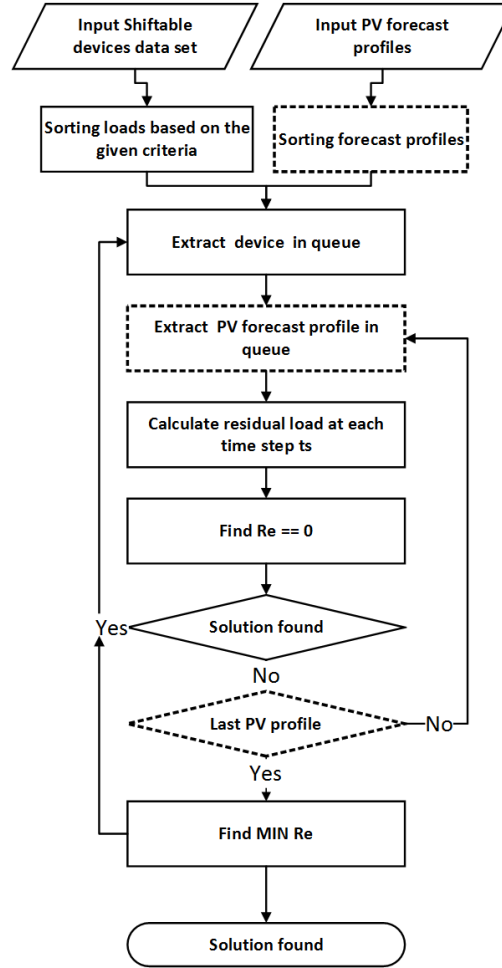


**Figure 3.3:** Flow chart of the load shifting algorithm.

The probability curves can be calculated for continuous range of probabilities, yet it was found in [49] that only  $q = \{70\%, 80\%, 90\%, 95\%, 99\%\}$  is of an interest for an EMS. Delivering other lower or continuous probability values would require the EMS to have a higher computational power and would not lead to better results.

In case of the reference forecast, the flow chart blocks with dashed lines shown in Figure 3.3 can be eliminated to operate in the conventional mode without any probabilistic

forecast. Thus, it can be assumed that the two algorithms have the same level of intelligence, as both use the same optimization technique with the difference being only in the type of forecast used, whether it is the reference or the probabilistic forecast. Thus, it should be considered that any other DSM algorithm could also be implemented given that devices are shifted not only on a single given PV forecast profile, but on multiple probabilistic PV forecast profiles

### 3.6 Evaluation metrics

To compare the potential of DSM with a probabilistic forecast to a reference conventional forecast, both strategies have to be evaluated under the same metrics. For a PV system within a household, self-consumption and self-sufficiency are two of the commonly used metrics [50]. Self-consumption is defined as the ratio of the self-consumed energy,  $E_{sc}$ , relative to the total production of the PV system, which is the summation of the self-consumed energy,  $E_{sc}$ , and the energy fed-in to the grid,  $E_f$ , as shown in Equation 3.8.

$$e_{sc} = \frac{E_{sc}}{E_f + E_{sc}}. \quad (3.8)$$

Self-sufficiency is the other metric used to show the sufficiency of the PV generation to the consumers' needs. Thus, it is defined as the ratio of  $E_{sc}$  to the summation of  $E_{sc}$  and the energy imported from the grid,  $E_g$ , as shown in Equation 3.9.

$$e_{ss} = \frac{E_{sc}}{E_g + E_{sc}}. \quad (3.9)$$

Using those two metrics, a proper indication of the used DSM algorithm and PV prediction efficiency can be obtained. Consequently, another metric is  $e_w$ , defined as the ratio between self-consumption and self-sufficiency as shown in Equation 3.10.

$$e_w = \frac{e_{sc}}{e_{ss}}. \quad (3.10)$$

In Equations 3.8 and 3.9,  $E_{sc}$  can be calculated by defining the overlapping profile  $O(t)$  between the generation  $G(t)$  and the load  $L(t)$  profiles. Consequently,  $O(t)$  is defined as the minimum of  $G(t)$  and  $L(t)$  as shown in Equation 3.11, since self-consumption will always be limited to the minimum of the load and the generation, whichever is lower.

$$O(t) = \min(L(t), G(t)). \quad (3.11)$$

Accordingly,  $e_{sc}$  and  $e_{ss}$  can be mathematically formulated as in Equation 3.12 and 3.13.

$$e_{ss} = \frac{\int_{t_1}^{t_2} O(t) dt}{\int_{t_1}^{t_2} G(t) dt}. \quad (3.12)$$

$$e_{sc} = \frac{\int_{t_1}^{t_2} O(t) dt}{\int_{t_1}^{t_2} L(t) dt}. \quad (3.13)$$

### *A.3 Publication 3*

Substituting Equations 3.12 and 3.13 in Equation 3.10, the ratio of generation to load can be determined. Therefore, this metric can be also used to indicate whether there is a sufficient generation capacity or not.

## 4 Results and Analyses

Two cases are considered. In the first case, a smart home is considered with the conventional white goods loads. In the second case, multiple generic loads of different sizes are used along with the 3 kWp PV system. The time horizon of the analysis is 66 days (07.07.2015 till 29.09.2015) due to the limited availability of the reference forecast data. This time horizon represents mostly the summer season, which is the worst case for the analysis of the potential of a PV probabilistic forecast, as most of the days are sunny and the PV generation variability is lower than other seasons of the year. In the two cases, the shifting time frame of the loads has been set to 24 hours, so that the maximum potential of the DSM can be calculated without the influence of any time constraints or the user behavior.

### 4.1 Case 1: DSM of Conventional white goods

In this case, the worst case scenario of a smart home is considered, where there is a low number of smart shiftable devices. In this smart home, only a dishwasher, a dryer, and a washing machine are considered as shiftable devices. The rest of the loads are considered fixed. Table 4.1 details the considered loads along with their share in the overall household energy consumption. In this case, the smart home is of a single family of two persons, the total shiftable devices' energy consumption is 40.9% of the overall energy consumption in typical days according to [51].

**Table 4.1:** Energy consumption of a single family household (2 persons) on a typical work day (Mon.-Fri.) [51].

<i>Shiftable devices</i>		
Washing Machine	926	10.3
Dryer	1612	18.0
Dishwasher	1121	12.5
Total (Shiftable)	3659	40.9
<i>Fixed Loads</i>		
Stove	672	7.5
Microwave	48	0.5
Refrigerator and freezer	1119	12.5
Multimedia (TV, PC, etc.)	2147	24.0
Light	1307	14.6
Total (Fixed)	5294	59.1

Within the analysis, fixed loads are ignored, and only the shiftable devices are considered. Figure 4.1 shows the difference between the DSM using the reference forecast and the DSM using the probabilistic forecast. In Figure 4.1(a), the white goods were sorted under the day-ahead reference PV forecast, such that  $R_e(t)$  is minimized and the earliest end time is reached. Consequently, all the devices were stacked consecutively between 06:30 and 12:00. Although the reference PV forecast can give a proper indication about the maximum PV generation within the day, it could not yet predict the high variability of the PV power generation under the weather conditions of that day. However, with the probabilistic forecast in Figure 4.1(b), the devices were sorted based on the certainty of the generation. The dishwasher and the dryer were placed under the  $q = 99\%$  curve, while the washing machine was placed under the  $q = 70\%$  curve. This is because it could not be set under any curve with a higher probability due to its high 2 kW peak.

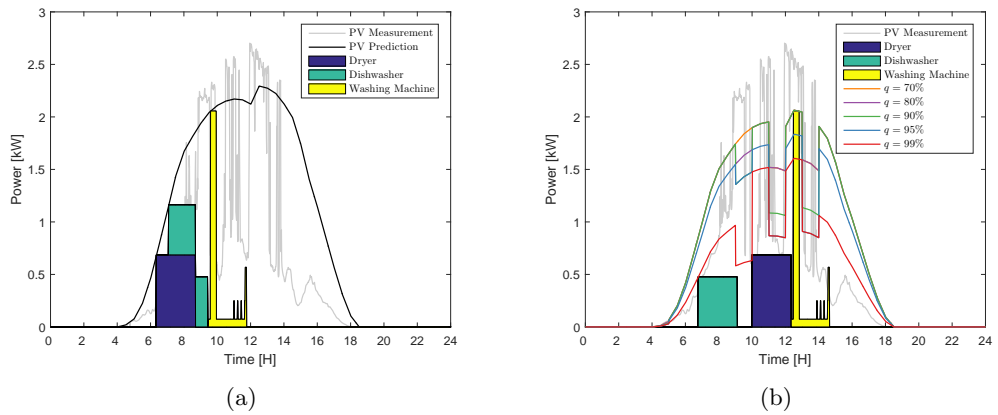


**Figure 4.1:** Comparison between the reference and the probabilistic on a typical day. White goods optimal shifted based on (a) reference forecast, and (b) probabilistic forecast.

Evaluating the fixed load profile of the given single family house, along with the shiftable devices under the metrics given in Section 3.6, reveals that using DSM along with the probabilistic forecast led to a higher self-sufficiency and a higher self-consumption compared to a DSM with the reference forecast or without using DSM at all, as shown in Figure 4.2. The difference between the median of the self-sufficiency and the self-consumption of the DSM using the two forecasting methods is 9.1% and 5.0%, respectively. Higher values can be reached if more shiftable devices are going to be integrated, but in this case only a washing machine, dishwasher and dryer were considered. Those devices have a low energy consumption and power peak, consequently having them optimally shifted did not make a significant difference. Thus, these results represent the worst case outcome of using the probabilistic forecast. It can only be seen in Figure 4.2 that the minimum and maximum of the self-consumption is higher for the probabilistic forecast. Yet in case of the self-sufficiency the minimum and maximum values of the two forecasts are rather almost equal due to availability of sunny days and full cloudy days where the performance of the two forecasts is similar using the self-sufficiency metric.

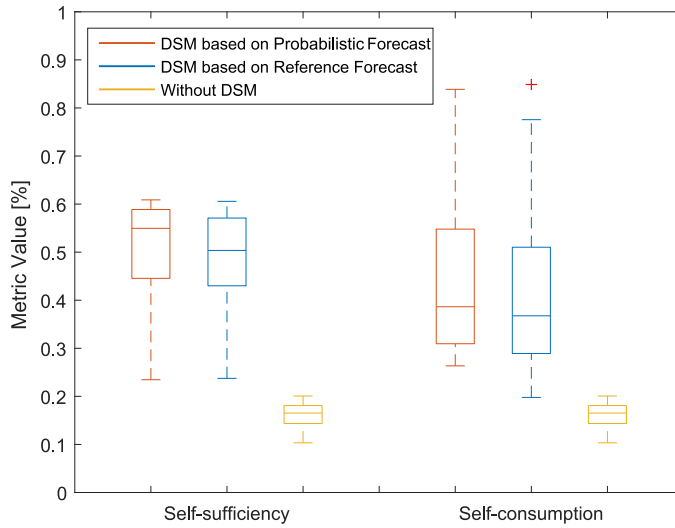


**Figure 4.2:** Effect of applying DSM using probabilistic forecast and reference forecast on a typical single family house.

## 4.2 Case 2: Different generic load sizes covered by a 3 kWp PV system

Generic loads were created of sizes 0.25 kW up to 1.5 kW and operated for a constant time of 1-hour using the same day presented in Figure 4.1. Consequently, energy blocks were created that vary from 0.25 kWh to 1.5 kWh. These blocks can represent any of the current smart shiftable devices such as a heat pump or an EV, and also can provide insight into the behavior of the DSM under the influence of possible future shiftable loads. The number of load blocks (devices) within the analysis was limited to 60 for the 0.25 kW loads, 30 for the 0.5 kW and 1.0 kW loads, and 15 for the 1.5 kW loads to evaluate the difference between the reference and the probabilistic forecast based on the metrics given in Section 3.6.

Figure 4.3 shows how the different probabilistic PV load profiles are packed with different generic load block sizes of 0.25 kW, 0.5 kW, 1 kW and 1.5 kW. The generic load blocks were set according to the algorithm presented in Section 3.5, where every block had a possible shifting time window of 24 hours to eliminate the time as a constraint. In Figures 4.3(a), 4.3(b), 4.3(c), and 4.3(d), it can be seen that the first 10 generic loads are sorted under the curve of the highest probability of occurrence  $q = 99\%$ , and the first device comes to operation first, followed by the rest of the devices. In Figure 4.3(a), as an example, the first device comes to operation at 06:30 under the highest probabilistic curve, which fits with the PV measurement. The 50th to 60th loads were accumulated on the lower probability curves. As a result, it can be seen that the algorithm is accumulating the loads from the center outward depending on the probabilistic

forecast curves given. Comparing the behavior of the algorithm in Figure 4.3 to Figure 4.4, it can be noticed that the scheme of sorting is from left to right, where the device that comes first operates first. Additional loads were placed anywhere else in the curve trying to minimize the residual load according to Section 3. The behavior of the DSM algorithm under the reference forecast led to misplacement of shiftable devices in areas where PV generation is rather low and fluctuating, due to the lack of the reference forecast ability to capture the behavior of the PV generation variability. Thus, applying the reference (conventional) forecast leads to a significant decrease in the self-sufficiency, self-consumption and consequently the overall energy bill of the consumer.

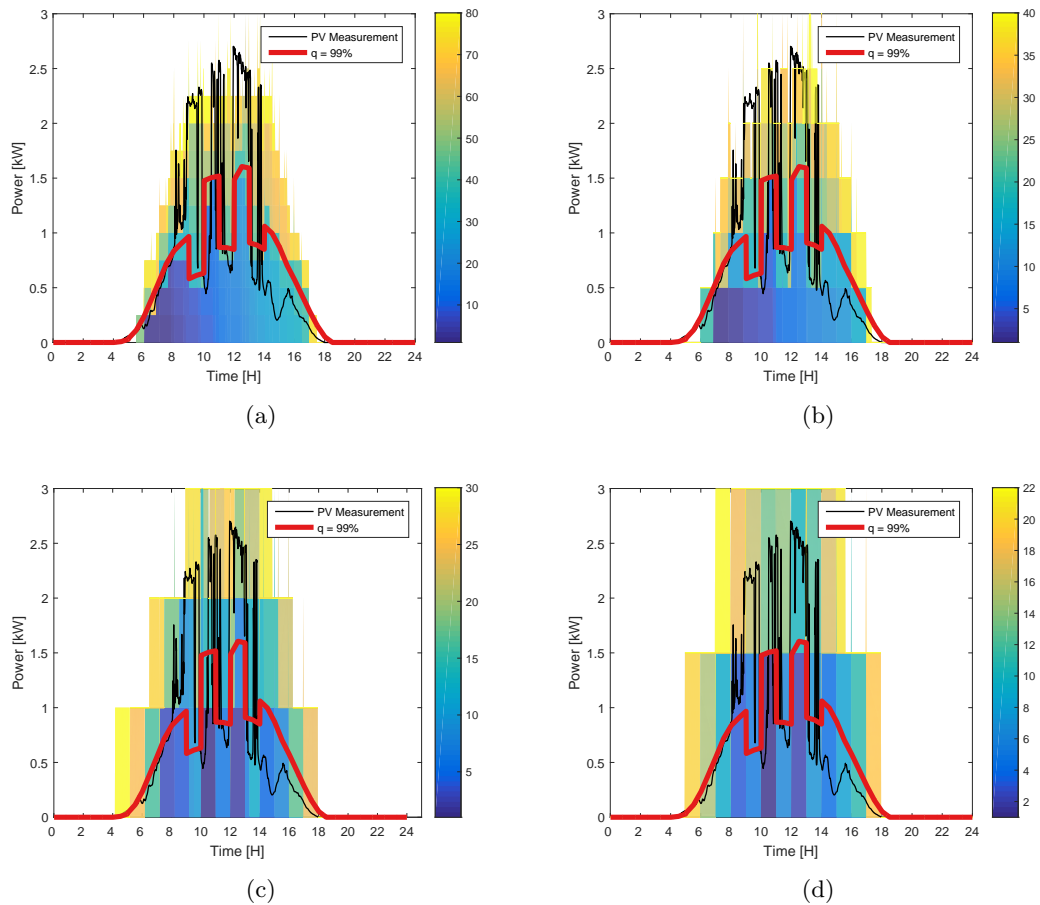


**Figure 4.3:** Different generic loads sizes shifted based on the probabilistic forecast - number of loads (colored). (a) 0.25 kW. (b) 0.5 kW. (c) 1 kW. (d) 1.5 kW.

## A Appendix

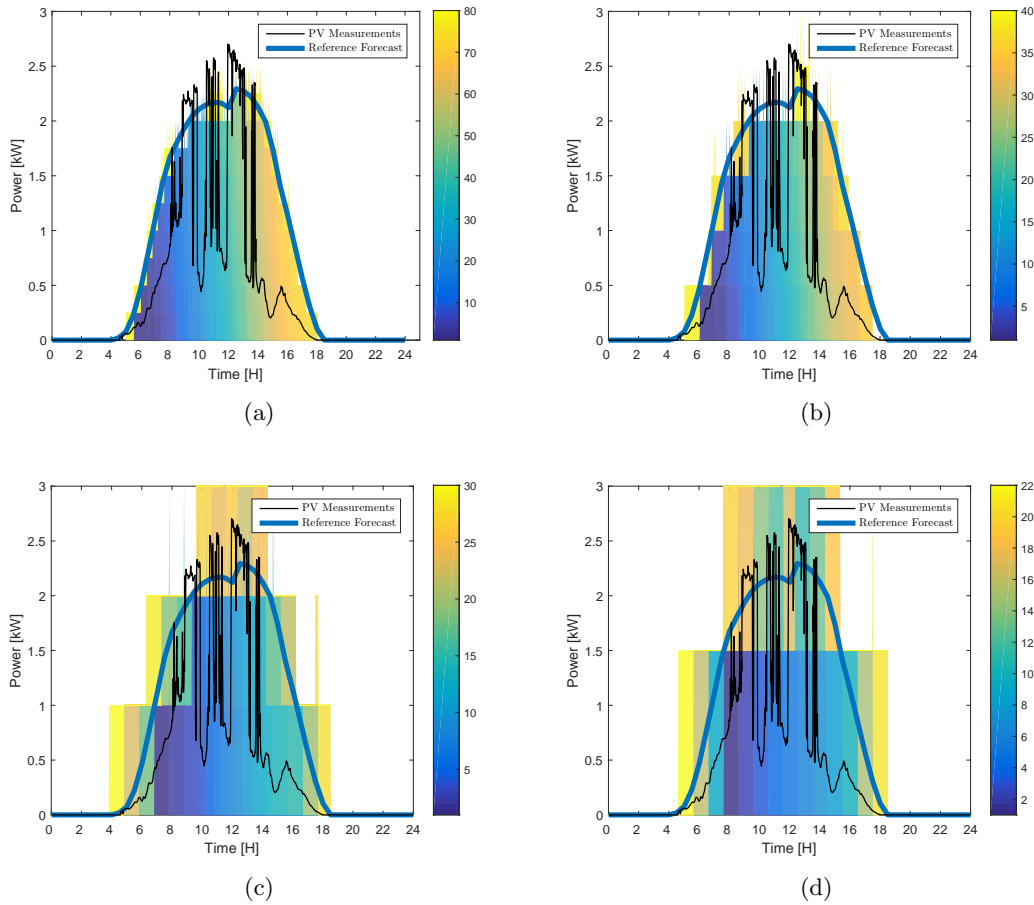


**Figure 4.4:** Different generic loads sizes shifted based on the reference forecast - number of loads (colored). (a) 0.25 kW. (b) 0.5 kW. (c) 1 kW. (d) 1.5 kW.

Figure 4.5 shows that the maximum mean self-sufficiency is 24.2% higher for the 0.25 kW load blocks with the probabilistic forecast than the reference forecast. As the number of devices increases under the 3 kWp PV curve, the difference between the reference and the probabilistic forecast decreases due to parallel decrease of the load shifting potential.

As the size of the load block increases, the load shifting potential decreases as well, leading to a smaller difference between the probabilistic forecast and the reference forecast. Hence, under a 3 kWp PV curve for the 0.5 kW blocks, the number of devices is limited to 25, for the 1 kW blocks it is 10, and for the 1.5 kW it is 6 devices. Yet, in all the cases, the probabilistic forecast successfully exceeds the performance of the reference forecast using the same level of intelligence of the DSM algorithm.

In Figure 4.6, mean self-consumption metric was used to compare the probabilistic forecast to the reference forecast. Focusing on the 0.25 kW and the 0.5 kW load block type, it can be noticed that the maximum mean self-consumption is 17.7% and 16.2% higher, respectively. As the number of devices increases or the load block size increases, the

difference of mean self-consumption between the probabilistic forecast and reference decreases. The reason behind this behavior is the ratio of the energy self-consumed to the overall energy generated. At higher loads, the ratio between the energy self-consumed to the overall energy generated is already high. As a result, the effect of the probabilistic forecast diminishes, due to the lack of generated energy compared to the load.

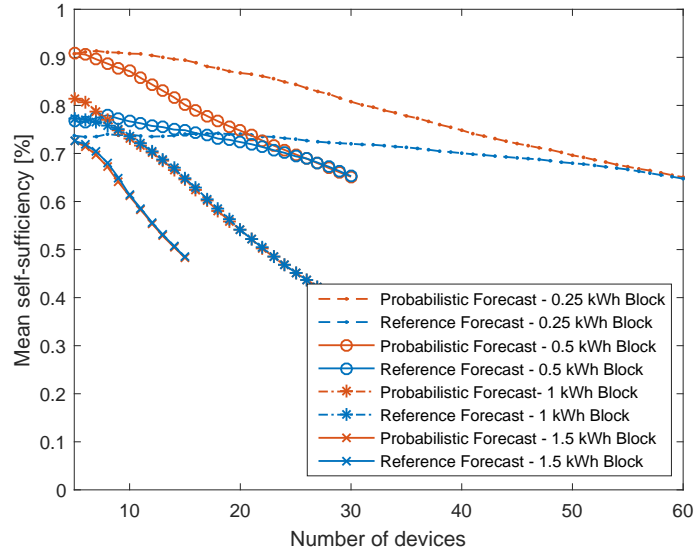


Figure 4.5: Mean self-sufficiency for different number of devices.

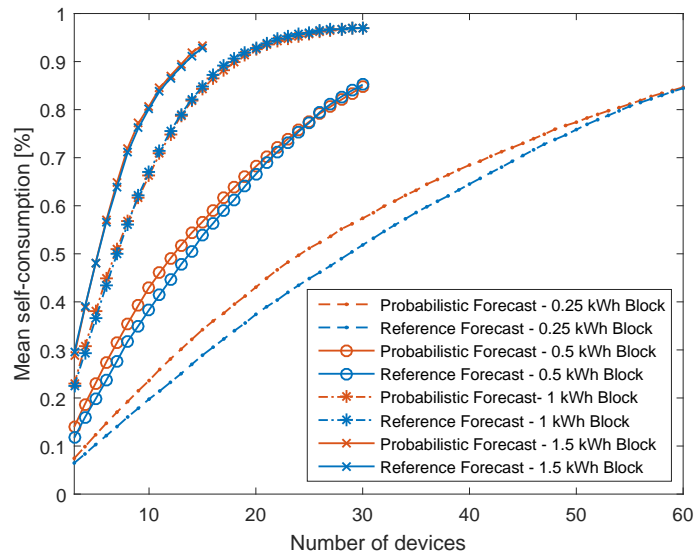
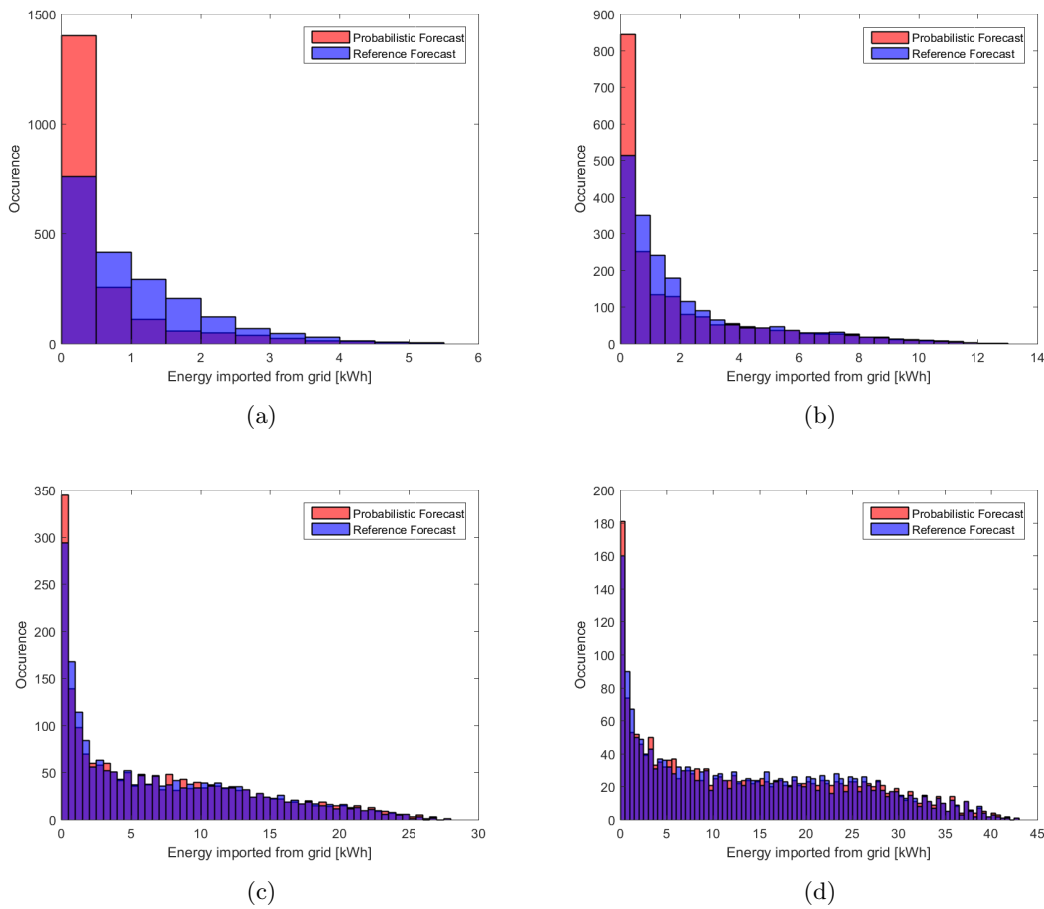


Figure 4.6: Mean self-consumption for different number of devices.

## A Appendix

Investigating only the energy imports as per Figure 4.7, it can be noticed that in all the cases of different block sizes, the highest number of occurrences of minimal energy imports is always achieved by the probabilistic forecast, but not by the reference forecast. In Figure 4.7(a), the highest number of occurrences is between 0 and 0.5 kW, where the probabilistic forecast significantly exceeds the reference forecast. The number of occurrences is 1402 for the probabilistic forecast versus 761 for the reference forecast, which means using the probabilistic forecast leads to decreasing the energy imports to values between 0 and 0.5 kW significantly. Between 0.5 to 5.5 kW, the probabilistic forecast has always a lower number of occurrences than the reference forecast, which confirms the ability of the probabilistic forecast to minimize energy imports. As the size of the load blocks increases, the same pattern of occurrences can be witnessed, but with a decreased magnitude, as shown in Figure 4.7(b), 4.7(c), and 4.7(d).



**Figure 4.7:** Histograms of energy imports of different block sizes. (a) 0.25 kW. (b) 0.5 kW. (c) 1 kW. (d) 1.5 kW.



## 5 Conclusions

This contribution presented the output of a numerical study based on real-measurements that analyzed the potential of using probabilistic forecast to enhance the performance of DSM within households. Three metrics were used to evaluate the difference between the potential of the probabilistic forecast and the reference deterministic forecast along with an optimal DSM algorithm: the self-consumption, self-sufficiency, and the ratio of the self-consumption to the self-sufficiency. A major finding is that the probabilistic forecast can significantly enhance the performance of DSM algorithms within households compared to the reference deterministic forecast. The significance of such performance enhancement varies depending on the available PV generation and shiftable loads within the household, yet the probabilistic forecast always guarantees a better performance compared to the given reference forecast. Two cases were presented and can be concluded in the following:

- In the first case, only shiftable white goods were considered as the worst case scenario of a single family household. The difference in median of self-sufficiency and self-consumption between the DSM with the probabilistic forecast and the DSM with the reference forecast was 9.1% and 5.0%, respectively.
- In the second case, multiple generic loads were used to evaluate the sensitivity of the DSM with each forecasting method against a different number of devices of different load sizes. The results emphasize that the DSM with probabilistic forecast can lead to an increase in self-sufficiency and self-consumption by 24.2% and 17.7%, respectively.

Consequently, it can be concluded that probabilistic forecast can enhance the DSM algorithms' performance under different possible load-generation configuration within the household. Moreover, it can decrease the burden of attaching additional batteries to the household to make up for the forecasting errors.



## Bibliography

- [1] R. Wüstenhagen and M. Bilharz. Green energy market development in Germany: effective public policy and emerging customer demand. *Energy Policy*, 34(13):1681–1696, 2006. doi:10.1016/j.enpol.2004.07.013.
- [2] Federal Ministry for Economic Affairs and Energy. Renewable Energy Sources in Figures. *National and Interantional Developments*, page 84, 2015.
- [3] H. Maron, H. Klemisch, and B. Maron. Marktakteure erneuerbare Energie-Anlagen in der Stromerzeugung. (August):1–92, 2011.
- [4] N. Nikmehr, S. Najafi-Ravadanegh, and A. Khodaei. Probabilistic optimal scheduling of networked microgrids considering time-based demand response programs under uncertainty. *Applied Energy*, 198:267–279, 2017. doi:10.1016/j.apenergy.2017.04.071.
- [5] B. Zhou, W. Li, K. W. Chan, Y. Cao, Y. Kuang, X. Liu, and X. Wang. Smart home energy management systems: Concept, configurations, and scheduling strategies. *Renewable and Sustainable Energy Reviews*, 61:30–40, 2016. doi:10.1016/j.rser.2016.03.047.
- [6] M. Shakeri, M. Shayestegan, H. Abunima, S. M. S. Reza, M. Akhtaruzzaman, A. R. M. Alamoud, K. Sopian, and N. Amin. An intelligent system architecture in home energy management systems (HEMS) for efficient demand response in smart grid. *Energy and Buildings*, 138:154–164, 2017. doi:10.1016/j.enbuild.2016.12.026.
- [7] B. Celik, R. Roche, S. Suryanarayanan, D. Bouquain, and A. Miraoui. Electric energy management in residential areas through coordination of multiple smart homes. *Renewable and Sustainable Energy Reviews*, 80(May):260–275, 2017. doi:10.1016/j.rser.2017.05.118.
- [8] Lehrstuhl für Energiewirtschaft und Anwendungstechnik. e-MOBILie - Schaufenster Elektromobilität. URL: <http://www.ewk.ei.tum.de/forschung/projekte/e-mobilie/>.
- [9] W. El-Baz, C. Kandler, P. Wimmer, and P. Tzscheuschler. Practical experiences with smart homes modelling and simulati. In *ESI SimulationX User Forum*, Dres, 2016. ESI ITI.

- [10] W. El-Baz and P. Tzscheuschler. Co-simulation of a smart home model based on a micro electricity market. *Proceedings of the Fifth German-Austrian IBPSA Conference RWTH Aachen University*, pages 30–37, 2014.
- [11] R. Hanna, J. Kleissl, A. Nottrott, and M. Ferry. Energy dispatch schedule optimization for demand charge reduction using a photovoltaic-battery storage system with solar forecasting. *Solar Energy*, 103:269–287, 2014. doi:10.1016/j.solener.2014.02.020.
- [12] A. L. Klingler and L. Teichtmann. Impacts of a forecast-based operation strategy for grid-connected PV storage systems on profitability and the energy system. *Solar Energy*, 158(July):861–868, 2017. doi:10.1016/j.solener.2017.10.052.
- [13] W. El-Baz, P. Tzscheuschler, and U. Wagner. Day-ahead Probabilistic PV Generation Forecast for Buildings Energy Management Systems (Under Review).
- [14] I. Lampropoulos, W. L. Kling, P. F. Ribeiro, and J. van den Berg. History of demand side management and classification of demand response control schemes. *2013 IEEE Power & Energy Society General Meeting*, pages 1–5, 2013. doi:10.1109/PESMG.2013.6672715.
- [15] C. Gellings. The concept of demand-side management for electric utilities. *Proceedings of the IEEE*, 73(10):1468–1470, 1985. doi:10.1109/PROC.1985.13318.
- [16] G. Strbac. Demand side management: Benefits and challenges. *Energy Policy*, 36(12):4419–4426, 2008. doi:10.1016/j.enpol.2008.09.030.
- [17] A. F. Meyabadi and M. H. Deihimi. A review of demand-side management: Reconsidering theoretical framework. *Renewable and Sustainable Energy Reviews*, 80(January 2016):367–379, 2017. doi:10.1016/j.rser.2017.05.207.
- [18] P. Finn, M. O’Connell, and C. Fitzpatrick. Demand side management of a domestic dishwasher: Wind energy gains, financial savings and peak-time load reduction. *Applied Energy*, 101:678–685, 2013. doi:10.1016/j.apenergy.2012.07.004.
- [19] B. Jiang, A. Muzhikyan, A. M. Farid, and K. Youcef-Toumi. Demand side management in power grid enterprise control: A comparison of industrial & social welfare approaches. *Applied Energy*, 187:833–846, 2017. doi:10.1016/j.apenergy.2016.10.096.
- [20] S. Gottwalt, W. Ketter, C. Block, J. Collins, and C. Weinhardt. Demand Side Management : A simulation of household behavior under variable prices. *Energy Policy*, 39(12):8163–8174, dec 2011. doi:10.1016/j.enpol.2011.10.016.
- [21] F. Yang and X. Xia. Techno-economic and environmental optimization of a household photovoltaic-battery hybrid power system within demand side management. *Renewable Energy*, 108:132–143, 2017. doi:10.1016/j.renene.2017.02.054.

- [22] A. Arteconi, E. Ciarrocchi, Q. Pan, F. Carducci, G. Comodi, F. Polonara, and R. Wang. Thermal energy storage coupled with PV panels for demand side management of industrial building cooling loads. *Applied Energy*, 185:1984–1993, 2017. doi:10.1016/j.apenergy.2016.01.025.
- [23] H. Shi, N. Blaauwbroek, P. H. Nguyen, and R. I. G. Kamphuis. Energy management in Multi-Commodity Smart Energy Systems with a greedy approach. *Applied Energy*, 167:385–396, 2016. doi:10.1016/j.apenergy.2015.11.101.
- [24] E. Matallanas, M. Castillo-Cagigal, A. Gutierrez, F. Monasterio-Huelin, E. Caamano-Martin, D. Masa, and J. Jimenez-Leube. Neural network controller for Active Demand-Side Management with PV energy in the residential sector. *Applied Energy*, 91(1):90–97, 2012. doi:10.1016/j.apenergy.2011.09.004.
- [25] E. Galvan-Lopez, T. Curran, J. McDermott, and P. Carroll. Design of an autonomous intelligent Demand-Side Management system using stochastic optimisation evolutionary algorithms. *Neurocomputing*, 170:270–285, 2015. doi:10.1016/j.neucom.2015.03.093.
- [26] X. Yang, Y. Zhang, B. Zhao, F. Huang, Y. Chen, and S. Ren. Optimal energy flow control strategy for a residential energy local network combined with demand-side management and real-time pricing. *Energy and Buildings*, 2017. doi:10.1016/j.enbuild.2017.05.076.
- [27] Z. Wu, H. Tazvinga, and X. Xia. Demand side management of photovoltaic-battery hybrid system. *Applied Energy*, 148:294–304, 2015. doi:10.1016/j.apenergy.2015.03.109.
- [28] a. Barbato and G. Carpentieri. Model and algorithms for the real time management of residential electricity demand. *2012 IEEE International Energy Conference and Exhibition (ENERGYCON)*, pages 701–706, sep 2012. doi:10.1109/EnergyCon.2012.6348242.
- [29] R. Perez, M. David, T. E. Hoff, M. Jamaly, S. Kivalov, J. Kleissl, P. Lauret, and M. Perez. Spatial and Temporal Variability of Solar Energy. *Foundations and Trends® in Renewable Energy*, 1(1):1–44, 2016. doi:10.1561/27000000006.
- [30] C. Rigollier, O. Bauer, and L. Wald. Radiation Atlas With Respect To the Heliosat Method. *Solar Energy*, 68(1):33–48, 2000. doi:10.1016/S0038-092X(99)00055-9.
- [31] P. Ineichen. Comparison of eight clear sky broadband models against 16 independent data banks. *Solar Energy*, 80(4):468–478, 2006. doi:10.1016/j.solener.2005.04.018.
- [32] R. W. Mueller, K. F. Dagestad, P. Ineichen, M. Schroedter-Homscheidt, S. Cros, D. Dumortier, R. Kuhlemann, J. A. Olseth, G. Piernavieja, C. Reise, L. Wald, and D. Heinemann. Rethinking satellite-based solar irradiance modelling: The

- SOLIS clear-sky module. *Remote Sensing of Environment*, 91(2):160–174, 2004. doi:10.1016/j.rse.2004.02.009.
- [33] R. H. Inman, H. T. C. Pedro, and C. F. M. Coimbra. Solar forecasting methods for renewable energy integration. *Progress in Energy and Combustion Science*, 39(6):535–576, 2013. doi:10.1016/j.pecs.2013.06.002.
- [34] T. E. Hoff and R. Perez. Quantifying PV power Output Variability. *Solar Energy*, 84(10):1782–1793, 2010. doi:10.1016/j.solener.2010.07.003.
- [35] Einleitung. In *Meteorologie und Klimatologie*, pages 1–4. Springer Berlin Heidelberg, Berlin, Heidelberg. doi:10.1007/978-3-540-37222-6\_1.
- [36] R. Perez, T. Hoff, J. Dise, D. Chalmers, and S. Kivalov. The cost of mitigating short-term PV output variability. *Energy Procedia*, 57:755–762, 2014. doi:10.1016/j.egypro.2014.10.283.
- [37] R. Perez, S. Kivalov, J. Schlemmer, K. Hemker, and T. E. Hoff. Short-term irradiance variability: Preliminary estimation of station pair correlation as a function of distance. *Solar Energy*, 86(8):2170–2176, 2012. doi:10.1016/j.solener.2012.02.027.
- [38] G. M. Lohmann, A. H. Monahan, and D. Heinemann. Local short-term variability in solar irradiance. *Atmospheric Chemistry and Physics*, 16(10):6365–6379, 2016. doi:10.5194/acp-16-6365-2016.
- [39] B. L. Norris and T. E. Hoff. Determining storage reserves for regulating solar variability. *Electrical Energy Storage Applications and Technologies Biennial International Conference*, (7), 2011.
- [40] T. E. Hoff and R. Perez. Quantifying PV power Output Variability. *Solar Energy*, 84(10):1782–1793, 2010. doi:10.1016/j.solener.2010.07.003.
- [41] S. Pelland, J. Remund, J. Kleissl, T. Oozeki, and K. D. Brabandere. Photovoltaic and Solar Forecasting: State of the Art. Technical report, International Energy Agency, 2013. doi:978-3-906042-13-8.
- [42] R. Haider and C.-H. Kim. *Integration of Distributed Energy Resources in Power Systems*. 2016. doi:10.1016/B978-0-12-803212-1.00007-6.
- [43] E. Lorenz, J. Remund, S. C. Müller, W. Traunmüller, G. Steinmaurer, D. Pozo, J. Antonio, V. L. Fanego, L. Ramirez, M. G. Romeo, C. Kurz, L. M. Pomares, and C. G. Guerrero. Benchmarking of different approaches to forecast solar irradiance. *24th European photovoltaic solar energy conference*, pages 25–34, 2009. doi:10.4229/24thEUPVSEC2009-5BV.2.50.
- [44] W. El-Baz, J. Honold, L. Hardi, and P. Tzscheutschler. High-resolution dataset for building energy management systems applications. *Data in Brief*, 54:1–5, 2018. doi:10.1016/j.dib.2017.12.058.

## A Appendix

- [45] C. Hainzinger, H. Martin, and K. Strasser. PV-Energy Monitoring and Prediction. Technical report, Institute for Energy Economy and Application Technology, Technical University of Munich, Munich, 2015. URL: [www.smartup.ei.tum.de](http://www.smartup.ei.tum.de).
- [46] Meteoblue.com. Meteoblue-Weather Forecast.
- [47] H. Malberg. Meteorologie und Klimatologie. page 354, 2007. doi:10.1007/978-3-662-22158-7\_7.
- [48] R. Bird and R. Hulstrom. Simplified clear sky model for direct and diffuse insolation on horizontal surfaces, 1981. doi:10.2172/6510849.
- [49] M. Seufzger. *Evaluation and Optimization of an Energy Management System based on PV Prediction Certainty (master's thesis)*. Technical University of Munich, Munich, 2017.
- [50] R. Luthander, J. Widen, D. Nilsson, and J. Palm. Photovoltaic self-consumption in buildings: A review. *Applied Energy*, 142:80–94, 2015. doi:10.1016/j.apenergy.2014.12.028.
- [51] I. Richardson, M. Thomson, D. Infield, and C. Clifford. Domestic electricity use: a high-resolution energy demand model. *Energy and Buildings*, 2010.

## **A.4 Publication 4 — Integration of Energy Markets in Microgrids: A Double-Sided Auction with Device-Oriented Bidding Strategies**

### **Abstract**

Energy trading markets are one of the most viable solutions to incentivize prosumers in Microgrids. They offer the utility a versatile access for flexible loads coordination without violating consumer privacy. In the literature, several models and designs were presented to address different aspects of energy trading markets, yet there is a gap between these models and their application in real-life. This paper describes a novel discrete-timely double-sided auction model that facilitates energy trading between prosumers in near real-time and forward markets. Since the practical realization of the model represents a crucial criterion, the market is designed with fast clearing mechanism and simple bidding rules that guarantee the benefits of the prosumers, their privacy, and consider their personal preferences. Additionally, a decentralized home energy management approach is followed at the prosumer level to maximize the system reliability and enable an easy integration of multiple devices from different manufacturers. Hence, a device-oriented bidding strategy is demonstrated that considers the physical characteristics and technical limitations of each device type such as electric vehicles (EV), micro-combined heat and power systems (micro-CHP) or heat pumps. Furthermore, an open-source day-ahead probabilistic forecast for the photovoltaic systems (PV) is integrated with a bidding scheme that maximizes the prosumers' commitment in the forward market. In the results, field measurements and testbed data are used to quantify the benefits of the market model to the utility and the prosumers based on different metrics such as self-sufficiency, self-consumption, peak load, CO<sub>2</sub> emission reduction, and total costs. The results indicate that the market model can increase self-sufficiency and self-consumption of a microgrid while reducing the prosumer costs on average by 23%.

### **Author Contribution**

I developed the market model and wrote the paper; Peter Tzscheutschler and Ulrich Wagner provided guidance in the model conception, revised the paper and prepared a detailed critical review.

# 1 Introduction

The power grid in Germany has been undergoing substantial transitions since the legislative support for the energy transition plan (Energiewende) was passed in late 2010 [1]. The legislation proposed strategies to increase the renewable energy resources share in energy production and energy efficiency [2]. According to [3], the renewable energy share should represent 60% and 80% of the gross final energy consumption and electricity consumption, respectively. Furthermore, primary energy consumption should be reduced by 20% by 2020 and 50% by 2050. Fixed financial incentives were introduced to renewable energy resources (RES) to deliver on these goals. Additionally, a priority was given to feeding renewable sources in the electricity grid, in order to provide a risk-free environment for investors and new market entrants [4]. Looking at the impact of these policies, renewable energy represented 31.7% of gross electricity consumption and a capacity of 103.6 GW in 2016, compared to 4.2 GW in 1990 [5]. These investments in RES were not led just by the electric power industry, but also by households and small-scale consumers. In 2016, households and farms investments share in RES reached 42.5% [6]. Consequently, traditional inelastic consumers are gradually transforming into prosumers and the power flow in the grid is no longer unidirectional, but bidirectional.

Conventional grid control methods are outdated given the constraints of the bidirectional flow and the weather-dependent variability of the integrated renewable energy resources. Control of both the generation and demand side is seen as essential for maintaining the stability of the grid. Consequently, demand-side management (DSM) strategies were proposed and evaluated by several researchers to shed or shift consumer loads to serve various goals such as minimizing costs, CO<sub>2</sub> emission or peak loads [7, 8, 9, 10, 11].

Home Energy Management Systems (HEMS) are seen as the key solution that enables a DSM in microgrids and households. A HEMS is considered the main communication and control gateway between the device, prosumer, and the utility. Various research projects discussed the optimization techniques and algorithms needed to be deployed in the HEMS. Examples of these techniques and algorithms are stochastic optimization [12], mixed integer quadratic programming [13], mixed integer linear programming (MILP) [7, 14], fuzzy logic [9, 15, 16], and other machine learning techniques [15, 17]. Over the last decade, the optimization techniques employed in HEMS applications did not vary, as much as the use-cases on which the model is based. However, several challenges arise when moving from the simulation and modeling environment to the real-life environment. On the utility-side, these challenges relate to scalability, decision decentralization, and guaranteeing the prosumers' reaction; on the prosumer-side, data privacy and fair division of the economic benefit.

At first, a HEMS reacting to real-time price signals seemed to be the optimal solution for solving the challenges faced both the utility and the prosumer. In such a system,

the utility sends a real-time price signal (RTP) that drives the prosumers to shift their load from peak hours to off-peak hours. HEMS load shifting and economic potential were studied from different perspectives and household configurations as in [14, 18, 19]. These studies and models did address and solve the challenges represented by scalability, decision decentralization, and data privacy, but they did not guarantee the prosumers' reaction to the signal. Assuming that each household has a HEMS that operates autonomously, all the prosumers might switch on their loads or feed energy to the grid at almost the same time. Consequently, the overall results would be the formation of a higher peak at another point in time. Moreover, on the prosumer-side, another challenge was revealed, which is the need for decentralization at the household level as discussed in [8] and the e-MOBILie Project [20]. Device manufacturers would not allow direct access to the household device if the device guarantee was to be maintained, especially for EVs. Consequently, another architecture was developed based on the RTP that enables decentralized HEMS, where the device handles the decision-making process itself. In this case, the HEMS is used only for communicating the user preferences and initiating the optimization process. Figure 1.1 (left) shows the difference between the centralized HEMS and the decentralized HEMS, where I/O is the switching signal forwarded to the device.

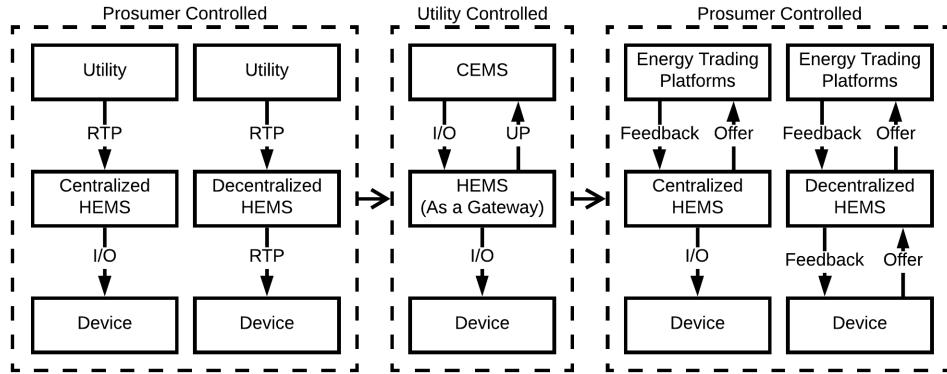


**Figure 1.1:** Development trends of energy management methods in the literature.

At the level of an island or grid-connected microgrids, central energy management system (CEMS), which is also referred to as local energy management system (LEMS), was introduced. The CEMS receives all the user preferences (UP) of all prosumers within the microgrid, then tries, based on the algorithms mentioned earlier, to achieve an optimum plan. Such a system can maximize the economic benefits, satisfy the prosumers' constraints, and exploit the maximum flexibility potential. Nevertheless, since the CEMS receives all the user information to start the optimization iterations, it violates the data privacy regulations and exhibits a limited scalability [21, 22]. The HEMS, in this case, acts as a gateway. It provides the UP and receives the switching plan of the given devices. Figure 1.1 (middle) shows the communication architecture between the HEMS and the CEMS.

Energy trading platforms and market models are the decentralized energy manage-

ment systems at the microgrid level. They are not only meant for energy trading but also for coordination of the microgrid as discussed in [23]. These platforms solve the privacy challenges faced by the CEMS as they handle the decision-making process without exchanging any detailed information (e.g., EV start time, end time, load). The prosumer has only to decide on the time, volume and price of energy offered. Although the technical realization of these platforms was seen to be somewhat sophisticated and economically infeasible, the development of information and communication technology (ICT) and the pressure imposed by regulations moved research in this direction. In Germany, the new regulations for the digitalization of the energy transition [24] led to investment in the information infrastructure (IIS) and development of the Smart Meter Gateway (SMGW) for maintaining a secure communication channel between the prosumer and the utility. Also, the development and advancement in Blockchain technology revealed the potential for realization of energy trading platforms.

In the literature, several models are presented tackling the challenges of the energy trading markets within microgrids. Each research paper focuses on either a specific device or aspect [25, 26, 27]. A model that studies the bidding mechanism and integration of every possible prosumer's consuming device (e.g., EV, and HP), generation (e.g., PV and micro-CHPs) or storage was challenging to be realized. In [25] developed a micro-market for EV in a parking facility. Based on this market, the EVs were allowed to buy and sell to the micro-market depending on their needs and the market situation. [28] studied heat boilers and CHP units integration in the distribution system from the market perspective. The author implemented an optimization model based on deterministic inputs to reach market equilibrium. The model did not consider the capability of the consumers to deliver power, and consequently, the residential users were participating as consumers in the presented market. [29] discussed the pricing schemes of interruptible and uninterruptible electrical appliances, yet the heat side of the prosumer was not considered. Hence, the potential flexibility that can be offered from the heat storage and the operational constraints of thermal systems such as micro-CHPs or heat pumps were not present. [30] presented a two-stage aggregated control framework for peer-to-peer energy trading with a pricing mechanism that ensures the economic benefit of the prosumers. The author focused on PV-Battery Systems in the assessment process, where a reduction of 30% of the bills can be expected and an increase in the annual self-sufficiency by 20%.

The technical constraints and physical characteristics of the devices are not usually modeled [27]. Consequently, the practicality and the possibility of implementation of the presented algorithms are hard to evaluate. Simplified models of the market participants were introduced in the literature to increase the accuracy while minimizing the system complexity. These models lack the dynamics of a real system, which might increase the results' uncertainties.

Several researchers focus on studying energy trading method and framework independent from the nature of the participating devices. In [31], an auction-based market was presented for hour-ahead trading. Within this model, a subscription charge is paid by the user to participate in the platform, which is later used as a price signal to reduce the load on the grid. [32, 33] applied game theory approaches within their energy trading models. [32] focused on self-organizing microgrids to balance the distribution network,

while [33] developed a trading platform (Elecbay) where energy from heterogeneous industrial and residential sources can be traded without an intermediate supplier. In [33], the focus is more on the bidding process of the trading, rather than control of the microgrid. [34] and [35] reviewed the potential of different approaches for energy trading. [34] focused the game theory approaches in energy trading and applications of cooperative and non-cooperative games, while [35] discussed the current implementation of the energy trading platforms from an international preservative.

In most of the presented models in the literature, the focus was on real-time, near real-time or hour-ahead [31, 34, 35, 36]. However, forward trading is crucial to exploit the full flexibility potential of the prosumers. Otherwise, the load shifting capability of the prosumer will be confined, which can lessen the economic feasibility of the energy market platforms and their infrastructure. Only a little research discussed forward and real-time trading such as the model of [37], where a bilateral contract network was developed to enable energy trading between prosumers and fuel-based generators. Furthermore, in the published work, centralized HEMS was integrated as in Figure 1.1 (left). This architecture, as discussed earlier, is not realizable due to the constraints of the devices manufacturers and their need to have the control algorithms on their own devices.

The forward market models in the literature did not also discuss the prosumer commitment thoroughly in case of a forecast or technical failure. As a convenient solution, [33] proposed that prosumers who failed to generate or supply energy have to be either charged a penalty or trade at lower prices. However, the risk the prosumer is taking and the possible penalties because of the forecast failures were not quantified.

To summarize the status quo of literature and identify research gaps:

- Simple models were used for prosumers devices in households to minimize the required computational power of the market, yet these models can influence the bid volume directly and consequently the market dynamics
- Most of the research was focused on either integration of the thermal side or the electrical side of the prosumer, but not both
- Complicated bidding strategies were applied to develop an optimal bid. These strategies can be hardly deployed in a real-life environment on the devices as it either requires high computational power or long wait time to communicate with all other market players. Hence, its synchronization with the energy market can be challenging.
- The reviewed models considered centralized HEMS structure and enabled the centralized HEMS to bid directly on behalf of the prosumer and all the devices
- In the review research of forward markets, prosumer commitment was not quantified or evaluated during the operation.
- Possibilities of integration the state-of-the-art forecast such as probabilistic forecasts were not presented

## A Appendix

The main goal of this paper is to present a model that addresses all the aforementioned gaps and provide a comprehensive solution for the integration of energy markets in microgrids. This model features the following:

- A discrete-timely sealed double-sided auction market with market rules suiting the German context, and a fast clearing mechanism that enables prosumers to trade their energy supply and demand in near real-time and forwards.
- Novel simple non-predictive bidding strategies that is constant, symmetric and pure for each device group to ease its implementation in real-life applications.
- Pricing and bidding scheme for the probabilistic PV prediction systems [38, 39].
- Integration of decentralized EMS for trading fixed prosumers' loads and updating the smart devices bids according to the user preferences.
- Experimentally validated devices' models (e.g.[40]) are integrated to provide an accurate bid volume and market dynamics.

Within the analysis of the model, the prosumer commitment under different prediction uncertainties is evaluated. The prosumers and the utility benefits are quantified based on multiple metrics such as self-sufficiency, self-consumption, peak loads, CO<sub>2</sub> emission and costs. Furthermore, evaluation of the added value of the ICT infrastructure for energy market applications in microgrids is presented.

The structure of the paper is as follows: Section 2 provides an overview of the market design and its operations concept. Section 3 describes the function and bidding strategy of every market component. Section 4 presents the co-simulation environment, integrated models, and their input data. Section 5 demonstrates a case study of 10 residential household microgrid and analyzes the potential of the implemented market model. Section 6 presents a conclusive summary and an outlook for future research.



## 2 Market Design and Operations

The literature is rich with multiple markets and auctions design that were discussed and evaluated numerically and experimentally as early as in [41, 42, 43]. This literature has set the foundation that is inspiring the recent research developing local energy markets for microgrids [23, 44, 45, 46, 47]. Although the recent auction-based markets presented in the literature have several standard features, their impact and operation dynamics can be defined through three major criteria: market-clearing rules, bidding rules, frequency and nature of the disseminated information to participants. These criteria define the difference between two different markets models, even if both lie under the same market category [48].

The proposed model in this paper is classified as a discrete-timely sealed double-sided auction with uniform pricing. The double-sided auction by definition is an auction where both buyers and sellers can communicate their bids and asks of standardized commodities as per [49]. In this paper, the bid and ask are referred to as buying and selling bid, respectively. The market is chosen to be discrete-timely to synchronize all traders communication with the market trading platform and to provide a fair environment to all traders where communication speed does not play a role. In the work of [50], it was shown that the continuous-timely trading can be inherently flawed as the traders reacting faster has an advantage of other traders. Given the real-life situation in microgrids, it is practically hard to guarantee a synchronized reaction from all the traders. Hence, it is considered that the discrete-timely trading is fairer for all the market participants. The market is chosen to be sealed to maintain the anonymity of the bidder. Consequently, the market players can not learn about other traders' bids to preserve their privacy. A uniform pricing mechanism is applied as it provides a fair competitive price to all the market participants independent of the given bid price. Moreover, it encourages the suppliers to bid their lowest price to increase their possibility of selling.

The double-sided auction market is designed to enable prosumers to trade their energy in the forward, day-ahead, intraday in independently of the wholesale market. In a smart community with an island or a grid-connected microgrid, the number of participants is denoted by  $N$ , where  $\{N \in \mathbb{Z}^+ : N \geq 2\}$ . A market participant can be either a prosumer or the utility. A prosumer can demand deficit energy and act as a buyer  $i$ , or supply excess energy and act as a seller  $j$ .  $i \in \mathcal{B}(t)$  and  $j \in \mathcal{S}(t)$ , where  $\mathcal{B}(t)$  and  $\mathcal{S}(t)$  are the time-dependent sets of buyers and sellers, respectively.  $t \in \mathcal{T} = \{1, 2, \dots, t_{fh}\}$  is the discrete time-step at which trading can occur, where  $t_{fh}$  is the length of finite trading horizon. Since it is a discrete-timely market, the trading can occur at any defined time interval  $\Delta t$ . A market participant can communicate multiple bids  $n$  with market platform equal to  $b_{i,n} = (p_{i,n}, q_{i,n}, t_{d_{i,n}})$ , where  $p_{i,n}$  is the price of bid  $n$  of buyer  $i$ ,  $q_{i,n}$  is the bid volume, and  $t_{d_{i,n}}$  is the delivery time.  $q_{i,n}$  must always be greater than

or equal to  $q_{min}$ , where  $q_{min}$  is the constant minimum quantity of energy that can be traded. In this model, the number of participants is always assumed to be constant at any time  $t$ . A market participant can submit a buying or selling bid for a value of zero, if he is not willing to trade in the market. The bid prices  $p_{i,n}$  are formed at the device level depending on the technical constraints and dynamic behavior of the device. In Section 3.3, the bidding strategy and bid formulation will be demonstrated for every device  $D$  that can communicate with the market. However, a price ceiling and floor is set for all  $D$  participating in the market such that  $p_{min} \leq p_i, p_j \leq p_{max}$ . For a grid-connected microgrid,  $p_{max}$  and  $p_{min}$  can represent the conventional utility energy consumption tariff and feed-in tariff, respectively. The  $p_{max}$  can be time-dependent, if real-time tariff (RTP) is applied. The intention behind applying a pricing ceiling and floor is to keep the prices higher than feed-in tariffs for the generators and less than the utility prices for the consumers at all times  $t$  so that the voluntary participation of the prosumers in the microgrid market can be ensured. The readiness of a prosumer to bid higher prices to use the community energy may vary depending on the background and the culture of the society where the market is located. Nevertheless, quantifiable economic gain supported by environmental benefits for the whole of society can attract more prosumers to participate in the market.

Given the high details of the model, Figure 2.1 presents a simplified overview of the system design including the market side and the prosumer side. It shows the HEMS, market agent and the device controllers on the prosumer side, in addition to the consumption and generation forecasts. A user interface is also available to maintain and receive the user's preferences. IIS is crucial to communicate all the necessary data for the market operation securely. However, IIS requirements are not discussed within the framework of this paper. The simplified following communication steps demonstrate the process from forming the bids to the operation of the device once the bid is accepted. These steps are marked in Figure 2.1.

**Step 1:** The device controller sends the status of device  $D$  to the market agent

**Step 2:** Depending on the device status, user preference and designed bidding strategy, the market agent develops the buy and sell bids,  $b_i$  and  $b_j$ , respectively. Consequently, for each  $D$  there is a market agent to maintain a decentralized structure. The bidding strategies are discussed later in Section 3.3.

**Step 3:** The HEMS receives the bids  $b_i, b_j$  from the market agent and modifies it according to the user operation mode (standard, comfort, or cost saving)  $b_i^*, b_j^*$ , as in Section 3.2, then sends them to the market platform.

**Step 4:** Applying a discrete-timely double-sided auction, the market price and volume at equilibrium are found. The market platform then forwards the market clearing price back to the HEMS. Detailed description is presented in Section 3.1

**Step 5:** The HEMS forwards the MCP to the market agents and user through the user interface.

**Step 6:** The market agent receives the MCP to identify the accepted and rejected bids.

**Step 7:** The device controller receives the operation signal from the market agent to switch the device at  $t_d$ .

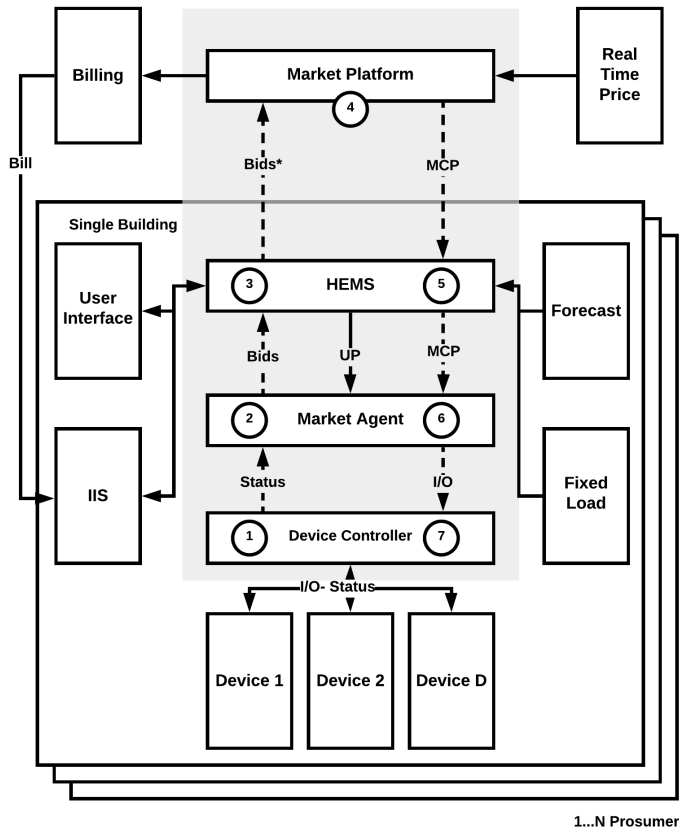


**Figure 2.1:** An overview of the model structure (main communication loop is in gray), circled numbers indicate the communication sequence.



## 3 Market Model Components

### 3.1 Market Platform

The market platform is the place where all the bids are received to clear the market. In this model, the market platform requires a market coordinator that acts as an auctioneer. The market coordinator can be the utility or the platform owner. The market coordinator roles can be summarized in the following points:

- Clearing the market and announcing the market clearing price.
- Rejecting any bid changes after the gate closure time  $t_g$ .
- Balancing the market to guarantee an equilibrium between supply and demand.
- Break the market ties at every trading period.

The first responsibility of the market coordinator to clear the market. It sorts the bids such that  $b_{i,n} \geq b_{i+1,n}$  for the buyers,  $b_{j,n} \leq b_{j+1,n}$  for the sellers. The bids are aggregated as step functions  $(p_{i,n}, q_{i,n})$  and  $(p_{j,n}, q_{j,n})$ . The resolution of the step functions can be defined by limiting the maximum bid volume. The intersection of supply and demand step functions represents the competitive equilibrium and defines the market clearing price value  $p_e$  and the cleared volume  $q_e$ . The  $p_e$  is then communicated to all the prosumers so that they can either operate at  $t_d$  or shift their loads to another time. Since the market price has a ceiling and a floor,  $p_e \leq p_{i,n} \leq p_{max}$  for all buyers, and  $p_{min} \leq p_{j,n} \leq p_e$  for the sellers. Hence the prosumers profit  $\varpi$  can be summarized in Equation 3.1, where  $q^\alpha$  is the volume of the accepted bid.

$$\varpi = \sum_1^n (p_{max} - p_e) q_{i,n}^\alpha + \sum_1^n (p_e - p_{min}) q_{j,n}^\alpha \quad (3.1)$$

The second responsibility of the market to manage the gate closure time. Since this model enables near real-time and forward trading, a gate closure time has to be defined as a deadline for any changes in bids or withdrawals. Assuming that  $t_g$  is set to 30 min, a market participant can make a bid at any  $t_d$  in the future and still change the bid up to 30 min before delivery.

The third responsibility of the market coordinator is to balance the market during each trading period in order to clear the market. The prosumers have to guarantee that their energy demand will be covered, even if there is no sufficient supply from the other prosumers in the market. Also, they have to make sure that their non-shiftable generation can be feed-in. Consequently, the market coordinator acts as a seller or a

buyer at any period. It sells the deficit energy required by consumers or buys the excess energy produced. Throughout the whole trading time horizon, the market assures that Equation 3.2 is maintained.

$$\sum_{i=1}^{\mathcal{B}} \sum_{1}^n q_{i,n} = \sum_{j=1}^{\mathcal{S}} \sum_{1}^n q_{j,n} \quad (3.2)$$

The fourth responsibility of the market coordinator is to break the ties to clear the market. Practically, the probability of having market ties is low, yet it is possible. Hence, market breaking ties rules have to be defined. In this model, the market model breaks the ties either randomly, or in the favor of agents bidding the highest volume  $q_i$  or  $q_j$ . A minimal value of  $\zeta = 1e^{-4}$  is added to the favored agent in order to clear the market.

### 3.2 Home Energy Management System (HEMS)

As discussed earlier, a decentralized HEMS is needed to maintain the practicality of the model. Conventionally, the HEMS are running optimization algorithms for the devices planning and can be also responsible for the bidding of the prosumer. However, in the project of [20] at the institute for energy economy and application technology (IfE), it was found that these methods are not realizable. Assuming that in a single family household there an EV from manufacturer A and heat pump from manufacturer B. Manufacturer A would not trust manufacture B managing the EV through his own EMS. Also, both do not allow a third party to control their devices. That's why all the products available in the market at the moment are just an interface between the prosumer and the manufacturer cloud.

Building over these experiences, a decentralized structure of HEMS is implemented that allows each market agents to develop its bid independently and communicate it to the market. Decentralized HEMS can not guarantee a global optimum for the prosumer, but a near-optimal solution. The role of the decentralized HEMS can be summarized in the following points:

- Broadcasting the  $p_e$  to market agents.
- Bidding for the non-shiftable (fixed loads) based on the load forecast at such that  $b_{i,n} = (p_{max}, q_f, t_{i,n}^d)$  to guarantee their bids allocation.
- Collecting bids from all market agents (i.e., devices) and forwarding them to the market platform.
- Adjusting the biddings depending on the user preferences.

The users' preferences can vary depending on their interest. Some users are interested in decreasing the costs; others can be more interested in increasing comfort [8, 51, 52]. The HEMS must adapt the bids to the users' preferences and interests. In this model, the

HEMS modifies the bid price  $p_{i,n}$  received from the market agent to  $p_{i,n}^*$  as in Equation 3.3.

$$p_{i,n}^* = \begin{cases} p_{i,n} & \text{if standard} \\ \varphi(p_{max} - p_i) + p_i & \text{if comfort} \\ \max(\gamma(p_{min} - p_{max}) + p_i, p_{min}) & \text{if cost saving} \end{cases} \quad (3.3)$$

$\varphi$  and  $\gamma$  are two variables such that  $\{\varphi, \gamma \in \mathbb{R} : 0 \leq \varphi, \gamma \leq 1\}$ .  $\varphi$  and  $\gamma$  could be set by the user to increase or decrease the comfort or cost savings, respectively.

### 3.3 Market Agents

As per [49], double-sided auctions is too complex to output a game-theoretic solution. In this market model, the market agent has no information about the number of bidders, the volume of bids, or the identity of bidders at any trading interval because the market is sealed to maintained the anonymity and data privacy of the prosumers, also to avoid collusion. If a game-theoretic approach would be applied, the market agent has to evaluate all the possible actions for all the market participants in the microgrids to find the solution maximizing its benefit. This strategy would lead to limiting the model scalability given the increasing computational capacity required per market participants. Moreover, as the number of participants increases in this market type, the less influential is market participant (player) actions.

In this model, simple non-predictive bidding strategies are evaluated. Every device group has a symmetric pure constant bidding strategy that do not need a price prediction or complex learning mechanism to develop the bid. The bidding strategy is designed to bid always the truthful price depending on its need. Hence, an agent who is requiring the energy in the next hour would bid more than an agent requiring the energy on the next day. The valuation is always time/need dependent. To optimize the bidding strategy, each agent can submit multiple bids at different time steps within a specific time frame, then use a simple enumeration search optimization technique to find the cheapest accept bid and withdraw/sell the rest additional purchased volume to the market. This concept is applied to each of the typical prosumer flexible devices and tailored to its technical and operational constraints.

The bid developing is not only a price but also a value. Using the non-linear experimentally validated models [40] and the novel probabilistic forecast [38] the exact bidding volume and the corresponding price are evaluated. The accuracy of these models enables to present the realistic dynamics of the market and deliver results comparable to field experiments. In the upcoming sections, the formulation of the bid price and volume is demonstrated for each device type.

#### 3.3.1 Electric Vehicle

In this model, the EV is assumed to operate only in the Grid to Vehicle mode (G2V) (i.e., only as a consumer). A user communicating with the HEMS will indicate the desired starting time of the charging  $t_s$  and the time by which the vehicle shall be charged and

ready  $t_r$ . The latest end time is defined as  $t_e = t_r - t_o$ . The typical charging power is between 3.6 kW (single phase) and 22 kW (three phase) [53].

Assuming a fixed charging power  $P_{CEV}$  is required to charge the EV any time between  $t_s$  and  $t_e$ , the EV market agent sends bids at every possible delivery time  $t_d$  between  $t_s$  and  $t_e$ . The readiness of the market agent to pay more increases linearly as the charging time approaches the  $t_e$  as in Equation 3.4. After  $t_e$ , the market agent always bids a fixed price of  $p_{max}$  to ensure the acceptance of the bid either from other prosumers or the utility depending on the market situation.

$$p_{i,n} = \begin{cases} \left(\frac{p_{max} - p_{min}}{t_e - t_s}\right)t_d + p_{min}, & \text{if } t_d \leq t_e \\ p_{max}, & \text{if } t_d > t_e \end{cases} \quad (3.4)$$

The set of accepted bids  $\beta_i^\alpha$  is always larger than the set of required bids  $\beta_i^r \subset \beta_i^\alpha$ , which is because the market agent creates bids for every period between  $t_s$  and  $t_e$  and bids the maximum price after  $t_e$ .

The market agent selects the most economic bids and withdraws rejected and unneeded bids. As shown in Equation 3.5, the bids with the lowest costs are selected such that the number of accepted bids  $c(\beta_i^r)$  can satisfy the energy demand  $E_D$  of the charging station.

$$\min C = \min_{b_{i,n}^\alpha \in \beta_i^r, \beta_i^r \subset \beta_i^\alpha} \sum b_{i,n}^\alpha = \sum p_{i,n}^\alpha q_{i,n}^\alpha \quad (3.5a)$$

$$\text{s.t. } \beta_i^\alpha = \{b_{i,1}^\alpha, b_{i,2}^\alpha, \dots, b_{i,n}^\alpha\} \quad (3.5b)$$

$$c(\beta_i^r) < c(\beta_i^\alpha) \quad (3.5c)$$

$$b_{i,n-1}^\alpha < b_{i,n}^\alpha, \forall b_{i,n}^\alpha \in \beta_i^\alpha \quad (3.5d)$$

$$E_D = c(\beta_i^r) q_{i,n}^\alpha \quad (3.5e)$$

### 3.3.2 Heat Pump

The behavior of heat pumps in the market platform is highly dependent on the heat pump hydraulic configuration, dynamics, modulation, predefined heating curves, and building load. Assuming that the heat pump is installed along with a combi-storage tank that can cover both the space heating (SH) demand and the domestic hot water demand as described in [40], the capacity of the storage  $Q$  is defined according to Equation 3.6 of [54], where  $\rho$  is the density of water,  $C_p$  is the heat capacity of water,  $A_s$  is the cross-sectional area of the storage,  $T_s(h)$  is the storage at height  $h$  and  $T_{ref}$  is the reference temperature. In practice,  $T_s(h)$  can be measured using a set of sensors across the heat storage as in [40]

$$Q = \rho \times C_p \times A_s \times \int_0^h (T_s(h) - T_{ref}) dh \quad (3.6)$$

$$\forall T_{st}(h) > T_{ref}$$

## A Appendix

Depending on the  $Q(t)$ , predefined set energy content,  $Q_{set}$ , minimum energy content,  $Q_{min}$ , and maximum energy content,  $Q_{max}$ , the heat pump can develop a bid [40]. Equation 3.7, 3.8, and 3.9 can summarize the process of defining the bid volume and price. Then, the market agent then selects the optimal bid to minimize the costs in a manner analogous to the EV, Equation 3.5.

$$p_{i,n} = \begin{cases} 0, & t < t_{rest} \\ (\frac{p_{max} - p_{min}}{\Psi^-})t_d + p_{min}, & \dot{Q} < 0, \text{ and } Q_{min} \leq Q \leq Q_{set} \\ -(\frac{p_{max} - p_{min}}{\Psi^+})t_d + p_{max}, & \dot{Q} > 0, \text{ and } Q_{min} \leq Q \leq Q_{set} \\ p_{min}, & Q_{set} < Q \leq Q_{max} \end{cases} \quad (3.7)$$

$$\Psi^- = \frac{Q - Q_{min}}{\dot{Q}_{SH} + \dot{Q}_{DHW} + \dot{Q}_{losses}} \quad (3.8a)$$

$$\Psi^+ = \frac{Q_{set} - Q}{\dot{Q}_{HP} - \dot{Q}_{SH} - \dot{Q}_{DHW} - \dot{Q}_{losses}} \quad (3.8b)$$

$$q_{i,n} = COP \times \dot{Q}_{HP} \times \Delta t, \quad (3.9a)$$

$$\text{where } COP = f(T_{su}, T_a) \approx f(Q, T_a) \quad (3.9b)$$

$$\dot{Q}_{HP} = f(T_a) \approx f(Q) \quad (3.9c)$$

$t_{rest}$  is the resting time required between Off and On switch.  $\Psi^-$  and  $\Psi^+$  is the negative and positive load shifting potential, respectively.  $\dot{Q}_{SH}$  is the space heating load,  $\dot{Q}_{DHW}$  is the domestic hot water load.  $\dot{Q}_{losses}$  is the thermal losses.  $\dot{Q}_{HP}$  is the heat pump thermal power.  $COP$  is the coefficient of performance of the heat pump.  $T_{su}$  is the supply temperature of the heat pump.  $T_a$  is the ambient temperature. More details about the technical constraints of the heat pump system, its control, and optimization requirements, in addition to its dynamics and validated model, are available in [40].

### 3.3.3 Micro-CHP

In this model, the micro-CHP is assumed to have the same hydraulic configuration as the heat pump. Thus, a combi-storage tank is attached to the micro-CHP to cover both the SH and DHW loads. The heat storage  $Q$  defines the flexibility of the micro-CHP unless the system configuration enables heat dumping. Consequently, the developed bid price and bid volume can be summarized by equations 3.10 and 3.11, where  $\kappa$  is the CHP coefficient, and  $\dot{Q}_{CHP}$  is the thermal generation power.

$$p_{j,n} = \begin{cases} 0, & t_d < t_{rest} \\ -(\frac{p_{max} - p_{min}}{\Psi^-})t_d + p_{max}, & \dot{Q} < 0, \text{ and } Q_{min} \leq Q \leq Q_{set} \\ (\frac{p_{max} - p_{min}}{\Psi^+})t_d + p_{min}, & \dot{Q} > 0, \text{ and } Q_{min} \leq Q \leq Q_{set} \end{cases} \quad (3.10)$$

$$q_{j,n} = \kappa \times \dot{Q}_{CHP} \times \Delta t, \quad (3.11)$$

### 3.3.4 Photovoltaic

Integration of small-scale PV systems as market suppliers in a day-ahead trading market raises several questions concerning the bid commitment. The commitment of HP, micro-CHP or an EV can be better managed by the prosumer when compared to the PV system. An over forecast in a day-ahead market can lead to an unrealistic bid and influence the prosumer's future ability to profit from the market, which can directly minimize participation in the market platform.

Typical residential prosumers who have small-scale PV systems with capacities between 1 kWp and 12 kWp are exposed to the highest uncertainties and generation variabilities as discussed in [55]. Figure 3.1(b) and 3.1(d) show the 1-min resolution measurement of a 3 kWp roof-top PV system. It can be seen that in 3.1(b) the PV generation is not exposed to high variabilities compared to Figure 3.1(d). Even if the PV forecasting algorithm is able to determine the mean PV profile for days with high variabilities, it would be rather complicated to forecast these variabilities.

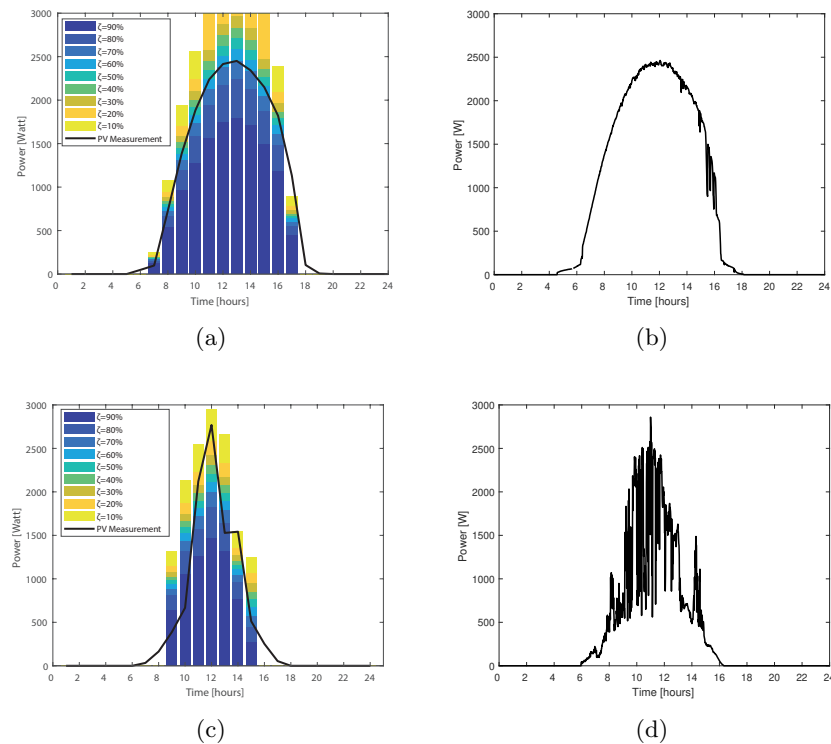


**Figure 3.1:** Selected days of probabilistic forecast output and PV measurements in different seasons, (a) summer (b) summer-1 min resolution (c) transient (d) transient-1 min resolution [38].

[38] presented a probabilistic PV generation forecast for HEMS applications and energy market models. The probabilistic PV forecast delivers a range of values depending

## A Appendix

on  $\zeta \in [10\%, 90\%]$ . Each value represented a probability of generation of a specific volume as shown in Figure 3.1. For the summer day in Figure 3.1(a), most of the power forecast lies by  $\zeta = 90\%$  and  $\zeta = 80\%$ . In the transient day shown in Figure 3.1(c), the probabilistic forecast was able to forecast the variabilities and indicates the expected power to be generated with lower uncertainties. In [38, 55], the model description, validation and demonstration are detailed. The prediction model is also open source and available through [39].

Equation 3.12 summaries the bidding strategy of the PV system. The bidding price is formed dependent on  $\zeta$ . The higher the probability of the generation profile, the lower the price. Thus, the less variable generation will be traded more on the market platform, compared to generation exposed to high variabilities.

$$p_{j,n} = p_{max} + \zeta(p_{min} - p_{max}) \quad (3.12)$$

Moreover, the prosumer can decide to bid the whole range of  $\zeta$ s or only the guaranteed range (e.g., 80% to 90%). The forecast delivers only the probabilities, but depending on the prosumers' system and configuration, the traded range can be decided. Through this bidding mechanism, the prosumers commitment to the communicated bids can be maximized, and certain bids can be traded. A means for increasing the traded range is discussed in the next section.

### 3.3.5 Batteries

In this model, the batteries are considered as a backup system to maximize the prosumers commitment in the market. Assuming that the prosumers have sent a bid, but could not deliver it, the battery discharges to make up for the unfulfilled bid. Equation 3.13 relates to the simplified battery charging and discharging behavior depending on the difference between the generated volume  $q_g$  and the accepted volume  $\sum_1^n q_{j,n}^\alpha$ , where  $\eta_{dch}$  and  $\eta_{ch}$  are the discharging and charging efficiencies of the battery, respectively.

$$E_{Batt}(t) = \begin{cases} E_{Batt}(t-1) - \frac{1}{\eta_{dch}}(\sum_1^n q_{j,n}^\alpha - q_g), & \sum_1^n q_{j,n}^\alpha > q_g \\ E_{Batt}(t-1) - \eta_{ch}(\sum_1^n q_{j,n}^\alpha - q_g), & \sum_1^n q_{j,n}^\alpha < q_g \\ E_{Batt}(t-1), & \text{otherwise} \end{cases} \quad (3.13)$$

Operation of the battery system under these conditions can make up for the forecast errors and enable the prosumers (i.e., the market agent) to commit to the communicated bid without violating the market rules.



## 4 Model Implementation and Co-Simulation

To maximize the model accuracy, and at the same time maintain a proper simulation speed. The model is co-simulated between Matlab, and the Modelica based software, SimulationX, as shown in Figure 4.1.

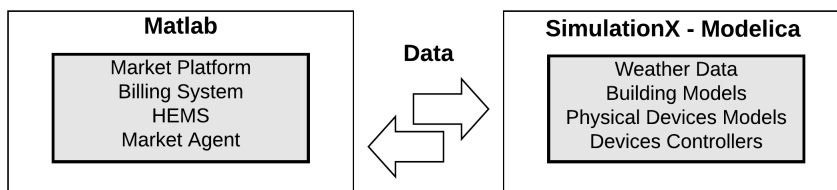


**Figure 4.1:** Model division on the co-simulation platform between Matlab and Modelica.

The market platform model, billing systems, HEMS, and market agents are integrated into the Matlab model, while SimulationX integrates all the models of the physical devices such as the EV, HP, micro-CHP, or PVs, in addition to the building models and the device controllers. The current structure of the model emulates the real-life situation in which a market platform is integrated. All the models running on Matlab can be assumed to be running in the cloud as a service, while all the Modelica-based models are real systems.

The Modelica-based models are developed and calibrated based on either testbeds or field measurement data. The heat pump model design, and validation, in addition to a demonstration of the testbed, is given in [40]. The micro-CHP model is developed based on the study of [56]. The PV measurements and PV system characteristics are detailed in [57]. The EV models and the buildings used are based on the Green City Package of [58]. A calibration for the building models depending on the IEE Project TABULA [59] was performed to maximize the overall model accuracy. Modelica was used to enable simulating of the non-linear models and present the dynamics of the systems as shown in the heat pump model of [40]. As an example, the difference between the developed heat pump model and the measured value revealed an error of 3%.

The integrated building model facilitates the evaluation of user comfort. Throughout the simulation process, the temperature profile of each zone of the building model is monitored to make sure that the room temperature never falls below the set temperature tolerance, which is  $\pm 1K$

The fixed electricity profiles are based on the representative load profiles of [60]. The

data includes measured high-resolution profiles of 74 residential houses managed by the same grid operator. The houses are located in the vicinity of each other. Consequently, it can be assumed the given houses lie in the same microgrid.

The hot water profiles are developed based on the standard VDI 4655 for each type day, while hot water circulation load used is based on field measurements of single-family houses in South Bavaria, Germany [61].

## 5 Case Study: Microgrid of Residential Buildings

### 5.1 Benchmark

A microgrid of 10 single family households is used, where each household has an EV, PV system, and a heat pump. The charging station has a maximum 3.6 kW. The PV system has a 6 kWp. A brine-water heat pump with a thermal power of 10.1 kW<sub>th</sub> and a COP of 5.02 is installed. 10 electrical load profiles are selected from [60] to represent the fixed loads. All the households are assumed to have the same area and thermal load profile. The building models of the prosumers are parameterized based on 1984 building standards. The building parameters can be found in [59] and the building's location is assumed to be Munich, Germany.

Identical user preferences are used in all the households with all the market participants operating using the standard mode as per Equation 3.3. The load shifting window of the EV is the same every day, where the difference between  $t_s$  and  $t_r$  is 24-h.

In this section, a comparison is made between the reference case, where no market platform or HEMS is implemented (conventional operation), and the case with a market platform and the HEMS. Same preferences and characteristics of the household are used to illustrate the market behavior, even in a situation of a simultaneous supply and demand. The comparison is based on a complete analysis of the year 2017.

### 5.2 Market Dynamics

To illustrate the market dynamics and the influence of the prosumer solely on the market price, it is assumed that the utility always participates in the market with a fixed tariff of 0.26 €/kWh and a feed-in-tariff of 0.12 €/kWh as per EEG 2017[62]. Consequently,  $p_{max}$  and  $p_{min}$  are equal to 0.26 and 0.12, respectively.

In the case study, the PV system is the sole energy generation system in each prosumers' house. Hence, the MCP is dependent on the PV system as a seller. The MCP falls or rises, depending on whether there is an underproduction, or overproduction from the PV system as shown in Figure 5.1. Hence, the mean values of all the summer days are relatively lower than the transient and the winter days. The standard deviation shown in Figure 5.1 is in this case dependent on the probabilistic forecast of the given location.

The presented MCP behavior is not a standard behavior. It is dependent on the given situation where the utility is providing a fixed tariff, and the prosumers can only sell the PV energy. The analysis of Figure 5.1 shows that the market is reacting to the

generation conditions and can indicate the demand and supply situation of the microgrid while maintaining the prosumers' privacy. An RTP signal or a whole market price can be used as an input for this model. Also, the utility could be represented by multiple market participants bidding at different prices.

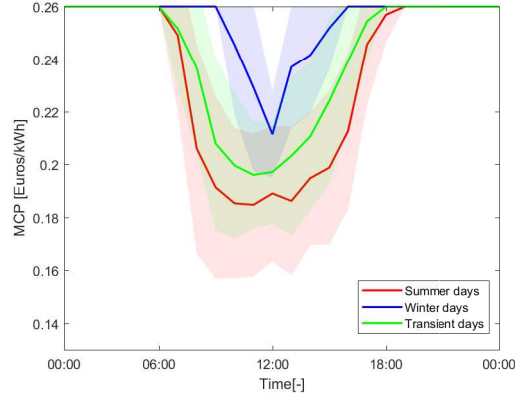


**Figure 5.1:** Market Clearing Price variation in summer days, transient days, and winter days.

### 5.3 Utility Benefit

The results in Figure 5.2 represent the behavior of the microgrid over different type days: summer, transient and winter day. It compares the behavior of the microgrid with and without the market model. The case in which the market platform is not integrated is denoted by the reference.

In the typical summer day shown in Figures 5.2(a) and 5.2(b), it can be seen that the loads that conventionally operates before the sunrise or the sunset are shifted due to low market prices to operate during the PV generation hours. An insight about the types of load being shifted can be obtained from Figures 5.3(a) and 5.3(b). Hence, a reduction in peak loads can be observed. The peak load of the microgrid export is from -58 kW to -39 kW, while the import peak load is reduced from 44.5 kW to 35 kW.

The transient day in Figures 5.2(c) and 5.2(d) exhibits the same behavior seen in the typical summer day, where the market agents shift the loads to the lowest possible market prices. On this day, the influence of the probabilistic forecast on energy trading is more noticeable since the PV generation is exposed to higher generation variabilities. The probabilistic forecast and its market agent were able to offer the energy with high variability at a price closer to the  $p_{max}$  so that other market agents could avoid operation in this period. Hence, it minimizes the exposure of the prosumer to fines for non-delivery. Figures 5.3(c) and 5.3(d) show a comparison between the behavior of each load in the reference and market model, respectively. It can be seen that most of the heat pumps operate and EV charging stations operate during the availability of PV generation. However, some EVs shifted their loads to a later time starting at 18:30. In this case, the market agent could not find a cheaper bid less than  $p_{max}$  at the PV generation time.

## A Appendix

Thus, it kept shifting the loads until  $t_e$ , waiting for cheaper bids to be offered in the market.

In winter, almost 100% PV generation power is used as shown in Figure 5.2(f), compared to Figure 5.2(e). The export peak load drops from -46 kW to -11 kW. The import power drops from 60 kW to 43 kW. Due to the high energy consumption of the heat pump in winter, the PV generation does not suffice. Thus, some loads, which are mostly heat pumps, were shifted to a later time of the day, as shown in Figure 5.3(f). For all the loads operating after 17:30, the start times are not similar, although they receive the same price and are locally controlled by the market agent. Thus, it can be concluded that the trading process occurred during the PV generation hours on that day, desynchronized the loads' operation later at the end of the day and minimized the peaks, even though there are no incentives or motivation for load shifting.

In all the reference model cases in Figure 5.3, the heat pumps operates at the same time as the same building model and DHW standard profile are used. In reality, minor differences can be found due to the consumer behavior as discussed in [63]. The EVs daily start charging time is based on a normal distribution between 15:00 and 05:00 of the next day.

A one year analysis shows that the market increases the self-sufficiency of the microgrid by 130% and the self-consumption by 120%. Also, it decreases the CO<sub>2</sub> emissions on average by 21% and the import peak load by 25%. The absolute values are discussed for all prosumers in Section 5.4. The presented results not only demonstrate the capability of the market platform to trade, shift the loads but also the accuracy of the probabilistic PV forecast in delivering the profiles that maximize the efficiency of the whole model.

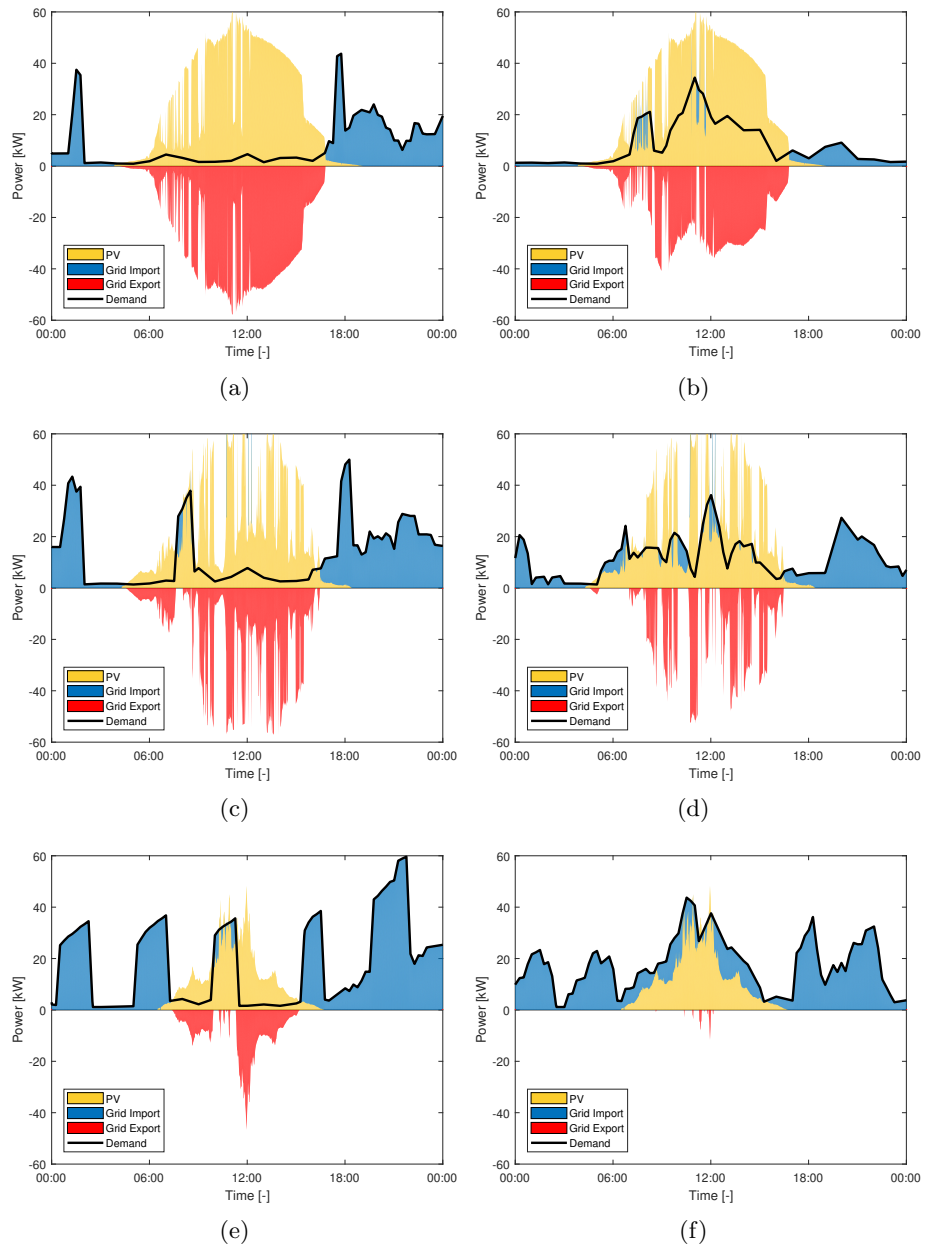


**Figure 5.2:** Type day profile of the whole microgrid, (a) summer day - reference (b) summer day - market (c) transient day - reference (d) transient day - market (e) winter day - reference (f) winter day - market.

## A Appendix

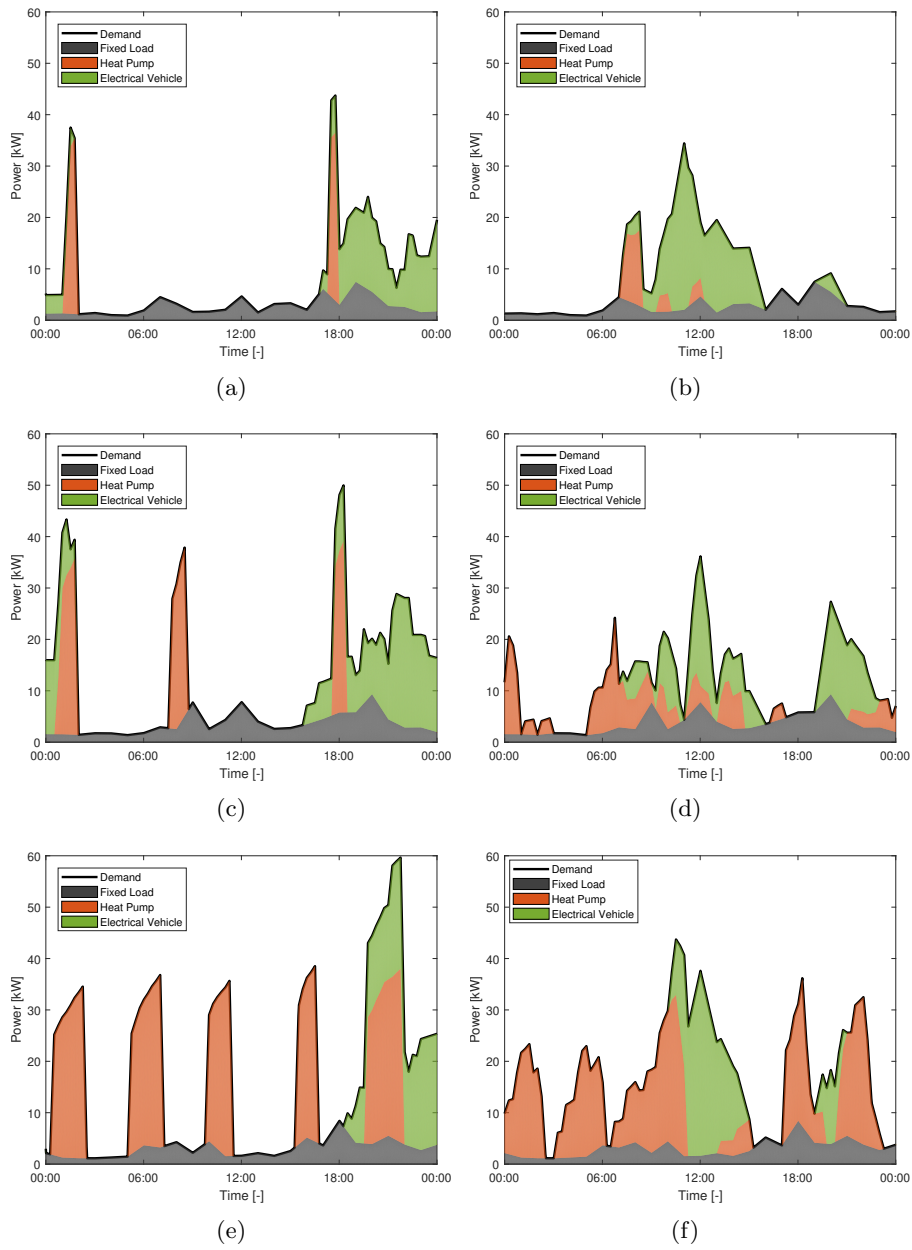


**Figure 5.3:** Detailed demand profile of the microgrid, (a) summer day - reference (b) summer day - market (c) transient day - reference (d) transient day - market (e) winter day - reference (f) winter day - market.

## 5.4 Prosumer Benefit

In this section, a detailed insight into the prosumer benefit is presented. Similarly to Figure 5.2, the supply and demand of a single prosumer on the same typical days are presented in Figure 5.4. The same conclusions can be drawn for this typical prosumer, in comparison with the reference model. Additionally, the amount of energy traded is shown. The highest energy exchange period was in transient and winter days. In summer, most of the prosumers in the microgrid are using their own generated energies and only a few kWhs can be traded as shown in Figure 5.4(b). Furthermore, in transient and winter days, as in Figures 5.4(d) and 5.4(f), the energy bought and sold are relatively higher due to the increase in the demand of the heat pumps and the decrease in PV generation. Hence, it can be deduced that the lower the capacities available on the prosumer side, the more the prosumers will be depending on each other to trade their energies and shift their loads. Excess capacities will limit the possible amount of energy that can be traded.

The trading dynamics and the behavior of the market agent can be further analyzed based on Figure 5.4(d). On that day, the market agent is not only shifting the load depending on the prosumer's own available energy but also depending on the situation in the microgrid. It can be seen that at around 05:30, the market agent bought energy to operate earlier, and sold the generated energy later to the microgrid. Moreover, it can be shown in Figure 5.4(f) that the market agent shifted the load that could be operated starting from 06:00 and sold the energy to the microgrid, to start later at 08:00. In the case of the reference model, the prosumers do not contribute to minimizing the peak load of the microgrid and did not have the opportunity to trade and exchange energy to maximize their economic welfare.

To quantify the benefits for the prosumer, the self-sufficiency, the self-consumption, the peak load, the  $CO_2$  emission, and costs are evaluated for each prosumer in the microgrid over a whole year. Two different costs are assessed: the costs based on the conventional billing systems (CB), and the costs based on the market billing system (MB). In the CB system, the current conventional metering systems (no smart meters) are used such that a fixed price is paid by the prosumer for the energy consumed and a fixed feed-in tariff is received for all the generated energy. In the MB system, the energy generation and consumption prices are decided based on the market price given by Equation 3.1. In both cases, the market operations are precisely the same, and the only fundamental difference is the billing. In the case of the CB, it is assumed that a non-certified communication to the market is implemented. The reason for comparing CB and MB is to evaluate the potential added value of the ICT infrastructure (i.e., IIS), as discussed earlier. Also, to assess the potential of applying the market platform immediately (e.g., using micro-computers) without the need of waiting for a smart meter certified billing in Germany.

Figure 5.5 shows the distribution of the 10 prosumers under the given metrics for both the market and the reference model. For all the prosumers, the self-sufficiency and self-consumption are higher compared to the reference model. The mean (green) and the median (orange) of the self-sufficiency both increased by 102%. The median of the self-

## A Appendix

consumption increased by 80% and the mean is slightly higher. Additionally, the median of the peak load decreased by 15%, while the mean decreased by 16%. By evaluating the CO<sub>2</sub> emissions within the boundaries of prosumers' household, the emissions are reduced by 26%.

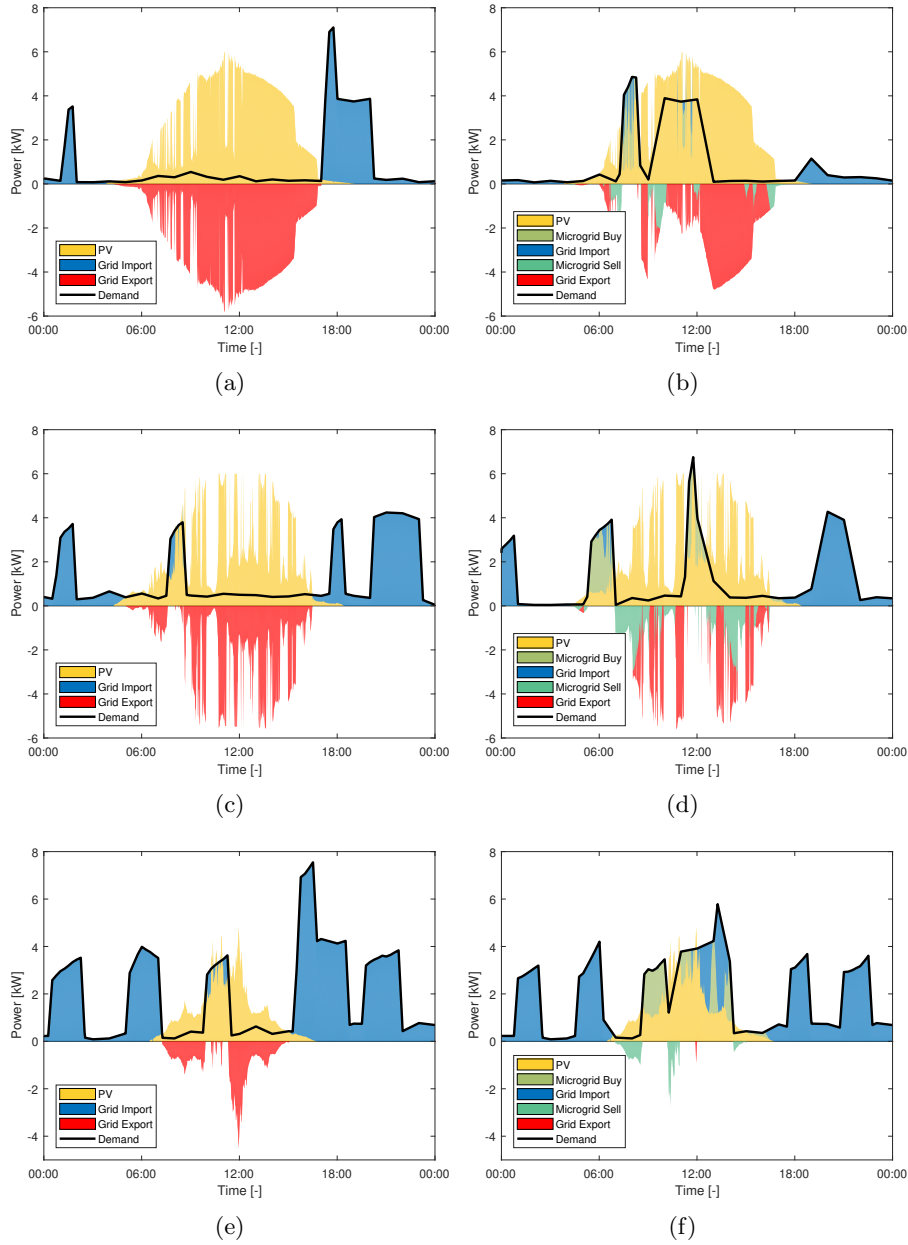


**Figure 5.4:** Type day profile of a typical household in the microgrid, (a) summer day - reference (b) summer day - market (c) transient day - reference (d) transient day - market (e) winter day - reference (f) winter day - market.

Comparing the values of the self-sufficiency and the self-consumption to the values produced by the centralized energy management algorithm used in [55]. It is found that the self-sufficiency and self-consumption are lower using the market platform and decentralized HEMS by 5% and 7%, respectively. Hence, the solution provided is not a global optimal, but a near-optimal solution.

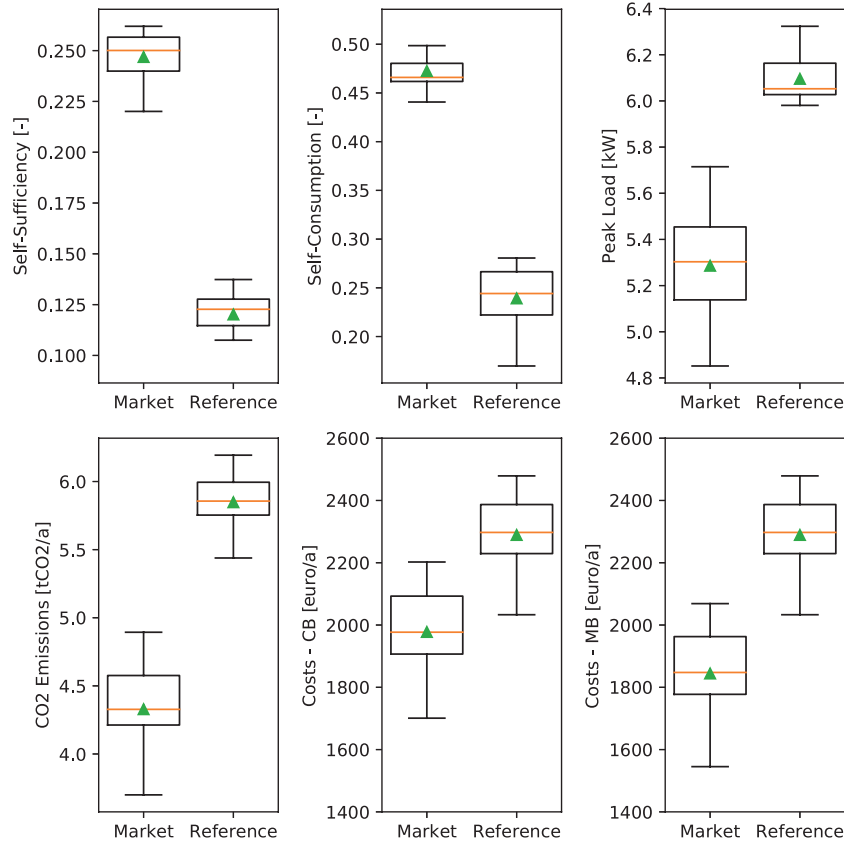


**Figure 5.5:** A comparison between the market and the reference model depending on different metrics.

Under both the CB and the MB billing systems, the market demonstrates its ability to minimize prosumer costs. The mean and median costs of the market model are 15% lower than the reference model using the CB, which are equal to 360 euro/a. These costs are based on the current metering infrastructure. Using ICT, the market bid and MCP can be binding. As shown in Figure 5.5, the costs of the market model are 23% lower than that of the reference model, and the overall absolute savings are equal to 530 euro/a. Thus, the expected saving from IIS could amount to an additional 170 euro/a in this configuration. These costs were calculated ignoring the transaction and service fees of the grid and market platform operator. Other fees might be considered depending on the regional regulations and the operating costs of the market platform. These costs will

## A Appendix

not influence the operation plan of the prosumers; in other words, the utility benefits will still be the same, but this would influence the economic benefit of the prosumer. Hence, the market platform operator and the utility must make sure that the economic benefit is maintained within specific boundaries. Otherwise, the prosumers will not be interested in trading their energy in the market platform.

Comparing the results of each prosumer to that of the utility, it can be seen that the self-sufficiency, self-consumption or CO<sub>2</sub> emission reduction of average prosumer is lower than that of the whole microgrid. Such a difference is due to the aggregation effect of the load profiles of all the prosumers. However, it is important to demonstrate the benefits share for each prosumer from the participation in the market platform.

The performed analysis assumed that no penalties are paid if the prosumer does not commit to the bid. However, if the prosumer submits a selling bid of a PV system with a  $\zeta = 10$ , it is probable that the PV system would not be able to deliver the expected bid volume. As discussed in Section 3.3.5, in this situation, the battery system is responsible for fulfilling the bids. Based on a full year analysis, Figure 5.6 demonstrates the required battery capacity per kWp PV that the prosumer needs to install to avoid any penalties. For  $\zeta \geq 58$ , no batteries need to be installed, and 100% of the bids communicated by the PV system can be satisfied. However, the lower the  $\zeta$ , the higher is the required battery capacity. The optimal battery capacity can only be determined based on the expected platform penalty and the readiness of the prosumer to be exposed to such risks. As discussed, the PV predictions provide an indicator of the certainty of the prediction but do not decide on the amount of energy that can be traded. If the prosumer needs to avoid any penalties, it would be advised to trade up to  $\zeta = 60$ . With lower  $\zeta$ , the profit of the prosumer can be increased as indicated by Equation 3.12, but penalties might be imposed.

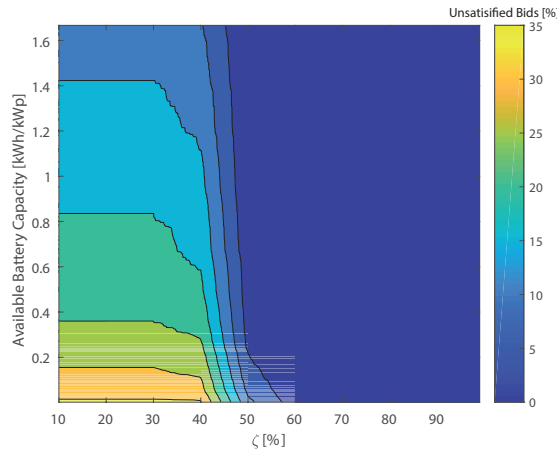


**Figure 5.6:** Percentage of unsatisfied bids against the  $\zeta$  of the PV prediction and the available battery capacity.



## 6 Conclusions

In this paper, a market model for energy trading platform is presented in which the prosumers are capable of trading their energy supply and demand. The prosumers communicate with the market via a decentralized HEMS, where each device develops its own bid depending on its physical characteristics and technical constraints. Hence, a bidding strategy is presented for each device type. The models of the integrated devices are based on either field test or testbeds to ensure the accuracy of the integrated model. Moreover, the devices are integrated as non-linear models in the market through a co-simulation platform to demonstrate the system dynamics and maximize their accuracy. Additionally, a probabilistic PV prediction system is integrated into the market model to show the mechanism of PV energy trading, given its generation uncertainty.

Furthermore, the model allows the prosumers not only to trade in a real-time market but also in a forward market to facilitate energy planning. Hence, the market will benefit both the prosumer and the utility. These benefits can be summarized as follows:

- At the level of the microgrid, the market model doubles the self-sufficiency and self-consumption. CO<sub>2</sub> emissions are reduced by 21%, and the import peak load decreased by 25%. Therefore, it can be concluded that the market not only facilitates energy trading but acts as a microgrid decentralized energy management system as well.
- At the level of the prosumer, it is ensured that benefits are distributed over the market participants. Using the same metrics implemented at the level of the microgrid, the model revealed that the benefit of each prosumer using the market model exceeds that of the reference model.
- Additional metrics are used to evaluate the economic benefit of the prosumers. The costs are calculated based on conventional billing metering infrastructure, then also using the soon-to-be-implemented IIS. In both cases, the prosumers benefits are higher with the market model. Thus, the implementation of the market model can be independent of the current ICT infrastructure. Using conventional infrastructure, the prosumer can save an average of 15% of the costs, while using IIS the prosumer can save 23%.

To maintain the prosumers commitment to the communicated bid, given the uncertainties of renewable generation prediction in the forward market, a battery system is required. The capacity of the battery system and the percentage of unsatisfied bids are calculated depending on the output of the probabilistic forecast model. The results show that the prosumer can participate without having a battery system or being penalized provided that the most probable generation profile is traded.

#### *A.4 Publication 4*

For future works, a more profound insight will be presented that discuss the factors influencing the market operations. Scenarios evaluating different microgrid and household configuration, pricing mechanisms, and prosumers preferences will be analyzed.

## Bibliography

- [1] Renewable Energies Agency. Press Fact Sheet: The German Energy Transition. *Berlin Energy Transition Dialogue*, (March):1–16, 2016.
- [2] Bundesministerium für Wirtschaft und Energie. BMWi - Erneuerbare Energien, 2017.
- [3] Federal Ministry of Education and Research. German Energy Transition - BMBF.
- [4] A. Federal Ministry of Food and C. Protection. The Renewable Energy Sources Act. 2012.
- [5] Federal Ministry for Economic Affairs and Energy (BMWi). Renewable Energy Sources in Figures. *National and International Development*, page 80, 2017.
- [6] Energy Transition. Share of German citizen renewable energy shrinking.
- [7] a. Barbato and G. Carpentieri. Model and algorithms for the real time management of residential electricity demand. *2012 IEEE International Energy Conference and Exhibition (ENERGYCON)*, pages 701–706, sep 2012. doi:10.1109/EnergyCon.2012.6348242.
- [8] W. El-Baz and P. Tzscheuschler. Co-Simulation of a Smart Home Model Based on a Micro Electricity Market. *Fifth German-Austrian IBPSA Conference*, 2014.
- [9] Z. Wu, H. Tazvinga, and X. Xia. Demand side management of photovoltaic-battery hybrid system. *Applied Energy*, 148:294–304, 2015. doi:10.1016/j.apenergy.2015.03.109.
- [10] B. Jiang, A. Muzhikyan, A. M. Farid, and K. Youcef-Toumi. Demand side management in power grid enterprise control: A comparison of industrial & social welfare approaches. *Applied Energy*, 187:833–846, 2017. doi:10.1016/j.apenergy.2016.10.096.
- [11] G. R. Aghajani, H. A. Shayanfar, and H. Shayeghi. Demand side management in a smart micro-grid in the presence of renewable generation and demand response. *Energy*, 126:622–637, 2017. doi:10.1016/j.energy.2017.03.051.
- [12] Y. Shen, X. Wen, L. Wang, and W. Guan. 2018 IEEE International Conference on Energy Internet A Visualization Compression Algorithm Considering Interactive Structure for Energy Trading of Microgrid System. *2018 IEEE International Conference on Energy Internet (ICEI)*, (3):49–54, 2018. doi:10.1109/ICEI.2018.00017.

- [13] M. Killian, M. Zauner, and M. Kozek. Comprehensive smart home energy management system using mixed-integer quadratic-programming. *Applied Energy*, 222(March):662–672, 2018. doi:10.1016/j.apenergy.2018.03.179.
- [14] M. Wang and L. Tian. Regulating effect of the energy market-Theoretical and empirical analysis based on a novel energy prices-energy supply-economic growth dynamic system. *Applied Energy*, 155:526–546, 2015. doi:10.1016/j.apenergy.2015.06.001.
- [15] Y. Han, Q. Zeng, Z. Geng, and Q. Zhu. Energy management and optimization modeling based on a novel fuzzy extreme learning machine: Case study of complex petrochemical industries. *Energy Conversion and Management*, 165(March):163–171, 2018. doi:10.1016/j.enconman.2018.03.049.
- [16] I. Ben Ali, M. Turki, J. Belhadj, and X. Roboam. Optimized fuzzy rule-based energy management for a battery-less PV/wind-BWRO desalination system. *Energy*, 159:216–228, 2018. doi:10.1016/j.energy.2018.06.110.
- [17] Y. Guo, J. Wang, H. Chen, G. Li, J. Liu, C. Xu, R. Huang, and Y. Huang. Machine learning-based thermal response time ahead energy demand prediction for building heating systems. *Applied Energy*, 221(November 2017):16–27, 2018. doi:10.1016/j.apenergy.2018.03.125.
- [18] S. Gottwalt, W. Ketter, C. Block, J. Collins, and C. Weinhardt. Demand Side Management : A simulation of household behavior under variable prices. *Energy Policy*, 39(12):8163–8174, dec 2011. doi:10.1016/j.enpol.2011.10.016.
- [19] Z. Chen, S. Member, L. Wu, and Y. Fu. Real-Time Price-Based Demand Response Management for Residential Appliances via Stochastic Optimization and Robust Optimization. 3(4):1822–1831, 2012.
- [20] Lehrstuhl für Energiewirtschaft und Anwendungstechnik. e-MOBILie - Schaufenster Elektromobilität. URL: <http://www.ewk.ei.tum.de/forschung/projekte/e-mobilie/>.
- [21] D. E. Olivares, C. A. Canizares, and M. Kazerani. A centralized energy management system for isolated microgrids. *IEEE Transactions on Smart Grid*, 5(4):1864–1875, 2014. doi:10.1109/TSG.2013.2294187.
- [22] K. Kok and S. Widergren. A Society of Devices: Integrating Intelligent Distributed Resources with Transactive Energy. *IEEE Power and Energy Magazine*, 14(3):34–45, 2016. doi:10.1109/MPE.2016.2524962.
- [23] W. El-Baz and P. Tzscheutschler. Autonomous coordination of smart buildings in microgrids based on a double-sided auction. In *2017 IEEE Power & Energy Society General Meeting*, number August, pages 1–5, Chicago, jul 2017. IEEE. doi:10.1109/PESGM.2017.8273944.

- [24] Bundesregierung. Gesetz zur Digitalisierung der Energiewende. *Bundesgesetzblatt*, 2016(43):2034–2064, 2016.
- [25] A. Kriukov, B. Vicol, and M. Gavrilas. Applying a micro-market inside an electric vehicles parking facility. *Proceedings of the Universities Power Engineering Conference*, 2014. doi:10.1109/UPEC.2014.6934793.
- [26] J. Kang, R. Yu, X. Huang, S. Maharjan, Y. Zhang, and E. Hossain. Enabling Localized Peer-to-Peer Electricity Trading among Plug-in Hybrid Electric Vehicles Using Consortium Blockchains. *IEEE Transactions on Industrial Informatics*, 13(6):3154–3164, 2017. doi:10.1109/TII.2017.2709784.
- [27] S. Bahrami and M. H. Amini. A decentralized trading algorithm for an electricity market with generation uncertainty. *Applied Energy*, 218(February):520–532, 2018. arXiv:1705.02577, doi:10.1016/j.apenergy.2018.02.157.
- [28] Y. Chen, W. Wei, F. Liu, E. E. Sauma, and S. Mei. Energy Trading and Market Equilibrium in Integrated Heat-Power Distribution Systems. *IEEE Transactions on Smart Grid*, PP(c):1–1, 2018. doi:10.1109/TSG.2018.2849227.
- [29] A. De Paola, D. Angeli, and G. Strbac. Price-Based Schemes for Distributed Coordination of Flexible Demand in the Electricity Market. *IEEE Transactions on Smart Grid*, 8(6):1386–1393, 2017. doi:10.1109/CDC.2017.8263848.
- [30] C. Long, J. Wu, Y. Zhou, and N. Jenkins. Peer-to-peer energy sharing through a two-stage aggregated battery control in a community Microgrid. *Applied Energy*, 226(March):261–276, 2018. doi:10.1016/j.apenergy.2018.05.097.
- [31] M. Khorasany, Y. Mishra, and G. Ledwich. Auction Based Energy Trading in Transactive Energy Market with Active Participation of Prosumers and Consumers. *2017 Australasian Universities Power Engineering Conference (Aupec)*, 2017. doi:10.1109/AUPEC.2017.8282470.
- [32] W. Kou and S. Y. Park. Game-theoretic approach for smartgrid energy trading with microgrids during restoration. *IEEE Power and Energy Society General Meeting*, 2018-Janua:1–5, 2018. doi:10.1109/PESGM.2017.8274437.
- [33] C. Zhang, J. Wu, Y. Zhou, M. Cheng, and C. Long. Peer-to-Peer energy trading in a Microgrid. *Applied Energy*, 220(February):1–12, 2018. doi:10.1016/j.apenergy.2018.03.010.
- [34] W. Tushar, C. Yuen, H. Mohsenian-Rad, T. Saha, H. V. Poor, and K. L. Wood. Transforming Energy Networks via Peer to Peer Energy Trading: Potential of Game Theoretic Approaches. *IEEE Signal Processing Magazine*, 35(July):90–111, 2018. arXiv:1804.00962, doi:10.1109/MSP.2018.2818327.
- [35] M. Millisterfer. *Transaktive Kontrolle in Projekten und Aktuellen Umsetzungen (Bachelor Arbeit)*. Technical University of Munich, 2018.

- [36] E. Mengelkamp, J. Gärttner, K. Rock, S. Kessler, L. Orsini, and C. Weinhardt. Designing microgrid energy markets: A case study: The Brooklyn Microgrid. *Applied Energy*, 210:870–880, 2018. doi:10.1016/j.apenergy.2017.06.054.
- [37] T. Morstyn, A. Teytelboym, and M. D. McCulloch. Bilateral Contract Networks for Peer-to-Peer Energy Trading. *IEEE Transactions on Smart Grid*, 3053(c):1–10, 2018. doi:10.1109/TSG.2017.2786668.
- [38] W. El-Baz, P. Tzscheuschler, and U. Wagner. Day-ahead probabilistic PV generation forecast for buildings energy management systems. *Solar Energy*, 171, 2018. doi:10.1016/j.solener.2018.06.100.
- [39] W. El-Baz, M. Eldakadosi, and C. Eren. P3- Prediction System. sep 2018. URL: <https://welbaz.github.io/p3/>, doi:10.5281/ZENODO.1412785.
- [40] W. El-Baz, P. Tzscheuschler, and U. Wagner. Experimental study and modeling of ground-source heat pumps with combi-storage in buildings. *Energies*, 11(5), 2018. doi:10.3390/en11051174.
- [41] I. F. Nymeyer. United States Patent. (723), 1971.
- [42] D. G. Devine and B. W. Marion. The Influence of Consumer Price Information on Retail Pricing and Consumer Behavior: Reply. *American Journal of Agricultural Economics*, 62(2):267, may 1980. doi:10.2307/1239699.
- [43] T. N. Cason and D. Friedman. Price formation in double auction markets. *Journal of Economic Dynamics and Control*, 20(8):1307–1337, 1996. doi:10.1016/0165-1889(95)00901-9.
- [44] A. M. Jadhav, N. R. Patne, and J. M. Guerrero. A Novel Approach to Neighborhood Fair Energy Trading in a Distribution Network of Multiple Microgrid Clusters. *IEEE Transactions on Industrial Electronics*, 0046(c), 2018. doi:10.1109/TIE.2018.2815945.
- [45] P. Goncalves Da Silva, D. Ilic, and S. Karnouskos. The Impact of Smart Grid Prosumer Grouping on Forecasting Accuracy and Its Benefits for Local Electricity Market Trading. *IEEE Transactions on Smart Grid*, 5(1):402–410, 2014. doi:10.1109/TSG.2013.2278868.
- [46] M. N. Faqiry, S. Member, and S. Das. Double-Sided Energy Auction in Microgrid : Equilibrium Under Price Anticipation. 2016.
- [47] Y. Zhou, J. Wu, and C. Long. Evaluation of peer-to-peer energy sharing mechanisms based on a multiagent simulation framework. *Applied Energy*, 222(February):993–1022, 2018. doi:10.1016/j.apenergy.2018.02.089.
- [48] S. Yoav and L.-B. Kevin. *MULTIAGENT SYSTEMS Algorithmic, Game-Theoretic, and Logical Foundations*. 2008. doi:10.1007/978-3-319-17130-2.

- [49] D. P. Friedman and J. Rust. The Double Auction Market: Institutions, Theories, and Evidence. In *Santa Fe Institute Studies in the Sciences of Complexity Proceedings*, volume 1993, pages 103–103. Routledge, 1993. doi:10.1016/j.joms.2013.02.009.
- [50] M. D. Haas and M. A. Zoican. Discrete or continuous trading? HFT competition and liquidity on batch auction markets. Technical report, 2016.
- [51] B. Asare-Bediako, W. Kling, and P. Ribeiro. Multi-agent system architecture for smart home energy management and optimization. *IEEE PES ISGT Europe 2013*, pages 1–5, 2013. doi:10.1109/ISGTEurope.2013.6695331.
- [52] W. El-Baz and P. Tzscheutschler. Co-simulation of a smart home model based on a micro electricity market. *Proceedings of the Fifth German-Austrian IBPSA Conference RWTH Aachen University*, pages 30–37, 2014.
- [53] S. Oberleitner. Impact of country-specific requirements on the costs of charging stations infrastructure ( Bachelor Thesis), 2017.
- [54] J. Lipp and F. Sanger. Potential of power shifting using a micro-CHP units and heat storages. Naples, Italy, 2013. Microgen3.
- [55] W. El-Baz, M. Seufzger, S. Lutzenberger, P. Tzscheutschler, and U. Wagner. Impact of probabilistic small-scale photovoltaic generation forecast on energy management systems. *Solar Energy*, 165, 2018. doi:10.1016/j.solener.2018.02.069.
- [56] J. P. Lipp. Flexible Stromerzeugung mit Mikro-KWK-Anlagen, 2015.
- [57] W. El-Baz, J. Honold, L. Hardi, and P. Tzscheutschler. High-resolution dataset for building energy management systems applications. *Data in Brief*, 54:1–5, 2018. doi:10.1016/j.dib.2017.12.058.
- [58] ESI ITI. SimulationX 3.8 — Green City.
- [59] EPISCOPE. IEE Project TABULA.
- [60] T. Tjaden, J. Bergner, J. Weniger, and V. Quaschnig. Representative electrical load profiles of residential buildings in Germany with a temporal resolution of one second. *Working Paper. HTW Berlin -HTW Berlin - University of Applied Sciences Research*, pages 1–7, 2015. doi:10.13140/RG.2.1.5112.0080.
- [61] J. Lipp and J. Jungwirth. Field Test with Stirling Engine Micro-CHP-Units in Residential Buildings. *MicroGEN II Conference*, 2011.
- [62] BSW Solar. EEG 2017 - feste Einspeise- vergütungen im Überblick vergütungen im Überblick \*. (April):1–2, 2018.
- [63] L. Kiesel. Optimal Occupancy Based Heating Algorithm for Multiple Single Family Home Types (Bachelor Thesis), 2015.

## **A.5 Publication 5 — Evaluation of Energy Market Platforms Potential in Microgrids: Scenario Analysis Based on a Double-Sided Auction**

### **Abstract**

Local energy markets represent a mean for distributed energy resources trading for prosumers and energy management for utilities. In these markets, prosumers either trade or shift their loads to maximize their trading gains via communicating with an energy market platform. The utility considers the trading process as an approach to maximize autonomy and minimize peak loads. The benefits of the prosumer and utility can vary depending on several parameters such as market rules, microgrid configurations, or lifestyle and social behavior of market participants. In this paper, selected scenarios are presented that discuss and analyze the major factors influencing the market dynamics and microgrid energy balance. These scenarios are divided into three scenario groups that consider market design parameters, microgrid configurations, and user behavior. A forward double-sided auction market model is used to evaluate these scenarios. Furthermore, the same scenarios are evaluated once more using a reference model, where no market platform is integrated, so that the results of the energy market can be compared. The results are analyzed based on multiple metrics from the perspectives of the prosumer and utility to quantify and compare the benefits of the two major market players.

### **Author Contribution**

I performed the scenario analysis and wrote the paper; Peter Tzscheutschler and Ulrich Wagner contributed to the scenario selection, revised the paper and provided a detailed critical review.

# 1 Introduction

Societies are transforming the traditional fossil fuel-based supply into a sustainable energy supply that is more environmentally friendly and economically viable. In Germany, energy system transformation is being realized through expanding the renewable energy sources' (RES) share and increasing energy efficiency [1]. Along the way of the energy transition, the nature of the electricity grid is transforming. The dependency on centralized power stations is decreasing, and electricity is being increasingly generated by small power systems that are distributed all over the grid. Between 2002 and 2017, the installed RES increased from 18 GW to 111 GW. Photovoltaic systems (PV) represent the highest share of the RES, where the capacity increased from 0.3 GW to 42.71 GW within the same period [1, 2]. According to [3, 4], 39.4% of the PV capacity is owned by the residential sector, while 19.2% is owned by the commercial and industrial sectors. As much as these figures indicate the progress of energy transition, it demonstrates the extent of transformation in the national grid, and the necessity to modernize the way of managing the grid to adapt to the growing RES. Using conventional concepts to manage bi-directional power flow is no longer valid. Moreover, more roles are being assigned to distribution network operators and energy consumers as well. Thus, traditional consumers are being transformed into prosumers, thus, becoming more aware of the energy system. Hence, using prosumers' flexibility is becoming more socially acceptable, as long as they are financially compensated.

Energy markets in microgrids represent not only an approach for energy trading between prosumers but also for demand side management. As discussed in [5], energy markets can overcome several challenges faced by current energy management systems such as scalability, decision decentralization, and data privacy. However, energy markets are among the most complex trading markets, given the nature of the energy product. The energy product is highly customizable and is exposed to several technical and commitment constraints [6]. Hence, there are numerous factors and possibilities to design and run the market.

The developments in information and communication technologies and introduction of the Blockchains increased the number of research discussing the applications of energy markets at the microgrid and distribution level [7, 8, 5, 9, 10]. [11] compared the centralized against the distributed trading approaches in the low voltage network under different optimization goals to demonstrate the importance of local energy markets. [12] developed a decentralized energy trading algorithm, where uncertainties of generation were considered. [13] presented an hour-ahead energy market, where a market subscription charge was used as a price signal. In [14], multiple energy sharing mechanisms based on a multi-agent framework were evaluated. The authors discussed the economic and technical benefits of the presented models for residential prosumers. Other studies were

performed to investigate different game theoretic approaches [15], prosumer grouping possibilities [9], scalability [16], or even weather forecasts requirements [17]. Using the Blockchain technology, [18] discussed the required components for designing an energy market for microgrids. [19] presented an electricity trading market for electric vehicles (EVs) using consortium Blockchain. [20] applied game theoretic approaches and Blockchains to enable transactions between individuals in the microgrid. [21] proposed a transaction model as a service for the prosumers. The authors worked on increasing the energy system efficiency while maintaining transparent and secure transactions.

The scenarios presented in the literature were limited given the multiple possibilities of market, microgrid, and prosumers' building configurations. [19, 22] studied EVs integration in microgrids energy markets. In the model of [23], micro turbines, wind turbines, and PV systems were present in a real-time single sided auction market. In this model, the prosumers were absent, and the loads were assumed to be fixed. [24] and [25] studied the integration of combined heat and power systems (CHPs) into the energy markets. [25] presented a multi-lateral trading model, yet prosumers were not actively integrated.

The objective of this paper is to analyze multiple scenarios of energy markets in microgrids to quantify the benefits of the prosumer and utility under different technical and economic constraints. The scenario analysis covers the following aspects:

- Market design parameters such as the trading intervals and market pricing mechanisms.
- Microgrid configurations that can be represented by the number of prosumers and installed RES capacities participating in the market.
- User behavior that influences the available flexibility within a building such as the fixed load consumption share.

The structure of the paper is as follows: Section 2 shortly describes the used market design and its concept of operation. Moreover, it presents the input parameters and defines the scenario groups. Section 3 demonstrates and discusses the results of the different scenario groups of both the market and reference model. Section 4 presents a conclusive summary of the whole study.

## 2 Methods and input data

### 2.1 Description of the model used

[26] presented a discrete-timely double-sided auction market, where prosumers can trade their energy for different time horizons. Figure 2.1 shows an overview of the model structure and the communication process. The model consists of different components such as a market platform, a home energy management system (HEMS), a market agent, a device controller, and devices  $D$ . At the prosumer level, a user interface is available to communicate the user preferences (UP). A forecasting system for the available RES and fixed load is necessary for forward trading. At the microgrid level, a billing system is required to inform the users about their costs. Additionally, the market platform can receive a real-time price (RTP) from the utility or directly from the wholesale market.

In the market model presented in [26], the market agent behaves depending on the type of device it is connected to. Thus, there is an independently operating market agent with a different strategy for each of the PV, EV, micro-CHP and heat pump. Depending on the device status and the UP, the market agent develops a bid  $b_i$  or  $b_j$ , where  $i$  is the index of a buyer (i.e., consuming device) and  $j$  is the index of a seller (i.e., generation device). The market rules define the bid price  $p_i$  or  $p_j$  such that  $p_{min} \leq p_i, p_j \leq p_{max}$ , where  $p_{min}$  and  $p_{max}$  are the feed-in price and import price of the utility, respectively. Hence, the market agent always creates the bid price between the predefined market ceiling and floor.

Once the market agent develops the bid, it is forwarded to the HEMS so that it can be modified depending on the chosen operation (comfort - cost saving). Additionally, the HEMS bids on behalf of the user fixed loads consumption  $q_f$  at a bid price always equal to  $p_{max}$  so that the bids can always be accepted by the prosumers or utility.

The market platform receives all the bids from the  $N$  participating prosumers to clear the market. The market clearing price is denoted by  $p_e$ . In this market model, the prosumers have the right to change their bids at any time until the time of the gate closure  $t_g$ . Also, they have the right to trade at any forward trading horizon. The benefit of the prosumer is evaluated based on Equation 2.1, where  $q^\alpha$  denotes an accepted bid volume and  $n$  is the number of buyers or sellers bids.

$$\varpi = \sum_1^n (p_{max} - p_e) q_{i,n}^\alpha + \sum_1^n (p_e - p_{min}) q_{j,n}^\alpha \quad (2.1)$$

For more details about market mathematical formulation, market rules, clearing process, and insights on the market dynamics, please refer to [26].

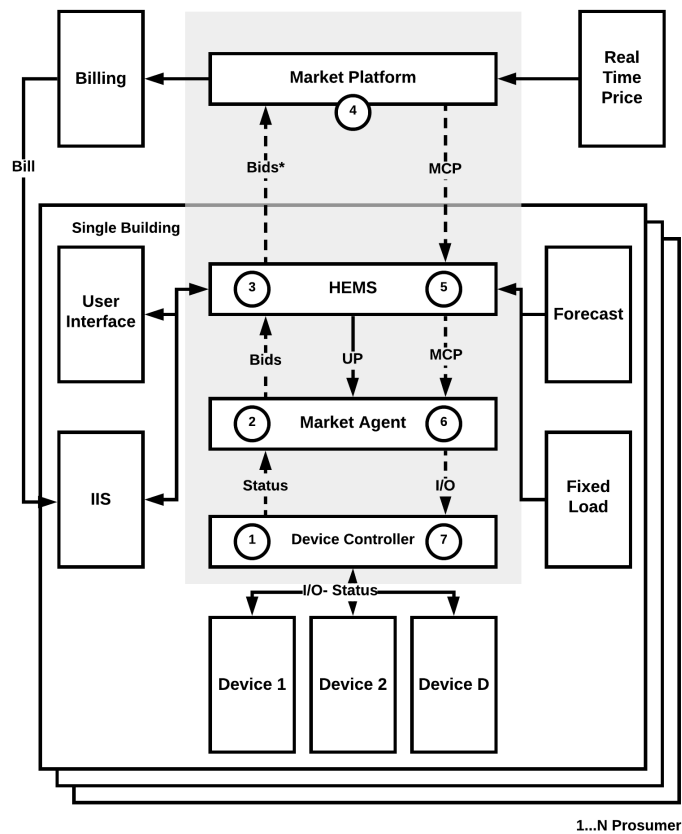


Figure 2.1: An overview of the model structure.

## 2.2 Scenarios definition

There is a various number of possible scenarios that can be used to analyze the behavior of an energy market in a microgrid. These scenarios can vary depending on the market design parameters which are not limited to trading time horizon, trading time interval, market rules, bidding strategies, and pricing mechanisms. At the microgrid level, several combinations can be analyzed for different microgrid sizes, distributed capacities, storage devices, and technical constraints. At the prosumer level, the type of devices integrated, their capacities and setup can vary. As an example, if a heat pump is installed, different storage sizes can be analyzed. Additionally, the building type and size, heat curves, set temperatures, and night setback can define the prosumer load curve.

The user behavior and lifestyle also have an impact on the prosumers bids in the market. The more available flexible loads, the higher is the potential of the prosumer to trade in the market. User preferences and optimization goals can also play an important role. However, they have to be defined based on the society where the market is used.

Calculating the combinations of these variables requires high computational capacity and time. Thus, specific scenarios are selected to represent the market behavior under the most probable configurations. In this paper, three scenario groups are discussed as per Figure 2.2.

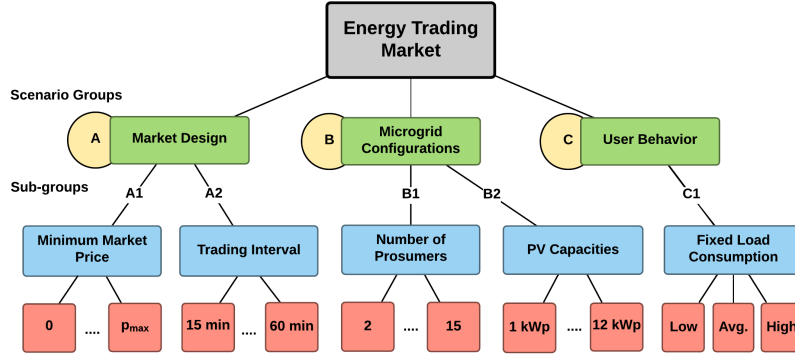


Figure 2.2: An overview of the scenario groups.

Group A discusses the market design variables such as  $p_{min}$  and trading intervals. The scenarios of A1 vary  $p_{min}$ , while holding every other variable constant as shown in Table 2.1.  $p_{min}$  is varied at a constant step size between 0 and  $p_{max}$ . At  $p_{min} = 0$ , the prosumers might not get any profit for their feed-in from the utility or trading in the market, but might be able to operate the loads at lower costs. At  $p_{min} = p_{max}$ , the market is inactive, as the market price is fixed. The goal behind the scenarios of A1 is to show the influence of different feed-in tariffs and foreseeable market fees on the benefits of the prosumers and the utility.

The influence of the trading intervals is also analyzed in group A. The trading interval  $\Delta t$  is varied between 15 and 60 minutes. The goal behind varying the trading intervals is to quantify the benefits of higher trading frequency, given the same system configuration and forecast quality.

Group B discusses the microgrid configurations, where the influence of the number of prosumers and the installed PV capacities are studied. An important aspect that needs to be analyzed is the number of participants required to operate the market. Given the decentralized structure presented in [26], each device in a prosumer’s building is a market participant. Hence, the number of market participants is the number of prosumers multiplied by the number of devices at each prosumer’s house. In this scenario group, the number of prosumers is varied between 2 and 15. Two represents the minimum possible number of prosumers and 15 is the simulation system limit, as each building and device is modeled non-linearly in Modelica. Additionally, the average peak load reaches a plateau for any microgrid size with more than 10 prosumers as discussed in the literature by [27]. Thus, evaluating a large number of prosumers would not be helpful.

Another sub-group of scenarios addresses the influence of the installed PV capacity at

each prosumer's building. The capacities are varied from 1 kWp to 12 kWp, which are the expected PV capacities to be possibly installed at a prosumer's building. The goal behind this scenario is to evaluate the influence of the over- and under-capacity on the market prices, prosumer, and utility.

The last group, group C, evaluates the user behavior. Although the user behavior can be evaluated based on different variables, fixed load consumption is used as an indicator of the user behavior and lifestyle. Three categories define the user consumption level: low, average and high. The range of each level is explained in the next section. The goal behind this scenario group is to present the influence of the fixed load consumption magnitude on the prosumer's profitability and behavior in the market.

Within this paper, a separate analysis is performed on each group of scenarios independently. The analysis discusses the results from both the utility's and the prosumer's perspective, as they are the two main stakeholders of the market. Furthermore, the scenarios are always compared to a reference case (no market) and the baseline scenario. The comparison can be performed based on several metrics, yet to summarize the results, only self-sufficiency, self-consumption, peak load, and costs are evaluated. Table 2.1 summarizes the scenarios including the constant and changing variables.

**Table 2.1:** Input parameters of the scenario groups

Scenario Groups	Variables							
	Max. Price	Min. Price	Trading Int.	Num. of Pros.	PV Capacity	EV	HP	Fixed Load Cons.
<b>Group A</b>								
A1	/	×	/	/	/	/	/	/
A2	/	/	×	/	/	/	/	/
<b>Group B</b>								
B1	/	/	/	×	/	/	/	/
B2	/	/	/	/	×	/	/	/
<b>Group C</b>								
C1	/	/	/	/	/	/	/	×

/ indicates that the value is constant

× indicates that value is changing

## 2.3 Baseline Scenario and Input Data

The baseline scenario is represented by a 10 single family houses microgrid located in Munich, Germany. It is assumed that these single-family houses are occupied by low energy consuming prosumers, and are equipped with a heat pump, an EV charging station, and a PV system. The fixed loads of the prosumers are based on the high-resolution measurements of [28]. All the measured households are connected to the same distributor. Thus, it can be assumed that they are located in proximity to each other and can represent a microgrid. Figure 2.3(a) presents the distribution of the households yearly energy consumptions, and Figure 2.3(b) presents the 10th to 90th percentiles of power variation over time on a typical day. From the typical day profile, it can be assumed that no PV is installed at these houses, given the load peak at noon. Also, no operation patterns of a heat pump, an EV charging station, or a micro-CHP are found in the separate analysis of the household profiles. Hence, it can be deduced that there are no flexible devices in these houses and these profiles can be treated as fixed load profiles.

Using the consumption distribution presented in Figure 2.3(a), the households consuming 1000-3000 kWh/a, 3001-7000 kWh/a, and 7001-9000 kWh/a are defined to be occupied by low, average, and high energy consuming prosumers, respectively. 10 representative profiles are picked from each category to represent the user behavior in scenario group C.

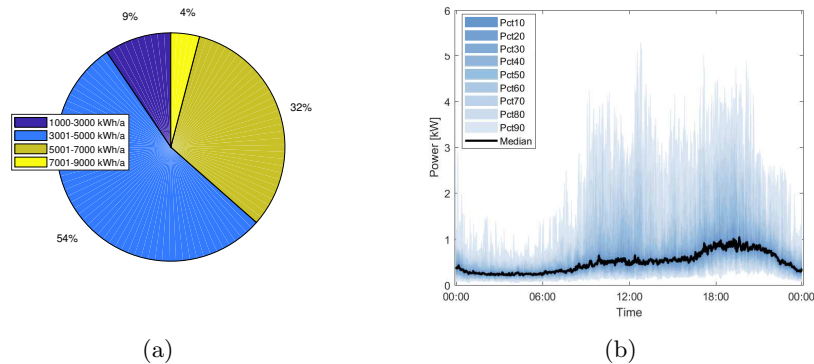


**Figure 2.3:** 74 representative household profile analyses, a) annual energy consumption b) electrical loads on a typical day.

The integrated heat pump has  $10.1 \text{ kW}_{th}$ , and a COP of 5.02 at B0/W35 according to the standard EN14511. The heat pump is responsible for covering the space heating and domestic hot water consumption through a 749 l combi-storage. The detailed system description and hydraulic configuration are in [29].

A conventional single-phase charging station is integrated with a power of 3.6 kW. The driving cycle of the EV is based on the worldwide harmonized light duty driving test cycle (WLTC) of class 3 [30]. The vehicle is assumed to be for private use on working

## A Appendix

days and weekends. More information on the implemented model is available in [31].

A 6 kWp PV system is integrated in each single-family house. The power profile of the year 2017 is used and scaled up based on the data of [32]. The prediction of the PV system is based on the work of [33, 34].

The building model is configured based on the research project data of [35]. A building of a single floor, a cellar, and an attic is integrated. The building construction year is between 1984 and 1994. It has a heated living area of 150 meters and a room height of 2.5 meters. The attic and cellar are assumed to be unheated, while the living area is heated based on a supply temperature curve that varies linearly depending on the outside temperature. The hot water consumption is defined based on the standard VDI 4655. The hot water circulation consumption is based on the field measurements of [36].

In the base scenario, the trading interval is set to 60 mins. The utility is assumed to be always participating to balance the market. Hence, the  $p_{max}$  and  $p_{min}$  are set by the utility according to the fixed import and feed-in tariff, respectively. The fixed import is 0.26 €/kWh, and the feed-in tariff is 0.12 €/kWh as per the EEG 2017 [37]. An RTP signal could have been implemented, yet it would have led to suppressing several effects in the selected scenarios (e.g., the impact of constant minimum price).



## 3 Results

### 3.1 Overview

This section describes the results of the analysis of the 3 aforementioned scenario groups. The scenarios are variations of the baseline scenario and are always compared to the reference scenario (no market). Each scenario was run for a complete year to represent the behavior of the system in all the seasons. The overall number of market model and reference scenarios is 98. Four metrics are used to evaluate the presented scenarios: self-sufficiency, self-consumption, peak load, and costs. Self-sufficiency describes the share of energy demand supplied by the prosumer, while self-consumption describes the share of on-site generated energy consumed by the prosumer. The peak load shows the maximum import load of the microgrid. Costs are calculated from the perspective of the prosumer to quantify the possible cost savings using the market model. The same metrics are used to quantify the benefits of the utility at the microgrid level.

### 3.2 Group A: Market design

Group A discusses two major factors influencing the market behavior. In A1, the impact of different minimum market prices on the load shifting behavior in the microgrid and the profitability of the prosumers is investigated. Figure 3.1 presents the results of multiple metrics against different values of  $p_{min}$ . It can be seen that the self-sufficiency, self-consumption, and peak load are almost constant and the cost results of the market model are always better than the reference. Self-sufficiency and Self-consumption are doubled, and the peak load is reduced for all the houses. At  $p_{min} = 0.24$ , which is 0.02 less than  $p_{max}$ , the results falls in comparison to the lower  $p_{min}$  values. This behavior occurs due to the small difference between  $p_{min}$  and  $p_{max}$  that negatively influences the market clearing algorithm and optimization models of the markets agents. At  $p_{min} = p_{max}$ , the market cannot operate since the price, in this case, is fixed and there are no incentives for the prosumers to trade their energy or shift their loads.

The costs are evaluated based on Equation 2.1. As shown in Figure 3.1(d), the costs of the market and reference model decrease as  $p_{min}$  increases. This reaction occurs as the prosumer gets the chance to feed-in energy at higher prices. Furthermore, it can be seen that the cost savings linearly decrease, as  $p_{min}$  increases. In other words, given that  $p_{max}$  is constant and equal to 0.26, the cost savings are directly proportional to  $\Delta p = p_{max} - p_{min}$ . At  $p_{min} = 0$ ,  $\Delta p = 0.26$ , the cost savings are around 30%, compared to 8% at  $p_{min} = 0.24$ ,  $\Delta p = 0.02$ .

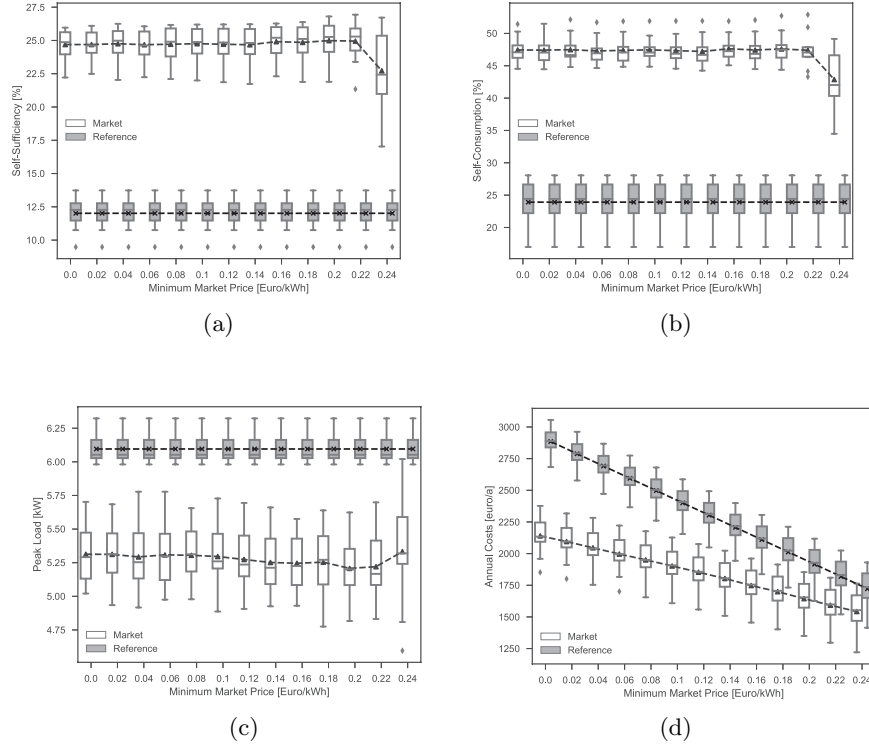


**Figure 3.1:** Metrics of the scenario subgroup A1, a) self-sufficiency, b) self-consumption, c) peak load, d) annual costs.

From another perspective, the increase in  $p_{min}$  can be seen as  $p_{min-basescenario} = 0$  plus transaction fees, utility fees, or ICT service fees. In all these cases, only the prosumer's costs are going to change. The load shifting behavior and overall load curve of the microgrid are not going to be influenced by any changes of additional fees, as long as there is still a minimal difference between the market floor and ceiling. Hence, if fees have to be charged to the prosumers by the market operator for using the platform or by the utility for using the grid to exchange energy, the magnitude of the fees should maintain at least minimal amount of profit or cost savings for the prosumers. Otherwise, the market will fail to operate as an energy management system.

In A2, different trading intervals are investigated. Figure 3.2 compares the 15, 30, and 60 min trading intervals' normalized results depending on the given metrics. The results are normalized to the highest absolute value of the same metric. Self-sufficiency decreases slightly as the trading interval increases. It can be seen that the difference is  $< 1.5\%$ . The standard deviation of the 15 min is also smaller than that of 30 and 60 min. Self-consumption exhibits the same behavior of self-sufficiency, where the 15 min is higher than the 30 and 60 mins. However, in this case, no significant difference can be noticed between the 30 and 60 min. The peak loads and annual costs in the 15 min trading interval are the lowest.

## A Appendix

The performance of the 15 min trading interval is always better than other trading intervals, as it enables the market agents to adapt the bids to the load curves without additional averaging. Also, it helps in placing bids that fit better with the supply curves of the PV systems. In a real-life environment, the prosumer can only place a bid and communicate with the market platform according to the forecast resolution constraints. Thus, if the forecasting resolution is half-hourly, but the trading intervals are quarter-hourly, the prosumer will place the bids on a half-hourly basis. In this model, the integrated probabilistic forecast has an hourly-resolution. A linear interpolation was used to increase the resolution of the forecast so that the scenarios of the 15 min and 30 min intervals can be evaluated. Although the results are in favor of the 15 min trading intervals, better results could have been achieved if the forecasting systems had higher resolutions.

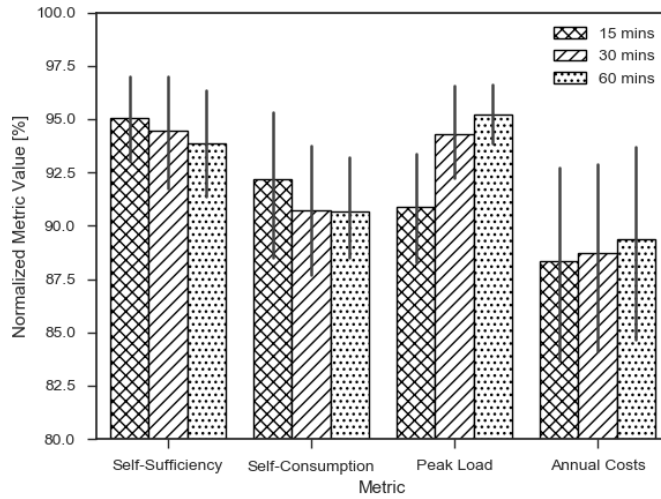


**Figure 3.2:** Comparison between different trading intervals at the prosumer level.

At the microgrid level, Table 3.1 shows the absolute values of the given metrics for different trading intervals using the market and reference models.  $\delta$  is calculated as  $\delta = \frac{Market - Reference}{Reference} \times 100$ . It can be seen that self-sufficiency and self-consumption for the whole microgrid decrease as the trading intervals increases.  $\delta$  drops from 134.1% to 122.4% and from 128.1% to 115.2% for self-sufficiency and self-consumption, respectively. Moreover, the peak load increases from 37.5 kW to 40.6 kW at the 60 min trading interval. This leads to a change in  $\delta$  by 6.2%. At the microgrid level, costs and cost savings are not calculated as they are calculated for each prosumer. The reference model values at the different trading intervals are constant as no market platform is integrated.

**Table 3.1:** Comparison between different trading intervals at the microgrid level.

Scenario	Self-Sufficiency [%]			Self-Consumption [%]			Peak Load [kW]		
	Market	Reference	$\delta$	Market	Reference	$\delta$	Market	Reference	$\delta$
15 mins	30.2	12.9	134.1	58.4	25.6	128.1	37.5	50.5	-25.7
30 mins	29.6	12.9	129.4	57.1	25.6	123.1	39.1	50.5	-22.6
60 mins	28.7	12.9	122.4	55.1	25.6	115.2	40.6	50.5	-19.5

### 3.3 Group B: Microgrid configuration scenarios

In group B, the impact of different microgrid configurations on the market is discussed. In B1, the influence of the number of prosumers on the microgrid and the market is described. Figure 3.3 shows the self-sufficiency, self-consumption, peak load and annual costs of a 2 to 15 prosumer microgrid. Generally, it can be seen that the market can operate properly even with a small number of prosumers. No major changes can be seen after 4 prosumers. The most affected measure is the standard deviation. As the number of prosumers increases, the standard deviation increases, which is typical in a real-life situation.

Self-sufficiency decreases slightly after 4 prosumers and then maintains an almost constant mean. This can be due to the fact that the first 4 houses have a lower yearly energy consumption. On the other hand, the self-consumption increases from 2 to 4 prosumers and then remains constant. In this case, the same behavior can be seen in the reference model.

The peak load increases as the number of prosumers increases. The reference model is not influenced by the increase in the number of prosumers, as much as the market model. The maximum standard deviation spread of the market model is between approximately 4.9 and 5.9 kW, compared to approximately 5.95 kW and 6.3 kW for the reference model. On the other hand, the mean varies between approximately 5.1 kW and 5.3 kW, compared to 6.1 kW for the reference model.

The mean annual cost also increases as the number of prosumers increases. However, it can be noticed that the market and the reference model increase almost simultaneously. This means that the increase in the annual costs is due to the addition of households with relatively higher energy consumption and not due to the inefficiency of the market model. The difference between the two means is almost constant in every case.

Figure 3.4 provides another insight at the microgrid level. Compared to self-sufficiency at the prosumer level, self-sufficiency at the microgrid level is almost constant as the number of prosumers increases. On the other hand, self-consumption at the microgrid level shows a similar behavior to self-consumption at the prosumer level, where it increases until four prosumers and then stays constant. Similar to the peak load at the prosumer level, the peak load at the microgrid level increases as the number of prosumers increases. However, it can be seen that the difference between the market and the reference model also increases. Thus, the percentage of peak load reduction achieved by the market

## A Appendix

improves as the microgrid size increases.

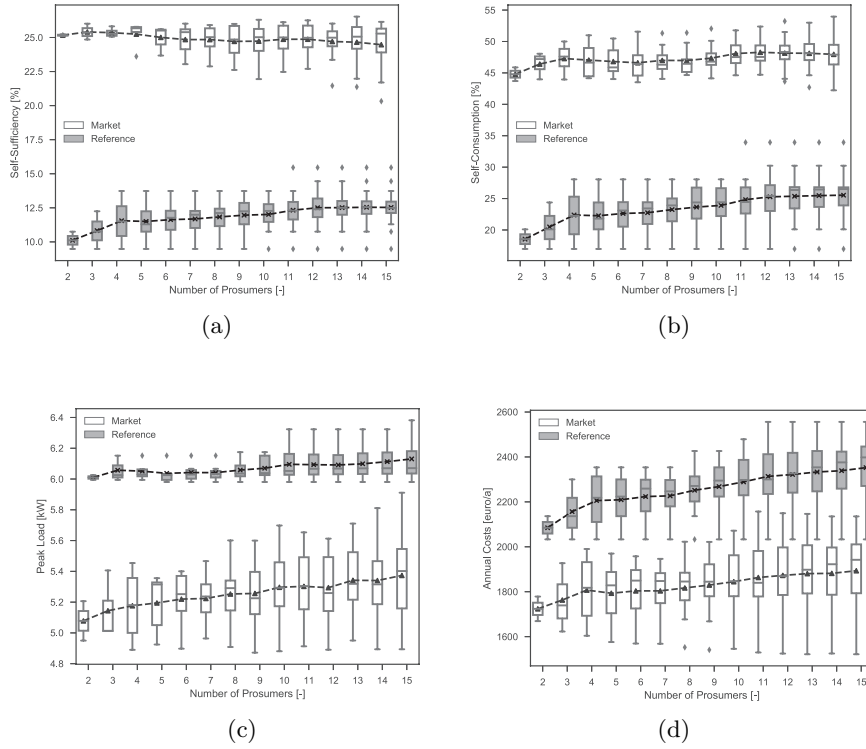


**Figure 3.3:** Metrics of scenario subgroup B1 at the prosumer level, a) self-sufficiency, b) self-consumption, c) peak load, d) annual costs.

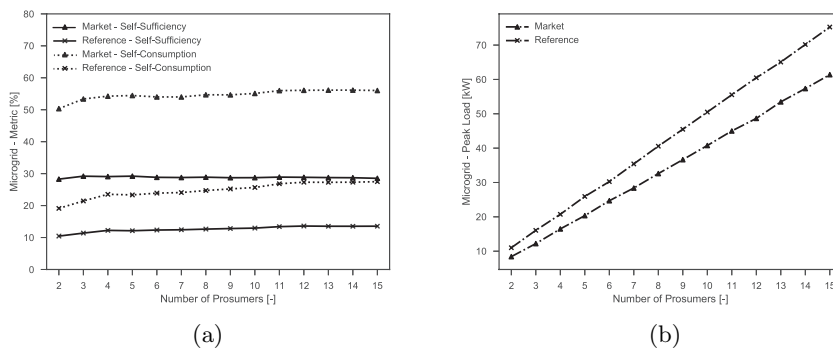


**Figure 3.4:** Metrics of scenario subgroup B1 at the microgrid level, a) self-sufficiency and self-consumption, b) peak load.

Another aspect that can be studied among several others is the increase in PV capacity installed at each prosumer's house. In B2, the PV capacity is varied from 1 to 12 kWp. Figure 3.5 shows the results of the given metrics for different PV capacities. The self-sufficiency of all the houses with the market model increases as the PV capacity rises. Also, the gap between the self-sufficiency of the market and that of the reference model increases in proportion with the installed PV capacity. It can be seen that at 1 and 2 kWp the difference in self-sufficiency is not significant compared to that of higher PV capacities. This is because the installed capacities are high enough to enable load shifting or trading. This interpretation can be assured by the self-consumption analysis. It can be seen that at 1 and 2 kWp the market and the reference model are almost identical and 45 to 65% of the PV energy is consumed on site. As the PV capacity increases, the reference model's self-consumption decreases. On the other hand, the self-consumption of the market model increases from 2 to 5 kWp. After 5 kWp, the self-consumption decreases due to the excess capacity of the PV system.

Using the reference model, the peak load of each prosumer does not change significantly, compared to the market model. This is because some loads operate after sunset, yet these loads are shifted using the market model. Hence, a linear decrease in the peak load can be seen, as the PV capacity increases.

The annual costs using the reference or market model decrease linearly as the PV capacity increases. This is because in both cases, the excess PV energy is supplied to the grid either at the market clearing price or at the fixed feed-in tariff for the market or the reference model, respectively. However, it can be noticed that the gap between the market and the reference model increases as the PV capacity increases. This gap indicates that the prosumers benefit from trading the excess energy supply as in Equation 2.1.

On the microgrid level, similar behavior can be observed for the self-sufficiency as the prosumer level. However, the magnitude of self-consumption is higher at the microgrid level. It can be seen that at 1 and 2 kWp the difference between the market and the reference is higher compared to the same case at the prosumer level.

Although the mean peak load of the prosumers is always higher using the reference model than the market model as in Figure 3.5(c), the peak load using the market model at the microgrid level is higher at 1 and 2 kWp than the reference model. The lack of energy supply in the market led to using the generated energy locally inside the prosumers' houses and exhibiting the same load shifting behavior. Thus, the peak load of the market model exceeds that of the reference model. As the volume of excess energy increases in the market, the lower the peak load gets. It can be seen that the peak load drops from 55 kW to 35.5 kW at 12 kWp PV.

## A Appendix

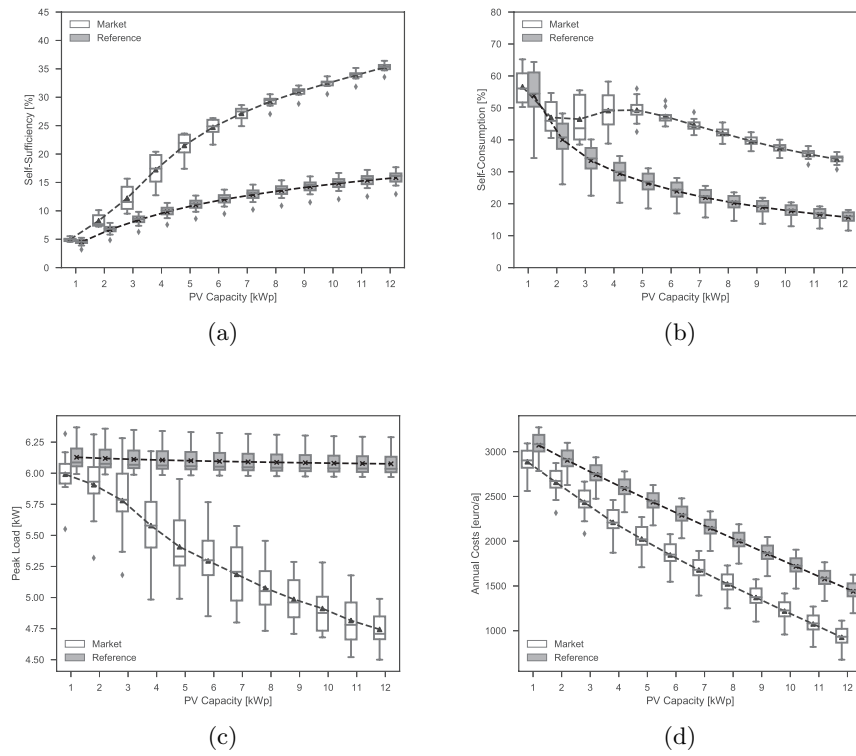


**Figure 3.5:** Metrics of the scenario subgroup B2, a) self-sufficiency, b) self-consumption, c) peak load, d) annual costs.

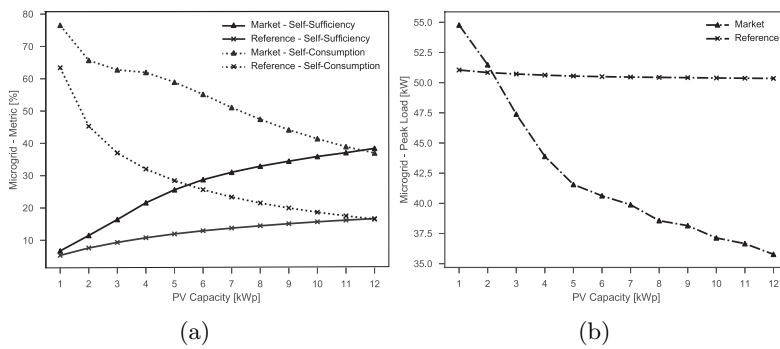


**Figure 3.6:** Metrics of scenario subgroup B2 at the microgrid level, a) self-sufficiency and self-consumption, b) peak load.

### 3.4 Group C: User behavior scenarios

Several variables can be used to study the impact of user behavior on the market platform. In group C, the fixed load consumption is used to indicate the user behavior. Since all the households have the same types and magnitude of flexible loads, higher fixed loads consumption means a lower share of flexible loads. Hence, more energy can be consumed locally by the household itself, and less can be shared with the market. Figure 3.7 compares the different consumption behavior of the prosumers against the metrics. The results are normalized based on the highest absolute value of the same metric. As anticipated, prosumers with the lowest fixed load energy consumption have the highest self-sufficiency, lowest self-consumption, peak loads, and annual costs.

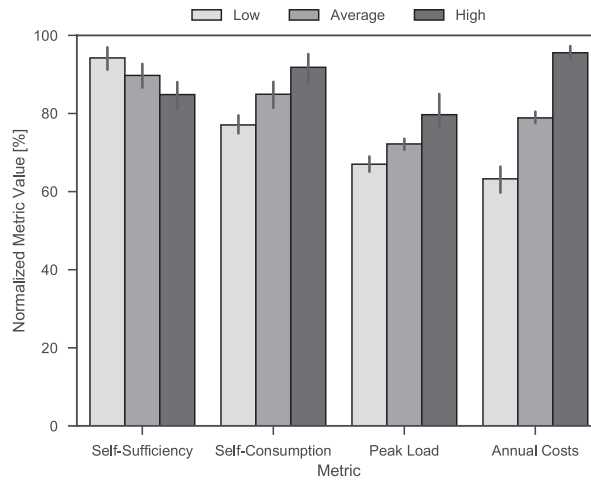


**Figure 3.7:** Comparison between different consumption behavior at the prosumer level.

The presented results in Figure 3.7 are valid and foreseen for the market and the reference model. However, the advantage of the market model over the reference model cannot be recognized. Hence, Figure 3.8 shows the benefits of the low, average and high consuming prosumers using the proposed metrics. These results show the normalized absolute value of the  $\delta$  of each metric. It can be seen that prosumers with the lowest fixed load energy consumption are the ones benefiting most from the market model. These prosumers can achieve the highest self-sufficiency and self-consumption. The differences in the peak load reduction are not as high as self-sufficiency, yet the prosumers with the low fixed load energy consumption are achieving the highest peak load reduction. Similar behavior can also be seen at the annual cost savings metric.

The reason behind the high benefits claimed by the prosumers with the low fixed load energy consumption is their capability to offer a higher share of the PV and their overall electrical energy consumption. The HEMS of the prosumers with high loads between 7000 kWh/a and 9000 kWh/a always eliminates the PV bids to satisfy the fixed load demands. Moreover, the HEMS always bids the fixed loads with a price equal to  $p_{max}$

## A Appendix

to guarantee the operation of the fixed loads. Hence, the higher the fixed load energy consumption of the prosumer, the less are the overall benefits from the market.

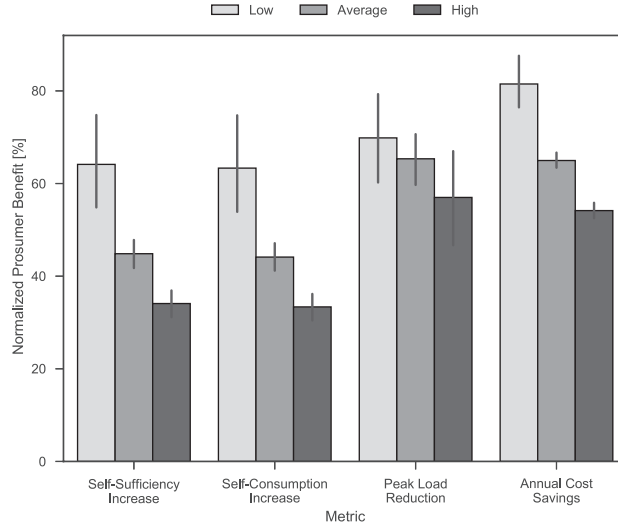


**Figure 3.8:** Benefits of different prosumers based on the fixed load consumption.

The analysis at the microgrid level shows another perspective. Table 3.2 shows the absolute values of the self-sufficiency, self-consumption, and peak load. It can be seen that as the fixed load consumption increases, the self-sufficiency of the whole grid using the reference model increases, yet it decreases using the market model. The 2.3% increase between low and high using the reference model can be driven by the share of load increase occurring during the availability of PV generation. Comparing the reference and market, it can be seen that between low and high, the  $\delta$  of self-sufficiency dropped from 122.4% to 65.4%, which is almost 50% decrease.

Self-consumption of the market and the reference model behaves similarly. Between low and high, self-consumption increases from 55.1% to 64.1% for the market model, and from 25.6% to 39.7% for the reference model. Although self-consumption increases in both models, the  $\delta$  decreases from 115.2% to 61.4%. This result builds upon the results of the same metric at the prosumer level in Figure 3.8. Hence, it can be deduced that increasing the share of the fixed load reduces the efficiency of the market.

Similarly, the peak load increases for both of the market and the reference model. This leads to decreasing the peak load reduction capability of the market model. The  $\delta$ , in this case, increases from -19.5 to -14.4%. Hence, 5.1% is lost due to changing the consumer behavior from low (1000-3000 kWh/a) to high (7001-9000 kWh/a).

**Table 3.2:** Comparison between different consumption behavior at the microgrid level.

Scenario	Self-Sufficiency [%]			Self-Consumption [%]			Peak Load [kW]		
	Market	Reference	$\delta$	Market	Reference	$\delta$	Market	Reference	$\delta$
Low	28.7	12.9	122.4	55.1	25.6	115.2	40.6	50.5	-19.5
Average	26.8	14.1	90.0	59.5	32.3	84.2	44.4	53.7	-17.3
High	25.3	15.2	65.4	64.1	39.7	61.4	48.0	56.1	-14.4

## 4 Conclusions

This paper presents a scenario analysis of an energy trading market model in microgrids. The used market model enables the prosumers to trade their energy supply and demand within the microgrids. This model does not only support the prosumers via offering a possibility for additional economic incentives but also presents the utility a decentralized approach to manage the microgrid and maintain the prosumers' privacy. Hence, the results were analyzed at the prosumer level and microgrid level to make sure that the two main stakeholders of the microgrid could be encouraged to participate in the market platform.

98 selected scenarios are presented. These scenarios are divided into three different groups. The first group studied market design parameters, the second group studied different microgrid configuration, and the third group studied the influence of the user behavior. The results of the three scenario groups can be summarized as follows:

- The capability of the market model to act as energy management system is independent of the price ranges ( $p_{max} - p_{min}$ ) or the transaction or service fees imposed by the market operator. The prosumers profit is the only sensitive output to the market prices and fees; however, the prosumer will keep bidding as long as there is a minimal profit.
- Trading intervals and resolutions can improve the benefits of the market model, yet the forecasts' resolution limits their impact. Forecast resolution should match the trading intervals to maximize the benefits of the market platform to the utility and prosumers.
- Number of prosumers and devices influence the performance of the market. The used model showed its capability to operate with 2 prosumers, 3 devices each. After 5 prosumers, 15 devices, the benefits of the market reach a plateau.
- Increasing the PV capacity in the microgrid influences directly the self-sufficiency, and self-consumption, even if no market platform is integrated. However, the market model can double the self-sufficiency and self-consumption of the microgrid. Moreover, it leads to a linear decrease in the peak loads and annual costs of the prosumers.
- Multiple parameters can be varied to indicate multiple user behavior. However, fixed load consumption is found to be able to reflect prosumer lifestyle, habits and consumption level. Based on the field measurements of different residential household, the results show that the higher the share of fixed loads, the lower is

the efficiency of the market. Hence, prosumers with the lowest share of fixed loads are expected to profit the most from the market platforms in microgrids.

Energy market platforms performance is highly dependent on the nature of the market, microgrids, and prosumers. In this paper, the most fundamental scenarios are presented. However, there is room for studying other multiple market design parameters, technical constraints or social behaviors. In future studies, the realization of these market platforms is still to be discussed under different national legislations and ICT constraints. Moreover, the impact of these local markets on the regional electricity market and the overall national grid is still to be investigated.

## Bibliography

- [1] Renewable Energies Agency. Press Fact Sheet: The German Energy Transition. *Berlin Energy Transition Dialogue*, (March):1–16, 2016. URL: <https://www.energiewende2016.com/>.
- [2] Bundesministerium für Wirtschaft und Energie. BMWi - Erneuerbare Energien, 2017.
- [3] H. Maron, H. Klemisch, and B. Maron. Marktakteure erneuerbare Energie-Anlagen in der Stromerzeugung. (August):1–92, 2011.
- [4] Federal Ministry for Economic Affairs and Energy (BMWi). Renewable Energy Sources in Figures. *National and International Development*, page 80, 2017. URL: [http://www.bmwi.de/Redaktion/EN/Publikationen/renewable-energy-sources-in-figures-2016.pdf?\\_\\_blob=publicationFile&v=5](http://www.bmwi.de/Redaktion/EN/Publikationen/renewable-energy-sources-in-figures-2016.pdf?__blob=publicationFile&v=5).
- [5] W. El-Baz and P. Tzscheuschler. Autonomous coordination of smart buildings in microgrids based on a double-sided auction. In *2017 IEEE Power & Energy Society General Meeting*, number August, pages 1–5, Chicago, jul 2017. IEEE. URL: <http://ieeexplore.ieee.org/document/8273944/>, doi:10.1109/PESGM.2017.8273944.
- [6] A. Weidlich and D. Veit. A critical survey of agent-based wholesale electricity market models. *Energy Economics*, 30(4):1728–1759, 2008. doi:10.1016/j.eneco.2008.01.003.
- [7] G. Santos, T. Pinto, H. Morais, Z. Vale, and I. Praca. Multi-agent Simulation of Continental, Regional, and Micro Electricity Markets. *2012 23rd International Workshop on Database and Expert Systems Applications*, pages 331–335, sep 2012. URL: [http://ieeexplore.ieee.org/lpdocs/epic03/wrapper.htm?arnumber=6327448http://ieeexplore.ieee.org/xpls/abs\\_all.jsp?arnumber=6327448](http://ieeexplore.ieee.org/lpdocs/epic03/wrapper.htm?arnumber=6327448http://ieeexplore.ieee.org/xpls/abs_all.jsp?arnumber=6327448), doi:10.1109/DEXA.2012.78.
- [8] M. C. Hu, S. Y. Lu, and Y. H. Chen. Stochastic programming and market equilibrium analysis of microgrids energy management systems. *Energy*, 113:662–670, 2016. URL: <http://dx.doi.org/10.1016/j.energy.2016.07.061>, doi:10.1016/j.energy.2016.07.061.
- [9] P. Goncalves Da Silva, D. Ilic, and S. Karnouskos. The Impact of Smart Grid Prosumer Grouping on Forecasting Accuracy and Its Benefits for Local Electricity

- Market Trading. *IEEE Transactions on Smart Grid*, 5(1):402–410, 2014. doi: 10.1109/TSG.2013.2278868.
- [10] K. N. Khaqqi, J. J. Sikorski, K. Hadinoto, and M. Kraft. Incorporating seller/buyer reputation-based system in blockchain-enabled emission trading application. *Applied Energy*, 209(September 2017):8–19, 2018. URL: <https://doi.org/10.1016/j.apenergy.2017.10.070>, doi:10.1016/j.apenergy.2017.10.070.
- [11] J. Guerrero, A. Chapman, and G. Verbic. A study of energy trading in a low-voltage network: Centralised and distributed approaches. *2017 Australasian Universities Power Engineering Conference (AUPEC)*, pages 1–6, 2017. URL: <http://ieeexplore.ieee.org/document/8282502/>, doi:10.1109/AUPEC.2017.8282502.
- [12] S. Bahrami and M. H. Amini. A decentralized trading algorithm for an electricity market with generation uncertainty. *Applied Energy*, 218(February):520–532, 2018. URL: <https://doi.org/10.1016/j.apenergy.2018.02.157>, arXiv:1705.02577, doi:10.1016/j.apenergy.2018.02.157.
- [13] M. Khorasany, Y. Mishra, and G. Ledwich. Auction Based Energy Trading in Transactive Energy Market with Active Participation of Prosumers and Consumers. *2017 Australasian Universities Power Engineering Conference (Aupec)*, 2017. doi: 10.1109/AUPEC.2017.8282470.
- [14] Y. Zhou, J. Wu, and C. Long. Evaluation of peer-to-peer energy sharing mechanisms based on a multiagent simulation framework. *Applied Energy*, 222(February):993–1022, 2018. URL: <https://doi.org/10.1016/j.apenergy.2018.02.089>, doi:10.1016/j.apenergy.2018.02.089.
- [15] W. Tushar, C. Yuen, H. Mohsenian-Rad, T. Saha, H. V. Poor, and K. L. Wood. Transforming Energy Networks via Peer to Peer Energy Trading: Potential of Game Theoretic Approaches. *IEEE Signal Processing Magazine*, 35(July):90–111, 2018. URL: <http://arxiv.org/abs/1804.00962>, arXiv:1804.00962, doi: 10.1109/MSP.2018.2818327.
- [16] S. A. Janko and N. G. Johnson. Scalable multi-agent microgrid negotiations for a transactive energy market. *Applied Energy*, 229(April):715–727, 2018. URL: <https://doi.org/10.1016/j.apenergy.2018.08.026>, doi:10.1016/j.apenergy.2018.08.026.
- [17] A. Agüera-Pérez, J. C. Palomares-Salas, J. J. González de la Rosa, and O. Florencias-Oliveros. Weather forecasts for microgrid energy management: Review, discussion and recommendations. *Applied Energy*, 228:265–278, 2018. URL: <https://doi.org/10.1016/j.apenergy.2018.06.087>, doi:10.1016/j.apenergy.2018.06.087.
- [18] E. Mengelkamp, J. Gärttner, K. Rock, S. Kessler, L. Orsini, and C. Weinhardt. Designing microgrid energy markets: A case study: The Brooklyn Microgrid. *Applied*

## A Appendix

- Energy*, 210:870–880, 2018. URL: <https://doi.org/10.1016/j.apenergy.2017.06.054>, doi:10.1016/j.apenergy.2017.06.054.
- [19] J. Kang, R. Yu, X. Huang, S. Maharjan, Y. Zhang, and E. Hossain. Enabling Localized Peer-to-Peer Electricity Trading among Plug-in Hybrid Electric Vehicles Using Consortium Blockchains. *IEEE Transactions on Industrial Informatics*, 13(6):3154–3164, 2017. doi:10.1109/TII.2017.2709784.
- [20] S. Noor, W. Yang, M. Guo, K. H. van Dam, and X. Wang. Energy Demand Side Management within micro-grid networks enhanced by blockchain. *Applied Energy*, 228(April):1385–1398, 2018. URL: <https://doi.org/10.1016/j.apenergy.2018.07.012>, doi:10.1016/j.apenergy.2018.07.012.
- [21] J. Hwang, M. I. Choi, T. Lee, S. Jeon, S. Kim, S. Park, and S. Park. Energy Prosumer Business Model Using Blockchain System to Ensure Transparency and Safety. *Energy Procedia*, 141:194–198, 2017. URL: <https://doi.org/10.1016/j.egypro.2017.11.037>, doi:10.1016/j.egypro.2017.11.037.
- [22] A. Kriukov, B. Vicol, and M. Gavrilas. Applying a micro-market inside an electric vehicles parking facility. *Proceedings of the Universities Power Engineering Conference*, 2014. doi:10.1109/UPEC.2014.6934793.
- [23] M. Marzband, A. Sumper, A. Ruiz-álvarez, J. L. Domínguez-García, and B. Toimoiagã. Experimental evaluation of a real time energy management system for stand-alone microgrids in day-ahead markets. *Applied Energy*, 106:365–376, 2013. doi:10.1016/j.apenergy.2013.02.018.
- [24] T. R. Nudell, M. Brignone, M. Robba, A. Bonfiglio, F. Delfino, and A. Annaswamy. A Dynamic Market Mechanism for Combined Heat and Power Microgrid Energy Management. *IFAC-PapersOnLine*, 50(1):10033–10039, 2017. URL: <https://doi.org/10.1016/j.ifacol.2017.08.2040>, doi:10.1016/j.ifacol.2017.08.2040.
- [25] Y. Chen, W. Wei, F. Liu, and S. Mei. A multi-lateral trading model for coupled gas-heat-power energy networks. *Applied Energy*, 200:180–191, 2017. URL: <http://dx.doi.org/10.1016/j.apenergy.2017.05.060>, doi:10.1016/j.apenergy.2017.05.060.
- [26] W. El-Baz, P. Tzscheuschler, and U. Wagner. Integration of Energy Markets in Microgrids: A Double-Sided Auction with Device-Oriented Bidding Strategies).
- [27] M. Huber, F. Sanger, and T. Hamacher. Coordinating smart homes in microgrids: A quantification of benefits. In *IEEE PES ISGT Europe 2013*, number c, pages 1–5. IEEE, oct 2013. URL: <http://ieeexplore.ieee.org/document/6695357/>, doi:10.1109/ISGTEurope.2013.6695357.
- [28] T. Tjaden, J. Bergner, J. Weniger, and V. Quaschnig. Representative electrical load profiles of residential buildings in Germany with a temporal resolution of one

- second. *Working Paper. HTW Berlin -HTW Berlin - University of Applied Sciences Research*, pages 1–7, 2015. doi:10.13140/RG.2.1.5112.0080.
- [29] W. El-Baz, P. Tzscheuschler, and U. Wagner. Experimental study and modeling of ground-source heat pumps with combi-storage in buildings. *Energies*, 11(5), 2018. doi:10.3390/en11051174.
- [30] M. Tutuianu, A. Marotta, H. Steven, E. Ericsson, T. Haniu, N. Ichikawa, and H. Ishii. Development of a World-wide Worldwide harmonized Light duty driving Test Cycle. *Technical Report*, 03(January):7–10, 2014. doi:10.3141/2503-12.
- [31] ESI ITI. SimulationX 3.8 — Green City. URL: <https://www.simulationx.com/simulation-software/simulationx3-8.html>.
- [32] W. El-Baz, J. Honold, L. Hardi, and P. Tzscheuschler. High-resolution dataset for building energy management systems applications. *Data in Brief*, 54:1–5, 2018. doi:10.1016/j.dib.2017.12.058.
- [33] W. El-Baz, P. Tzscheuschler, and U. Wagner. Day-ahead probabilistic PV generation forecast for buildings energy management systems. *Solar Energy*, 171, 2018. doi:10.1016/j.solener.2018.06.100.
- [34] W. El-Baz, M. Seufzger, S. Lutzenberger, P. Tzscheuschler, and U. Wagner. Impact of probabilistic small-scale photovoltaic generation forecast on energy management systems. *Solar Energy*, 165, 2018. doi:10.1016/j.solener.2018.02.069.
- [35] EPISCOPE. IEE Project TABULA. URL: <http://episcope.eu/iee-project/tabula/>.
- [36] J. Lipp and J. Jungwirth. Field Test with Stirling Engine Micro-CHP-Units in Residential Buildings. *MicroGEN II Conference*, 2011.
- [37] BSW Solar. EEG 2017 - feste Einspeise- vergütungen im Überblick vergütungen im Überblick \*. (April):1–2, 2018.

## A.6 Publication 6 — Hardware in the loop (HiL) for Micro CHP systems

### Abstract

Micro combined heat and power (CHP) systems have been always offering multiple potential advantages compared to conventional thermal or electric power generation systems. At the Institute of Energy Economy and Application Technology (IEE), micro CHP test beds based on multiple technologies have been set up to be evaluated under different operating conditions and control schemes. The performed evaluations and applied control schemes have been dependent on the static load being fed to the test bed. The static load has been representative for the system evaluation, yet the system dynamics have been concealed during operation. To provide an accurate analysis of a micro CHP system, the experimental analysis and simulation must tend to show out the system dynamics under multiple real-life conditions. To achieve this goal, a Hardware in the loop (HiL) test bed has been set up on site. In this system, a Stirling engine based micro CHP, Whispergen 1 kWe-14.5kWth, is used along with an 800 liter heat buffer storage in a simulation loop. The loop includes as well a single family house, room temperature controller, and the micro CHP controller. The hardware data acquisition system is based on LabVIEW, while the single family house, temperature controller, and micro CHP controller have been modelled in SimulationX, a Modelica based software. A Matlab code has been also developed to act as a communication manager between the two programs, LabVIEW and SimulationX. Throughout this contribution, a novel test approach of a HiL system will be presented that enhance both accuracy and flexibility of the running system. Detailed description of both the software and the hardware side will show the system operation strategy and the interactions between them. Furthermore, system performance will be analyzed to evaluate the system general functionality, accuracy, robustness, and flexibility.

### Author Contribution

I developed the communication system and wrote the paper; Florian Sanger integrated the communication system with the Micro-CHP testbed; Peter Tzscheuschler reviewed the method and the paper.

# 1 Introduction

An affordable, sustainable, and reliable energy supply is one of the fundamental pillars of a stable economy. Consequently, Europe has tended towards a decentralized small-scale energy supply sources in form of renewable energy sources and combine heat and power units [1]. CHPs have presented one of the main competing solutions towards a sustainable energy supply and a pressure relief to the grid due to enabling participation of consumers in the grid and its high availability factor. Consequently, the German government has legalized policies, the Combined Heat and Power Act (KWKG) that empowers CHP systems. Within the KWKG, a goal was set to have a 25% of electricity generated in 2020 by co-generation and to minimize the CO<sub>2</sub> emissions due to power generation [2].

Several micro CHP types have been developed for residential use. At the Institute of Energy Economy and Application Technology (IfE), multiple micro CHP test benches have been set up to evaluate different micro CHP technologies (i.e., Stirling engines, internal combustion engines and fuel cells). They are operated to evaluate the capability of micro CHP to satisfy either or both electricity and heat demand of a household or a building. Yet all these test beds have been operated under a static heat load profile. The building model was initially designed in an independent software then, the heat load was transferred to the micro CHP to fulfill it.

## 1.1 Motivation

Static loads have been the acceptable conventional way to operate the test bed. The static loads might be sufficient in testing the basic operation of the micro CHP, yet it enfolds several dynamics within the operation. These enfolded dynamics might be affecting the comfort of the heated zone through going excessively over or below the reference room temperature. Consequently, a feedback loop was needed not only to ensure the comfort temperature of the zone, but also to evaluate appropriately the micro CHP operation under different operating conditions and control algorithms. Moreover, this feedback loop should allow the investigation of a building thermal mass activation and its impact on micro CHP operation.

## 1.2 Objectives

The objective of this contribution is to present a more accurate simulation system, a Hardware in the Loop (HiL) system, which enables integration of both Micro CHPs as the hardware, and building models within a feedback loop. Consequently, the dynamics

## *A Appendix*

of the HiL system will be presented to show out both of the building zone temperature and the micro CHP reactions to different control scenarios, also to demonstrate the physical system capability to cope up with the simulation system. Through this contribution, the methodology of developing and operating a HiL system will be presented. The data exchange, synchronization methodology, and control parameters will be clarified. Furthermore, results of operation of a micro CHP HiL system will be discussed to demonstrate the ability of integrating both of building simulation and test beds in one environment and in the same loop.

## 2 Simulation system components

### 2.1 Overview

The simulation system has been developed over three platforms, where each of them have a basic rule towards the system coherence and integration. The building models and the micro CHP controllers have been developed using SimulationX with Green Building Package, a Modelica based software, which enables modelling and simulation of building models, energy management systems and micro CHP units as well. On the other hand LabVIEW has been used to control the current test beds setup and acquire data.

To integrate both of the two platforms. Matlab has been used as a HiL manager to coordinate the communication between both SimulationX and LabVIEW. As shown in Figure 2.1, the communication between Matlab and SimulationX is based on a Component Object Model (COM) Interface, while the Transmission Control Protocol/Internet Protocol (TCP/IP) is the communication protocol between Matlab and LabVIEW. The COM is an interface that specifies certain methods which is supported by the object, which is SimulationX in this case. These methods do not stipulate a specific way of implementation, but rather send calls for processing [3]. In other words, Matlab does not dictate SimulationX about the way of processing the data through the COM interface. Matlab just sends calls for reading or writing the data and starting the simulation. On the other hand, Matlab feeds this data to LabVIEW through using the client/server TCP/IP communication protocol that is most commonly used within networks for data exchange.

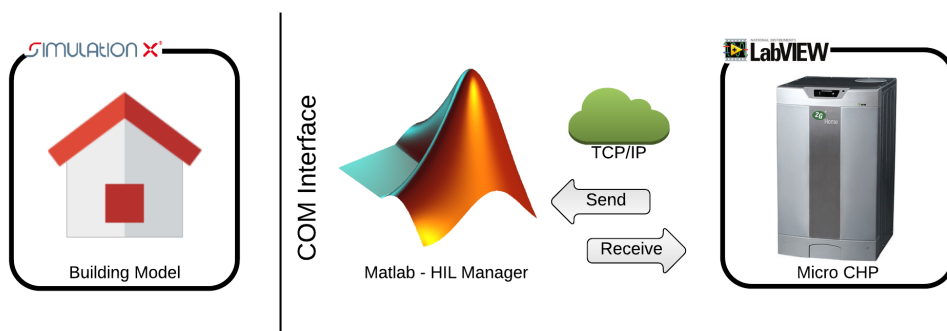


Figure 2.1: HiL communication structure.

## 2.2 Building Model

The main goal behind the building model is to simulate the influences of different factors over the internal zone temperature. These factors include and are not limited to heat transmission through walls, heat bridge losses, solar yields, ventilation losses, internal yields and losses via persons, internal heat storage, and heating via multiple heating systems.

Through SimulationX multiple zones can be independently modeled and interconnected to simulate a whole building. Yet, since the goal is to simulate a single family house. It was modeled as a single temperature zone which has a surface area of 200m<sup>2</sup> and a height of 5m. The heating system used within the single family house was assumed to be a radiator.

It should be mentioned that the heat yields per person such as heat of the body, heat losses due to cold water consumption, and heat yields due to electrical devices operations have been ignored within this model due to their limited effect on the overall heat demand profile.

The hot water demand was not included as well within this model, as a measured hot water demand profile out of a single family house in Miesbach, Germany [4] has been fed directly to the test bed.

## 2.3 Room Temperature Controller

The room temperature control is based on a hysteresis control around a reference room temperature, 21°C. To achieve this temperature, the room temperature controller alters two main variables that significantly affect the amount of energy transferred to the room and heating power, the supply reference temperature to the radiators and the flow rate of the circulation pump. The supply reference temperature has been predetermined through a heating curve that varies linearly based on the ambient temperature. It dictates 35°C for an ambient temperature greater than 15°C and it goes up to 55°C for less than -10°C. Another heating curve, night set-back curve. A night set-back curve has been also used. It has the same exact variation but the temperature drops by 10°C between the following hours 22:00 and 05:00 of the next morning. Within the simulation, the pump flow rate is calculated based on the following equation

$$q_v = \frac{(T_{Ref} + H_{Up} - T_{Act}) \times q_{vmax}}{H_{Up} - H_{Low}} \quad (2.1)$$

- $q_v$ : Pump flow rate
- $q_{vmax}$ : Maximum pump flow rate
- $T_{Ref}$ : Reference room temperature
- $T_{Act}$ : Actual room temperature
- $H_{up}$ : Hysteresis upper limit
- $H_{low}$ : Hysteresis lower limit

Thus, the pump flow rate is simply determined based on the difference between the actual and the reference temperature, as a factor of the maximum flow rate that can be supplied by the pump.

## 2.4 Micro-CHP Controller

The micro CHP controller used is a heat-led controller that fits the natural of the Whispergen Stirling engine outputs. The main inputs to the controller are:

- CHP supply reference temperature
- Heat storage reference temperature
- Temperature of the micro CHP flow
- Temperature of the micro CHP return

The output of the controller is simply a Boolean signal to the micro CHP and the peak load boiler.

The algorithm behind the operation of the micro CHP heat-led controller is simple a hysteresis control around the reference temperature defined by the user. Throughout all the simulations, the heat storage reference temperature is set to 60°C and the micro CHP supply reference temperature is set to 70°C. The upper and lower limit of the hysteresis is set to  $\pm 5\text{K}$ . The peak load boiler control is based on a hysteresis control around the same temperature as well, but with a smaller upper and lower limits  $\pm 3\text{K}$ . Yet, the peak load boiler controller does not switch on unless a specific amount of time has passed without reaching the reference temperature.

## 2.5 Micro-CHP testbed setup

As shown in Figure 2.2, the test bed consists of a 800 liter combined heat buffer (CHB) storage tank [5], which is connected to a Whispergen Stirling engine that has a 7.5-14.5 kW<sub>th</sub> and 1 kW<sub>el</sub> as per [6]. The micro CHP is connected to the heat storage via an internal heat exchanger in which the flow has a constant flowrate. For the Domestic Hot Water (DHW), three pneumatic valves have been set up at different flow rates to simulate different consumption categories of the domestic hot water. The domestic hot water supply is delivered through an internal heat exchanger within the heat storage.

Space heating (SH) is directly supplied through the heat storage. It passes a mixer, as shown in Figure 2.2, through which the space heating flow temperature is set. The flow goes as well through a heat exchanger which connects the heat flow of the heat storage to a 20 kW cooling circuit, that represents the heat demand within the single family house. The flow rate of the cooling circuit is varied to control the return temperature of the space heating according to desired reference value.

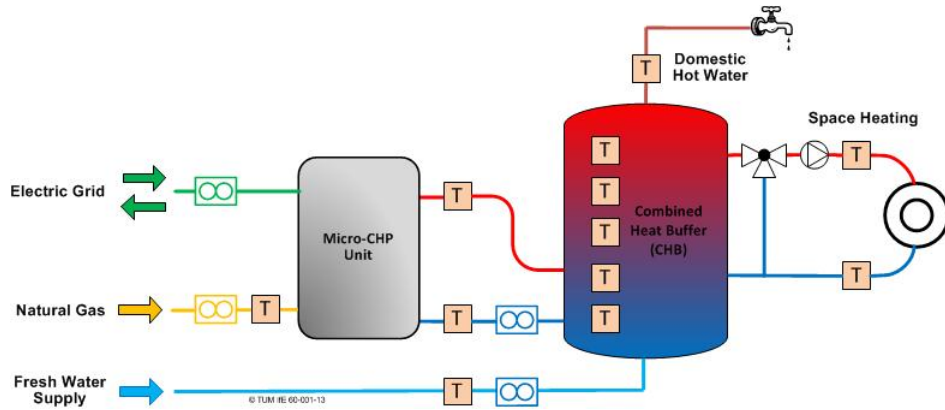


Figure 2.2: Hydraulic Scheme [7].

## 2.6 System integration

Figure 4.6 shows the overall system components integrated in SimulationX. On the top left is the ambience block, which provides the ambient conditions to the building heated zone. Then, the building is connected via temperature and thermal measurement block to a temperature and volume flow defining block. This block simply receives the actual signal from the micro CHP test bed and feeds it into the building model. Also, the return pipe is connected to a similar system to feed back the return temperature as a reference return temperature to the micro CHP.

Also, in Figure 4.6, the room temperature controller can be observed. It is connected to the supply and return temperature sensor, in addition to the actual room temperature so that it can maintain the reference temperature defined by the user. Moreover, it is connected to the heating curve look up table to generate the reference heat supply temperature according to the ambient conditions.

Furthermore, the micro CHP controller is integrated as independent block that is directly connected to the micro CHP via the HiL communication manager to observe the heat storage and the micro CHP supply and return temperature so that it can provide the appropriate control signals.

## 3 Simulation Methodology

### 3.1 Synchronization

Synchronization is one of the most critical requirements that needs to be fulfilled within a HiL system to generate accurate results. The presented HiL system is designed to synchronize and exchange data up to 1-second rate. Such high data exchange rate might not be always needed. Yet, it is preferred to design the system initially to produce the best possible resolution. Within this second, the HiL communication manager must exchange the data between LabVIEW and SimulationX. Also, this second includes the processing time of the SimulationX and data processing code within the HiL communication manager. Thus, achieving such high data communication is highly dependent on the complexity of the model, amount of data exchange, quality of the connection, and the computational power available.

Figure 3.1 shows out the flow chart of the HiL system run. As an initial step, an initialization signal is sent to LabVIEW to initiate the connection. Then, the HiL manager starts up the COM server to communicate with SimulationX as well. At this phase, the HiL communication manager is ready to exchange the data between the two software tools. The data exchange process is a looping process that keeps going till the end of simulation time. To achieve synchronization, the HiL communication manager calculates the processing time of SimulationX and the data processing algorithm. If the processing time is less than one second, it waits the reminder of a second to start the next communication iteration. Yet, if the overall processing time exceeds a second, HiL communication manager automatically fails and recommends decreasing the communication rate.

A post processing code has been developed to collect the data out of SimulationX with a real-time stamp in a time series to be matched with the data and time stamps generated by LabVIEW. Through, this post processing algorithm a validation for the synchronization between LabVIEW and SimulationX can be confirmed. Also, it enables proper analysis to the control signals transferred from SimulationX to LabVIEW. Another important advantage, is that the post processing code makes up for the minor connection losses, as the TCP/IP connection gets lost. At this moment, the post processing can be adjusted to either interpolate linearly or to repeat the last received signal.

### 3.2 Data Exchange

As shown in Figure 3.2 the data being exchanged between the LabVIEW and SimulationX is fixed throughout the whole simulation. The SimulationX initiates the communi-

## A Appendix

cations with LabVIEW through the HiL communication manager, Matlab, with a signal of zeros. Then, the LabVIEW replies back with the values of the following variables:

$T_{Supply}$ : Supply temperature of CHP  
 $T_{Return}$ : Return temperature of CHP  
 $T_{Act}$ : Actual temperature of heat storage  
 $T_{SHsupply,act}$ : Actual SH supply temperature  
 $q_{SH,act}$ : Actual SH supply flow rate

After processing these values within SimulationX, it feeds back the following variables:

$CHP_{ON}$ : CHP switch Boolean  
 $Peak_{ON}$ : Peak load boiler boolean switch  
 $T_{SHsupply,ref}$ : Reference SH supply temperature  
 $T_{SHreturn,ref}$ : Reference SH return temperature  
 $q_{SH,ref}$ : Reference SH supply flow rate

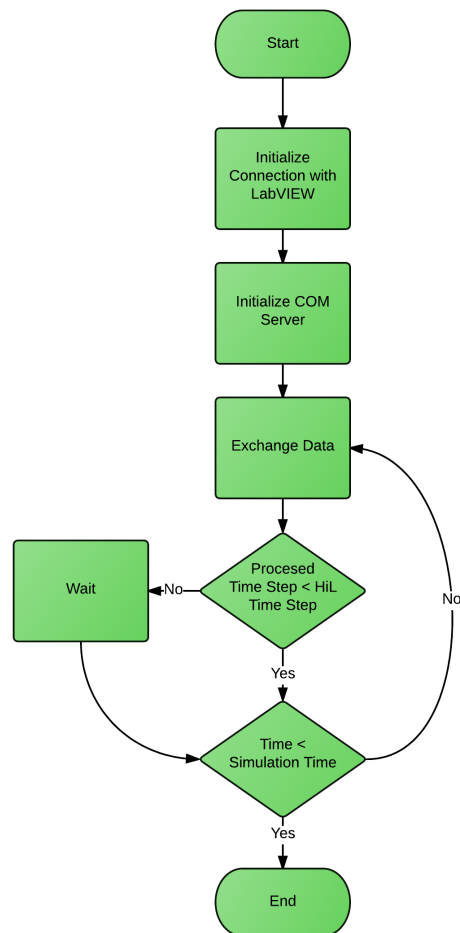


**Figure 3.1:** HiL Flow chart.

The processing within SimulationX is done through two basic blocks, the micro CHP controller and the building model. As previously explained the micro CHP controller receives  $T_{Supply}$ ,  $T_{Return}$  and  $T_{Act}$  to decide whether to switch on the micro CHP and peak load boiler.

The building model processes the input data,  $T_{SHsupply,act}$  and  $q_{SH,act}$ , then based on the current ambient temperature and the building parameters the return temperature,  $T_{SHreturn,ref}$ , is calculated.

Through the COM interface the  $T_{SHreturn,ref}$  is read over and bypassed to LabVIEW through the TCP/IP connection. After the signal is received by LabVIEW, the test bed works on reaching the required,  $T_{SHreturn,ref}$ , through controlling the flow rate of the cooling circuit supplying the heat exchanger that represents the building's thermal load.

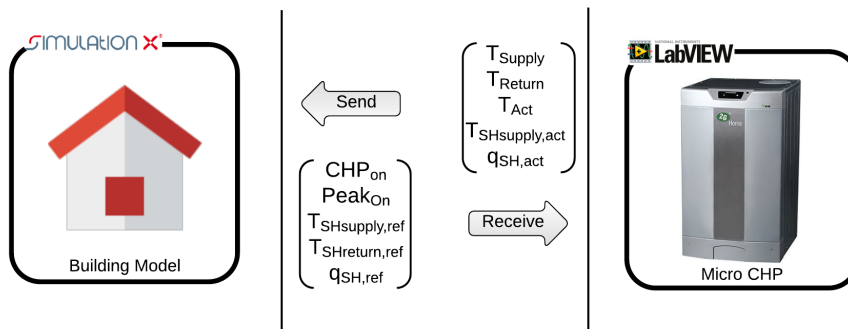


**Figure 3.2:** Data exchange within the HiL.

*A Appendix*

## 4 Results

### 4.1 Micro-CHP control

The initial priority is to validate the operation of the micro CHP controller, to make sure that the most important component of the test bed is well operated. Figure 4.1 shows three basic plots of the SimulationX Boolean signals for the micro CHP and the peak load boiler, the gas and thermal power of the micro CHP, then the 10 temperature sensors that have been installed all over the height of the heat storage tank.

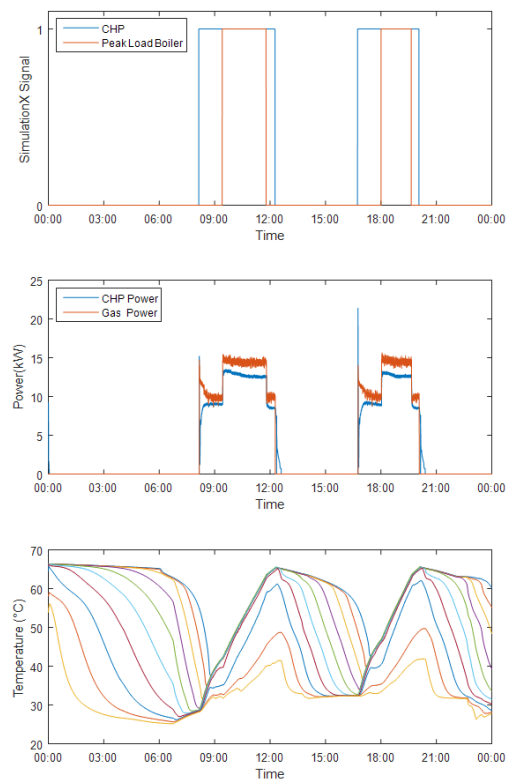


**Figure 4.1:** Micro-CHP control.

As previously explained, the micro CHP controller is a hysteresis controller that con-

## A Appendix

trols the maximum temperature of the heat storage around the reference temperature. Since the reference temperature was set to  $60^{\circ}\text{C}$  and there is an upper and lower limit of  $\pm 5\text{K}$ , the heat storage as shown in Figure 4.1, was charged to a maximum temperature of  $65^{\circ}\text{C}$ . The micro CHP was operated again when the heat storage maximum temperature went down to  $55^{\circ}\text{C}$ .

Throughout the charging and discharging cycles shown, it can be concluded that the system was highly synchronized and was able to maintain an appropriate control over the micro CHP. For the peak load boiler controller, it is based as well on a hysteresis controller around the same reference temperature of the micro CHP,  $60^{\circ}\text{C}$ , but with an upper and lower limit of  $\pm 3\text{K}$ . Yet, the peak load boiler controller is switched on only when the micro CHP fails to reach the reference temperature within 60 minutes. This switching delay can be easily observed within the SimulationX signals. It can be noticed that around 08:30 the micro CHP was switched on, but it could not reach the reference temperature till 09:30. Consequently, the peak load boiler switched on till the maximum temperature of the heat storage reached  $62^{\circ}\text{C}$ , and then switched off back again.

## 4.2 Space heating

To validate the operation of the space heating heat exchangers, the interaction between the SimulationX and the test bed must be evaluated. Such interaction can be analyzed based on the dynamics of the HiL system operation and synchronization. In another words, it can be assessed based on the reaction of the test bed towards the SimulationX signals back and forth. Figure 4.2 can show out the space heating pump reaction towards the SimulationX reference signal. As expected the pump started out with its maximal flow, 0.14 l/s, due to the initial temperature of the zone. Then, it varied along with the variation of the room temperature. It can be noticed that the test bed has been following almost perfectly the SimulationX reference signal.

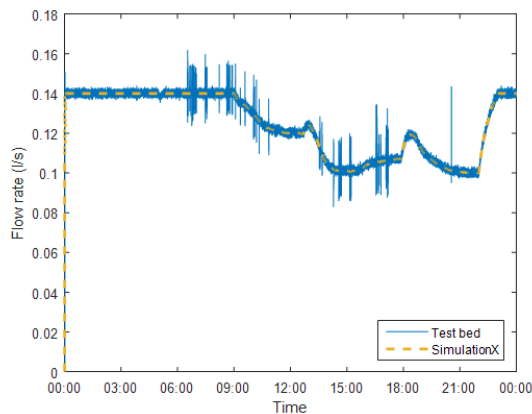


**Figure 4.2:** SimulationX reference flow rate versus the testbed.

Yet, it can be also observed that there are some spikes in the test bed measurements.

These spikes occurred due to the fast response of the pump to the TCP/IP connection loss between the LabVIEW and the HiL communication manager. Despite the occurrence of these minor connection losses, the results have not been majorly affected and the pump was able to restore itself immediately to the reference signal. The TCP/IP connection minor connection losses did not affect the supply and return temperature as much as the pump due to the heated zone inertia. Figure 4.3 can show out the actual supply and return temperatures compared to the SimulationX signal and it can be noticed that there are few spikes compared to the pump.

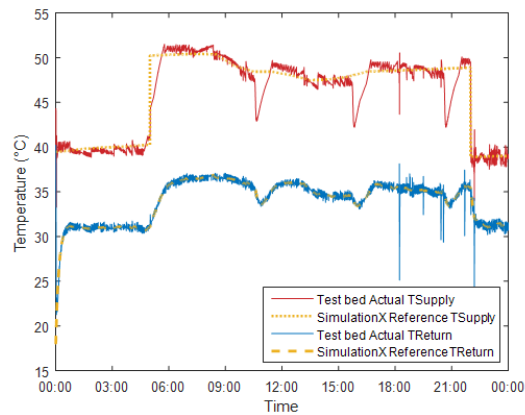


**Figure 4.3:** Actual and reference supply/return temperatures.

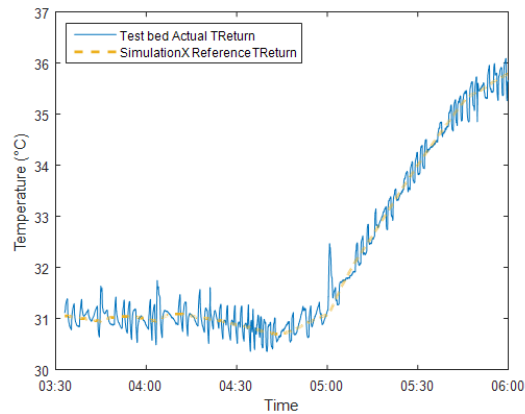


**Figure 4.4:** Return temperature comparison.

For the supply temperature, the variation of the SimulationX reference signal between the morning supply temperature and the night set-back temperature can be observed between 00:00 and 05:00, also between 22:00 and 23:59. With minor tolerance, the test bed was able to successfully follow the SimulationX supply temperature reference signal.

## A Appendix

Also, the return temperature has been perfectly fitted throughout the whole operation. The upper and lower fluctuation have been limited to almost  $\pm 0.5\text{K}$  within most of the operation time steps as presented in Figure 4.4.

The only unusual behavior within Figure 4.3 was the three temperature drops within the day in both of the supply and return temperatures. These temperature drops can be detailed through Figure 4.5. In that figure, the data of 10 temperature sensors that have been installed across the heat storage tank height have been plotted throughout the whole day. T-1 is the uppermost temperature sensor, while T-10 is the lowest temperature sensor.

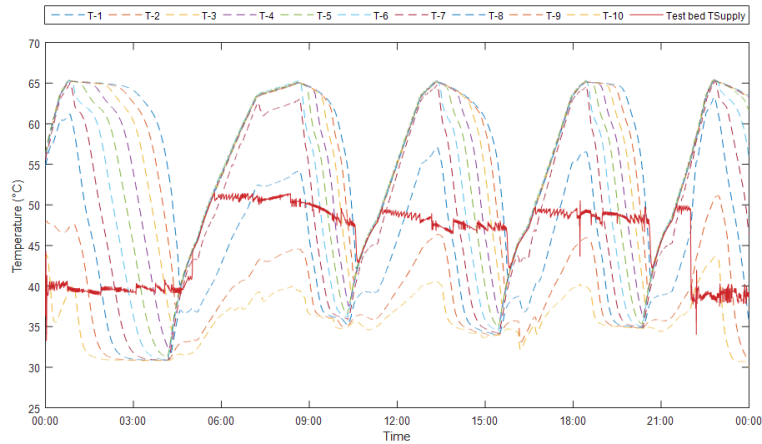


**Figure 4.5:** Heat storage temperature versus space heating supply temperature.

Through comparing the space heating supply temperature to the heat storage tank temperature sensors, it can be concluded that the drop in the space heating supply temperature is due to low storage content. The micro CHP controller switches on when T-1 reaches  $55^{\circ}\text{C}$ , yet the energy demand of space heating and DHW did not enable the micro CHP to make up for the low storage content. Consequently, the space heating supply temperature dropped simultaneously with the storage content. Yet, as soon as the micro CHP started to charge back the heat storage tank, the space heating supply temperature increased accordingly back to the reference value. Same conclusions can be drawn at 05:00, it can be noticed that the SimulationX had a reference supply temperature signal of  $50^{\circ}\text{C}$ , yet the test bed could not satisfy it due to low storage content.

The effect of low space heating supply temperature has been reflected on the return temperature. It can be noticed that the return temperature dropped as well, but not as significantly as the supply temperature due to the zone heat inertia. Such reaction of the return temperature represents one of the main advantages of the HiL system over the static loads feed to the test bed. In similar situation using static loads, the test bed decreases the return temperature of the space heating significantly to fulfill the same desired heating power.

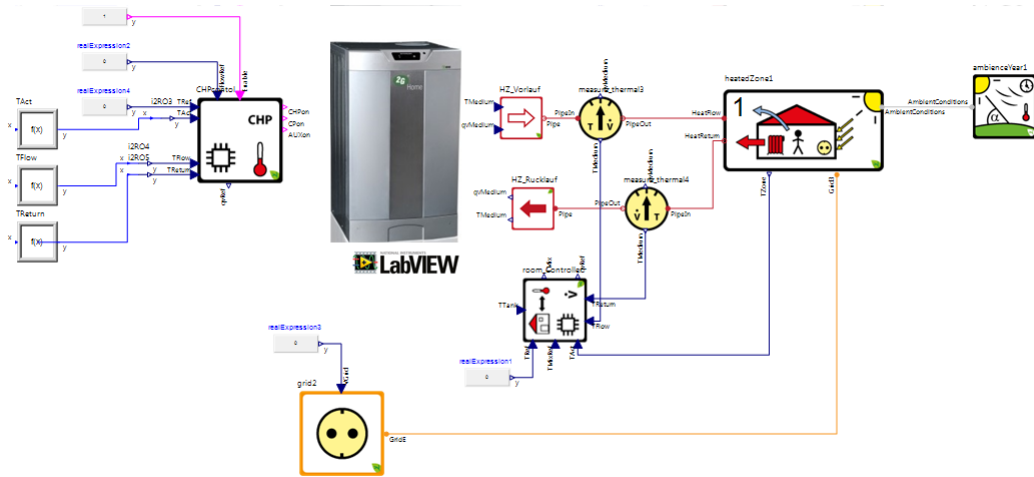


Figure 4.6: The SimulationX model.

## *A Appendix*

## 5 Conclusion and outlook

Throughout this contribution, a HiL system has been presented. The methodology of integrating both of building simulation and test bed control software has been detailed. Also, the components of each system, the test bed and SimulationX, have been shown along with their integration into one environment. A HiL communication manager has been developed over Matlab to enable communication and synchronization between LabVIEW and SimulationX.

Within the results of this contribution, it can be concluded that the designed HiL system is able to successfully takeover the control of the test bed. Also, it has been proven that system is capable of simulating accurately a realistic single-family house with all the possible conditions that could be raised throughout space heating. An example was presented to show out the effect low heat storage content on space heating supply temperature and the ability of SimulationX to reflect the fluctuation of the supply temperature over the return temperature of the heated zone. Including these dynamics into the system evaluation do not only lead to proper evaluation to the energy consumed by the building, but also it can easily show out the thermal comfort of the house occupants. Also, an occupancy profile can be included to show out whether the occupants of the house were affected by the thermal discomfort.

Furthermore, such HiL system is based on COM interface and TCP/IP connection. Consequently, the HiL communication manager can easily integrate the simulation model with any software that can use TCP/IP protocol for data transfer, not only LabVIEW. Also, the COM interface enable easy changes in the SimulationX model to enable automated variable simulation runs.

*A Appendix*

## Bibliography

- [1] IEA. International CHP/DHC Collaborative, Advancing Near-Term Low Carbon Technologies, 2012. URL: <https://www.iea.org/media/files/chp/profiles/germany.pdf>.
- [2] M. Altmann, A. Brenninkmeijer, J.-C. Lanoix, E. D., A. Crisan, A. Hugyecz, G. Koreneff, and S. Hanninen. Decentralised Energy Systems. *Ip/a/Itre/St/2009-16*, page 96, 2010. URL: <http://www.europarl.europa.eu/activities/committees/studies.do?language=EN>.
- [3] Microsoft Development Center. What Is a COM Interface — Microsoft Docs, 2015. URL: <https://docs.microsoft.com/de-de/windows/desktop/LearnWin32/what-is-a-com-interface->.
- [4] P. Tzscheutschler. Experiences from Field Testing of Stirling Micro-CHP Systems. Prague, Czech Republic, 2013. CLIMA 2013: 11th REHBA World Congress & 8th International Conference IAQVEC.
- [5] Sanevo Whispergen. Produktdatenblatt- Sanevo Typ 800, 2011.
- [6] WhisperGen. WhisperGen product specification, 2011. URL: <http://www.whispergen-europe.com/productspec{ }en.php?fm=whispergen{&}fp=ProductSpecs>.
- [7] J. Lipp and F. Sanger. Potential of power shifting using a micro-CHP units and heat storages. Naples, Italy, 2013. Microgen3.

## **A.7 Publication 7 — Hardware in the Loop Real-Time Simulation for Heating Systems: Model Validation and Dynamics Analysis**

### **Abstract**

Heating systems such as heat pumps and combined heat and power cycle systems (CHP) represent a key component in the future smart grid. Their capability to couple the electricity and heat sector promises a massive contribution to the energy transition. Hence, these systems are continuously studied numerically and experimentally to quantify their potential and develop optimal control methods. Although numerical simulations provide time and cost-effective solutions for system development and optimization, they are exposed to several uncertainties. Hardware in the loop (HiL) approaches enable system validation and evaluation under different real-life dynamic constraints and boundary conditions. In this paper, a HiL system of a heat pump testbed is presented. It is used to present two case studies. In the first case, the conventional heat pump testbed operation method is compared to the HiL operation method. Energetic and dynamic analyses are performed to quantify the added value of the HiL and its necessity for dynamics analysis. In the second case, the HiL testbed is used to validate a model of a single family house with a heat pump participating in a local energy market. The energetic analysis indicates a deviation of 2% and 5% for heat generation and electricity consumption of the heat pump model, respectively. The model dynamics emphasized its capability to present the dynamics of a real system with a temporal distortion of 3%.

### **Author Contribution**

I designed the experiments, developed the HiL system and wrote the paper; Lukas Mayerhofer operated the testbed and prepared the energetic analysis data; Peter Tzscheutschler and Ulrich Wagner provided a detailed critical review; All authors discussed the documented results.

# 1 Introduction

Installed renewable energy capacities are growing fast worldwide. At the end of 2017, 2179 GW were installed, with a growth rate of 8.3% [1, 2]. These capacities are expected to continue growing to minimize the CO<sub>2</sub> emissions and mitigate the climate change. In Germany, several legislations were introduced to create a nuclear and fossil-free economy within the framework of the energy transition [3]. Among these acts are the renewable energy act, Erneuerbare Energien Gesetz (EEG), and the combined heat and power act, Kraft-Wärme-Kopplungsgesetz (KWKG). The EEG prioritizes the renewable energy sources (RES) in the energy market [4]. It guarantees a fixed feed-in tariff for the supplier to minimize the risk of the investors. Hence, the RES reached 111 GW in 2017 [4]. On the other hand, KWKG empowers the integration of combined heat and power (CHP) systems in the national grid. A goal was set to generate 25% of the electricity by co-generation by 2020 [5]. As these two acts increased the renewable energy capacities and increased the system efficiency, they raised several challenges in the national grid and made the traditional grid management techniques rather obsolete.

Sector coupling is one way to address these challenges faced by the grid. Heat pumps and CHP systems are the key drivers behind the electricity and heat sectors coupling. The attractive costs and lifespan of heat storages enable these heating systems to be the most economically feasible candidates to offer flexibility and mitigate the fluctuating RES. Moreover, the continuous improvement of these systems efficiency led to a significant decrease in the operation and maintenance costs [6].

Given these heating systems potential in the current and future national energy system, several researchers modeled and studied these heating systems [7, 8, 9, 10, 11, 12, 13]. Although the presented heating system models can predict to a reasonable extent the energy generation or consumption of a real-system, they are exposed to several uncertainties as they are designed to be integrated into larger models under specific system constraints. Hence, field tests and testbeds were used to investigate the quality of the results and analyze the real-life system dynamics. Although field tests provided the utmost accurate results, they are costly and do not offer enough control flexibility [8]. For control algorithms' development and evaluation, testbeds are considered the most feasible option [14, 15]. However, the testbed operation approach can significantly influence the results.

Hardware in the loop (HiL) is an approach to simulate and evaluate thermal system dynamics under multiple environmental constraints. The fundamental idea of the HiL is to integrate real hardware in a simulation loop. Real hardware replaces the numerical model of a system to study and evaluate the quality of a developed control or optimization algorithm [16]. Hardware can also be integrated with multiple numerical models to investigate its reaction to different model combinations. As an example, a HiL system

of a heat pump as hardware and a controller as software can be used to evaluate the quality of the control system. Also, a building model can be integrated to show the heat pump dynamics and reaction to different building types, ages or sizes.

In the literature, HiL simulation is being used in several fields. According to [16, 17], it has been used for over 50 years. An early application was in the flight and missiles control industry as in the Sidewinder program in 1972 [18]. It has also become more popular in other industries. As an example, HiL represents a crucial tool in the automotive industry nowadays [17, 19]. It is extensively used for engine and suspension systems control and design. Moreover, Hil is also used for testing unmanned aerial vehicles as in [20]. In the electrical power sector, applications of HiL for testing and validating are growing. Sun et al. [21] used a HiL system to study the dynamic performance of a switch-mode power amplifier. In [22] a power HiL system was introduced and used to evaluate a case study of a Great Britain network. Rosa et al. [23] implemented a HiL system to investigate and compare the performance of multiple control techniques for Single-Ended Primary Inductance Converter (SEPIC). Castaings et al. [24] investigated different energy management strategies with electric vehicles using a HiL system in real-time. The author's setup facilitated the evaluation of the effectiveness of the designed EMS strategies in real-time. Furthermore, Ruuskanen et al. [25] designed a HiL system for water electrolysis system emulation. Through this system, the author was able to study the electrolyzer characteristics in a smart grid. In [26], voltage control coordination scenarios were validated based on a HiL system. The authors used HiL in a real-time simulation to validate the capability of RES to provide voltage control in a smart grid.

Although several publications are available for power HiL systems, a limited number of publications discussed the heating systems in buildings. Among these publications is the work of [27], where a HiL simulation system was developed to evaluate the control strategies of a hydronic radiant heating system. The author replaced the model of a hydronic network with real hardware to minimize the results uncertainties. In [28], a HiL system was developed to simulate micro-CHP systems with different building models. The author showed the necessity of a HiL system in the operation of micro-CHP testbeds and evaluation of optimization and control algorithms.

At the Institute of energy economy and application technology (IfE), several testbeds were developed to evaluate the common heating systems at different scales as in [29, 15, 30] and recently in [14]. A testbed is necessary to demonstrate and validate the novel optimization algorithms and control strategies being developed. Through these testbeds, the operational requirements and technical constraints were easily defined. Ideally, a heating system testbed should also be able to demonstrate and emulate a real building with a heating system and is expected to eliminate all the uncertainties, as real hardware is used. However, as the buildings are emulated by heat sinks, uncertainties can emerge, and the building dynamics in certain cases diminish. Thus, a HiL system was introduced in [28] to address these uncertainties with micro-CHPs operation. In this paper, the recent advanced HiL version of [28], the testbed in [14] and model presented in [31] are used to demonstrate the following aspects:

- A comparison between heating systems testbeds operation with HiL and without

HiL system simulation

- An energetic and dynamics analysis to quantify the benefits of HiL simulation with heating systems
- A model validation of the heat pump dynamics and interactions within a microgrid

The structure of the paper is as follows. Section 2 shortly describes the different numerical and experimental methods used to analyze a heating system. Section 3 demonstrates the HiL system structure including the testbed and building model. Moreover, it presents the input system parameters. Section 4 demonstrates the results of the two different case studies. Section 5 presents a conclusive summary.

*A Appendix*

## 2 Heating Systems Analysis Methods

Numerical simulation provides the ideal environment for testing and evaluation of a heating system performance connected to different buildings types. Compared to experimental testing, it saves efforts, costs, and time to investigate a specific heating system. However, it is exposed to several uncertainties, and its accuracy is questionable. Hence, the experimental investigation has always an edge over the numerical simulation as it eliminates the modeling uncertainties.

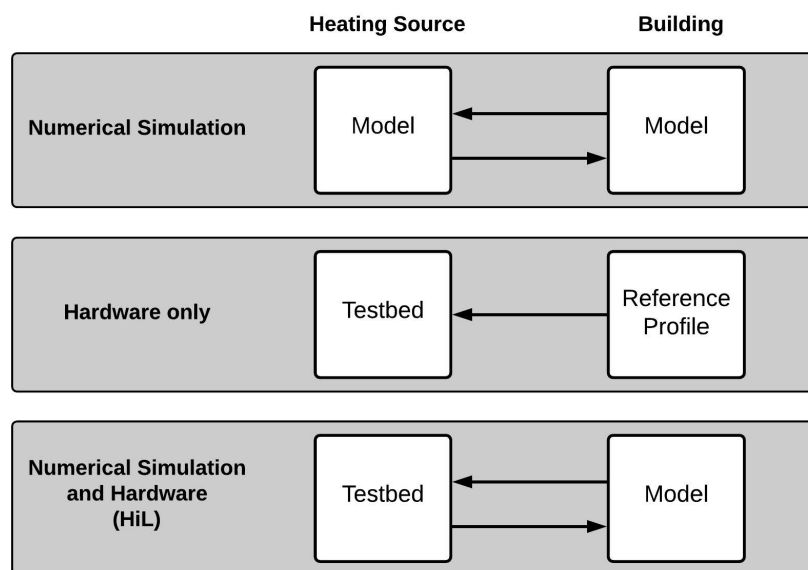


**Figure 2.1:** Abstract diagram of different methods for heating system analysis.

The experimental testing can only be performed using hardware, or hardware and numerical models as HiL. Figure 2.1 presents an abstract comparison between heating system analysis using numerical simulation, hardware only (without HiL), and hardware and numerical models (HiL). The conventional method to evaluate the heating system experimentally is using hardware only. A reference profile that is obtained within a field test or by a simulation model is fed directly to the testbed. This reference profile contains the thermal load of the building over a specific period of time. The testbed hydraulic circuit emulates this load profile using a heat sink to evaluate the reaction of the heat source and heat storage. Although the heating source such as a heat pump or a micro-CHP system is a real system, the results of the whole experiment are exposed to uncertainties because of the heat sink emulation of the reference load profile. The heat

## *A Appendix*

sink always tries to reach the set reference profile, even if it has to decrease the return temperature to or below the room temperature. As a conventional alternative solution, return temperature can be held constant, yet it diminishes the dynamics of the whole testbed operation.

A combination of hardware and numerical simulation is considered to be the optimal method for heating systems analysis and models validation. The heat source and heat storage are integrated as hardware with a building model using HiL system to evaluate and validate heating systems dynamics and performance. Consequently, the building model can calculate realistic return temperatures and the feedback of the building for any violations introduced by the heating source. Furthermore, the room temperature can be simulated by the building model to analyze the user comfort in real-time.

## 3 HiL Simulation System

### 3.1 Communication Structure

Figure 3.1 shows the detailed control loop of the implemented HiL model. The heat pump (HP) controller, temperature controller, building model, and the tapping profiles are implemented in SimulationX, which is a Modelica based software. More details about the models are explained later in this section. The testbed, the hardware, is presented by three modules: heat sink, heat storage, and heat source, which are the typical components of a heating system testbed. A LabVIEW program controls the different components of the testbed and feeds the output to the database.

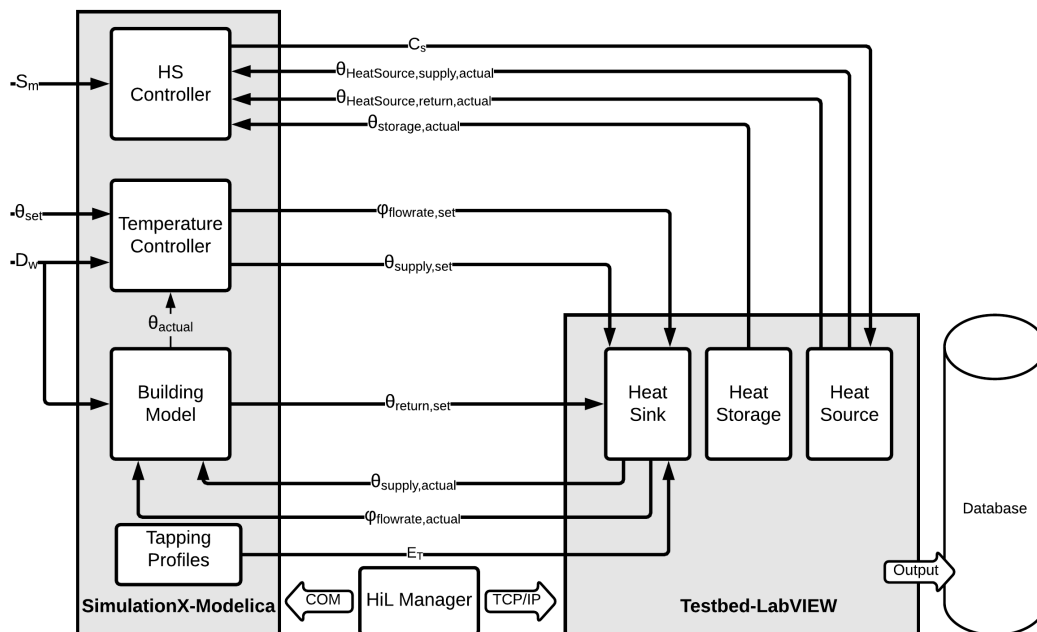


**Figure 3.1:** Detailed control diagram of the HiL system.

The communication between the model in SimulationX and LabVIEW is managed by the HiL manager, which is based on MATLAB. The data is transferred using the TCP/IP protocol between the HiL manager and LabVIEW, while COM interface is used to manage the SimulationX. The details of the HiL manager communication protocols and sequence are thoroughly documented in [28].

Other communication systems were tested such as exporting the building models in

the C programming language (C-code) and importing the model in LabVIEW. However, processing the C-code in real-time desynchronizes the LabVIEW real-time control loop. Moreover, the number of inputs and outputs to and from the C-code are limited. Hence, using C-code for integrating models in real-time LabVIEW control systems is not feasible for heating systems applications.

The communicated data between the testbed and the SimulationX models is dependent on the functionality of the model and testbed module. The HS controller receives the actual heat source supply temperature  $\theta_{HeatSource, supply, actual}$ , actual heat source return temperature  $\theta_{HeatSource, return, actual}$ , and temperature of the storage  $\theta_{storage, actual}$  from the testbed. Moreover, it receives an external control input signal  $S_m$  that is developed from the model described in [31]. Based on these input signals, the HS controller sends a binary operation signal  $C_s$  to the testbed heat source. The temperature controller receives  $\theta_{set}$  and  $\theta_{actual}$ , which are the set room temperature and the actual room temperature, respectively. Based on these two inputs and weather data  $D_w$ , the temperature controller can calculate the set flow rate  $\varphi_{flowrate, set}$ , and the set space heating supply temperature of the  $\theta_{supply, set}$ . The building model receives  $D_w$ , actual flow rate  $\varphi_{flowrate, actual}$ , and the actual supply temperature of the space heating  $\theta_{supply, actual}$ . Based on these inputs and the building model, the return temperature  $\theta_{return, set}$  can be calculated and forwarded to the testbed. Communicating the  $\theta_{return, set}$  each second in this HiL simulation system maximizes the results accuracy and enables the testbeds to present realistic dynamics that is comparable to field measurements. Tapping profiles can also be integrated as a model and communicated as energy profiles  $E_T$  to the heat sink.

### 3.2 Testbed Components and Description

The testbed system consists of three modules and a brine water heat pump with a thermal power of 10.31 kW and a COP of 5.02 by B0/W35 as per standard EN14511. Two circulations pumps are integrated into the heat pump on the brine and the water side. Moreover, it is equipped with an emergency electrical heater of 8.8 kW. Figure 3.2 shows the simplified hydraulic schematic of the used testbed.

A ground-source heat pump required an emulator to show the dynamics of the ground heat exchanger. Module A includes a ground-source emulator that can provide any required brine temperature to the heat pump. It consists of 300 L heat storage, filled with a water-glycol mixture as an anti-freezing heat transfer fluid. The storage is heated by a 12.5 kW electrical heater that is controlled via a hysteresis regulator to maintain the tank temperature during the whole operation time at 40 °C. The set temperature of the tank and the hysteresis bandwidth can be defined by the user depending on the simulation goals. A mixer, similar to the conventional space heating mixers, is used to mix the supply of brine tank with the return of the heat pump to reach the required ground-source set temperature. Depending on the HiL system and the goal of the simulation, the mixer can maintain a constant brine temperature or a time-dependent temperature profile.

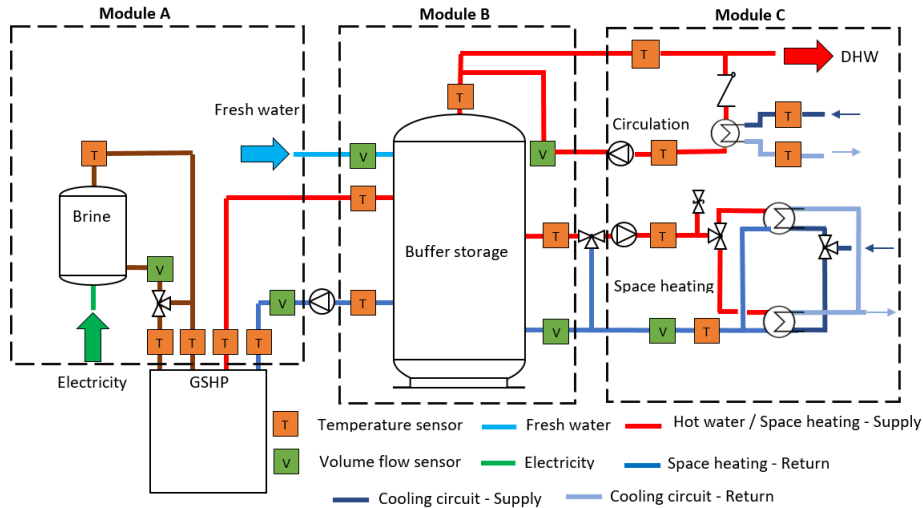


**Figure 3.2:** Hydraulic schematic of the heat pump testbed [14].

Module B shows the combi-storage system of a conventional residential house. It includes a 749 L combi hygienic buffer storage to cover the space heating and domestic hot water consumption. A stainless steel heat exchanger extracts heat from the storage to cover the hot water consumption. Moreover, a coaxial pipe, pipe-in-pipe system, is used to enable the hot water circulation and maintain the pipe temperatures at a certain level.

Module C is the most complex module as it represents the heat sink of the testbed. It can emulate the space heating and domestic hot water consumption depending on the building type and user behavior. The space heating circuit consists of a space heating mixer, circulation pump, and two heat exchangers. Through the mixer, the supply of the tank with the return of the space heating is mixed to reach the required  $\theta_{supply,set}$ . The circulation pump is controlled according to  $\varphi_{flowrate,set}$ , which varies depending on the heat demand. Two heat exchangers of two different sizes are used to emulate different building loads depending on their required maximum heat power. The domestic hot water consumption is emulated through three magnetic valves that have different consumption flow rates. These valves can represent different consumption activities such as washing, showering or cooking.

The hydraulic configuration in Figure 3.2 shows only one of the most common hydraulic configurations. However, the testbed can allow several other configurations, such as a direct connection of the heat pump to module C or using additional heat storage for hot water consumption. More details about the hydraulics, control, and dynamics of the testbed are available in [14].

### 3.3 Models Description

Earlier in [31], a market model is presented based on a double-sided auction, in which different household devices and heating systems can participate. The heating system bids their energy needs to either decrease costs or increase comfort. In this paper, the market control approach is going to be used to develop the external control signal,  $S_m$ . The control signal provided in this case is a binary signal, either 0 or 1. The HS controller reacts to the signal as in Equation (3.1), where  $\theta_{HeatSource,supply,max}$  is the maximum heat source supply temperature,  $\theta_{HeatSource,return,max}$  is the maximum heat source return temperature, and  $\theta_{storage,max}$  is the maximum storage temperature at a specified sensor position.

$$C_S = \begin{cases} 0, & \text{if } \theta_{HeatSource,supply,actual} \geq \theta_{HeatSource,supply,max}, \\ 0, & \text{if } \theta_{HeatSource,return,actual} \geq \theta_{HeatSource,return,max}, \\ 0, & \text{if } \theta_{storage,actual} \geq \theta_{storage,max}, \\ S_m, & \text{otherwise} \end{cases} \quad (3.1)$$

The  $S_m$  is considered in full control, yet the HS has to make sure that the heat source operation never exceeds the operation limit set by the manufacturer.

The temperature controller sets the flow rate and the supply temperature of the heating circuit. The flow rate is determined based the room actual temperature  $\theta_{actual}$  and set temperature  $\theta_{set}$ . It operates based on a hysteresis algorithm. The set flow rate of the heating circuit  $\varphi_{flowrate,set}$  is calculated based on  $\theta_{actual} - \theta_{set}$ ,  $\Delta_r^+$ , and  $\Delta_r^-$ , where  $\Delta_r^+$  and  $\Delta_r^-$  are the hysteresis upper and lower limits, respectively. These limits are determined by the user depending on the level of comfort required. The smaller the absolute value of  $\Delta_r^+$  and  $\Delta_r^-$ , the higher the comfort. Equation (3.2) details the control cases of the flow rate.

$$\varphi_{flowrate,set} = \begin{cases} \varphi_{flowrate,min}, & \text{if } \theta_{actual} - \theta_{set} > \Delta_r^+, \\ \varphi_{flowrate,max}, & \text{if } \theta_{actual} - \theta_{set} < \Delta_r^-, \\ \frac{\varphi_{flowrate,max} - \varphi_{flowrate,min}}{\Delta_r^+ - \Delta_r^-} \\ \times (\theta_{actual} - \theta_{set}) + \varphi_{flowrate,min}, & \text{otherwise} \end{cases} \quad (3.2)$$

The supply temperature is determined based on the outside temperature given in  $D_w$ . The supply temperature varies linearly against the outside temperature. The lower the outside temperature, the higher the supply temperature of the space heating system. The limits and the magnitude of this linear relationship between the outside temperature and the heating system supply temperature are defined based on the age of the building and the type of the radiators. In Section 3.4, the used supply temperature curve is explained.

### 3.4 Model Input Data and Parameters

The building model is created and calibrated based on the research project data of [32]. It consists of three heated zones to represent an attic, a living area, and a cellar. The base model is available in the Green City package of SimulationX [33]. The construction year of the building is between 1984 and 1994. The living area has 150 square meters and a room height of 2.5 m. The cellar and attic are unheated. The living area is heated, and the temperature is maintained at 21 °C. In Table 3.1, a summary of the most important input data parameters is presented.

**Table 3.1:** Building and control models basic parameters.

Description	Value	Units [-]
Building age	1984–1994	-
Building type	residential	-
Flanking	none	-
Number of occupants	4	-
Heated living area	150	m <sup>2</sup>
Clear room height	2.5	m
Body heat dissipation per person	80	Watt
Set temperature— $\theta_{set}$	21	°C
Initial zone temperature	21	°C
Upper hysteresis limit— $\Delta_r^+$	0.5	K
Lower hysteresis limit— $\Delta_r^-$	-0.5	K
Heating system exponent	1.2	-
Max. flow rate— $\varphi_{flowrate,max}$	0.24	L/s
Min. flow rate— $\varphi_{flowrate,min}$	0	L/s
Max. heat source supply temperature— $\theta_{HeatSource,supply,max}$	65	°C
Max. heat source return temperature— $\theta_{HeatSource,return,max}$	55	°C
Max. storage temperature (lowest layer)— $\theta_{storage,max}$	55	°C
Night setback	10	K

A winter cloudy type day is selected based on the VDI Standard 4655. The ambient weather temperature, the global solar irradiation, and the cloudiness are shown in Figure 3.3. According to the standard, the average temperature should be below 5 °C and the cloudiness should be higher than 5/8. On the selected day, the average temperature and cloudiness were 3.15 °C and 7/8, respectively. The number of cloudy winter days in the reference year was 85 days. The presented profile represents a typical average day of the given year in Munich, Germany. A winter type day is chosen to show clearly the influence of HiL on the quality of the results. A summer type day could have been selected, yet the space heating circuit would not be activated in this case. Hence, the HiL influence would not be noticed.

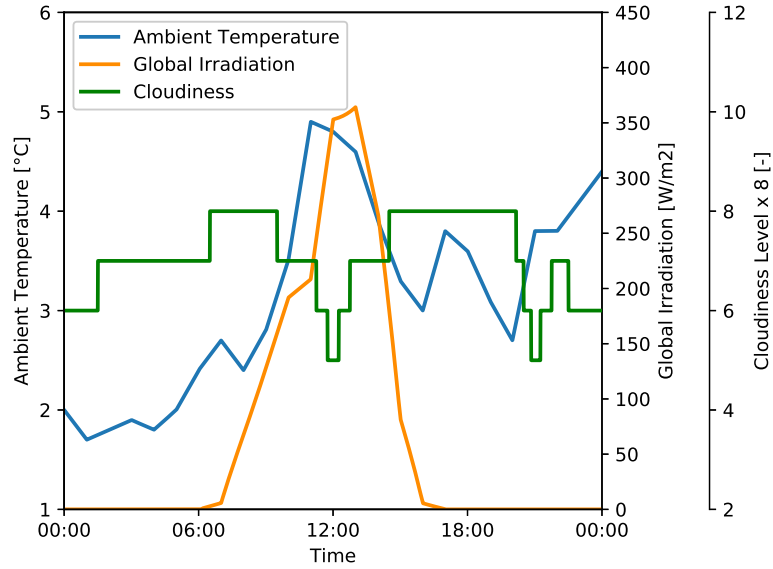


**Figure 3.3:** A winter cloudy type day temperature and global irradiation.

The heating circuit supply temperature is defined according to Equation (3.3), where  $\theta_a$  is the ambient temperature. As shown, the supply temperature varies depending on the outside ambient temperature. The slope of the supply temperature is defined according to the recommended operation constraints and the nature of the building itself. Moreover, the required set temperature and user comfort level play an important role in deciding the slope of the heating curve. A change in the set temperature or the comfort level can be accompanied by a parallel shift of the heating circuit supply curve. As an example, if an increase in comfort is required, a parallel, upwards shift can be made. Alternatively, if the user needs to decrease the costs, the heating curve can be shifted downwards.

$$\theta_{Supply,set} = \begin{cases} 50, & \text{if } \theta_a < -20 \\ -0.625 \times \theta_a + 37.5, & \text{if } -20 \leq \theta_a \leq 20, \\ 25, & \text{if } \theta_a > 20 \end{cases} \quad (3.3)$$

## 4 Results and Analysis

In this paper, two cases are evaluated. The first case compares the testbed operation with and without HiL to present the added value and necessity of the HiL system. The comparison is based on energetic and dynamics analysis of the two experimental methods. The energetic analysis compares the energy consumption of the heat source and heat sink on the given type day. The dynamic analysis investigates and compares power and temperatures over time of the two experiments.

In the second case, the HiL system is used to validate a single family house model with a heat pump participating in an energy market. The preliminary market model was presented in [31]. The system dynamics evaluation of the model is crucial as it influences the time, volume and price of the heat pump energy bid in the market. Hence, a comparison is conducted between the HiL system and the model to evaluate and demonstrate the model accuracy.

### 4.1 Case 1: Testbed Operation with and without HiL

The goal of this case study is to evaluate the testbed operations with and without HiL to quantify the added value and present the necessity of the HiL systems. A reference load profile is generated from the building model using the type day presented in Section 3.4. The building model is connected to an over-sized heating source or a district heating to simulate the exact heat demand profile of the building without any compromises on the comfort side of the user.

Figure 4.1 presents the energy consumption and generation of the type day experiment, where  $E_{el}$  is the electric energy consumption of the heat pump,  $E_{th}$  is the thermal energy generation of the heat pump,  $E_{brine}$  is the energy consumed on the brine side, and  $E_{sh}$  is the energy consumed by the building. It can be seen that the deviation is between 0.2% to 5.5%, which is relatively small. However, it can be noticed that using the same metrics, the operation without HiL always has a lower consumption than the one with HiL. The reference space heating profile consumption is 132.8 kWh, compared to 135.3 kWh for the operation with HiL and 128.4 kWh for the operation without HiL. Although the experiment with HiL system is closer to the reference, it does not indicate a significant failure in the experiment without HiL. Hence, operating heating system testbeds without a HiL communication system has been widely accepted over the past years.

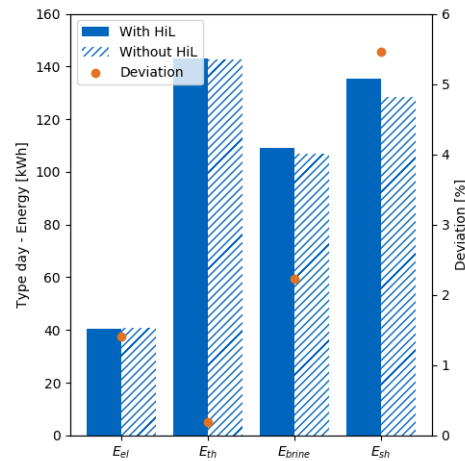


**Figure 4.1:** Energetic analysis of the testbed performance with and without HiL.

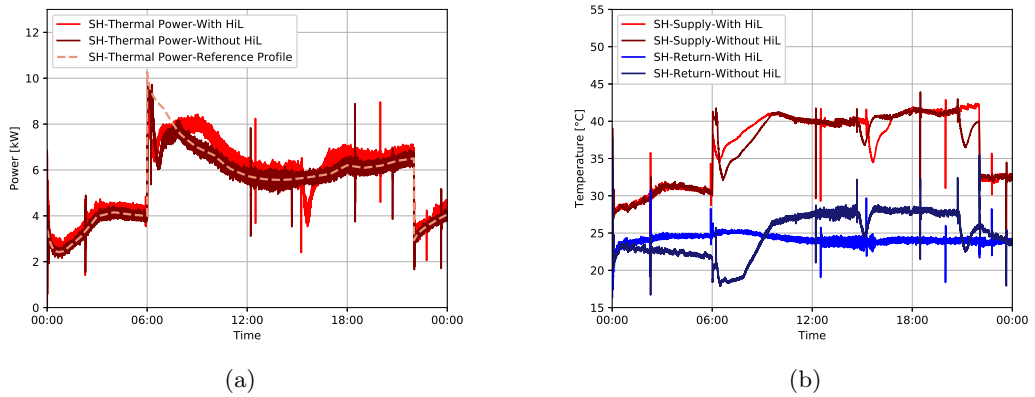


**Figure 4.2:** Comparison between the space heating dynamics of the testbed operation with and without HiL against the reference profile, (a) space heating thermal power (b) space heating supply and return temperatures.

Insight on the dynamics and the difference between the testbed operations with and without HiL can be presented in Figure 4.2. Although the energy consumption is almost equal, a significant difference can be seen in the space heating dynamics between the operation with HiL, without HiL and the reference profile. Between 00:00 and 06:00 in Figure 4.2a, no differences can be noticed. The testbed operations are identical to the reference profile. With the increasing demand after 06:00 and the lack of sufficient energy in the heat storage, the power dropped. The testbed operation without HiL reaction was to reduce the return temperature trying to maintain the same power, as in Figure 4.2b. The return temperature, in this case, decreased to 17 °C, which is a major violation as the return temperature became lower than the room temperature. The

testbed would have reduced the return temperature even to a lower level than  $17^{\circ}\text{C}$ , but the cooling circuit capacity constrained it. On the other hand, the HiL system maintained a plausible return temperature due to the integration of a building model in the loop. Moreover, the HiL increased the thermal power after 08:00 to make up for the thermal power drop started at 06:00 and maintained a proper temperature, while the testbed operation without HiL continued to simulate the reference profile.

Another drop in power can be noticed between 12:00 and 18:00 for the HiL system. The testbed operating without HiL maintained the reference load profile power, even though there was not a sufficient amount of energy in the storage. This can be confirmed by the decrease in supply temperature noticed in Figure 4.2b. This drop is due to incapability of the heat pump to meet the demand. The HiL maintained a plausible return temperature, but return temperature without HiL decreased significantly. Although the power of the testbed operation without HiL seems acceptable, the return temperature dynamics are not realistic and can not be relied on for model validation or further research.

The behavior of the space heating circuit without HiL led to another operation plan for the heat pump, although the same control strategy is used. As in Figure 4.3, the heat pump started at the same time and behaved similarly within the first operation cycle. With the second cycle starting at 06:00, a difference can be seen that is increasing over time as seen at 15:00 and again at 20:00. This difference can lead to a significant error in the evaluation of energy management systems and cost optimization models based on variable electricity tariffs, or in energy market model as in Section 4.2. The exact operation plan represents a necessity in evaluating and validating the flexibility potential of heat pumps.

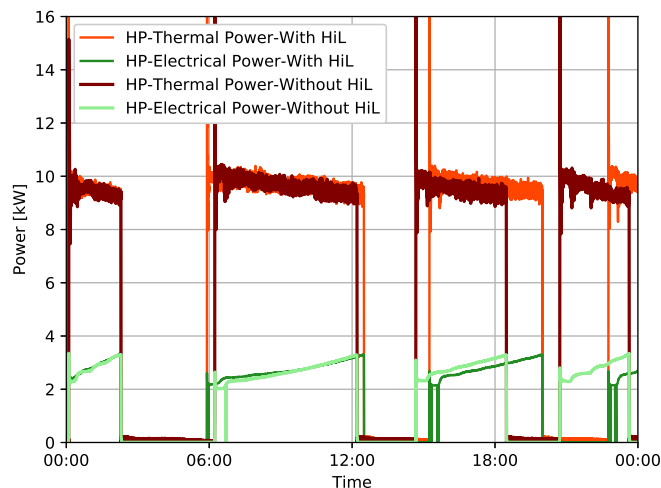


**Figure 4.3:** Thermal and electrical power of the heat pump with and without HiL.

## 4.2 Case 2: Model Validation Based on HiL

Based on the model presented in [31], 10 single family residential houses are simulated located in Munich, Germany. These houses are participating in a local energy market, where each device sell or buy energy depending on its operation mode. Each house is equipped with a photovoltaic system, an electric vehicle and a heat pump. The installed PV capacity at each house is 6 kWp. The technical details and the data of the integrated PV system can be found in [34]. A 3.6 kW charging station is used for the electric vehicle, while the integrated heat pump is represented by the testbed in Section 3.2. More details about the heat pump testbed can be found in [14]. A single family house is selected from these 10 houses to be validated based on the HiL system and the heat pump testbed.

The goal of the model validation is to compare the operation of the heat pump in the model to the testbed with HiL while making sure that the building load is covered and the room temperature is properly maintained. On the heat sink side, Figure 4.4a shows that the space heating power of the testbed with HiL and the simulation are behaving similarly. Even when a drop in the thermal power occurred at 17:00, it did not influence the room temperature as shown in Figure 4.4c. The room temperatures of the completely simulated model and HiL are showing similar dynamics. A difference can be noticed between 09:00 to 22:00, yet this difference is below 0.02 °C. In Figure 4.4b, the supply and return temperature of the HiL testbed and simulation model can be compared. The supply temperature is varying based on the supply curve earlier defined in Equation (3.3). It can be seen that the supply temperature shows plausible results except at 17:00, where a drop in the temperature can be noticed because of the low storage content. An operation without HiL would have led to a proportional decrease in the return temperature, yet the HiL system maintained realistic dynamics. Comparing the model to the HiL, it can be noticed that the return temperatures are not violated, and both the HiL and simulation dynamics are comparable except at the starting point, where minor fluctuation occurred by the simulation solver. In the HiL measurements, spikes can be noticed to due few data packet losses in the communication between the testbed and model. However, it does not influence the overall results.

The behavior of the heat pump in the HiL and simulation is almost identical as in Figure 4.5. The magnitude of the thermal and electrical power is equivalent, which means that the heat pump has been providing power to the heat storage almost at the same supply temperature. In this type day, the energy difference between the HiL system and the simulation is 2% and 5% for the heat generation and electricity consumption, respectively. However, the HiL based validation in this paper does not only concern the energetic consumption but also the temporal distortion of the power. The time and volume of the heat pump bid in an energy market have to be evaluated to validate the accuracy of the model.

In [14], the thermal and electrical power of the heat pump model were validated independently based on mean absolute percentage error (MAPE) and root mean square error (RMSD). However, since the temporal distortion of the model compared to the HiL is crucial to evaluate the model capability in participating in energy markets at the estimated times, the temporal distortion index (TDI) of [35] is used. This metric

is based on the dynamic time warping (DTW) developed in the 1970s, which is used to evaluate the temporal distortion between two different time series. In this paper, the two time series are the HiL measurements and simulation model time series of the heat pump electrical power. The DTW finds the optimal warping path (i.e., a common set of instants) by minimizing the distance between the two given time series. The TDI can be calculated then according to Equation (4.1), where  $i$  and  $j$  are the HiL measurements time series index and simulation model time series index, respectively.

$$TDI = \frac{1}{N^2} \sum_{l=1}^{k-1} |(i_{l+1} - i_l)(i_{l+1} + i_l - j_{l+1} - j_l)| \quad (4.1)$$

The output of the TDI is between 0 and 1. The lower the value of the TDI metric, the lower is the temporal distortion. The metric result in this type day is 3%, which means that temporal distortions between the HiL measurements and the simulation model are low.

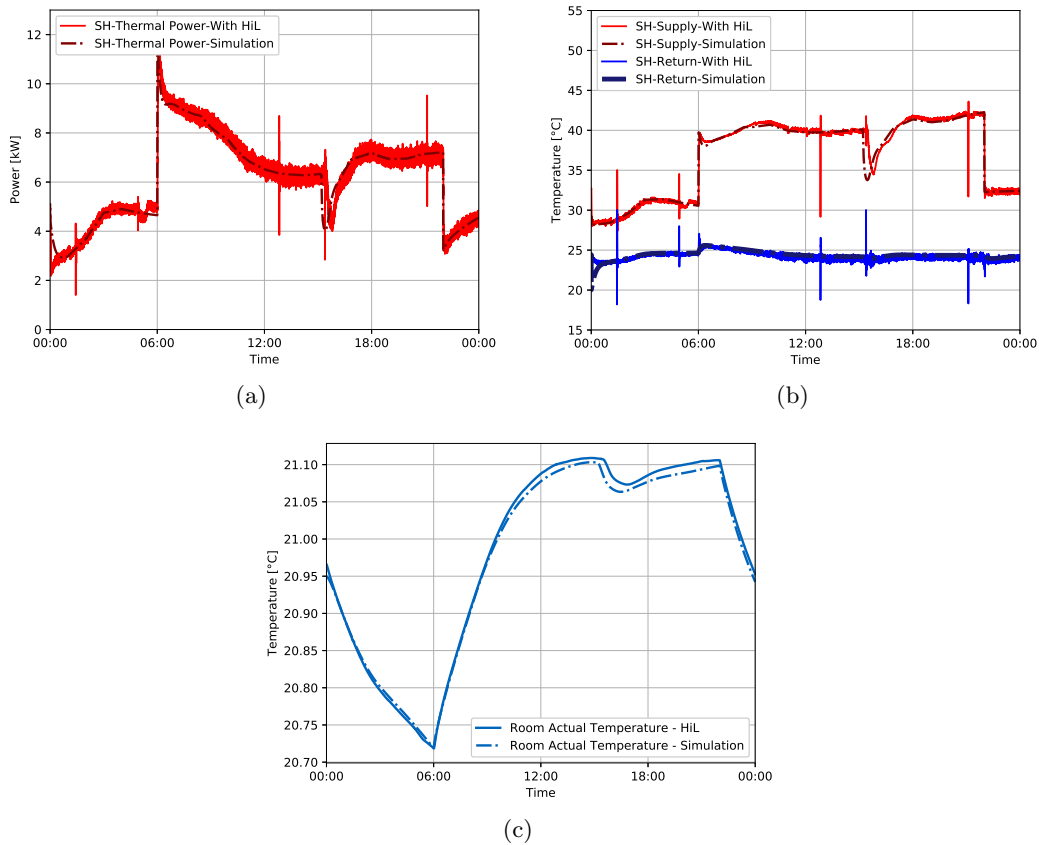


**Figure 4.4:** Comparison between the heat pump dynamics of the testbed operation with HiL and simulation model, (a) space heating thermal power (b) space heating supply and return temperatures (c) room temperature.

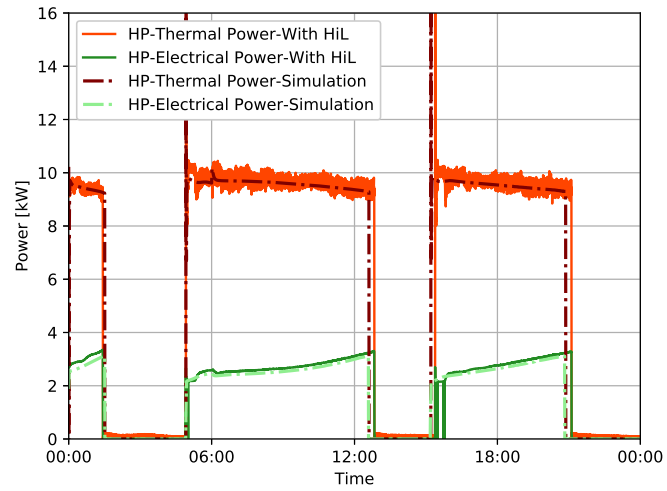


Figure 4.5: Heat pump thermal power and electrical power on the type day.

## 5 Conclusions

In this paper, hardware in the loop (HiL) real-time system is presented. The HiL communication structure, models and testbeds are explained to show the experimental setup of HiL for heating systems. Two case studies are demonstrated to evaluate the potential and applications of the HiL. The first case study evaluates the energy consumption and dynamics of the testbed operation with and without HiL. The results of the case study are summarized as follows:

- Testbed operation with or without HiL does not influence the heat energy consumption of the heat sink (space heating), or the heat energy generation from the heat pump. The variations in results are between 0.2% and 5.5%. Hence, energetically no significant difference can be noticed.
- The dynamics of the testbed operation without HiL showed that a drop in the space heating supply temperature is always accompanied by an equivalent drop in the return temperature of the space heating. Thus, testbed operation without HiL can not emulate real-life return temperature dynamics and can lead to system violations.
- The HiL system is able to maintain realistic dynamics due to the availability of a building model in the loop.
- The violations of the testbed operation without HiL led to a shift in the operation plan of the heat pump. Hence, the testbed operation without HiL is not reliable for heating system models validation.

In the second case study, the HiL system is used to validate a single family house building participating in a local energy market. HiL is chosen as it is necessary to validate not only the energy consumption but also the system dynamics and the temporal distortion of the model. The simulation model showed its capability to present the heat pump system dynamics including any drops in the supply temperature or the heat storage of the tank. The HiL also showed the advantage of demonstrating the room temperature of the building model for the given type day, which facilitates evaluating the comfort of the residents and comparing it to the simulation model. Furthermore, TDI is used to quantify the temporal distortion of the heat pump to make sure that the electric energy consumption is communicated at the right time of the day. The TDI value is 3%. Hence, a minimal temporal distortion can be noticed between the HiL and the simulation model.

As an outlook, HiL for heating systems can be used for several further studies. It enables not only an accurate validation of a simulation model but also experimentation using a building model inertia to offer flexibility to the grid. The HiL can also be further

## *A Appendix*

developed to include multiple heating systems that can communicate and interact in the same local heating network or microgrid.

## Bibliography

- [1] IRENA International Renewable Energy Agency. Renewable capacity highlights. (March):2, 2018. URL: <http://www.irena.org/DocumentDownloads/Publications/RE{ }stats{ }highlights{ }2017.pdf>.
- [2] L. Capuano. International Energy Outlook 2018 (IEO2018). 2018:21, 2018. URL: [www.eia.gov](http://www.eia.gov).
- [3] Renewable Energies Agency. Press Fact Sheet: The German Energy Transition. *Berlin Energy Transition Dialogue*, (March):1–16, 2016.
- [4] Federal Republic of Germany. Act on the Development of Renewable Energy Sources - RES Act 2017. (July):179, 2017.
- [5] German Ministry of Economics and Energy. BMWi - Kraft-Wärme-Kopplung. URL: <https://www.bmwi.de/Redaktion/DE/Artikel/Energie/moderne-kraftwerkstechnologien.html>.
- [6] M. Y. Haller, R. Haberl, I. Mojic, and E. Frank. Hydraulic integration and control of heat pump and combi-storage: Same components, big differences. *Energy Procedia*, 48:571–580, 2014. URL: <http://dx.doi.org/10.1016/j.egypro.2014.02.067>, doi:10.1016/j.egypro.2014.02.067.
- [7] G. Salvalai. Implementation and validation of simplified heat pump model in IDA-ICE energy simulation environment. *Energy and Buildings*, 49:132–141, 2012. URL: <http://dx.doi.org/10.1016/j.enbuild.2012.01.038>, doi:10.1016/j.enbuild.2012.01.038.
- [8] M. Miara, D. Guenther, R. Langner, S. Helmling, and J. Wapler. "WP Monitor" Feldmessung von Waermepumpenanlagen. Technical report, Fraunhofer Institute For Solar energy Systems, Freiburg, 2014.
- [9] A. Bloess, W. P. Schill, and A. Zerrahn. Power-to-heat for renewable energy integration: A review of technologies, modeling approaches, and flexibility potentials. *Applied Energy*, 212(August 2017):1611–1626, 2018. URL: <https://doi.org/10.1016/j.apenergy.2017.12.073>, doi:10.1016/j.apenergy.2017.12.073.
- [10] J. Braun, P. Bansal, and E. Groll. Energy efficiency analysis of air cycle heat pump dryers. *International Journal of Refrigeration*, 25(7):954–965, nov 2002. URL: <https://www.sciencedirect.com/science/article/pii/S0140700701000974>, doi:10.1016/S0140-7007(01)00097-4.

- [11] H. Willem, Y. Lin, and A. Lekov. Review of energy efficiency and system performance of residential heat pump water heaters. *Energy and Buildings*, 143:191–201, 2017. URL: <http://dx.doi.org/10.1016/j.enbuild.2017.02.023>, doi: 10.1016/j.enbuild.2017.02.023.
- [12] M. Badache, M. Ouzzane, P. Eslami-Nejad, and Z. Aidoun. Experimental study of a carbon dioxide direct-expansion ground source heat pump (CO<sub>2</sub>-DX-GSHP). *Applied Thermal Engineering*, 130:1480–1488, 2018. URL: <https://doi.org/10.1016/j.applthermaleng.2017.10.159>, doi:10.1016/j.applthermaleng.2017.10.159.
- [13] S. Ikeda, W. Choi, and R. Ooka. Optimization method for multiple heat source operation including ground source heat pump considering dynamic variation in ground temperature. *Applied Energy*, 193:466–478, 2017. URL: <http://dx.doi.org/10.1016/j.apenergy.2017.02.047>, doi:10.1016/j.apenergy.2017.02.047.
- [14] W. El-Baz, P. Tzscheutschler, and U. Wagner. Experimental study and modeling of ground-source heat pumps with combi-storage in buildings. *Energies*, 11(5), 2018. doi:10.3390/en11051174.
- [15] U. Wehmhörner. Multikriterielle Regelung mit temperaturbasierter Speicherzustandsbestimmung für Mini-KWK-Anlagen. 2012. URL: <http://mediatum.ub.tum.de/doc/1084367/1084367.pdf>.
- [16] M. Bacic. On hardware-in-the-loop simulation. *Proceedings of the 44th IEEE Conference on Decision and Control*, pages 3194–3198, 2005. doi:10.1109/CDC.2005.1582653.
- [17] M. Bonvini, F. Donida, and A. Leva. Modelica as a design tool for hardware-in-the-loop simulation. pages 378–385, 2009. URL: <http://www.ep.liu.se/ecp/article.asp?issue=43%26article=42>, doi:10.3384/ecp09430087.
- [18] M. Bailey. Contributions of hardware-in-the-loop simulations to Navy test and evaluation. In *Proceedings of SPIE*, volume 2741, pages 33–43. SPIE, 1996. URL: <http://link.aip.org/link/?PSI/2741/33/1&Agg=doi>, doi:10.1117/12.241122.
- [19] D. Winkler and C. Gühmann. Hardware-in-the-Loop simulation of a hybrid electric vehicle using Modelica/Dymola. *22nd International Battery, Hybrid and Fuel Cell Electric Vehicle Symposium*, pages 1054–1063, 2006. URL: <http://citeseerx.ist.psu.edu/viewdoc/download?doi=10.1.1.404.7637&rep=rep1&type=pdf>0Ahttp://mathpros.com/papers/hybrid/Hardware\_in\_the\_Loop\_Simulation\_of\_a\_Hybrid\_Electric\_Vehicle.pdf.
- [20] C. Kamali and S. Jain. Hardware in the Loop Simulation for a Mini UAV. *IFAC-PapersOnLine*, 49(1):700–705, 2016. URL: <http://dx.doi.org/10.1016/j.ifacol.2016.03.138>, doi:10.1016/j.ifacol.2016.03.138.

- [21] J. Sun, C. Yin, J. Gong, Y. Chen, Z. Liao, and X. Zha. A stable and fast-transient performance switched-mode power amplifier for a power hardware in the loop (PHIL) system. *Energies*, 10(10), 2017. doi:10.3390/en10101569.
- [22] E. Guillo-Sansano, M. H. Syed, A. J. Roscoe, and G. M. Burt. Initialization and synchronization of power hardware-in-the-loop simulations: A Great Britain network case study. *Energies*, 11(5), 2018. doi:10.3390/en11051087.
- [23] A. Rosa, T. de Souza, L. Morais, and S. Seleme. Adaptive and Nonlinear Control Techniques Applied to SEPIC Converter in DC-DC, PFC, CCM and DCM Modes Using HIL Simulation. *Energies*, 11(3):602, 2018. URL: <http://www.mdpi.com/1996-1073/11/3/602>, doi:10.3390/en11030602.
- [24] A. Castaings, A. Bouscayrol, W. Lhomme, and R. Trigui. Power Hardware-In-the-Loop simulation for testing multi-source vehicles. *IFAC-PapersOnLine*, 50(1):10971–10976, 2017. URL: <https://doi.org/10.1016/j.ifacol.2017.08.2469>, doi:10.1016/j.ifacol.2017.08.2469.
- [25] V. Ruuskanen, J. Koponen, T. Sillanpää, K. Huoman, A. Kosonen, M. Niemelä, and J. Ahola. Design and implementation of a power-hardware-in-loop simulator for water electrolysis emulation. *Renewable Energy*, 119:106–115, 2018. doi:10.1016/j.renene.2017.11.088.
- [26] K. Shahid, L. Petersen, R. Olsen, and F. Iov. ICT Based HIL Validation of Voltage Control Coordination in Smart Grids Scenarios. *Energies*, 11(6):1327, 2018. URL: <http://www.mdpi.com/1996-1073/11/6/1327>, doi:10.3390/en11061327.
- [27] K. N. Rhee, M. S. Yeo, and K. W. Kim. Evaluation of the control performance of hydronic radiant heating systems based on the emulation using hardware-in-the-loop simulation. *Building and Environment*, 46(10):2012–2022, 2011. doi:10.1016/j.buildenv.2011.04.012.
- [28] W. El-Baz, F. Sängler, and P. Tzscheutschler. Hardware in the Loop ( HIL ) for micro CHP Systems. *The Fourth International Conference on Microgeneration and related Technologies*, (October 2015), 2015.
- [29] H. Mühlbacher. Verbrauchsverhalten von Wärmeerzeugern bei dynamisch variierten Lasten und Übertragungskomponenten. page 127, 2007.
- [30] J. P. Lipp. Flexible Stromerzeugung mit Mikro-KWK-Anlagen, 2015.
- [31] W. El-Baz and P. Tzscheutschler. Autonomous coordination of smart buildings in microgrids based on a double-sided auction. In *2017 IEEE Power & Energy Society General Meeting*, number August, pages 1–5, Chicago, jul 2017. IEEE. doi:10.1109/PESGM.2017.8273944.
- [32] EPISCOPE. IEE Project TABULA.

## A Appendix

- [33] ESI ITI. SimulationX 3.8 — Green City.
- [34] W. El-Baz, J. Honold, L. Hardi, and P. Tzscheutschler. High-resolution dataset for building energy management systems applications. *Data in Brief*, 54:1–5, 2018. doi:10.1016/j.dib.2017.12.058.
- [35] L. Frías-Paredes, F. Mallor, T. León, and M. Gastón-Romeo. Introducing the Temporal Distortion Index to perform a bidimensional analysis of renewable energy forecast. *Energy*, 94:180–194, 2016. doi:10.1016/j.energy.2015.10.093.